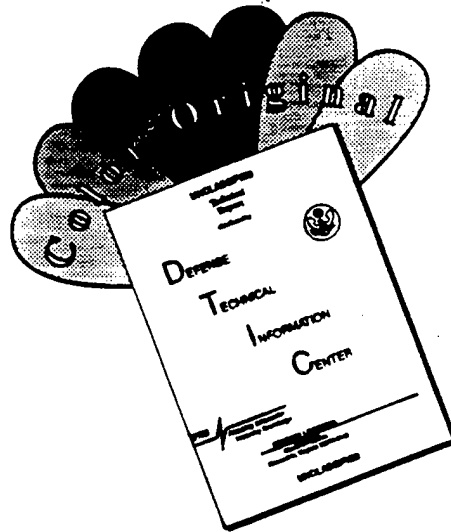


DISCLAIMER NOTICE



THIS DOCUMENT IS BEST QUALITY AVAILABLE. THE COPY FURNISHED TO DTIC CONTAINED A SIGNIFICANT NUMBER OF COLOR PAGES WHICH DO NOT REPRODUCE LEGIBLY ON BLACK AND WHITE MICROFICHE.

THESIS

**IDENTIFICATION OF POTENTIAL AIRCRAFT ICING REGIONS
THROUGH MULTISPECTRAL ANALYSIS OF GOES-8 IMAGERY**

Submitted by

Bradford D. Schrumpf

Department of Atmospheric Science

In partial fulfillment of the requirements

for the Degree of Master of Science

Colorado State University

Fort Collins, Colorado

Summer 1996

COLORADO STATE UNIVERSITY

June 24, 1996

WE HEREBY RECOMMEND THAT THE THESIS PREPARED UNDER OUR SUPERVISION BY
BRADFORD D. SCHRUMPF ENTITLED IDENTIFICATION OF POTENTIAL AIRCRAFT ICING
REGIONS THROUGH MULTISPECTRAL ANALYSIS OF GOES-8 IMAGERY BE ACCEPTED AS
FULFILLING IN PART REQUIREMENTS FOR THE DEGREE OF MASTER OF SCIENCE.

Committee on Graduate Work

Charles-yon He
Thomas Wondol

Wayne Schubert
Adviser

Stephen K. Cox
Department Head

ABSTRACT OF THESIS

IDENTIFICATION OF POTENTIAL AIRCRAFT ICING REGIONS THROUGH MULTISPECTRAL ANALYSIS OF GOES-8 IMAGERY

Aviation weather forecasters are still greatly challenged to forecast aviation weather hazards for large areas of atmosphere with few in-situ observations and little detailed information from which to work. Forecasters generally lack sufficient guidance to assist them in the prediction of icing occurrences or intensity. In-flight aircraft icing remains a significant aviation hazard. Icing intensity is related to the rate of accretion as well as the aircraft type and the icing's effects on aircraft flight performance. Icing regions currently can only be identified from subjective reports made by aircraft pilots (PIREPs).

The severity of aircraft icing is found to be quite sensitive to temperature, liquid water content, and droplet size distribution along the flight path within the icing cloud. The difficulty of their direct measurement and the variability of these factors with altitude, position, and time, coupled with variable aircraft sensitivities, make forecasting and identifying icing environments quite difficult.

With the advent of the next generation of Geostationary Operational Environmental Satellites (GOES), additional spectral channels with improved ground resolution are available for use in a wide variety of research applications. One important outcome of applied research based on improved GOES-8 imager products is analysis technique developments that will lead to better forecasts of hazardous aircraft flying conditions.

In this study, GOES-8 multispectral satellite images and imagery data are manipulated, combined, and enhanced to retrieve clues about cloud phase (ice or liquid), supercooled cloud liquid water (SLW), and cloud-top temperature (CTT). To retrieve information on cloud phase, SLW, and CTT, the known spectral characteristics of several GOES-8 channels (specifically 1, 2, and 4) are used to interrogate the cloud top's radiative properties. This information is used to determine whether aircraft icing is likely

within these clouds through application of a simple, multispectral analysis scheme. The period of study consists of known, significant in-flight aircraft icing events that occurred in April 1995.

This thesis includes a survey of the literature on previous and current icing studies and the use of PIREPs as a verification tool, research on new techniques using improved satellite imagery to better identify regions of aircraft icing potential, and suggestions for future work or research towards the goal of the improvement of aircraft icing forecasts.

The multispectral channel difference method is most useful when only large-scale stratiform cloud regions are considered. In these two case studies, scatter plots of the GOES-8 channel 2 cloud reflectance component versus channel 1 cloud albedos show how the more intense icing PIREPs cluster within a small range according to the clouds' microphysical characteristics. Inclusion of convective clouds to this multispectral scheme leads to erroneous assumptions of cloud phase and SLW based on their colder CTTs when this technique is applied.

In both cases, the majority of the icing PIREPs occurred within areas with CTTs colder than the typical icing CTT zone (IZ) (73% in Case 1), however many significant intensity icing PIREPs did occur within the IZ in Case 2 (44%) when the cloud shield became more stratiform. The icing PIREP verification was fairly inconclusive for stratiform regions due to a relative lack of icing reports in some portions of the stratiform cloud deck.

The multispectral RGB color enhancement method does a good job at distinguishing clouds of different heights with the greatest color and shade contrast between the high and low clouds. Some information on cloud phase and SLW clouds seems evident from inspection of the middle cloud deck color hues, but the result is not yet reliably quantitative. This information could be used qualitatively to help in initial icing assessment for larger-scale cloud regions.

Detection of potential icing environments using infrared and visible satellite imagery remains a challenge for cloud regions made up of convective clouds or a mix of both convective and stratiform types.

Bradford D. Schrumpf
Department of Atmospheric Science
Colorado State University
Fort Collins, CO 80523
Summer 1996

ACKNOWLEDGEMENTS

I wish to thank my advisor, Dr. Wayne H. Schubert, and my other committee members, Dr. Thomas H. Vonder Haar and Dr. Chiao-yao She, for their guidance and support during this study. It was during Dr. Vonder Haar's excellent AT737 satellite course that I became interested in the subject of this thesis. Thankfully, Dr. Schubert gave me the freedom to pursue some meteorological topics for my thesis research that are very applicable to my sponsor's (U.S. Air Force) graduate objective and very interesting to me.

Many thanks also go to Rick Taft and Kelly Dean for their invaluable help with the computer systems that I used to generate the PIREP and satellite imagery products. Thanks also to Nan McClurg for her assistance in satellite imagery data collection and for keeping the CIGS Room IRIS terminal open for me when I needed it. I also appreciated Robert Kerr's months of patience and help in trying to acquire PIREP data from the Aviation Weather Center in Kansas City.

A special note of appreciation goes to Greg Thompson, Dr. Barbara Brown, Dr. Marcia Politovich, and Ben Bernstein of NCAR for their expert advice and inciteful discussions on PIREP usage and aircraft icing forecast problems. In particular, I'm indebted to Greg Thompson for the use of some of his PIREP decoding and plotting software and for supplying the bulk of the raw PIREP data used for the verification.

Most importantly, I thank my wonderful wife, Alison, for her love, ideas, support, encouragement and constructive critiquing during the process of completing this study. It has been quite a wonderful experience for the both of us here at CSU.

----- Brad Schrumpf

TABLE OF CONTENTS

1	Introduction / Motivation	1
1.1	Overview of the Aircraft Icing Hazard.....	1
1.2	Types and Causes of Icing	2
1.3	Current Aircraft Icing Forecast Methods	3
1.4	Overview of Research on Aircraft Icing Variables	4
1.5	Research Objective.....	7
2	Aircraft Icing.....	9
2.1	Aircraft Ice Accretion (Icing).....	9
2.1.1	Types	9
2.1.2	Growth.....	10
2.1.3	Intensity	13
2.2	Meteorological Factors Contributing to Icing	14
2.2.1	Temperature.....	14
2.2.2	Liquid Water Content (LWC).....	15
2.2.3	Droplet Sizes.....	16
2.2.3.1	Environmental Conditions for Large Drop Regions	17
2.2.3.2	Hazards from Large Drop Regions	18
2.2.4	Cloud Phase	19
2.2.5	Cloud Type	20
2.2.6	Frontal Zones.....	20
2.2.7	Vertical Updrafts and Turbulence	23
2.2.8	Seasonal and Geographic Influences	23
2.3	Aircraft Icing Forecasting	25
2.3.1	AWC Method	25
2.3.2	AWS Method.....	26
2.4	Aircraft Influences on Icing	28
2.4.1	Structural Airframe Icing.....	28
2.4.2	Type of Aircraft.....	29
2.4.3	Induction (Carburetor) Icing.....	30

2.4.4	Results of Aircraft Icing Accident Study.....	31
2.5	Past and Current Studies on Icing Detection and Prediction.....	32
2.5.1	Field Program (WISP).....	32
2.5.2	Icing Algorithm Research.....	33
2.5.2.1	Icing Algorithms	33
2.5.2.2	Algorithm Verification.....	34
2.5.2.3	Model Comparisons	35
2.5.3	Other Recent Important Icing Studies	35
2.5.3.1	Using An Array of Ground-Based Remote Sensing Systems	35
2.5.3.2	Satellite Sensing of Cloud Liquid Water Over Oceans	36
2.5.3.3	Satellite Sensing of Cloud Liquid Water Over Land.....	38
2.5.3.4	Using Multispectral GOES-8 Imagery	39
3	Pilot Reports (PIREPs).....	41
3.1	Description of PIREPs.....	41
3.2	Methods of Scientific Research Verification Using PIREPs.....	43
4	Satellite Background	46
4.1	Passive Visible and Infrared (IR) Remote Sensing	46
4.1.1	Atmospheric Windows	46
4.1.2	Radiative Transfer Theory.....	48
4.1.3	Spectral Properties of Clouds	50
4.2	Satellite Sensing	53
4.2.1	Passive Satellite Imaging.....	53
4.2.2	Satellite Spectral Band Characteristics	54
4.2.2.1	Visible Band.....	55
4.2.2.2	Longwave IR (LIR) Band	56
4.2.2.3	Shortwave IR (SIR) Band	59
4.2.2.4	Water Vapor Band.....	63
4.2.2.5	Microwave Region	63
4.3	Analysis and Display Methods for Satellite Imagery.....	64
4.3.1	Black and White / Grayscale / Color Enhancements	64
4.3.2	Multispectral RGB Color Enhancement Method.....	65
4.3.3	Multispectral Channel Differencing Method.....	66
4.4	GOES-8 Imager.....	67
4.4.1	GOES Background	67
4.4.2	Imager Characteristics Compared to GOES-VAS	70

4.4.3	Spectral Improvements Over GOES-7	72
5	Icing Case Studies Research.....	77
5.1	Overview.....	77
5.2	Data Collection.....	78
5.2.1	PIREPs.....	78
5.2.1.1	Collection and Display	78
5.2.1.2	Selection for Verification	80
5.2.2	Case Selection.....	80
5.2.2.1	Case 1 (10 Apr 95)	80
5.2.2.2	Case 2 (11 Apr 95)	82
5.2.3	Satellite Imagery.....	88
5.2.3.1	Collection	88
5.2.3.2	Display	94
5.2.3.3	Selection	94
5.2.4	Rawinsonde (Sounding) Data	95
5.2.5	Upper Air, Surface, and Forecast Weather Charts.....	95
5.3	Icing Study.....	96
5.3.1	Methodology.....	96
5.3.1.1	Temperature Regime	96
5.3.1.2	Supercooled Liquid Water (SLW) Locations	97
5.3.2	Multispectral Channel Differencing (ΔT_b) Study	97
5.3.2.1	Past Studies	97
5.3.2.2	Application to Cases 1 and 2	97
5.3.2.3	Strengths and Weaknesses of Method	98
5.3.3	Multispectral RGB Color Enhancement Study.....	99
6	Results and Conclusions of the Icing Studies.....	101
6.1	Discussion of Results	101
6.1.1	ΔT_b Method for Case 1	101
6.1.2	ΔT_b Method for Case 2	103
6.1.3	RGB Method for 10 Apr 95.....	105
6.2	Conclusions.....	106
6.3	Suggestions for Future Work	109
7	References.....	150

LIST OF FIGURES

2.1	Typical dry (rime) and wet (mixed/clear) ice shapes (from Hansman 1989).....	11
2.2	Modes of energy transfer from an icing surface (from Hansman 1989).....	12
2.3	Effects of temperature on ice shape (from Olsen et al. 1984).....	15
2.4	Collection efficiency versus impacting droplet diameter for different airfoil sizes and airspeeds (from Politovich 1993).....	17
2.5a	Cold front icing zone (from USAF 1992).....	22
2.5b	Warm front icing zones (from USAF 1992).....	22
2.6	Plot of aircraft icing accidents (1975-88) on U.S. map (from Cole and Sand 1991).....	24
2.7	Sample AIRMET Icing Forecast Product	27
2.8	Sample AFGWC Icing Forecast Product	27
3.1	Example pilot report (PIREP) plot with icing intensity codes, icing type symbols, and icing base / top altitudes (in hundreds of feet AGL).....	42
3.2	Spatial distributions of PIREPs in 1° latitude/longitude regions (each X represents at least 40 PIREPs over a two year period (1990-1992) (from Brown 1993).....	43
4.1	Visible and infrared transmittance versus wavelength showing atmospheric windows (from Kidder and Vonder Haar 1995).....	48
4.2	Scattering regimes (from Kidder and Vonder Haar 1995).....	50
4.3	Uninverted IR image for 10 Apr 95 1745Z.....	57
4.4	Inverted IR image for 10 Apr 95 1745Z	58
4.5	Schematic showing the radiation components reaching channel 2 of GOES-8 imager (from Liljas 1986).....	61
4.6	Brightness temperature versus time for SIR and LIR channels on GOES-VAS (from Kleespies 1995).....	61
4.7	Sketch of GOES-8 spacecraft (from Kidder and Vonder Haar 1995).....	69
4.8	Sketch of the GOES-8 Imager (from Kidder and Vonder Haar 1995).....	70
5.1	Plot of pilot reports of 4+ (lgt-mdt or greater) intensity for 6 hr period on 10 Apr 95	79
5.2	Example grid overlaying visible image at 10/1745Z Apr 95	81
5.3	Example visible GOES-8 image from 10/1815Z Apr 95	83

5.4	Example SIR GOES-8 image from 10/1815Z Apr 95	84
5.5	Upper air weather chart (500mb) for 10/1200Z Apr 95.....	85
5.6	Surface weather chart for 10/1800Z Apr 95	85
5.7	Weather radar summary for 10/2135Z Apr 95.....	86
5.8	Upper air weather chart (850mb) for 10/1200Z Apr 95.....	87
5.9	Upper air weather chart (700mb) for 10/1200Z Apr 95.....	87
5.10	Upper air weather chart (500mb) for 11/1200Z Apr 95.....	89
5.11	Surface weather chart for 11/1800Z Apr 95	89
5.12	Weather radar summary for 11/2135Z Apr 95.....	90
5.13	24 hr precipitation summary for 11/1200Z Apr 95.....	91
5.14	24 hr precipitation summary for 12/1200Z Apr 95.....	91
5.15	Observed snow cover summary for 11/1200Z Apr 95.....	92
5.16	Observed snow cover summary for 12/1200Z Apr 95.....	92
5.17	Upper air weather chart (850mb) for 11/1200Z Apr 95.....	93
5.18	Upper air weather chart (700mb) for 10/1200Z Apr 95.....	93
6.1a	Scatter plot of null (0 intensity - no icing) PIREPs (Case 1)	115
6.1b	Scatter plot of all icing (1-7 intensity) PIREPs (Case 1).....	115
6.1c	Scatter plot of null and all icing PIREPs (Case 1)	116
6.1d	Scatter plot of all (1-7), moderate or greater (4+), and extreme (5+) icing PIREPs (Case 1).....	116
6.2a	Scatter plot of all PIREPs (0-7 intensity) within the Icing Zone (IZ) (Case 1).....	121
6.2b	Scatter plot of all PIREPs within the Convective Zone (CZ) (Case 1)	121
6.3	Grid showing shaded sectors of stratiform clouds (Case 1).....	122
6.4a	GOES-8 channel 1 (visible) image of U.S. for 10/1745Z Apr 95 (Case 1)	123
6.4b	GOES-8 channel 1 (inverted visible) image of U.S. for 10/1745Z Apr 95 (Case 1)	124
6.4c	GOES-8 channel 2 (inverted SIR) image of U.S. for 10/1745Z Apr 95 (Case 1).....	125
6.4d	GOES-8 channel 4 (inverted LIR) image of U.S. for 10/1745Z Apr 95 (Case 1)	126
6.5	Composite plot of all PIREPs from 1500-2100Z on 10 Apr 95 (Case 1)	127
6.6	Skew-T, log-P diagram for North Platte, NE (LBF) at 10/1200z Apr 95 (Case 1).....	128
6.7	Skew-T, log-P diagram for Dodge City, KS (DDC) at 10/1200z Apr 95 (Case 1).....	128
6.8a	Scatter plot of null (0 intensity - no icing) PIREPs (Case 2)	133
6.8b	Scatter plot of all icing (1-7 intensity) PIREPs (Case 2).....	133
6.8c	Scatter plot of null and all icing PIREPs (Case 2)	134
6.8d	Scatter plot of all (1-7), moderate or greater (4+), and extreme (5+) icing PIREPs (Case 2).....	134
6.9a	Scatter plot of all PIREPs (0-7 intensity) within the Icing Zone (IZ) (Case 2).....	139
6.9b	Scatter plot of all PIREPs within the Convective Zone (CZ) (Case 2)	139

6.10	Grid showing shaded sectors of stratiform clouds (Case 2)	140
6.11a	GOES-8 channel 1 (visible) image of U.S. for 11/1745Z Apr 95 (Case 2)	141
6.11b	GOES-8 channel 2 (inverted SIR) image of U.S. for 11/1745Z Apr 95 (Case 2)	142
6.11c	GOES-8 channel 4 (inverted LIR) image of U.S. for 11/1745Z Apr 95 (Case 2)	143
6.12	Composite plot of all PIREPs from 1500-2100Z on 11 Apr 95 (Case 2)	144
6.13	Skew-T, log-P diagram for North Platte, NE (LBF) at 11/1200z Apr 95 (Case 2)	145
6.14	Skew-T, log-P diagram for Omaha, NE (OAX) at 11/1200z Apr 95 (Case 2)	145
6.15a	Skew-T, log-P diagram for Topeka, KS (TOP) at 11/1200z Apr 95 (Case 2)	146
6.15b	Skew-T, log-P diagram for Denver, CO (DNR) at 11/1200z Apr 95 (Case 2)	146
6.16	Skew-T, log-P diagram for Springfield, MO (UMN) at 11/1200z Apr 95 (Case 2)	147
6.17	Skew-T, log-P diagram for Green Bay, WI (GRB) at 11/1200z Apr 95 (Case 2)	147
6.18	Multispectral RGB-411 Imagery for 10/1815Z Apr 95	148
6.19	Multispectral RGB-241 Imagery for 10/1815Z Apr 95	149

LIST OF TABLES

2.1	Icing intensities, types, and a sample pilot report (from FAA 1977).....	13
4.1a	GOES-8 imager instruments' characteristics (from Kidder and Vonder Haar 1995)	74
4.1b	GOES-8 imager channels' characteristics (from Kidder and Vonder Haar 1995).....	74
4.2	GOES-8 imager and sounder instrument features (from Menzel and Purdom 1994)	75
4.3a	GOES-7 and GOES-8 imager characteristics (from Menzel and Purdom 1994).....	76
4.3b	Expected improvements in GOES-8 imager products (from Menzel and Purdom 1994).....	76
6.1a-c	PIREPs for Case 1 (10 Apr 95 1500-2100Z)	112
6.2a-d	Grid of pixel dump values for Case 1 from 1745Z imagery	117
6.3a-d	PIREPs for Case 2 (11 Apr 95 1500-2100Z)	129
6.4a-d	Grid of pixel dump values for Case 2 from 1745Z imagery	135

Chapter 1 — Introduction / Motivation

1.1 Overview of the Aircraft Icing Hazard

In-flight aircraft icing poses a significant hazard to the aviation community, as witnessed by the crash of a commuter airplane in northern Indiana in the fall of 1994. This crash had a major impact on the commuter airline safety regulations in the U.S., which resulted in significant economic and other impacts on the airline industry as a whole (Brown, 1995b).

The great hazards of icing, including structural airframe icing and induction (carburetor) icing, on both fixed-wing and rotary aircraft have long been realized. With over 1000 aviation accidents in the continental United States during the last twenty years (Cole and Sand, 1991) citing aircraft icing as a major factor, it is a problem that has not been overlooked. However, due to the relative inaccuracy of icing forecasts during this period and lack of detailed information from which to work, aviation weather forecasters have not been very successful at pinpointing altitudes and areas of icing hazard without creating large false-alarm (over-forecasted) areas. When this over-forecasting occurs, the pilots' confidence in these forecasts go down; analogous to the little boy who cried wolf too often. Consequently, pilots are more apt to ignore these forecasts and sometimes cause accidents as a result.

Cole and Sand (1991) showed compelling statistics to support this view and their findings are summarized in Chapter 2. They found that it is not predominantly the low-time, inexperienced pilots who are involved in icing accidents. Apparently, many pilots are not taking appropriate evasive or precautionary actions, when hazardous icing conditions are encountered during flight or forecasted in their required weather briefings prior to takeoff. Surprisingly, nearly 60 percent of those pilots involved in aircraft icing accidents had been properly informed on the icing threat and conditions during pre-flight weather briefings. This suggests that there exists a lack of understanding or concern in the seriousness of icing's effects on the performance of the aircraft, a lack of faith in the forecast, and/or a general lack of understanding of the many factors contributing to icing conditions.

Ultimately, it is the pilot's duty to know the strengths and weaknesses of their type of aircraft and to evaluate its sensitivities to icing conditions for different environments before making the flight through a potentially hazardous region. On the other hand, it is the aviation forecaster that must be considerate of the

flying community's needs and by striving to maximize the icing forecast's precision, so as to limit the spatial extent (both horizontally and vertically) of areas which would prohibit reasonable access to a substantial variety and number of aircraft. Thus, for aviation purposes, the goal of any icing forecast system and for most recent aircraft icing studies should be to minimize the forecasted area while maintaining a high detection/verification rate. It is undesirable to over-forecast regions of icing and unnecessarily make them virtually inaccessible to aircraft. This goal is also true for AIRMETs, the current operational aviation hazard forecast, as well as for the forecast model algorithms and remote sensing techniques that are being developed to improve them (Brown, 1996b).

1.2 Types and Causes of Icing

An abundance of literature has identified and verified the general meteorological conditions required for aircraft in-flight icing in clouds (Schultz and Politovich, 1992; USAF, 1992; Hansman, 1989; AWS, 1980; Politovich, 1993; etc.) with some new factors presently being discovered and further researched. Many of these factors are discussed further in Chapter 2, but are summarized below.

Two distinct processes control the accretion of ice onto aircraft surfaces as determined by Hansman (1985). First, supercooled liquid water (SLW; water existing colder than 0°C) cloud droplets must impact the air frame. Secondly, these SLW droplets must freeze onto the airframe as allowed by local heat-transfer processes along the airframe. As supercooled liquid cloud droplets impact on the aircraft, they can splash and freeze immediately, or they can flow back along the airframe somewhat before freezing. If the droplet can release its latent heat relatively quickly (typically in an icing environment of colder temperatures, smaller droplets, and lower total liquid water mass), it will freeze at the impingement point, and rime ice will form. This is usually most dangerous when occurring in large amounts on smaller aircraft. When the impacting droplets have more time to flow prior to freezing due to a slower removal of latent heat (typically in an icing environment of warmer (sub-freezing) temperatures, larger droplets, and higher total water mass), clear ice or glaze will form. This type of icing is much harder to detect visually by the pilot, which gives less time to take precautionary measures against it. While clear icing is the most uncommon, it is the most dangerous type for aircraft. Transitions between clear and rime icing can occur

within the same cloud, and flight through these conditions can cause both types of ice to accumulate. This condition is often reported as mixed ice.

In the past, the method of forecasting meteorological conditions favorable to aircraft icing was largely a matter of predicting cloudy environments (as the source for the generation of SLW) in the appropriate temperature range (between +4 and -40 degrees Celsius). As described in further detail in Chapter 2, the type and intensity of the ice accretion is strongly and non-linearly dependent on many environmental variables such as temperature, liquid water content (LWC), cloud droplet sizes and distributions, cloud water phase, and turbulence or shear layers aloft. Additionally, the intensity of the icing and its effect on aircraft performance depends on both the type and condition of the aircraft. The icing forecasting challenge lies in the fact that most of these factors are somewhat hard to determine due to the natural variability of clouds (Schultz and Politovich, 1992; Pobanz, 1994), and this characteristic makes it difficult, if not impossible, to completely isolate the individual effects of these icing factors in nature. One would like to ultimately quantify these variables prior to flight, yet scientific methods at present do not allow for this.

1.3 Current Aircraft Icing Forecast Methods

Presently, there exists no formal training program for icing forecasting within the NWS. Prediction is based on a loose set of guidance tools and their emphasis can vary with each forecaster. This results in a variety of methods in use by icing forecasters at the Aviation Weather Center (AWC; formerly the National Aviation Weather Advisory Unit (NAWAU)), which in turn leads to high degree of variability in forecast accuracy, since the method used for each forecast is not recorded (Politovich and Olson, 1991). The standard aircraft icing forecasts, or AIRMETs (Airmen's Meteorological Information), are created by NWS forecasters using a wide variety of available information and are issued operationally every six hours and are amended as necessary by the National Oceanic and Atmospheric Administration's National Weather Service (NOAA/NWS) Aviation Weather Center (AWC) in Kansas City.

The Air Force also issues time-phased icing forecasts for the Northern Hemisphere for the layer between 10,000 and 55,000 feet from their Air Force Global Weather Center (AFGWC) at Offutt AFB,

Nebraska (AWS, 1980). However, they are generally a high altitude supplement to (and normally consistent with) the AIRMETs given to military aircrews. Both forecasting methods are described further in Chapter 2. The icing AIRMETs were also used in the icing forecast, numerical model algorithm comparison by Brown et al. (1996b), as a standard-of-reference. For the comparison, it is important to note that the NWS forecasters issuing the AIRMETs have other supplementary information, such as satellite imagery, and current PIREPs, available to them to enhance their forecasts and this additional data is not taken into account as of yet by present automated icing algorithms. In fact, AIRMET forecasters are able to use the present AWC/NAWAU icing algorithms as forecast guidance.

1.4 Overview of Research on Aircraft Icing Variables

Aircraft certified for flight in known icing conditions can operate for only a limited time. However, they may not be able to cope with prolonged exposure or with extreme encounters. The general aviation community has been particularly vocal in calling for improved icing forecasts and for renewed attention to this hazard. In recognition for this need, the office of the Federal Coordinator for Meteorological Services and Supporting Research (FCM) issued a document in 1986 addressing these needs, entitled "The National Aircraft Icing Technology Plan. It called for an evaluation of existing techniques and the development of improved methods for detecting and forecasting icing conditions. In 1988, the Federal Aviation Administration (FAA) funded the National Center for Atmospheric Research (NCAR) Research Applications Program (RAP) to plan a multi-year program to improve aircraft icing forecasting. The FAA Icing Forecasting Improvement Program Experimental Design (Politovich, 1989a; Sand and Politovich, 1991) was completed in the Fall of 1989, and the 6 year FAA Icing Forecast Improvement Program began in October of that year.

In the past, aircraft icing studies have taken several approaches (Rasmussen et al., 1992). Some of the aircraft icing environment research has been conducted in wind tunnels, where the nature of accreted ice is examined on different airfoils (including Gayet et al., 1984; Hansman, 1985; Hansman and Kirby, 1986; Shin et al., 1991) and using remote sensing devices (Arking and Childs, 1985; Popa Fotino et al., 1986; d'Entremont, 1986; Osborne, 1989). Numerical models have simulated accretion, predicted

supercooled liquid water, and determined the effects of temperature, liquid water content, droplet size, and other factors on icing type and intensity (e.g., Newton, 1978; Hansman, 1985; Smart et al., 1992). Many in-flight icing studies have concentrated on the analysis of environmental factors and their relation to ice accretion in both continental and maritime regions (Bain and Gayet, 1982; Hansman and Kirby, 1986; Hoffmann, 1988; Politovich, 1989b; Hoffmann, 1990; Politovich, 1993; Cober et al., 1995; Fuchs and Schickel, 1995) or its performance degradation on the aircraft (Cooper et al., 1984; Sand et al., 1984; Sand, 1985). Relatively little research has been conducted on the relationship of icing-related parameters to icing observations (mainly pilot reports) routinely available to operational forecasters (Sand et al., 1984; Guttman and Jeck, 1987). The FAA Icing Forecasting Improvement Program chose to emphasize the latter studies, using the NOAA Forecast Systems Lab (FSL), and Aviation Weather Center (AWC; formerly NAWAU) as test-beds.

As this program evolved, it became clear that there existed excellent opportunities for a collaboration between investigators interested in the applied topic of aircraft icing and those interested in the physical processes of winter storms and production of supercooled cloud water. It was then decided to form a larger field research program, known as WISP, to incorporate a broadening interest in these variables. The Winter Storms and Icing Project (WISP; Rasmussen et al., 1992) was designed to further the understanding of the dynamical and microphysical processes leading to the production and depletion of supercooled liquid water (SLW) in winter storm clouds and to improve icing forecasts. The observational strategy utilized for WISP was based on collecting in-situ and remotely sensed data that could be used to increase our understanding of the various processes active during winter storm events. Since the AWC was the eventual recipient of the product improvements, WISP research focused on automating techniques currently used in AWC forecasting, and in developing improvements on these methods based upon their research results.

From WISP, came a new surge in research in the area of aircraft icing and production of SLW. Most of these studies have focused on the development of algorithms that can be applied to the output of national or regional-scale numerical weather prediction models in order to diagnose and predict aircraft icing conditions (e.g., Rasmussen et al., 1992, Schultz and Politovich, 1992, Knapp, 1992, Forbes et al.,

1993, Thompson et al., 1995 and 1996b, Marwitz et al., 1996). Availability of such algorithms would be very useful for pilots and air-traffic controllers if the algorithms can be shown to be accurate and reliable. Currently, these algorithms are rather unsophisticated, being based simply on whether modeled atmospheric conditions meet specified temperature and humidity criteria (Brown et al., 1995a). Unfortunately, determining the accuracy of aircraft icing forecasts is not straightforward, primarily due to limitations in the availability and quality of data to verify such products. Currently, the best available data for verification of icing regions are pilot reports.

Icing forecast verification via pilot reports (PIREPs) is hampered by several deficiencies that will be discussed in Chapter 3. First, PIREPs are a function of the number of aircraft flying through an area at any given time, place, or altitude. Icing conditions will not be reported, even if they exist, if no aircraft fly through the area. Also, PIREPs are made at the discretion of the pilot. They are made according to the pilot's interpretation of the atmospheric conditions, how it affects aircraft performance, and his/her experience. Additionally, reported intensities are also dependent on the individual aircraft type, so that reports are not always consistent with the existing meteorological conditions. The result of these defects in the verification procedure is that icing probably occurs more often and over wider areas than is reported. This lack of positive icing reports may also result from the lack of pilots deciding to fly their aircraft through regions for which they have been warned may be an icing threat.

Other recent research has focused on the emergence of new ground-based remote sensing and satellite sensing technologies as a tool to better detect icing conditions and predict icing environments (e.g., Jones and Vonder Haar, 1990; Curry and Liu, 1992; Schickel et al., 1994; Stankov and Bedard, 1994; Lee et al., 1994; Kleespies, 1995; Brandes et al., 1995; Lawyer, 1995; Politovich et al., 1995; Ellrod, 1996a). Several of these studies will be summarized in Chapter 2. Unfortunately, routine atmospheric measurements of relevant icing parameters are not nearly dense enough to accurately predict temperatures and LWC, or determine SLW distributions within clouds on a large scale. Also, measurements or estimates of cloud droplet size are simply not widely available, except for short, field research flight experiments.

Research continues on the use of ground-based microwave radiometers, satellite-borne sensors, and other techniques for remote detection of icing environments. Satellite imagery can be useful for diagnosing icing / no-icing regions when combined with a three-dimensional temperature analysis of the cloudy environment. Thermal infrared (IR) imagery can detect cloud-top temperatures and imply cloud height when not contaminated by overlying cirrus clouds. But with the improved imaging package on the next generation of GOES, better resolution and additional spectral channels hold hope for an improvement forecasts of icing conditions, as sensed by satellites.

1.5 Research Objective

Aviation forecasters are still greatly challenged to forecast aviation weather hazards for large areas of atmosphere with few detailed observations and little guidance information from which to work. One encouraging tool for these forecasters are the satellites that orbit our planet. With the advent of the next generation of Geostationary Operational Environmental Satellites (GOES-8), additional spectral channels with improved areal resolution are available for use in a wide variety of research applications. One important outcome of this applied research is technique developments that will lead to improved forecasts of hazardous aircraft flying conditions.

In this study, GOES-8 multispectral satellite imagery data (using channels 1, 2, and 4) are manipulated, combined, and enhanced to retrieve clues about cloud phase, supercooled cloud liquid water (SLW), and cloud-top temperature (CTT). To retrieve information on cloud phase and SLW, the known characteristics of several GOES-8 spectral channels are used to investigate the cloud top's emissivity/absorptivity/reflectivity. This information is used to determine whether aircraft icing is likely within these clouds through a simple, cloud-top analysis scheme. The period of study consists of known, significant icing events that occurred in April 1995. The purpose is to infer through inspection of cloud-top IR channel brightness temperatures and visible channel albedos whether the cloud is an icing threat to aircraft by comparison to known hazard regimes for icing variables.

The goals of this study are to test multispectral techniques based on the improved GOES-8 spectral package and satellite imagery that can be used simply as an operational forecasting tool for the

purpose of identifying regions with aircraft icing potential, and the analysis and short-range prediction of aircraft icing. This paper will also discuss some results after applying these techniques to known icing events. In particular, Chapters 2 and 3 will go into more depth on icing and PIREPs. An overview of the applicable radiative transfer theory for satellite sensing / imaging of clouds, and the GOES-8 satellite imager with its improvements and spectral package will be described in Chapter 4. Then, Chapter 5 will describe the data collection, study methodology, and data processing (computer) resources used to accomplish the study. Lastly, the results from the PIREP verification analyses, research conclusions, and suggestions for future work will be discussed in Chapter 6.

Chapter 2 — Aircraft Icing

Past methods of forecasting meteorological conditions favorable to aircraft icing depended mainly on predicting cloudy environments (as the source for the generation of SLW) in the appropriate temperature range (between +4 and -40 degrees Celsius). However, the ice accretion process has been found to be also greatly affected by temperature, liquid water content (LWC), the size and concentration of the cloud droplets, the cloud phase, and the presence of shear layers in the cloud's environment, among others. This chapter will go into detail on these different factors that affect the ice accretion process. The accurate forecasting of meteorological conditions favorable to aircraft icing is difficult for several reasons. Most importantly, because these parameters are hard to measure or estimate within the forecasting environment.

2.1 Aircraft Ice Accretion

The aircraft icing process is controlled by two physically distinct processes. The first is the in-flight collision of liquid water droplets from the ambient cloud environment to the surface of the aircraft (typically leading edge of wings and fuselage). Then, once the droplets have impacted the airframe, their freezing is mainly controlled by the droplet's size, aircraft velocity and shape, and thermodynamic processes (Hansman, 1985).

2.1.1 Types

If the heat transfer from the surface is sufficient to remove all of the latent heat of freezing of the impinging water, then the droplets will freeze on impact resulting in a dry ice surface. The ice shape typically protrudes forward into the airstream and is commonly reported as "rime icing". Rime ice is opaque or whitish in color and rough in texture due to the quick freezing of small, supercooled water droplets trapping large amounts of air between the impacting droplets, making it also quite brittle (AWS, 1980). Rime ice is most likely encountered in stratiform clouds, but may also occur in cumulus-type clouds, with temperatures typically between 0°C and -20°C (but as cold as -40°C in cumulonimbus). It is

relatively easy to remove by conventional de-icing methods, even though it distorts the airfoil more than "clear icing" (USAF, 1992)

When the heat transfer from the surface does not remove all of the latent heat from impacting droplets, the ice surface becomes wet and is reported as glaze or "clear icing". This clear or glossy glaze is much like that which forms on trees as freezing rain falls to the ground. Clear ice is perhaps the least common type, but the most dangerous form of icing for aircraft because it adheres so firmly to the airframe (Politovich, 1993). It is most commonly encountered in cumuliform clouds, freezing rain or drizzle, and environments with high liquid water contents, large droplet sizes ($>40\mu\text{m}$), and warmer cloud temperatures between 0°C and -10°C (but as cold as -25°C in deep convection) (USAF, 1992). Clear ice is generally smooth, but can be rough textured. It is smooth when deposited from large SLW or drizzle size droplets that spread back and freeze slowly, taking the shape of the leading edge on which they impinge. If the impacting droplets are smaller and/or mixed with ice crystals or graupel (soft hail), the clear ice takes on a more rough, irregular look that builds horn-like shapes back into the airflow. This is sometimes referred as "mixed icing" and can also occur during flight through clouds with environments exhibiting both types of icing. The most severe aircraft performance degradation is typically associated with such horned ice formations (Hansman, 1989).

2.1.2 Growth

The physical processes which govern icing are distinctly different for wet and dry ice growth. In dry growth, the ice accretion is controlled by the local rate of liquid water impacting the surface. This mass flux of water is determined by the droplet trajectories as they pass through the flow field surrounding the airframe. Because the airframe is not permeable, flow streamlines do not intersect the body of the aircraft and the collection efficiency is typically highest at the stagnation point for the body, while decreasing downstream. The collection efficiency of the body (airframe or wing) is a strong function of droplet size and body geometry (Hansman and Kirby, 1986). Large water droplets will tend to cross the streamlines more readily and consequently impact more easily (leading to higher collection efficiencies) due to their greater inertia with respect to smaller droplets. Small droplets will follow the streamlines

more, resulting in lower collection values with most impacts at the stagnation point (Figure 2.1). Also important to note, smaller airframe surfaces (e.g. leading edges of wings, tails, and propellers) are more efficient droplet collectors, because there is less room for the droplets to turn prior to impingement. Thus, the relatively thick wings and canopies of larger commercial and cargo jet aircraft have a smaller collection potential than those of the trimmer, commuter turbo-prop or recreational aircraft. Smaller aircraft also have less available power to counteract the flight degradation from icing and typically little to no equipment to counteract icing effects.

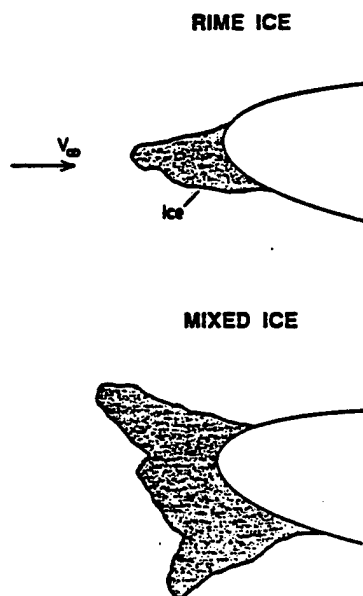


Figure 2.1 Typical dry (rime) and wet (mixed/clear) ice shapes (from Hansman 1989)

During wet growth, the ice collection is determined by the rate at which the latent heat of fusion can be removed from the surface of the airframe or the existing ice surface. This thermodynamic heat balance determines whether the accumulating ice surface grows through clear/mixed or rime processes. Figure 2.2 depicts the principle modes of energy transfer associated with an icing surface. Heat is added to the body surface primarily by the latent heat of fusion released as the droplets freeze, but also include the

aerodynamic heating based on the aircraft's velocity, and droplet kinetic energy impacting the surface to an even smaller extent. Heat is removed from the surface primarily by convection, and to a lesser degree by sublimation (for a dry surface) or evaporation (for a wet surface) (Hansman and Kirby, 1987). Also, heat is absorbed from the surface as the supercooled droplets impact and warm to 0°C. The factors which primarily influence the heat balance are the temperature difference between the surface and the droplet environment, the convective heat transfer, and the amount of impinging liquid water mass. For mixed icing, both the droplet impingement and heat transfer mechanisms play important roles in the icing process. The actual hazard for large propeller-driven aircraft comes from the reduction in aerodynamic heating at lower airspeeds and their longer flights at lower altitudes more conducive to icing.

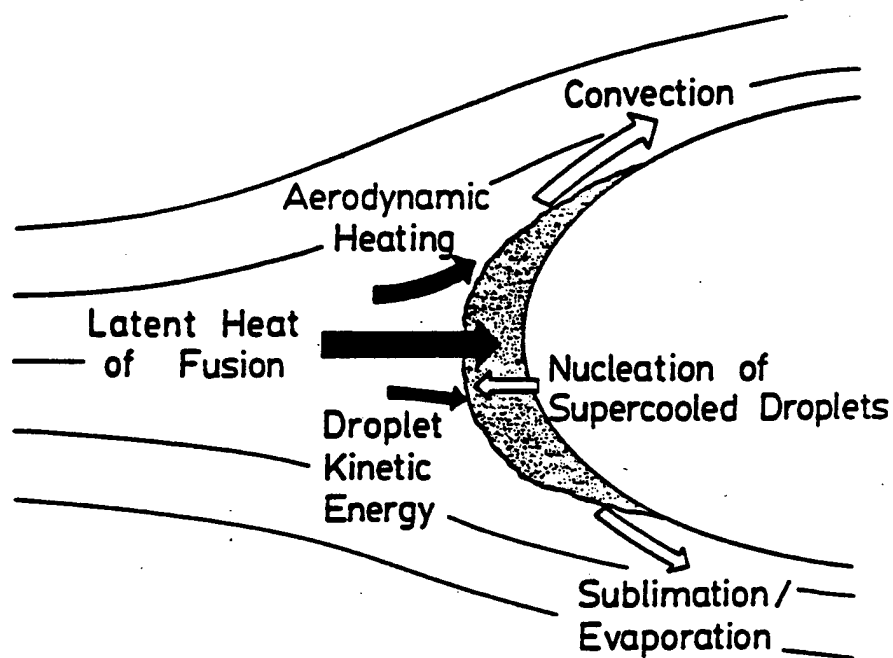


Figure 2.2 Modes of energy transfer from an icing surface (from Hansman 1989)

2.1.3 Intensity

Icing intensity levels, as reported by pilots, are based on the pilot's visual assessment of how well his/her aircraft can deal with the ice accumulating on the airframe. Thus, severity or intensity is quite subjective. Table 2.1 shows the different icing intensities as reported in icing pilot reports. It depends not only on aircraft type, but also on the pilot's experience in icing conditions. A more serious problem for the scientific researcher is that the current index of intensities reflects little basis in meteorological parameters giving forecasters little scientific basis for including icing severity in their forecasts. Sand and Politovich (1991) have developed an icing severity index to replace the current scheme of "trace-light-moderate-severe." During WISP91, a preliminary version of this icing severity index (ISI) was used to visually display icing severity on a pilot's briefing display terminal to gain feed back on the method. User reaction was favorable and more research has been planned.

Table 2.1 Icing intensities, types, and a sample pilot report (from FAA 1977)

Intensity	Airframe ice accumulation	Pilot report
Trace	Ice becomes perceptible. Rate of accumulation slightly greater than rate of sublimation. It is not hazardous even though deicing/anti-icing equipment is not used unless encountered for an extended period of time—over one hour.	Aircraft identification, location, time (GMT), intensity and type of icing,* altitude/FL, aircraft type, IAS
Light	The rate of accumulation may create a problem if flight is prolonged in this environment (over one hour). Occasional use of deicing/anti-icing equipment removes/prevents accumulation. It does not present a problem if the deicing/anti-icing equipment is used.	
Moderate	The rate of accumulation is such that even short encounters become potentially hazardous and use of deicing/anti-icing equipment or diversion is necessary.	Example of pilot's transmission: Holding at Westminster VOR 1232. Light Rime Icing. Altitude six thousand, Jetstar IAS 200 kt
Severe	The rate of accumulation is such that deicing/anti-icing equipment fails to reduce or control the hazard. Immediate diversion is necessary.	

* Icing may be rime, clear, or mixed.

Rime ice: Rough milky opaque ice formed by the instantaneous freezing of small supercooled water droplets.

Clear ice: A glossy, clear or translucent ice formed by the relatively slow freezing of large supercooled water droplets.

Mixed ice: A combination of rime and clear ice.

2.2 Meteorological Factors Contributing to Icing

2.2.1 Temperature

Air temperature is one of the most important icing parameters. Typically, the ambient cloud temperature range, which is most closely associated with the greatest hazard for all types of aircraft, occurs between 0°C and -20°C (or 273-253K). Meteorologists normally work with the ambient or environmental temperature, but pilots and aircraft designers use the concept of Total Air Temperature (TAT) to include aircraft velocity (aerodynamic heating) effects. The TAT is the temperature at the stagnation point of the aircraft and corresponds to the ambient temperature plus an additional temperature rise due to the deceleration of the oncoming flow, which can be significant at high velocities (as much as 30° at 500 knots of airspeed) (Hansman, 1989). This boost in temperature upon droplet impact results in a very wide range of temperatures (with common occurrences between +4°C and -40°C) for which icing can occur based upon the type and properties of the aircraft. Since the airframe surface temperature can be lower than the TAT to the rear of the stagnation point, the normal procedure in commercial jet aircraft is to run the anti-icing equipment at TAT values between +10°C and -10°C in the presence of visible moisture. In some cases, aerodynamic heating is just barely sufficient to prevent ice accumulation on the leading edge of the wing, but insufficient to prevent icing aft of the leading edge (thus to the rear of the anti- or de-icing equipment), if the intercepted droplets flow back over the wing surface.

An experiment by Olsen et al. (1984) using the NASA Lewis Icing Research Tunnel demonstrated how small temperature changes can affect the ice shapes formed and the resulting drag coefficients (shown in Figure 2.3). They found that at cold temperatures (< -15°C) rime icing caused drag increases of 2 to 3 times the clean values. But as the temperature increased above -10°C, the drag increased sharply with temperature, to a peak value of nearly 8 times the clean drag (shown in FIG5 Hans89). This was caused by a transition from dry rime growth to a wet mixed growth icing regime. The horns characteristic of mixed growth can be observed in the high drag ice accumulations. A relatively small temperature change can cause transition from relatively benign rime icing into the dangerous mixed icing condition, but the non-linear dependence of icing intensity on Total Air Temperature make temperature alone a necessary, but not sufficient predictive variable for aircraft icing.

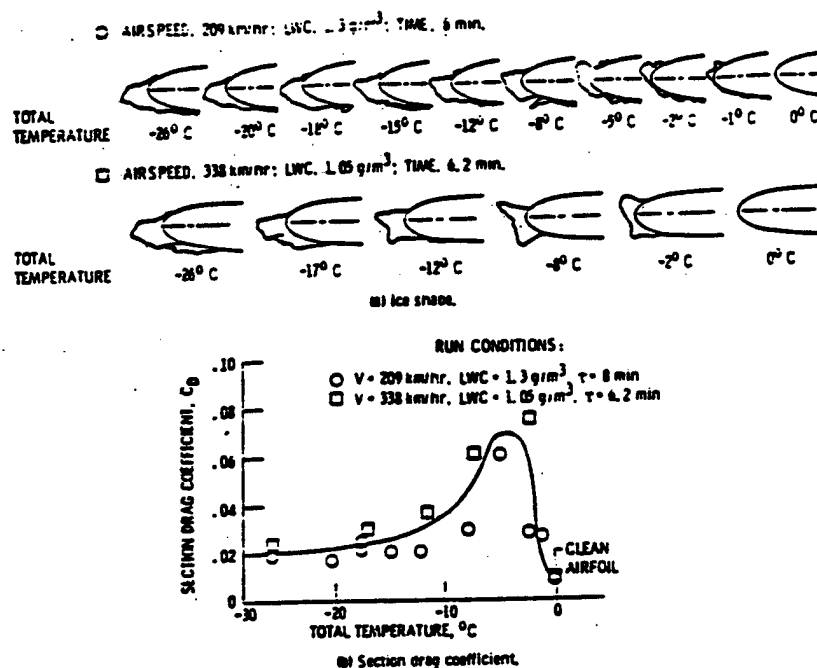


Figure 2.3 Effects of temperature on ice shape (from Olsen et al. 1984)

2.2.2 Liquid Water Content (LWC)

Liquid Water Content (LWC) affects the intensity of icing in two primary ways. First, increased LWC implies more potential supercooled water and larger accretions within a given time. Thus, high LWC reflects a greater severity of the icing encounter with a shorter duration of flight needed to achieve a higher icing intensity. The other effect of high LWC is to cause the icing to transition from rime to mixed icing due to the higher impingement of water mass on the airframe, since at a higher LWC the threshold for the transition will occur at colder temperatures (Hansman and Kirby, 1987). Another factor which complicates the icing process is the large variability of LWC within the cloud and for different types of clouds. Various studies (Pobanz et al., 1994; Politovich, 1989b; Hoffmann, 1988) have found from aircraft flights through confirmed icing clouds that liquid water contents can vary according to the size distribution of the droplets (large droplets in low LWC regions and small droplets in high LWC), but remained generally much less than 1 gm⁻³ (usually between 0.1 - 0.5 gm⁻³). Interestingly, several wind tunnel tests

needed to greatly increase the LWC (from 0.5 gm^{-3} to over 1 gm^{-3}) to get greater desired icing accumulations. This leads to the conclusion that other factors are at work within natural clouds. Sadly, present drop collection instruments and methods of quantitatively determining the observed LWC for large cloudy regions, needed to make icing forecasts, are not consistently accurate or currently available to the operational forecaster.

2.2.3 Droplet Sizes

The size of the ambient supercooled water droplets both in terms of the Median Volumetric Diameter (MVD) and the actual shape of the droplet size distribution can be important to the icing process (Hansman, 1989). MVD is defined as the diameter for which half the total water mass of a distribution of droplets is contained in larger or smaller sizes. MVD provides a good characterization of the collection efficiency of the entire size spectrum. Typical values of MVD for non-precipitating droplets in icing clouds average near $20\mu\text{m}$, but can range from near $10\mu\text{m}$ to several hundred microns (e.g. $\sim 400 \mu\text{m}$ with drizzle size defined by approx. $200\mu\text{m}$ (0.2 mm) to $500\mu\text{m}$ (0.5 mm)). As will be described later, larger SLW droplets are more efficiently accumulated by the airframe (Politovich, 1993) (see Figure 2.4). Within a typical cumulus cloud, the droplet size distribution is such that the bulk of the water mass for the cloud results from only a small number of large droplets. This analysis can naturally vary by cloud type, yet if these larger droplets are found to reside together in regions within the cloud, it would signify a much greater hazard for aircraft that should venture through it. The MVD and the droplet size distribution seem to determine the effective collection efficiency for the aircraft. It is not uncommon to have trace or no icing even at high LWC for clouds with predominantly high numbers of small droplets. Likewise, for clouds with smaller numbers of large droplets at relatively low LWC, it is possible to have moderate to severe icing. Again, owing to the large variability of clouds, the uncertainty in the limits of measurement of MVD and droplet size distributions in clouds is still a topic of controversy and information is based mainly on idealized cloud models.

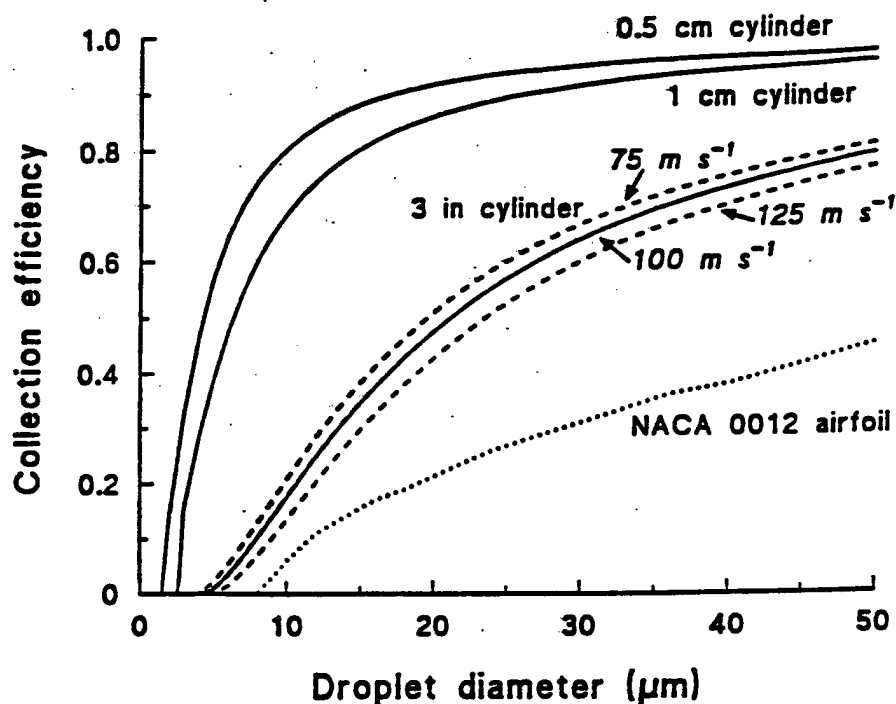


Figure 2.4 Collection efficiency versus impacting droplet diameter for different airfoil sizes and airspeeds (from Politovich 1993)

2.2.3.1 Environmental Conditions for Large Drop Regions

Several recent studies have concentrated on characterizing the production environment of large supercooled liquid water (SLW) droplets in light of its significant hazard potential for aircraft icing (Cooper et al., 1984, Sand, 1985, Politovich, 1989a, Rasmussen et al., 1992, Pobanz et al., 1994, Marwitz et al., 1996). They found that the meteorological conditions accompanying large drop regions (30-250 μm diameter) include warm cloud top temperatures ($> -15^{\circ}\text{C}$), weak thermodynamic instability, usually lower droplet concentrations in vicinity of the large drops, and shallow wind shear layers within cloud and near cloud top. In addition, ample moisture and time must be available for their growth and enough vertical lift must be present to condense the moisture in the updrafts. Warm cloud tops are favored since they decrease the probability of ice initiation, which in turn, would deplete cloud liquid water through depositional growth and riming. A minimum of thermodynamic instability leads to weaker convective updrafts providing time and liquid water for hydrometeor growth in the cloud. Additionally, it tends to result in

cloud-top dry air entrainment and evaporation of some cloud liquid. Lower droplet concentrations while common are not necessary to enable the fewer but larger droplets to collide and coalesce more readily than smaller droplets. Dynamically unstable shear layers at cloud top may result in Kelvin-Helmholtz waves, the entrainment of subsaturated air, and turbulent mixing resulting in large SLW droplet regions.

Pobanz et al. (1994) have made a compelling argument that dynamically unstable wind shear layers of small depth (generally less than 200 meters) within the cloud environment (both inside and outside of clouds) can contribute to the formation of higher concentrations of large SLW droplets (30-250 μ m diameter) in regions near cloud top of stratiform clouds. At cloud top, this vertical wind shear layer (in direction and/or speed) may cause turbulence and Kelvin-Helmholtz waves, resulting in the inhomogeneous mixing (with dry air entrained from above cloud) leading to large SLW drops. The presence of vertical wind shear appears to either initiate or accelerate the collision-coalescence or "supercooled warm rain" (i.e. without ice crystals) droplet growth process in such a way that has not been sufficiently physically explained and confirmed. Unfortunately, due to their shallow nature, it is unlikely that ground based detection systems such as wind profilers or Doppler radars could resolve them. Likewise, they may be beyond the resolution of numerical forecast models.

2.2.3.2 Hazards from Large Drop Regions

The Winter Icing and Storms Project (WISP) was designed specifically to study the production and depletion of supercooled liquid water in winter storms (Rasmussen et al., 1992). Large drop formation regions received special attention, as flight plans were designed to specifically sample these environments by quick ascents and descents through the entire depth of the storm clouds. Ironically, drops in this range of interest (30-250 μ m diameter) are particularly hard to detect unambiguously using instrumentation typically mounted on current research aircraft (Pobanz et al., 1994). Forecasting large SLW droplet regions presents a challenge, since they seem to be confined to thin shear layers such that accurate detection is beyond the capability of current forecast models.

The presence of large droplets within the cloud distribution can result in additional hazard through increased droplet impingement over the aircraft's designed limits. Current FAA design guidance

recommends that a diameter of 40 microns be used to determine impingement limits for aircraft safety. Since the droplet impingement on an airframe increases with droplet size, the presence of significant numbers of droplets in excess of 40 microns can result in ice accretions occurring behind protected regions of the aircraft (aft of the anti- or de-icing equipment) (Hansman, 1989). Cooper et al. (1984) found anomalously high performance degradations when flight passed through a cloud of droplets with diameters from 40 to 300 microns. Marwitz et al. (1996) states that the mere presence of large droplets with $MVD > 30\mu m$ was not sufficient to provide extreme decreases in flight capability. In fact, LWC of $> \sim 0.2 \text{ gm}^{-3}$ were also needed to produce severe flight degradation, since lower LWC with $MVD > 30 \mu m$ produced performance loss similar to that from smaller droplet encounters. The problems resulting from large droplets are compounded in freezing rain or drizzle in or below clouds, where both large droplet sizes and high LWC are combined. Freezing rain frequently causes clear ice accumulations with significant run-back icing behind otherwise protected regions of the airframe (to the rear of the de-icing boot). This is an extremely hazardous situation (to be avoided by pilots), since these conditions can extend downward to the earth's surface and leave the pilot little choice of evasion if at low altitude (FAA, 1977).

2.2.4 Cloud Phase

The icing potential for a particular cloud is directly related to the phase of the hydrometeors it contains. Icing normally results from the collection of supercooled liquid water (SLW) droplets on the airframe. Generally, pristine ice crystals do not adhere to the aircraft surfaces after impact and are not alone considered a hazard. But, if the ice crystals are wet from vapor deposition or partial melting, the impacting crystals can stick as long as the aircraft surface is also wet due to recent de-icing or flight through a region of high LWC (like a rainshower or drizzle). However, rarely do these conditions combine to adversely affect the performance for an aircraft. Though, it is known that if a significant number concentration of ice crystals are present within a cloud, the chance for icing will be greatly diminished (Gayet et al., 1984). This mainly occurs from the scavenging of water vapor by the ice crystals for riming and depositional growth. Most icing forecasting efforts are concentrated on identifying regions of SLW in clouds. Techniques are available to predict cloud phase in stratiform clouds (AWS, 1980) and glaciation

usually results in overestimation of the icing severity. However, within cumuliform clouds, the cloud phase uncertainty represents a potential source of forecast error, since ice phase and SLW phase environments can both be present in significant amounts within updraft and downdraft regions.

2.2.5 Cloud Type

Potential icing zones in the atmosphere are highly dependent on a cloud's structure and the synoptic or mesoscale environment in which it is formed. Icing in stable, middle and low-level stratiform clouds is typically confined to a layer less than 1 km thick and generally ranges in intensity from Trace to Light-Moderate with the larger accretions occurring in the upper portions of the cloud (near cloud top). Both rime and mixed icing are common in stratiform clouds owing to their typical make-up of a narrower size distribution of small cloud droplets. The main icing hazard lies in the great horizontal extent of some of these cloud decks and the possibility of a long flight duration through them. In addition, it has been shown that the presence of conditionally unstable lapse rates increases the potential for significant icing, even in stratiform cloud systems, by triggering embedded convection (Forbes et al., 1993). High-level stratiform clouds are composed mainly of ice crystals and present little chance of icing.

The zone of probable icing in cumuliform clouds is smaller horizontally but greater vertically than in stratiform clouds. Icing conditions are considerably more variable in these clouds depending on the stage of development of each particular cloud. Intensities can span the full range of possibilities and icing types are usually clear or mixed with rime with the most intense/severe icing in the upper half of the cloud and near the freezing level (USAF, 1992). Aircraft icing rarely occurs in cirriform clouds, although some contain small numbers of SLW droplets. However, aircraft icing has been reported during flight through the dense, cirrus anvil tops of cumulonimbus clouds where strong updrafts are able to maintain considerable SLW at rather low temperatures.

2.2.6 Frontal Zones

About 85 percent of all icing conditions reported occur in the vicinity of frontal zones either in the warm air above or the cold air beneath (AWS, 1980). Usually, the greatest horizontal extent of icing is

associated with warm fronts, and the most intense icing with cold fronts within the unstable cumuliform clouds (Figure 2.5a and 2.5b). Also, incidences of freezing rain or drizzle are more common around warm fronts. For significant icing to occur above a frontal surface, the warm air must be lifted and cooled to saturation at temperatures below freezing producing the SLW. If the warm air is unstable, icing may be sporadic. But if it is stable, icing may be continuous over an extended area with studies finding significant mixed and clear icing up to 200 miles ahead and rime icing in stratocumulus up to 300 miles ahead of the surface warm frontal position. Moderate amounts of clear icing is usually limited to supercooled cumuliform clouds within 100 miles to the rear of the surface cold frontal position with increasing intensity towards the frontal zone. Lighter icing is often encountered within the extensive layers of supercooled stratocumulus clouds frequently existing behind cold fronts. Another weather situation that is sometimes conducive to icing conditions is the deep, cold-core upper level low pressure systems, when not specifically associated with a surface frontal system. This situation is characterized by weak to moderate convective activity triggered mainly by the greater instability from the colder air aloft. Light to moderate mixed icing is commonly encountered in this environment. Forbes et al. (1993) found that nearly 52 percent of the icing cases in their study occurred during warm advection / overrunning events versus 45 percent for cold advection / cold air aloft events. Interestingly, they discovered cold advection / cold air aloft regimes accounted for 83 percent of the west coast (CA) cases, but only 12 percent of the central plains (IA/MO) episodes. This presumably due to the dominating local effects that are characteristic of the weather systems moving through these parts of the country.

Marwitz et al. (1996) has suggested another preferred location for the development of large droplet SLW within a mature mid-latitude cyclone. It is the area known as the "dry slot" in the comma cloud that is often evident from satellite imagery. They hypothesize that the subsidence or advection of dry air can remove the predominantly snow crystal laden, upper level clouds that would otherwise rapidly deplete the SLW through its seeding from above. Under optimal conditions, the temperature, moisture, and wind profiles in this region could readily combine to create conditions conducive to large droplet SLW formation via the vertical wind shear process described previously.

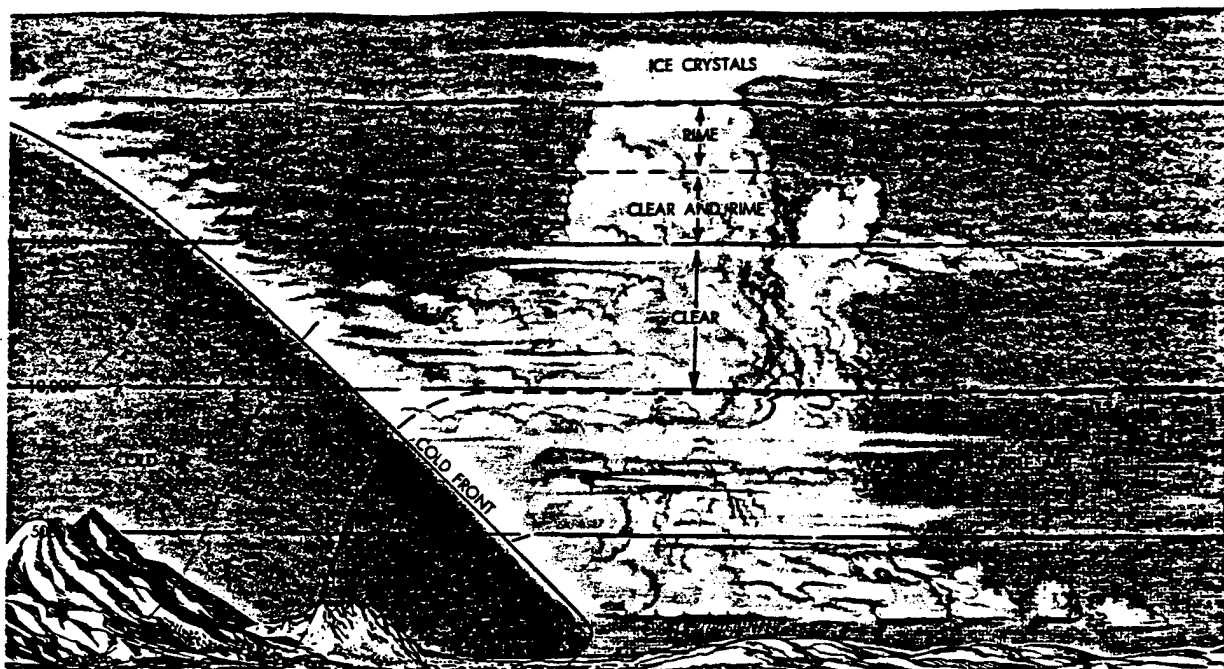


Figure 2.5a Cold front icing zone (from USAF 1992)

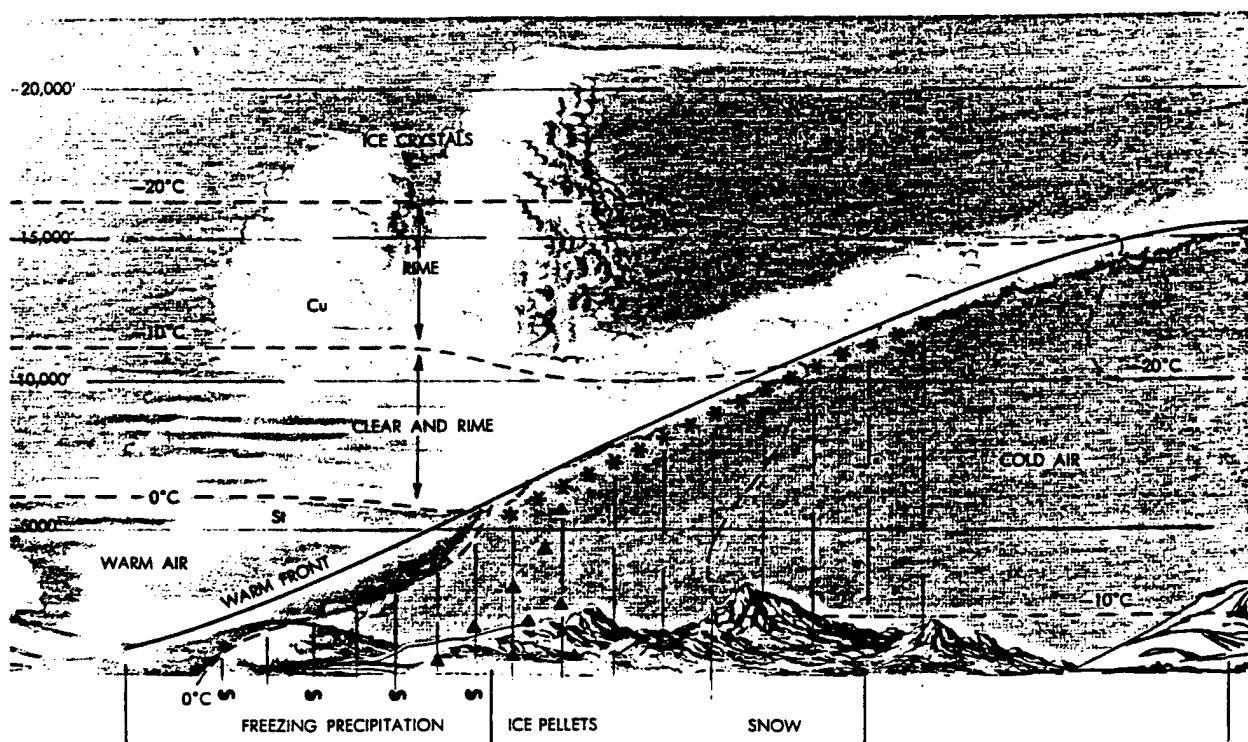


Figure 2.5b Warm front icing zones (from USAF 1992)

2.2.7 Vertical Updrafts and Turbulence

In past icing forecasting methods, vertical updrafts within clouds have been used to help infer icing environments. It is thought that these updrafts would support the formation of distributions of large SLW droplets by holding them aloft and allowing them to grow through collision-coalescence processes. The AWC (formerly NAWAU) has typically used vertical velocity information at the 700mb level from the latest numerical weather prediction models, in conjunction with model estimates of temperature and relative humidity to infer clouds with greater probabilities of icing conditions (Schultz and Politovich, 1992).

Small scale ambient turbulence has recently been hypothesized to potentially assist in the icing process (Hansman and Kirby, 1987). This fine scale (centimeter or smaller) turbulence is believed to strongly influence the convective heat transfer from the icing surface. Flight test observations showed a wide variability in the transition threshold between rime and mixed icing. The variability was thought to be due to variations in the heat transfer resulting from the ambient turbulence level. While this effect has not been directly shown, it may be an additional source of uncertainty in the process or it may be a function of the work done by Pobanz et al.(1994) described above.

2.2.8 Seasonal and Geographical Influences

A continental U.S. survey of USAF aircraft accidents attributed to icing over the previous 30 years (AWS, 1980), showed that 95 percent of the accidents occurred during fall, winter, or spring with nearly 50 percent during winter alone. Those accidents that occurred in the summer were all due to carburetor icing (discussed below) or flight through strong thunderstorms (which normally implies higher intensities of icing). This should be no surprise since these are the seasons where most of the previously discussed factors in aircraft icing are commonly present (more cold/warm fronts, favorable temperature and humidity combinations, larger cloud systems, etc.). In the same study (also confirmed by Cole and Sand, 1991), geographical maximums of aircraft icing accidents occurred in the Great Lakes region and similarly in the Northern Rockies and Plains region (Figure 2.6). These results tend to reinforce the existence of previously mentioned factors in icing, namely the available moisture to make clouds

Airframe Icing Accidents (1975–88)

(352 Airframe Icing Accidents on U.S. Map)

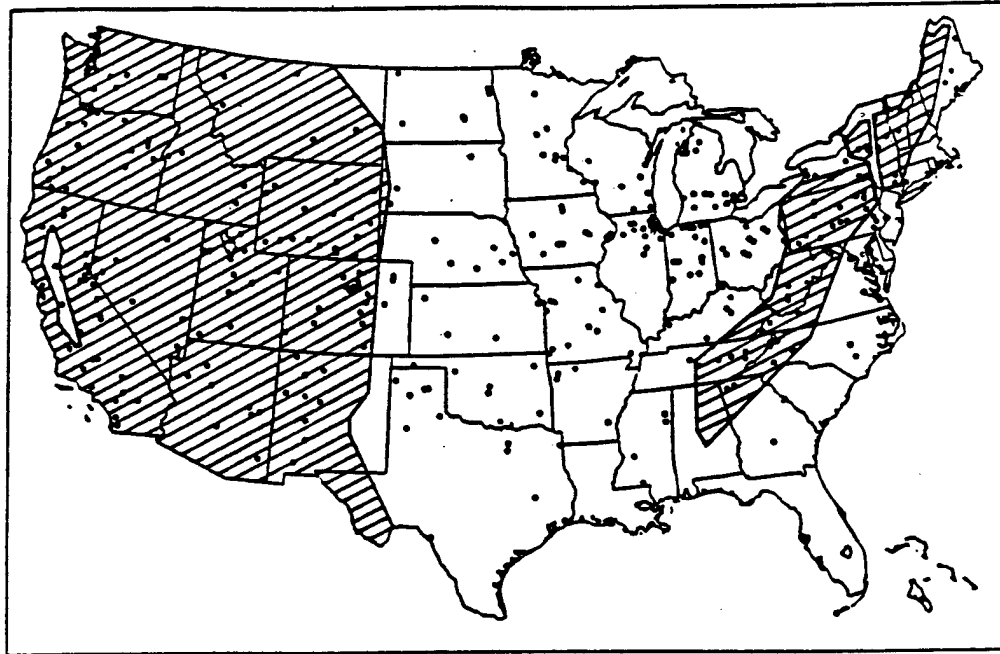


Figure 2.6 Plot of aircraft icing accidents (1975–88) on U.S. map (from Cole and Sand 1991)

(advection from the lakes or Gulf of Mexico), colder temperatures (higher latitude, lower freezing level, and more cold front passages), and the availability of a lifting mechanism to form large cloud regions (be it a cold/warm front or orographic lifting from the hills and mountains). Particularly for orographic mountain clouds, the effects of orographic lifting can be evident up to 30,000 ft or more, but the effects are greatest at altitudes between 5,000 and 18,000 ft AGL, since the majority of aircraft involved in icing accidents fly at these altitudes (Cole and Sand, 1991).

Over the continents, the aviation icing hazard generally extends farther equatorward than over the sea for two reasons (Lee et al., 1994). First, low-level polar air masses can push relatively far into mid-latitude continental areas without warming to temperatures above 0°C, which contrasts the oceans where cold advection is quickly neutralized by warming below. Second, certain orographic structures over land,

such as radiatively-cooled valleys and elevated terrain, can be associated with icing conditions even when surrounding areas have none. The potential for aircraft icing in marine environments is generally confined to high latitudes where SLW is based at or near the ocean surface. This coincides with landing and takeoff routes from coastal or island airports (Curry and Liu, 1992). Additionally, the U.S. Navy is particularly concerned with the low-level icing threat for aircraft landing or departing aircraft carriers.

2.3 Aircraft Icing Forecasting

The AWC provides aircraft icing forecasts (AIRMETs) covering the continental United States every six hours and are amended as conditions warrant (example in Figure 2.7). The icing forecasts are updated as SIGMETs (Significant Meteorological Information) when more severe events (normally a "nowcast" situation based on PIREP information) are encountered, or AIRMET reports for icing issued. AWC forecasting procedures are generally based upon guidance from numerical weather prediction model graphics distributed by the NMC (now the NCEP), satellite imagery, radar observations, upper air soundings, synoptic analyses, and PIREPs (Tucker, 1983). The accuracy of this forecast is then largely dependent upon the experience of the forecaster, his/her skill at quickly assessing the available data, the receipt of PIREPs, and the accuracy of the numerical prediction models. Currently, the NMC models in use do not explicitly include either an icing hazard or a cloud liquid water forecast (though it is being tested on experimental versions of the Eta model). Therefore, operational forecasters must infer icing conditions from other information, such as temperature, humidity, and vertical velocity. Although specific methodologies differ, the AWC forecasts focus mainly on larger synoptic scale events. The standard graphical display products from the Eta model are presently being used.

2.3.1 AWC Method

The basic steps taken by the AWC to infer icing are to forecast the freezing level and the presence of sufficient level at altitudes above that level. After the areas of probable icing have been defined, the forecaster carries out a more detailed analysis, employing empirically derived rules to establish the likely intensity and type of the icing. The synoptic situation dictates the degree of additional analysis required to

produce the icing forecast by establishing the frontal zones, associated clouds, and the general air mass temperatures for each storm system. Altitudes with the desired icing temperatures can be inferred from the Eta 500-1000-mb thickness analysis and forecasts with thicknesses between 5220 and 5580 m considered appropriate. The 850-mb temperature field (range of -15 to +4°C) is also sometimes used as a guideline for supercooled cloud. The Eta model provides relative humidity (RH) information for the 500-1000-mb layer and experience has shown that a threshold of $RH > 55\%$ for this layer usually implies widespread cloudiness. Finally, the forecasters consider vertical motion, which is provided only at the Eta 700-mb panel (Schultz and Politovich, 1992). This is used to infer a condensation of the available moisture into clouds and the ability of the atmosphere to hold larger cloud droplets aloft. If the preceding conditions are met, the area is considered to be an aircraft icing threat.

2.3.2 AWS Method

In the Department of Defense, the U.S. Air Force Air Weather Service (AWS) and the Naval Weather Service both forecast icing. The AWS is also responsible for forecasting for the Army aircraft. The Navy's techniques are very similar to those used by the Air Force which will be discussed briefly below. For a long time, the definitive document on icing forecasting in both the military and civilian communities was the Forecaster's Guide on Aircraft Icing (AWS, 1980). Since its publication, little has changed except for the general improvement of and heavier reliance on the prediction models on which some of the guidance is based. It goes into much depth on the factors for icing listed above and the methodology of the icing forecast summarized in the previous paragraph. The guide lists numerous empirical rules and techniques, many of them requiring manipulations of upper-air soundings for icing threat regions. Unfortunately, the forecaster has precious little time to use some of the more complex techniques, while trying to put out the icing forecast in addition to his/her many other duties. Military aviators obtain pre-flight weather briefings, including Air Force Global Weather Central (AFGWC) icing products (example shown in Figure 2.8) and AWC produced AIRMETs and SIGMETs, from their local weather support units. These icing forecasts give an integrated picture of icing conditions in time and space (both horizontal and vertical) along the flight path.

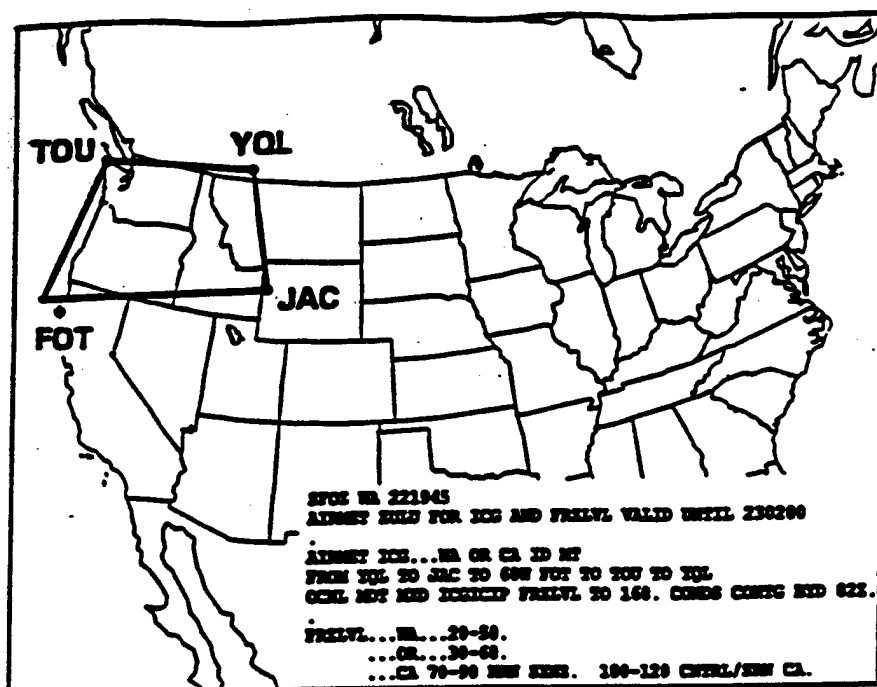


Figure 2.7 Sample AIRMET Icing Forecast Product

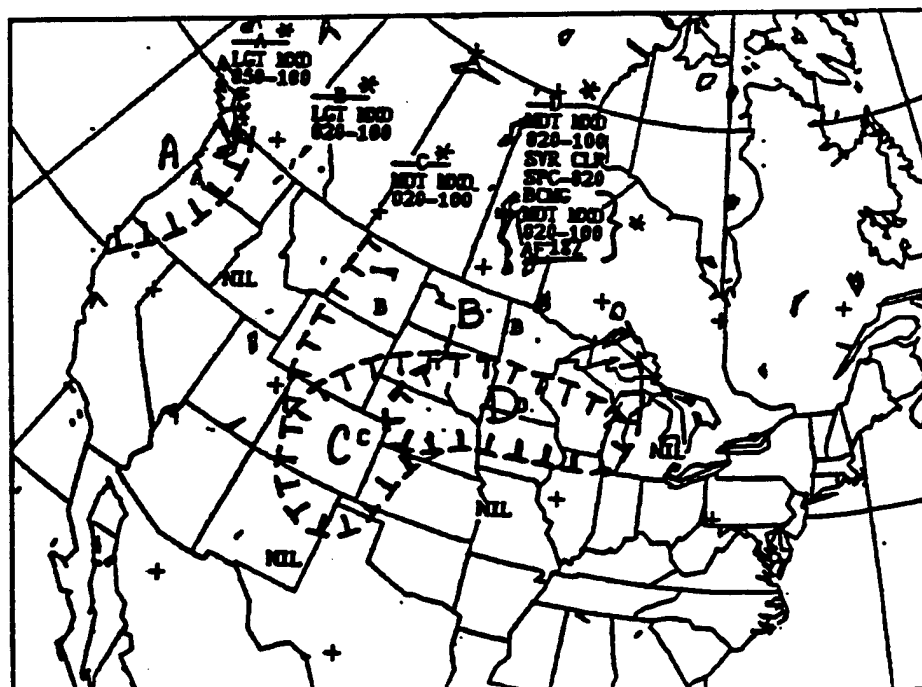


Figure 2.8 Sample AFGWC Icing Forecast Product

2.4 Aircraft Influences on Icing

Several aircraft parameters which considerably influence in-flight icing are discussed below in terms of their effect on the physics and severity of the ice accretion. As has been previously demonstrated, the aircraft's airspeed (velocity) effects both the collection of liquid water droplets and the thermodynamics of the icing process. Greater velocity can result in more severe icing due to a larger potential liquid water exposure by increasing both the path swept out over time and the collection efficiency of the aircraft's surfaces. But it can also affect the heat load by first, bringing more liquid water into contact with the airframe (requiring more latent heat to be dispersed), and increasing the stagnation point temperature for higher airspeeds (requiring a colder environment to offset for icing to occur or decreasing the transition temperature between rime and mixed icing) (Hansman, 1989).

2.4.1 Structural Airframe Icing

The aircraft's shape has a significant effect on the local collection efficiency around the airframe. Generally, smaller bodies (as measured by their cross-section into the airstream) are better collectors than large bodies. Therefore, slender components of the aircraft (e.g. propellers, fan blades, antennae, and narrow wing and tail sections) will tend to be most sensitive to icing accumulation. In fact, because of their high collection efficiencies, windshield wipers, outside air temperature probes, pitot tubes or other static pressure ports are frequently used to visually identify and estimate icing conditions in flight (USAF, 1992). Ice accretion on wing and tail surfaces disrupt the flow of air around these airfoils. This results in a loss of lift, an increase in drag, and possibly most important, causes the aircraft to stall at a higher airspeed than normal. The weight of the ice deposit presents less danger, but may become important when too much lift and thrust are lost.

When ice forms on the wings or the fuselage of an aircraft, or the rotor of a helicopter, it may seriously endanger the aircraft. Within a short time after passing through a region of SLW, it can become destabilized by ice loading. At times, an aircraft can climb or descend to exit a region of icing, but these strategies are not always effective. An ice-loaded aircraft may be too heavy to climb or descent may be hazardous if the supercooled water layer extends to near the surface. Experiments have shown that ice

accretions of only one-half inch on the leading edge of airfoils on some aircraft reduce their lifting power as much as 50 percent and increase drag by an equal amount, thereby increasing the stalling speed. The serious consequences of this are obvious, since one-half inch or more ice accumulations can occur in only a minute or two, in some cases.

Icing on the propeller hub and blades reduce the efficiency of the propeller, which in turn reduces airspeed. Increased power settings may then fail to produce sufficient thrust to maintain flying speed, all the while consuming more fuel. An even grater hazard is the vibration of the delicately balanced propeller, caused by the uneven distribution of ice on the propeller blades. This places dangerous stress levels on the propeller and the engine mounts (USAF, 1992). Thus, propellers with low revolutions-per-minute (RPM) typical of smaller recreational and business aircraft are more susceptible to icing degradation than those with higher RPM. Icing of the pitot tube or other static pressure ports is dangerous, because it causes an inaccurate indication of the airspeed, altimeter, and vertical velocity instruments. Also, ice accumulations on radio antennae may result in a loss of radio communication, therefore not allowing the crew to request a change of altitude or course to fly out of the icing region.

2.4.2 Type of Aircraft

The effect of icing varies significantly with the individual aircraft design. Jet aircraft (including turbojet and turbofan types) are considered to be the least susceptible to icing, since they can operate with greater quantities of excess thrust which can be used to offset performance degradation from icing. Additionally, the jet's characteristic flight profile is to quickly climb, cruise at higher altitudes, and descend rapidly through the lower troposphere where icing potential is greatest (Hansman, 1989). The primary hazard for jet aircraft is engine failure due to Foreign Object Damage (FOD) usually from chunks of ice which are shed from other sections of the airframe and ingested into the engine.

Sensitivity to icing conditions is quite variable for propeller-driven, general aviation type aircraft (including turboprops and smaller reciprocating engines). Most large turboprops have been designed to be fairly ice protected and can operate in most icing conditions. On the other hand, small reciprocating engine aircraft are generally not equipped with icing protection and even short flights through a light icing

environment poses a great hazard to the aircraft. Most propeller-driven aircraft operate at lower altitudes which make them vulnerable to a longer duration of flight through regions of higher icing potential. Icing tends to affect conventional aircraft most through accumulations on the propeller hub and blades, since it directly leads to a loss of thrust (USAF, 1992). Because these aircraft are already using the bulk of their thrust in normal flight conditions, there is little margin to overcome large degradations in performance due to icing.

Helicopter icing has become more important within the last decade where flight in Instrument Meteorological Conditions (IMC) has become more frequent. Helicopter operations occur almost exclusively at low altitudes where there is significant icing potential for both in-cloud and sub-cloud regions. Although the slow forward speed of the helicopter reduces ice build-up on the fuselage, the rotational speed of narrow, main and tail rotor blades can produce a rapid growth rate on certain surface areas (particularly the inner two-thirds of the rotor blades). Rotor icing simultaneously degrades the lift and thrust efficiency of the helicopter. Furthermore, they typically operate with very, slim power margins and can therefore tolerate only minimal ice accretion. Other perilous results from flight through icing conditions include the blockage of engine inlets and air intake screens, and vibrations due to asymmetrical ice loading or shedding of ice from the rotors (Fuchs and Schickel, 1995).

2.4.3 Induction (Carburetor) Icing

In addition to hazards to structural icing, an aircraft frequently is subjected to icing of the power plant itself. Ice formation can be found in the air induction system or the fuel system. While beyond the scope of this study, it is important to mention these types of icing for completeness due to their significant impacts on aircraft. Carburetor icing is most treacherous and frequently causes complete engine failure. It may form under conditions that structural icing cannot. If the relative humidity of the outside air being drawn into the carburetor is high, ice can form inside the carburetor in cloudless skies with the temperature as high as 22°C or as low as -10°C. Carburetor ice forms during vaporization of fuel, combined with the expansion of air as it passes through the carburetor. The temperature drop in the carburetor due to thermodynamic cooling can be as much as 40°C, but is usually less than 20°C. Ice will form in the

carburetor passages, if cooling is sufficient to bring the temperature inside below freezing and with sufficient moisture. Most aircraft have a carburetor heater, an anti-icing device which preheats the air before it reaches the carburetor keeping the air above freezing, which can be turned on manually if flight in humid conditions is anticipated. However, the heater will not melt any ice build-ups if they have previously formed. Since the use of the heater affects the engine performance, it must be used sparingly according to the aircraft's flight manual. Because water mixes easily with jet fuel, the fuel absorbs considerable water when the humidity is high. This can cause fuel system icing problems when the fuel temperature is at or below freezing. In addition, structural icing on smaller air intake ducts and inlet guide vanes can build up enough to restrict airflow to the engine or pieces of the ice can break away and be ingested by the engine causing severe damage.

2.4.4 Results of Aircraft Icing Accident Study

The National Transportation Safety Board (NTSB) determined that icing was a cause or factor in 803 aircraft accidents between 1975 and 1988. Cole and Sand (1991) conducted a statistical study of these icing accidents and the orographic and meteorological parameters that could have had a systematic effect on them. Their findings reveal some obvious trends and some surprising factors which help to emphasize the potential dangers of aircraft icing. A summary of some of their results is listed below.

Larger concentrations of accidents were found in most of the major mountain ranges (53 percent) and near the Great Lakes region (14 percent) (see Figure 2.6). These findings coincide with the geographical factors described above. It seems that conditions in these areas can better increase the moisture content of the atmosphere through lifting of air masses and more efficient condensation of larger increased amounts of moisture. In addition, the relatively cooler environment can lead to a better production of supercooled cloud droplets.

Accidents were equally distributed among takeoff, in-flight, and landing of the aircraft with an average of nearly 65 per year during the study. The takeoff cases are most concerning, since they mostly occurred while the pilots attempted to take off with known frost, snow, or ice on the airframe, and could have been prevented. The specific effects that icing have on the type of aircraft have been described

above. Most of the aircraft involved in aircraft icing accidents in the study were the smaller general aviation type aircraft. Few of which were equipped for flight into known icing conditions, nor did they have excess power to deal with the airframe ice loading.

Examination of the pilot-in-command's experience indicated that icing accidents were not clearly attributable to the less experienced, low-time pilots. The average pilot had over 2000 hour of command time. Despite this, pilots did not always take evasive action when icing conditions were encountered in flight. Also, they did not always remove ice prior to takeoff, instead sometimes believing the snow or ice would blow off or not affect flight performance.

Weather briefings are important since it is a violation of FAA regulations to fly into known or forecasted icing conditions, based on icing intensity and type of aircraft. Though 57 percent of the pilots in the accident study had received weather briefings and icing had been forecast. Forecasts were substantially correct in all but a few cases according to the NTSB findings. Shockingly, 43 percent of the pilots had no record of receiving a pre-flight weather briefing, which is also a violation of FAA rules.

One surprise was that fully one-half of the aircraft accidents were attributed to carburetor icing with remaining amount structural airframe icing accidents. Carburetor and induction system icing as discussed previously can occur under a much wider range of conditions than for structural icing. Although its effects are far less apt to result in fatalities, carburetor icing causes dozens of accidents each year. It is mainly an engineering and operating problem rather than a meteorological one, but a concern to aviation all the same.

2.5 Past and Current Studies on Icing Detection and Prediction

2.5.1 Field Program (WISP)

One goal of the Winter Icing and Storms Program (WISP) was for the detection and forecast of regions of supercooled liquid water (SLW) cloud droplets which would lead to the improvement of forecasts of aircraft icing (Rasmussen et al., 1992). Comparative verification of forecasting systems and algorithms clearly is an integral part of the process towards their improvement. Such a comparative evaluation was one of the primary goals of the WISP Real-Time Icing Prediction and Evaluation Program

(WRIPEP), which was conducted as a part of a winter field program, WISP94. Additionally, another goal of WRIPEP was to develop an in-flight icing algorithm that can be used as an operational forecast tool (Brown, 1995a, 1996b). WRIPEP involved a real-time display of icing forecasts based on several algorithms and numerical weather prediction models. Model data and associated verification data were collected and archived to allow an in-depth comparison of the models and algorithms following the real-time field project. More details regarding WRIPEP, the models, and algorithms can be found in Thompson et al. (1995).

2.5.2 Icing Algorithm Research

Many studies using varying methods have been accomplished to try and address this aviation forecasting problem of aircraft in-flight icing. Some previous evaluations of algorithms designed to identify and forecast aircraft icing regions using numerical model data have included a study by Schultz and Politovich (1992). They used data from the Nested Grid Model (NGM) to formulate and evaluate an algorithm with two "threat levels" of icing. Forbes et al. (1993) expanded on this work through the development of an enhanced algorithm which used verification results to optimize the Schultz-Politovich scheme with data from the 80-km version of the Eta model. Another algorithm was developed and tested by the United States Air Force (Knapp, 1992) using rawinsonde data. The main purpose of the current algorithm comparisons was to aid in the development of a better automated method to improve on the current state of icing environment forecasting for commercial and military aircraft represented by Airman's Meteorological Information (or AIRMETs) (Brown et al., 1995a).

2.5.2.1 Icing Algorithms

As part of the WRIPEP for the WISP94 period (25 Jan - 25 Mar 1994), several icing algorithms were evaluated using two different weather prediction models. One was an experimental version of the National Center for Environmental Prediction's (NCEP) Eta model with 40-km horizontal resolution and 38 vertical levels. The other was a version of the Mesoscale Analysis and Prediction System (MAPS), which is also run by the NCEP as the Rapid Update Cycle (RUC) model. The primary icing algorithms

evaluated by Brown et al. (1996b) are listed below. In addition, cloud liquid water (CLW) estimates by the Eta model were evaluated to see how it would perform as a prediction variable for icing environments and supercooled liquid cloud water (SLW) forecasts.

The RAP algorithm is an enhanced version of the algorithm developed by Forbes et al. (1993) (also included in the comparison) which was an extension of the Schultz and Politovich (1992) algorithm. The RAP algorithm includes four different categories of icing (stable, unstable, freezing rain, and freezing drizzle), but the primary criteria for the yes/no forecasts are based on temperature and relative humidity thresholds. The AWC / NAWAU algorithm also was derived from the Schultz-Politovich scheme, with improvements and adjustments based on their operational experience. Like the Schultz-Politovich algorithm, it predicts two (threat) levels of icing with the second level having more restrictive temperature and humidity criteria, corresponding to a greater icing threat. The Air Force algorithm was developed using rawinsonde data and is designed to predict type and severity categories of icing (Knapp, 1992) using pre-determined temperature and relative humidity thresholds. However, for WRIPEP the algorithm was evaluated only in terms of its ability to predict yes/no icing conditions.

2.5.2.2 Algorithm Verification

Murphy and Winkler (1987) describe a general framework for forecast verification which encompasses the characteristics of the forecasts, the corresponding observations, and their relationship. In particular, this framework is based on the joint distribution of the forecasts and observations, and on two conditional distributions and marginal distributions underlying the joint distribution. Then, to fully characterize the quality of a forecasting system, all of these distributions must be known.

Brown et al. (1995a, 1996b) goes into further detail regarding icing algorithm forecasts by describing whether a binary yes/no icing forecast and PIREP verification will fit this framework and how the Probability of Detection (POD) and False Alarm Ratio (FAR) can be properly used with PIREPs in this case. Due to the nature of PIREPs, forecast area and volume were used as measures of the forecasted attribute, since it is difficult to estimate overforecasting parameters. Because this framework assumes that forecasts and observations are collected in a way that is representative and consistent, problems arise in the

use of PIREPs in the icing observation and individual verification process due to their relative unsystematic nature in time and space (much unlike the gridded data fields from the models). (See Chapter 3 for more information on PIREPs) However, they found that a POD value from traditional icing verification could be used to advantage in a relative sense, such as comparing the detection rates of those different algorithms listed above.

2.5.2.3 Model Comparisons

Brown et al. (1996b) did a thorough comparison of the present algorithm methods as part of the Winter Icing and Storms Program (WISP) Real-Time Icing Prediction and Evaluation Program (WRIPEP) and found most algorithms to be adequate and promising, but none superior to the AIRMETs, in forecasting these factors or atmospheric conditions and the implication of icing regions. The verification results for the explicit CLW output from the Eta model suggest that it has particular potential usefulness as an icing predictor. Differences between the two models on which the algorithms were run, showed only a slight improvement in Probability of Detection (POD) with the Eta forecasts over the MAPS model. The results point to an obvious need for a greater physical basis in the icing algorithms. Other comparisons have been accomplished on a smaller scale by Kieth and Cornell (1995).

2.5.3 Other Recent Important Icing Studies

2.5.3.1 Using An Array of Ground-Based Remote Sensing Systems

Other recent approaches to determine the meteorological factors related to aircraft icing have focused on remotely sensing the environment (whether from ground-based or satellite based platforms). Stankov and Bedard (1994) used an array of ground-based remote sensors to successfully predict aircraft icing conditions aloft. The combination of profiling radars, radio-acoustic sounding systems (RASS), multi-channel microwave radiometers, and lidar ceilometers were effectively used to define the spatial and temporal distributions of supercooled liquid water (SLW) which would be used to infer icing conditions. The remote sensing techniques were applied to obtain vertical wind, temperature, and humidity profiles, as

well as other physical parameters relating to clouds (LWC, water vapor content, cloud-base height). Also, using the measurements and the moist adiabatic approximation, a cloud-top height was inferred.

While successful in some cases, this system of remote sensors has some drawbacks. Liquid water falling below cloud base or its presence on the radiometer reflector surfaces causes errors in its retrieval of moisture or temperature profiles and precipitation can also adversely affect the lidar ceilometers by degrading cloud base information. In addition, the vertical limit of these sensors as a whole is around 3 km or 10,000 ft AGL. While this may provide valuable icing environmental data at lower levels where a majority of aircraft fly, it cannot be very successful at higher altitudes. Moreover, the cost to fully implement their system of sensors would be enormous if it were required to cover large spatial extents. This horizontal limit ($< 100 \text{ km}^2$) of usefulness makes it ideal though for placement around the major airports with increased flight traffic requiring ascent/descent through possible icing conditions and larger budgets to cover the cost of safety.

Ideally, Stankov and Bedard's (1994) suite of ground-based sensors could be used in conjunction with satellite-sensed information in order to provide top-to-bottom detection for the suspected icing environment. The fact that upper-level cloud cover can reduce the usefulness of the satellite to detect cloud-top temperatures and infer SLW of lower cloud layers, emphasizes the need for combining a range of remote sensor information (including the Doppler radar) to receive optimum results. However, the emphasis will need to be automation of each of the analyses, since it would take a forecaster quite awhile to timely assimilate all of the information into a usable icing forecast product.

2.5.3.2 Satellite Sensing of Cloud Liquid Water Over Oceans

Satellite remote sensing of integrated cloud liquid water provided the basis for a study to estimate aircraft icing regions over the oceans (Lee et al., 1994). They used the Special Sensor Microwave Imager (SSM/I) 85.5 GHz channels aboard the polar-orbiting Defense Meteorological Satellite Program (DMSP) satellite to skillfully retrieve images of low-level water clouds over the northern Pacific Ocean. While an accurate satellite, integrated cloud liquid water parameter has yet to be successfully applied over large continental regions, the microwave sensor has proven more reliable over oceanic environments in sensing a

column of cloud liquid water through the atmosphere, owing to the fact that the surface emittance is fairly constant for water surfaces in this spectral regime. Using the integrated cloud liquid water (CLW) retrieval images, additionally with infrared sensed cloud-top temperatures and numerical model output for vertical temperature and geopotential height structure from the Navy Operational Global Atmospheric Prediction System (NOGAPS), they developed a prototype aircraft icing forecasting system that could be used quickly and simply by a forecaster to assess potential icing environments over oceanic regions. Scientifically-based icing zone temperature (from 0°C to -20°C) and CLW (0.2 kg m⁻² or greater) thresholds were specified and evaluated as potential forecasted watch areas, and further hone the accuracy of the retrieval. Their inclusion of satellite data helped to considerably refine icing watch areas, as compared to those from the Schultz-Politovich forecast algorithm.

Unlike ground-based microwave radiometry, which estimates integrated cloud liquid water continuously at a single geographical point (or over a small area), the SSM/I gives a day or night, "snapshot" view of integrated CLW over a much wider area (~1400 km swath), but unfortunately only when it passes over the area. Though the method can produce overestimates of icing potential when ice clouds cover the lower water clouds, thus blocking the infrared (IR) view of the water cloud-top temperature. Even known errors in the DMSP IR cloud-top temperatures of 1-2 K introduce an additional source of error into icing top estimates. However, the resulting 100-200m height assessment errors are small compared to beneficial improvements in icing top measurements (usually 500 m or more) when the IR method is incorporated. Scattered convective clouds can cause an under estimation of icing potential owing from their cloud-top temperatures below -20°C.

Precipitation-sized droplets (> 500µm) can also cause erroneous retrievals due to their scattering properties in the 85 GHz channel. Since the presence of significant precipitation can infer some amount of supercooled liquid cloud water at that point in the cloud system, Lee et al. (1994) tried to use this information to their advantage by spatially averaging the integrated CLW through the precipitation areas and setting a threshold of greater than about 1 kg m⁻² to indicate precipitation. Unfortunately, due to the relative scarcity of icing reports over the oceans, they were unable to perform a validation of their system. Their method is most appropriate for use in poleward regions, where subfreezing temperatures and liquid

cloud water are likely to exist near the surface. Fortunately, the polar-orbiting DMSP satellite provides relatively frequent coverage in these regions. Also, at high latitudes where traditional daytime visible imagery has a hard time distinguishing low clouds, the CLW images are available day and night and are free from sunglint and cirrus that tend to obscure low clouds in the visible channel.

2.5.3.3 Satellite Sensing of Cloud Liquid Water Over Land

Cloud liquid water (CLW) has been shown to be a very important variable to the study of aircraft icing. With the abundance of commercial and military air traffic flying within typical altitudes for icing hazards, mainly below 15,000 ft AGL, over the continental U.S., the importance of icing environment detection and forecasting over land areas is much more important than over most oceanic regions. With most research concerning satellite microwave remote sensing of cloud liquid water restricted to oceanic regions (as evidenced by Lee et al. (1994) above), the need for a viable method to detect cloud liquid water over large regions of land remained. One advantage of using the microwave frequencies lies in the fact that they can penetrate thin ice clouds or cloud tops enabling better sensing of non-precipitating convective clouds. Again however, the effective use of satellite microwave remote sensing breaks down, when precipitation size droplets are encountered within or below the cloud.

Lawyer (1995), in his M.S. thesis written at Colorado State University, developed a satellite derived icing index based mainly on passive microwave imaging data from Defense Meteorological Satellite Program (DMSP) polar orbiting satellites. His methods followed closely those of Jones and Vonder Haar (1990) and helped to retrieve accurate vertically integrated cloud liquid water estimates over continental areas. Similar to Lee et al. (1994), Lawyer (1995) also used the high frequency 85.5 GHz channel of the SSM/I instrument aboard the DMSP polar orbiter. Additionally, visible and infrared (IR) satellite imagery from the GOES-7 and rawinsonde information were used to supplement the microwave image data.

The main problem for accurate microwave CLW retrievals over land areas is resolving their surface emittance characteristics. Over water surfaces, the emittance from the surface in the microwave portion of the spectrum is fairly uniform and small. This fact makes the CLW calculations based upon the

microwave radiative transfer equation much simpler. Retrieval of CLW over land is more difficult due to the greater emittance magnitude and variability (mainly from soil moisture differences) from the land surfaces, which causes the microwave radiometer to be insensitive to CLW content variations. In order to retrieve CLW estimates, both SSM/I and GOES-7 IR data under clear sky conditions over land only were used to make the surface emittance calculations, which acted as a surface boundary condition for the total emittance sensed by the microwave radiometer. Lawyer's resulting CLW values were consistent with those made during research aircraft experiments under similar conditions.

Then, by combining seemingly accurate CLW measurements with estimated cloud-top temperatures, inferred cloud depths, and cloud texture information from GOES-7 imagery, Lawyer developed an icing index nomogram as a proposed icing forecasting tool. A positive comparison to a small set of icing PIREPs for verification showed that the prospects for a microwave CLW retrieval and multispectral satellite imagery technique for icing prediction is encouraging. However, further testing and automation of the various computational tasks within the method must be completed before its operational use would be possible.

More importantly, Lawyer's (1995) research has shown that with proper knowledge of the land surface properties (specifically ground moisture and surface emissivity), the satellite-retrieved estimates of cloud liquid water will give a fairly good depiction of the cloud regions' icing potential for non-precipitating clouds (i.e. stratiform cloud areas and some cumuliform clouds). Especially when used in conjunction with other remote sensing methods in the future, passive microwave imaging can be a powerful tool for the researcher or forecaster. However, for improved spatial coverage and more timely forecasting, a dedicated microwave radiometer placed aboard a geostationary satellite would allow for a more complete observational system (better temporal resolution) and increase the amount of information that could be used to further improve icing environment detection and prediction.

2.5.3.4 Using Multispectral GOES-8 Imagery

Another more recent application of satellite remote sensing towards detection of aircraft icing regions has been undertaken by Ellrod (1996a). Using the availability of geostationary satellite imagery

from the advanced GOES I-M series, he was able to infer the presence and spatial extent of some of the meteorological factors important in aircraft icing. His technique uses characteristic information garnered from each of three separate GOES-8 spectral channels (CH1-Visible, $0.7\mu\text{m}$; CH2-Shortwave IR, $3.9\mu\text{m}$; CH4-Thermal IR, $10.7\mu\text{m}$) to diagnose potential aircraft icing zones. As they pertain to this study, these channel characteristics will be further explored in Chapter 4. Ellrod mainly explored stratiform cloud systems over the northeastern U.S. for known significant icing events (from pilot reports), where the reported icing intensities ranged from light to severe (although most were of moderate or greater intensity).

Digital infrared (IR) brightness temperatures and visible brightness counts were collected. Imagery in each channel was also studied for any qualitative information that would help to detect the heavier icing regions. As noted in the study, when displayed in the normal IR convention (cold shown as white), CH2 IR often appeared significantly warmer (darker gray; higher brightness temperature) than CH4 due mainly to the respective emission and reflection characteristics of cloud liquid water droplets and ice crystals during daytime for each channel. This temperature difference between the two channels ($\Delta T = \text{CH2} - \text{CH4}$) was utilized by use of an empirical scheme that would combine the ΔT and the visible (CH1) channel brightness counts of known icing cases into a decision tree that would assess icing risk in stratiform clouds. Ellrod also suggests that using a visually displayed and enhanced combination of channels 2 and 4, it may be possible to detect icing potential for clouds in the absence of obscuring cirrus cloud layers. His preliminary results show some skill in assessing aircraft icing potential by combining data from the three imager channels listed above. While there was little skill in icing detection or prediction using the channels individually, the CH2 imagery revealed some success at highlighting cloud-top regions where heavier icing was possible, owing from its increased sensitivity to larger liquid cloud droplets. While this method is not currently a stand-alone solution to the discovery of aircraft icing environments, it shows promise for use in combination with improved numerical modeling data and/or other ground-based or satellite-based remote sensing techniques.

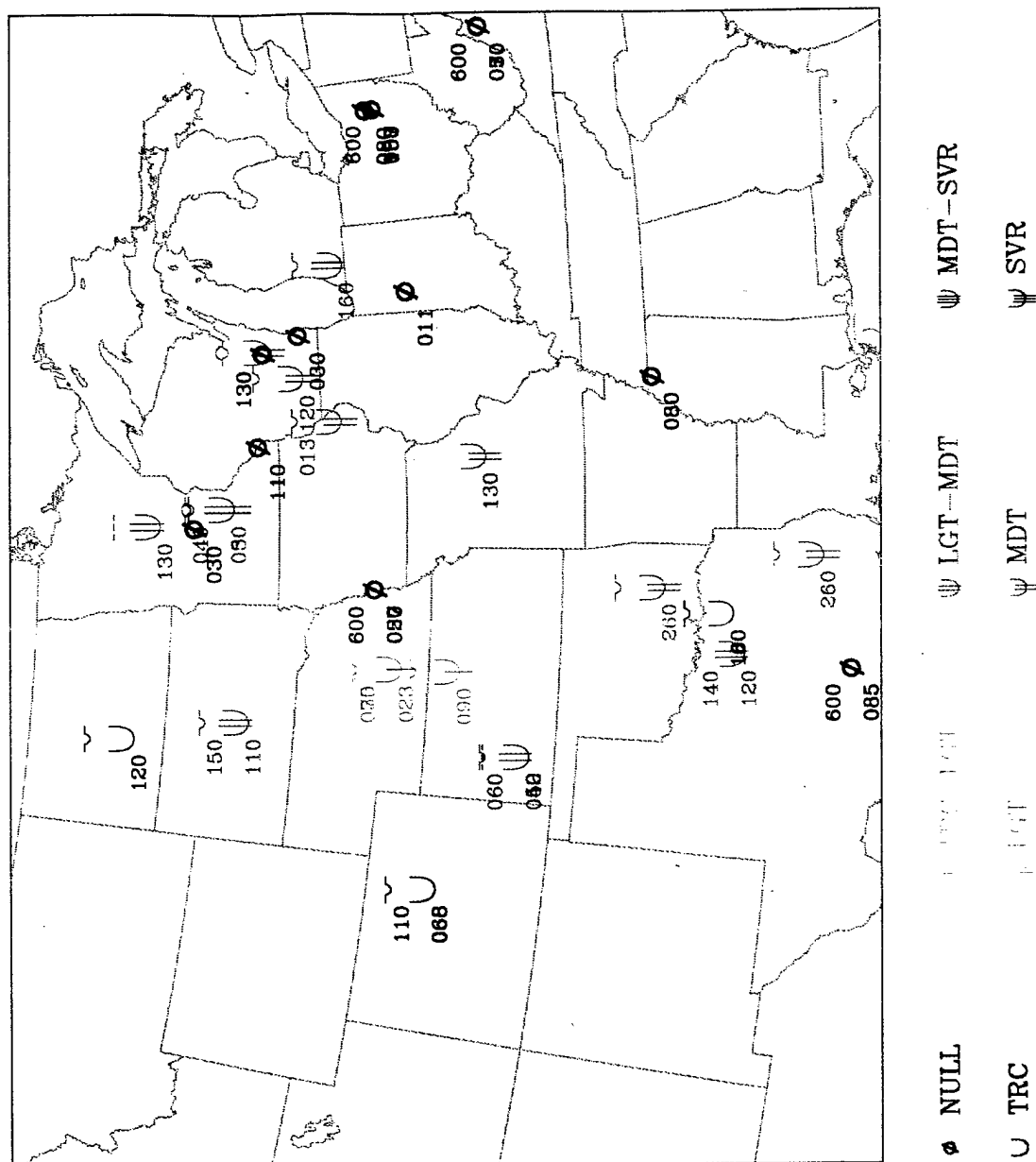
Chapter 3 — Pilot Reports (PIREPs)

3.1 Description of PIREPs

Because of the lack of physical measurements of icing conditions in the atmosphere, icing forecasts have primarily been verified from subjective observations made by aircraft pilots. Pilot reports (PIREPs) can provide valuable information about numerous weather conditions observed by aircraft pilots while in flight, during landing (descent) or taking off (ascent). Some examples can include cloud cover, freezing level, air temperature, and turbulence and icing with altitudes and intensities as determined by the pilot. Unfortunately, most pilots flying commercial aircraft do not include the ambient air temperature in their pilot reports. In the U.S., all pilots are required by FAA rules to report hazardous aviation conditions, including the existence of icing (Brown, 1995b). The pilots voluntarily issue these PIREPs, as soon as aircraft safety allows, by voice over the radio to the nearest FAA Flight Service Station, though sometimes at the request of an air-traffic controller. The reports are manually entered into a computer as part of the air traffic control system.

PIREPs of icing indicate both the intensity and type of aircraft icing (see Figure 3.1). Severity/intensity is rated on a scale from "Trace" to "Severe" and types of icing include Rime, Clear, and Mixed. The reported severity depends on a subjective assessment of how well the aircraft handles the accumulated ice, which, in turn, depends on the aircraft's deicing or anti-icing capability while in flight. This variability with aircraft type somewhat diminishes the utility of the icing intensity forecast information. PIREPs also may be "negative", indicating that no icing was observed. However, negative reports are rare, since the pilot will usually not take the time to send a PIREP stating that there is no significant weather hazard unless prompted by the air-traffic controller (usually during takeoff or landing).

PIREPs have some drawbacks though. Appropriate to the voluntary nature of PIREPs, they are biased both in time and space. This represents the most significant problem when applying them to a forecast verification analysis. For example, very few PIREPs are recorded at night due to the relative lack of aircraft flights during this time. Moreover, large regions of the U.S. have very few or sparse reports (see Figure 3.2). Larger U.S. cities (defined as population centers of 250,000 or larger with a major airport in the vicinity) with correspondingly greater amounts of air traffic are found to be well covered with PIREPs.



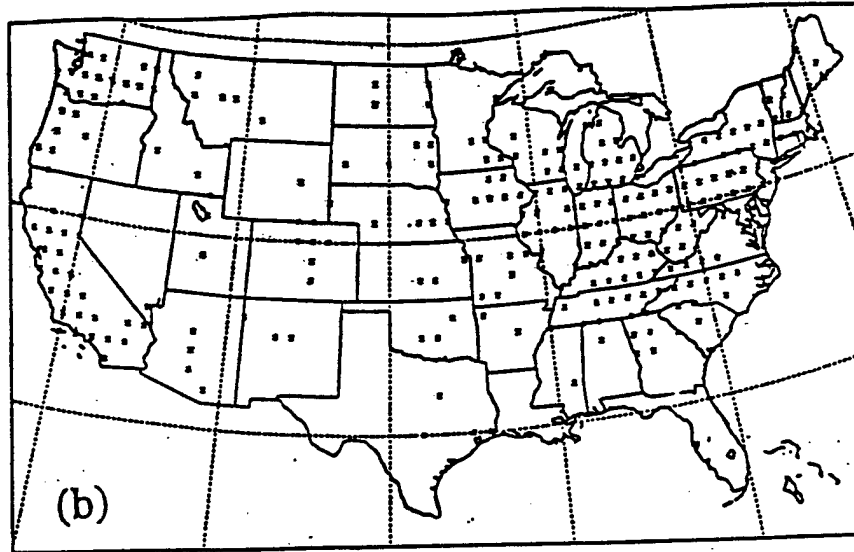


Figure 3.2 Spatial distributions of PIREPs in 1° latitude/longitude regions (each X represents at least 40 PIREPs over a two year period (1990-1992) (from Brown 1993)

Although these large cities have more opportunities for PIREPs, many parts of the U.S., particularly the West, have few large cities. Brown (1995b) found that of 58,000 PIREPs in her study, 33 percent of these reports were located within 80-km regions around large cities. These facts give rise to a bias in PIREP icing reporting mainly during daytime and around large cities or along the heavier commercial air traffic corridors. Additionally, because PIREPs, overall, are not systematic in time or space, they represent a difficult data set on which to build an icing climatology (Brown, 1995b). Other problems with PIREPs result from errors in location and time. The pilots often can pass incorrect information, when due to aircraft safety concerns, they cannot take note of the proper time or place of the aviation hazard, and were too busy to pass on the information immediately. Thus, times and places get roughly estimated, and weather information gets entered into the PIREP system archive incorrectly.

3.2 Methods of Scientific Research Verification Using PIREPs

Since PIREPs do not give a representative spatial or temporal identification of the icing regions outside areas of higher air traffic volume, they are to be used very carefully for icing study verification

purposes. These aspects of the statistical use of PIREPs are covered well in Brown (1996a, 1996b) and are discussed below. Unfortunately, at this time there is no better available or reliable piece of data, or less expensive method that enables the verification of this variable to such a large spatial extent as needed by the operational forecaster.

In weather forecast verification, the verifying data typically are a direct measure of the quantity that is being forecast with the verification data measured systematically (with one observation, yes/no, to match each forecasted occurrence). It is important to note that the non-occurrence of an event is as important to measure as the occurrence of an event. For such weather phenomenon as precipitation, the non-occurring events are systematically recorded in time and space, but for icing events this is generally not the case. Although negative (no icing) reports are sometimes recorded, they are far from systematic, and the lack of reported icing in an area cannot usually be interpreted to mean that there was no icing present. In fact, the small relative frequencies of negative PIREPs do not accurately reflect the large proportion of the country that is not experiencing icing conditions at any particular time.

Instead of being recorded at regular time intervals and over locations of interest spread equally over large spatial domains, pilot reports (PIREPs) are recorded in a seemingly haphazardly fashion. Ironically, the distribution of PIREPs is actually quite non-random. Patterns of icing reports generally represent flight patterns for day-of-the-week, time-of-day, and altitude (Schultz and Politovich, 1992). For instance, air traffic is normally heavier during mid-week than on weekends, such that more PIREPs are received on weekdays. Approximately 93 percent of the 1990-1992 PIREPs occurred between 1200 and 0400 UTC, which corresponds roughly to the daylight hours over the continental United States. Icing report altitudes for that same period were mainly concentrated below 5 km (~15,000 ft) above mean sea level, where most aircraft are likely to fly; only 7 percent of the PIREPs occurred at altitudes higher than 5 km and 70 percent were between 1 km and 3.5 km (3000 and 10,000 ft) (Brown et al., 1993). These findings suggest that it would be best to restrict icing verification analyses to the daylight hours on weekdays to ensure maximum PIREP representation. However, PIREPs are also a function of the severity of the weather present during flight, so PIREPs would also be more abundant any time there is flight through significant weather systems.

The verification of icing and turbulence forecasts has a number of serious pitfalls, some of which were noted in Brown et al. (1995a, 1996b). These problems are primarily related to the nature of the only data that is presently widely available for verification of aircraft icing events, namely the pilot reports (PIREPs). Characteristics of the PIREPs and their collection have important implications for the types of verification analyses that can be undertaken. Moreover, they make it difficult to apply techniques based on a more general and recognized forecast verification scheme based on work by Murphy and Winkler (1987) and further applied by Brown et al. (1995a, 1996a, 1996b). Despite their drawbacks, PIREPs have been used to estimate standard verification measures such as the Probability of Detection (POD) and False Alarm Ratio (FAR), but their interpretation is not straightforward owing to the nature of PIREP collection. Brown et al. (1995a) concluded their verification study that estimates of POD obtained do not provide an absolute measure of the capability of the algorithms to properly forecast icing events, but POD can be useful as a comparison to the capabilities of different icing algorithms. Also, estimates of FAR were found to be inappropriate when used with observation-based measurements (PIREPs), because of the lack of negative reports and the PIREPs poor coverage of the forecast grid. The inability to measure FAR in this fashion means that the extent of overwarning cannot be measured.

In Brown and Murphy's (1996a) paper, a procedure is described that may possibly overcome the problem of estimating the icing forecast FAR through application of the concept of "extending the argument". This method is based on the use of a third variable (covariate) on which to condition the joint probabilities of forecasts and observations. To be useful in this context, the covariate values should be strongly related to the observations. For an icing event, such a covariate might be cloud coverage, supercooled liquid water (SLW) clouds, or integrated liquid water as estimated from satellite data or icing inferred from surface remote sensing or surface observations of precipitation. One distinct advantage of this approach is that the covariate can be a variable that is measured at the forecast valid time rather than the forecast issue time. The covariate approach shows promise in better estimating FAR and overforecasting of icing regions. However, the actual icing region is unknown in real-world cases, which limits the ability to realistically determine the reliability of the statistics (Brown and Murphy, 1996a).

Chapter 4 — Satellite Background

Satellite imagery seems to be a relatively under-utilized source of information for potential icing detection and prediction. When compared to ground-based sensors, satellites have a greater capability to accurately measure various meteorological parameters over larger areas, but yet with sufficient detail for smaller scales. Some work on detecting icing conditions has been done using microwave imagery over oceans from polar-orbiting satellites (Curry and Liu, 1992; Lee et al., 1994; Thompson et al., 1996a). While microwave retrieval of integrated cloud liquid water from satellite has been relatively restricted to ocean regions, some skill has been shown in summer over the central U.S. (Jones and Vonder Haar, 1990; Lawyer, 1995). With the more frequent and higher resolution imaging data attainable from the next-generation GOES-8/9 satellites, the potential is there to improve the icing hazard assessment over large continental as well as oceanic regions. This chapter will focus on the radiative transfer theory and desirable characteristics of the infrared (IR) and visible (VIS) spectral regimes important to this study. It will also describe the GOES-8 imager platform, applicable characteristics of common spectral channels, and the improvements made over past meteorological satellites.

4.1 Passive Visible and Infrared (IR) Remote Sensing

4.1.1 Atmospheric Windows

The propagation of radiation through the atmosphere is affected mainly by two processes: absorption and scattering. During absorption, a fraction of the energy passing through a volume element of the atmosphere is absorbed by atmospheric constituents and re-emitted at different wavelengths. Most absorption is spectrally selective by major gases, such as CO_2 , O_2 , O_3 , and H_2O vapor, with lesser amounts due to atmospheric contaminants. Additionally, a fraction of the radiant energy passing through the atmosphere is scattered. The amount and direction of this scattering is largely a function of the scattering element's size as compared to the wavelength of the incident radiation being scattered.

Passive imaging sensors, responding to radiation in atmospheric windows, are very important in the study of cloud properties, and their variability and distribution in space and time. Atmospheric windows in the infrared and visible spectrum, so-called from their relative insensitivity to certain

atmospheric molecules (water vapor, in this case), are used so that the tops and edges of low clouds as well as high clouds can be seen (or their respective cloud particles detected). Moreover, the lack of atmospheric interference in these wavelengths will ensure that the emitted radiation being sensed will be dependent on only the cloud's microphysical properties or the Earth's surface. For example, the top of a low cloud might be only a few hundred meters above the ground leaving about 99% of the mass of the atmosphere between the cloud and the satellite sensor. Thus, energy sent from the cloud towards the satellite would be very sensitive to attenuation (reduction in returned energy; i.e. absorption or scattering) by atmospheric molecules. To get an accurate indication of the cloud properties, the amount of attenuation by the atmosphere must be minimized, and transmittance must be maximized.

Atmospheric windows which have been commonly used for cloud detection and are relatively unaffected by water vapor are in the approximate wavelength ranges of 0.4 - 1.3, 1.6 - 1.7, 2.1 - 2.3, 3.5 - 4.0, and 10 - 13 microns (μm) (shown in Figure 4.1). The spectral response of satellite imagery is usually narrower than these bandwidths since it is desirable to avoid some molecular absorption bands within the water vapor window and also to take advantage of variations in the reflectivity of Earth surfaces (Bunting and Hardy, 1984). The reflectivity or albedo of most land surfaces in the visible spectrum tends to increase as a function of wavelength between 0.5 - 1.0 μm , so a spectral response in the shorter wavelengths from 0.55 - 0.75 μm may give a sharper contrast for clouds over land than a response from 0.5 - 1.0 μm . For the shorter wavelength windows, sunlight (solar radiation) is mostly reflected, so that they are mainly useful during the daytime. The water vapor windows at longer wavelengths sense thermal energy (temperature) originating from the clouds or their backgrounds with only small contributions from the atmosphere itself and can be used day or night. The 3.5 - 4.0 μm window senses radiative contributions from both reflected solar and emitted thermal radiation. It marks the transition between the dominant effects of reflected solar (visible / near-infrared) and thermal infrared (IR) regions of the radiation spectrum on Earth. Thermal radiation windows are also found at longer wavelengths known as millimeter or microwave frequencies. The microwave spectrum roughly extends from 1 mm (1000 μm) to 1 m in wavelength. These windows are generally more sensitive to larger, raindrop-size water particles (> 500 μm) within or below clouds

rather than the entire cloud itself. While not the purpose of this study, these frequencies are commonly used to gather information on precipitation and cloud liquid water.

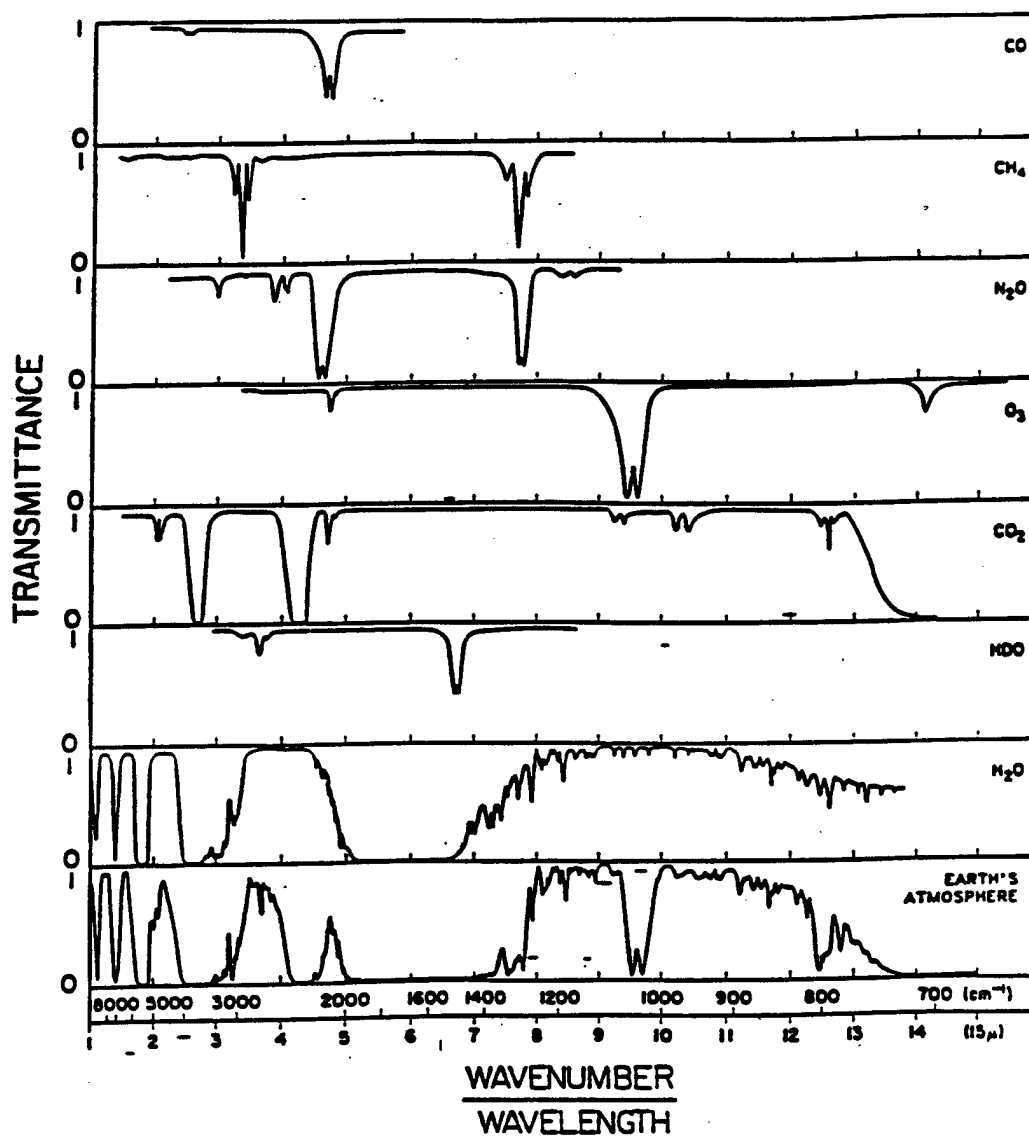


Figure 4.1 Visible and infrared transmittance versus wavelength showing atmospheric windows (from Kidder and Vonder Haar 1995)

4.1.2 Radiative Transfer Theory

Since a cloud's characteristics are very important to satellite sensing, the interplay between the clouds, and solar and terrestrial radiation must be understood. A cloud's optical properties such as reflectivity or emissivity depend on the cloud's physical properties as well as the wavelength of radiation

observed by a satellite. For many applications, it is important to distinguish cloud particles from the larger precipitation droplets and water particles from ice particles. Though greatly variant, typical continental clouds tend to consist of particles on the range of 5 to 300 microns in diameter with most between 15 - 40 μm . Usually, water-cloud droplets tend to be much smaller than precipitation and ice-cloud particles, although sizes vary greatly depending on the cloud type and the particular environment in which the cloud is formed. In general, pure water clouds have many small particles, while ice clouds have fewer, but larger particles.

Given particle sizes and number distributions, it is possible to calculate the radiation sent from the cloud towards the satellite (Bunting and Hardy, 1984). The calculations start with the amount of energy scattered, absorbed, and emitted by individual particles. The results depend on the refractive index and scattering efficiency, which varies with the wavelength of the radiation and the water or ice phase of the cloud particle. Also, the results hinge on the radius of the particle (r) and the wavelength (λ) consistent with the relation,

$$\chi = 2 \pi r / \lambda$$

where χ is known as the size parameter.

For smaller non-precipitation sized, spherical liquid cloud droplets in the visible and infrared regimes with χ between about 0.1 and 50 (where droplet size is nearly equal to the incident wavelength), Mie theory determines the scattering and absorbing characteristics for the particles, while the calculations are less straightforward for ice particles and their irregular shapes (Figure 4.2). In the Mie regime, the angular distribution of scattered radiation is quite complicated and varies rapidly with χ , but at larger χ (> 10) forward scattering dominates over back scattering with little radiation scattered back towards the source (Kidder and Vonder Haar, 1995). In the case of infrared radiation whose source is the Earth, this forward scattering preference for cloud droplets in the Mie regime results in more terrestrial radiation sensed by satellite sensors. Since a satellite can detect billions of cloud particles in every pixel, the radiative interaction between them (multiple scattering across the droplet size spectrum) must be included in the calculations of cloud-sensed energy. Because all visible wavelengths are scattered nearly as well, the cloud appears white in this wavelength. For larger precipitation-size particles and drizzle droplets in the

visible and IR regime, and most cloud droplets in the visible with $\chi > 50$, geometric optics are used to deduce the reflecting and refracting radiation at the scatterer's surface. Again, at larger size parameters, the scattering phase function shows a greater inclination for forward scattering.

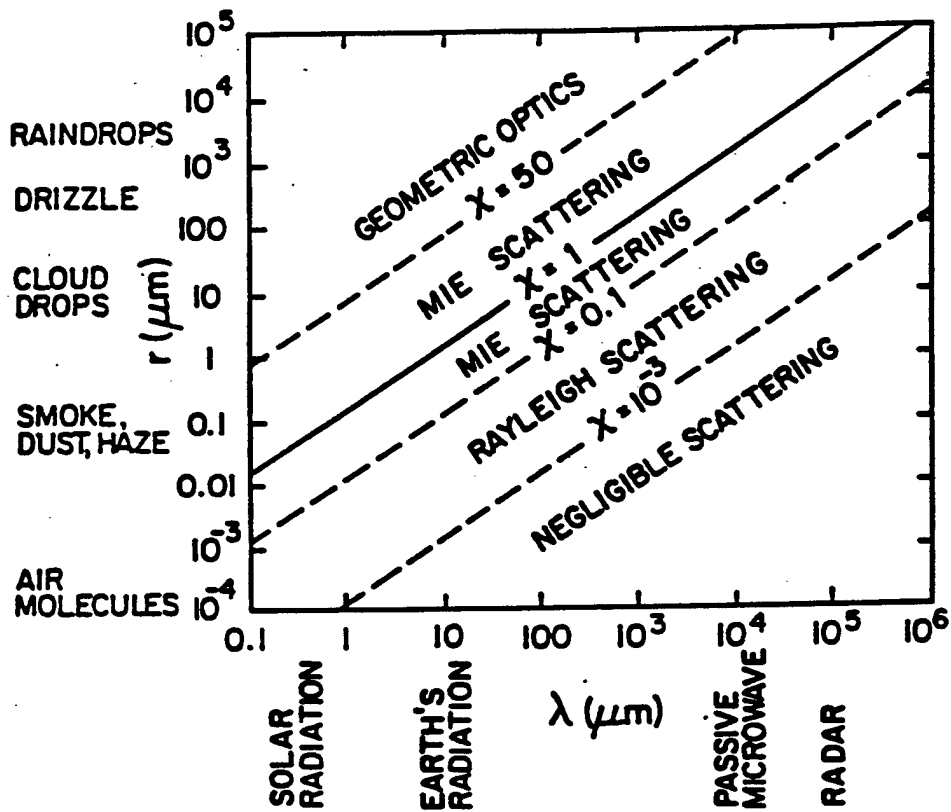


Figure 4.2 Scattering regimes (from Kidder and Vonder Haar 1995)

4.1.3 Spectral Properties of Clouds

A detailed, quantitative theoretical study of the radiative properties of water droplet and ice clouds at visible and infrared wavelengths in water vapor windows is presented by Hunt (1973). The results of his calculations of cloud optical properties are presented below. There are three processes which control the incident radiation upon a body (cloud): Absorptivity (α), Reflectivity (ρ), and Transmissivity (τ), and they can vary according to cloud density, thickness, height, and phase of particles. For energy conservation of the incident beam, the three quantities are related by $\alpha + \rho + \tau \approx 1$. Assuming the cloud tops are in local

thermodynamic equilibrium, Kirchoff's law states that at each wavelength, a body that has good absorptivity (α) will have an equally good emissivity (ϵ) or $\alpha \approx \epsilon$. For a Planckian radiator or perfect blackbody, $\alpha \approx \epsilon = 1$, and $\rho = \tau = 0$ (Schott and Henderson-Sellers, 1984). For opaque objects (optically thick clouds), the transmission goes to zero and $\alpha + \rho = 1$ for objects in the visible wavelengths, where the primary concern is with reflected energy. Then, in the longwave infrared wavelengths, $\epsilon + \rho = 1$, where self-emission is dominant. For water clouds, visible wavelengths are more sensitive to optical depth, while shortwave infrared wavelengths are more sensitive to the cloud particle size. A good synopsis of IR radiance retrieval theory is contained in d'Entremont (1986).

Assuming the water clouds to be horizontally homogeneous, and optically thick (cloud optical depth (δ) > 10 or clouds at least several hundred meters thick) or poorly transmitting at shorter (visible) wavelengths, they have high reflectivities due to low emission / absorption in the visible regime. A high albedo from the clouds due to more solar radiation reflected and scattered back to the satellite by smaller (ice or liquid) cloud particles, results in a higher brightness count from the satellite sensor. Larger cloud particles have the effect of lowering of the sensed albedo slightly in the visible band due to lesser amounts of multiple scattering interactions.

In the near-IR (1.2 - 1.3, 1.6 - 1.7, and 2.1 - 2.3 μm) and shortwave IR (3.5 - 4.0 μm) windows, water clouds do not behave as perfect radiators. The shortwave IR band marks the transition of dominant radiant energy from the reflected solar regime to the longwave thermal infrared region of the Earth's electromagnetic (EM) spectrum. Although the absorption by liquid water clouds increases in these windows, their emission is much less than in the thermal IR window. However, there is a large contribution to the emergent radiation field due to reflection by the cloud top at the shorter IR wavelengths that is absent in the longer IR wavelengths. The reflectivity in the shortwave IR window is 0.10-0.17 for optically thick water clouds, but only 0.02-0.05 for thin clouds according to Hunt (1973), but more importantly, the reflectance is highly dependent upon particle size and phase with smaller particles (radii $< 15 \mu\text{m}$) being better reflectors than larger ones (Arking and Childs, 1985). When the sun is rising or setting, the optical depth for the incident solar radiation is relatively high. The water cloud reflectivity is thus increasing with decreasing sun elevation angle.

The emissivities of ice clouds are less than that of water droplet clouds, as a consequence of the ice cloud's lower water content and much larger particle sizes. Water clouds also will reflect more energy than ice clouds in this region of the spectrum. Thus, more radiant energy will be received at the satellite sensor from water clouds with respect to ice clouds during the daytime. Also, small cloud water droplets are more reflective than a like number of larger droplets (Kleespies, 1995). Plus, number distributions of small droplets within a cloud are generally much greater than that of larger droplets, which would tend to multiply this effect. Kleespies (1995) also found that for water cloud droplets with radius $> 6 \mu\text{m}$, the optical depth of the cloud was not a significant factor in the cloud reflectance returned to a satellite sensor. These conclusions reveal some of the useful qualities of the shortwave infrared band for distinguishing water and ice clouds during the daytime.

In the longwave or thermal IR (10 - 13 μm) window, both water and ice clouds are very poor reflectors or scatterers, but excellent emitters / absorbers. The emergent cloud top radiance is dominated by the emission from the cloud layer ($\rho \approx 0$, so $\epsilon \approx 1$). Therefore, because the cloud behaves nearly as a blackbody in this wavelength, the radiance emitted by the cloud tops can be used to estimate the temperature of the clouds by means of the Planck function (which relates temperature and wavelength to emitted radiance). Some ice clouds can be optically thin, therefore they transmit a significant amount of energy from beneath the cloud and emit correspondingly less energy from the cirrus cloud. In turn, they usually appear warmer than their true temperature, due to "warmer" radiances being transmitted through the thin clouds. The energy sensed by the satellite radiometer is not a reliable indicator of cloud temperature for these thin cirrus clouds, and their effects on the returned radiance are not negligible. The radiative properties of clouds in the thermal IR are fairly sensitive to the size spectra of the cloud particles. Increasing the size of the particles has the effect of increasing the transmissivity (from the Earth source below), decreasing the reflectivity (scattering), and increasing the absorptivity / emissivity of the cloud layer.

4.2 Satellite Sensing

4.2.1 Passive Satellite Imaging

Satellite-based imaging radiometers (imagers) are commonly used for cloud identification and characterization purposes. These sensors are designed to provide broad horizontal coverage of areas beneath the satellite at the finest resolution possible while enabling the satellite to sense, store, or transmit the data back to Earth. Most meteorological satellite imaging devices scan the Earth back and forth, taking radiance measurements at discrete time steps and producing a series of digitized elements along each scan line. This process is repeated until the entire Earth or a portion thereof has been sensed. Each rectangular element is assigned a specific location within the image by referring to a line (or scan) number and an element (or sample) number (Kidder and Vonder Haar, 1995). When displayed on a monitor, each element is referred to as a picture element or pixel. Using the sensed digital value (i.e. brightness temperature or count) for each pixel, a color or gray-shade can be assigned and displayed on the image.

A satellite instrument's resolution is defined as the size of the smallest element of a scene that can be resolved by the instrument. It is a function of the field of view of the sensor optics and its distance from the scene. Also known as the imager's footprint, the resolution can be thought of as the dimensions of the rectangular box on the scene from which radiation is gathered at each time step during the scan. The resolution is usually dependent on the wavelength (spectral) band or channel being interrogated. Present geostationary satellites are capable of 1 km visible and 4 km IR ground resolution directly under the satellite (at the satellite subpoint). Polar-orbiting satellites are capable of 1 km or better resolution in both visible and IR channels, but they are often limited by the data storage capability of the spacecraft. It should be noted that for individual cloud structures, cloud breaks, or other bodies smaller than the pixel size, the sensed radiance is integrated from the object and its background into a single response. Hence, the radiometer is unable to satisfactorily detect in isolation any source that is less than the resolution of the channel (Brimacombe, 1981). Each pixel sampled by the radiometer is recorded as a voltage, which is then converted to a digital brightness count onboard and transmitted to the ground on a scale from 0 to 255. Calibration tables are used to convert these numbers into radiance values, whereby temperatures can be inferred and/or images can be produced using a gray scale from white to black.

The fact that the Earth's surface is curved leads to some important effects when its surface is viewed from satellites. First, the degradation of the horizontal resolution of the as a result of changing the nadir angle imagery (known as foreshortening) is accentuated, since most sensors scan out for some distance from the satellite subpoint. Also, the data require corrections at oblique viewing angles for changing viewing geometry between the sun, the cloud, and the satellite for solar channels, and for the increasing path length through the atmosphere for IR channels. Additionally, the satellite tends to see more clouds at oblique viewing angles, since it looks through more atmosphere and has a higher probability of encountering a cloud. This also leads the sensor to confuse sides and lower cloud layers for the tops of clouds. Lastly, higher clouds when viewed at oblique angles may not be correctly assigned spatially due to parallax errors. Thus, pixels may be misrepresented horizontally and in height. Other potential errors in satellite sensing, such as sensor lag, signal interference, and normal atmospheric attenuation or contamination, may also introduce non-trivial errors into the remotely sensed product.

4.2.2 Satellite Spectral Band Characteristics

At first, the spectral bands used on weather satellites included only the visible and thermal (longwave) infrared (IR) regions of the electromagnetic spectrum, since these windows held most of the obvious cloud information. But over the past few decades, the operational and scientific use of other bands, such as the near-IR window, shortwave IR window, and water vapor band, has become more commonplace. While most meteorological satellites now make measurements throughout the visible and infrared regions of the spectrum, others have additional capabilities in the ultraviolet and microwave realms. A brief description follows below regarding the more commonly used satellite channels and some of their uses that apply to cloud sensing. The reader is referred to other detailed guides on satellite imagery interpretation and detection of atmospheric phenomena that go much further beyond the scope of this study (Weber and Wilderotter, 1981; Brimacombe, 1981; Scorer, 1986; Rao et al., 1990; Bader et al., 1994; Kidder and Vonder Haar, 1995).

4.2.2.1 Visible Band

Probably the most commonly and longest used spectral band from satellite imagers is in the visible portion of the spectrum. The visible channel typically includes wavelengths from 0.4 to 0.9 μm and exists within a water vapor window and at the peak of the solar EM irradiance spectrum. This channel gives us imagery in colors (or gray-shades), contrast, and textures that are most recognizable to the human eye and makes for a quick assimilation of land, water, and cloud features. Also, the visible channel typically offers the greatest spatial resolution from the satellite sensor. The main drawback is that its imagery is only useful during the daylight hours unless the sensor is specially equipped with a low-light (moonlight illumination) capability (Kidder and Vonder Haar, 1995). The visible brightness or albedo of a target depends on three factors - the intensity of the solar radiation, the sun's elevation angle or illumination, and the reflectivity properties of the body itself. The reflectivity of a cloud depends primarily on its thickness, but also on the nature of the cloud particles, whether ice or water and their sizes. Sometimes a higher thin cloud's brightness may be enhanced when the underlying surface has a high albedo and the radiation from this surface increases the net radiance, making it hard to detect thin cirrus layers. However, under similar illumination, a water droplet cloud will appear brighter than an ice crystal cloud of comparable thickness due to the greater number of multiple reflections that are possible in a liquid cloud, especially for smaller water droplets (Brimacombe, 1981).

During visible data processing, the image is displayed such that the greater the returned radiance, the brighter the pixel. Visible imagery can assist in the interpretation of high and low cloud layers, since generally, thicker or higher clouds will appear whiter or brighter due to higher reflectivities (albedo). Visible data is often used to discern texture, and thus cloud type, from the tops or edges of clouds. It can also help to detect high clouds (cumulonimbus) embedded within lower cloud decks through recognition of their shadows during low sun (elevation) angle periods. Visible imagery is good for locating low cloud or fog covered areas that don't show up well in the infrared, but it can cause problems discerning snow or ice cover from clouds with little contrast.

4.2.2.2 Longwave IR (LIR) Band

The thermal or longwave infrared (LIR) window channel from 10.0 - 12.5 μm is generally the most commonly used portion within the middle IR realm (about 3 to 15 μm). In this band, where the terrestrial radiation spectrum peaks, reflectivity is negligible and the emissivity of land, water, and thick clouds is very near one. What little atmospheric absorption occurs in this channel is principally due to water vapor and may cause the radiating surface to appear slightly colder than it actually is. This factor becomes most pronounced when the path length is long or where there is a high water vapor content along the path (Brimacombe, 1981). After a slight correction for these effects, these surfaces can be assumed to be blackbody radiators. Brightness temperature, also known as the equivalent blackbody temperature, is often used in the infrared regime to express the amount of radiant energy impinging upon the satellite sensor. However, unlike in the microwave spectrum where radiance is simply proportional to temperature, the infrared brightness temperature must be determined by inverting the Planck function rather than by simple division (Kidder and Vonder Haar, 1995). Inversion of remotely sensed radiances into atmospheric or cloud parameters is never a simple problem when accuracy is a must. Calculations must be made of atmospheric transmittance, Mie scattering parameters, and of the radiative transfer for a variety of conditions, and potential instrument calibration errors and assumptions in the methodology must be taken into account.

Since IR radiation can be related to the emitting temperature of a body, and because the troposphere generally cools with height, using the thermal IR channel can be used to give us valuable data about the temperature, thickness, and height of clouds. Thus, the images constitute a thermal map of the earth's surface and cloud tops. In visible imagery the contrast between clouds can be poor, whereas IR imagery can easily discern higher clouds and lower clouds from their temperature differences. Another important aspect of infrared imagery is the ability to provide information on clouds during the night, when visible imagery is useless.

While images received from visible wavelengths are produced like ordinary photographic prints, LIR images, as well as all other IR channel imagery, are generally produced and displayed in negative (Scorer, 1986) (see Figures 4.3 and 4.4 for a comparison of univerted and inverted IR images).

Uninverted GOES-8 CH4



Figure 4.3 Uninverted IR (CH4) image for 10 Apr 95 1745Z

Inverted (Normal) GOES-8 CH4

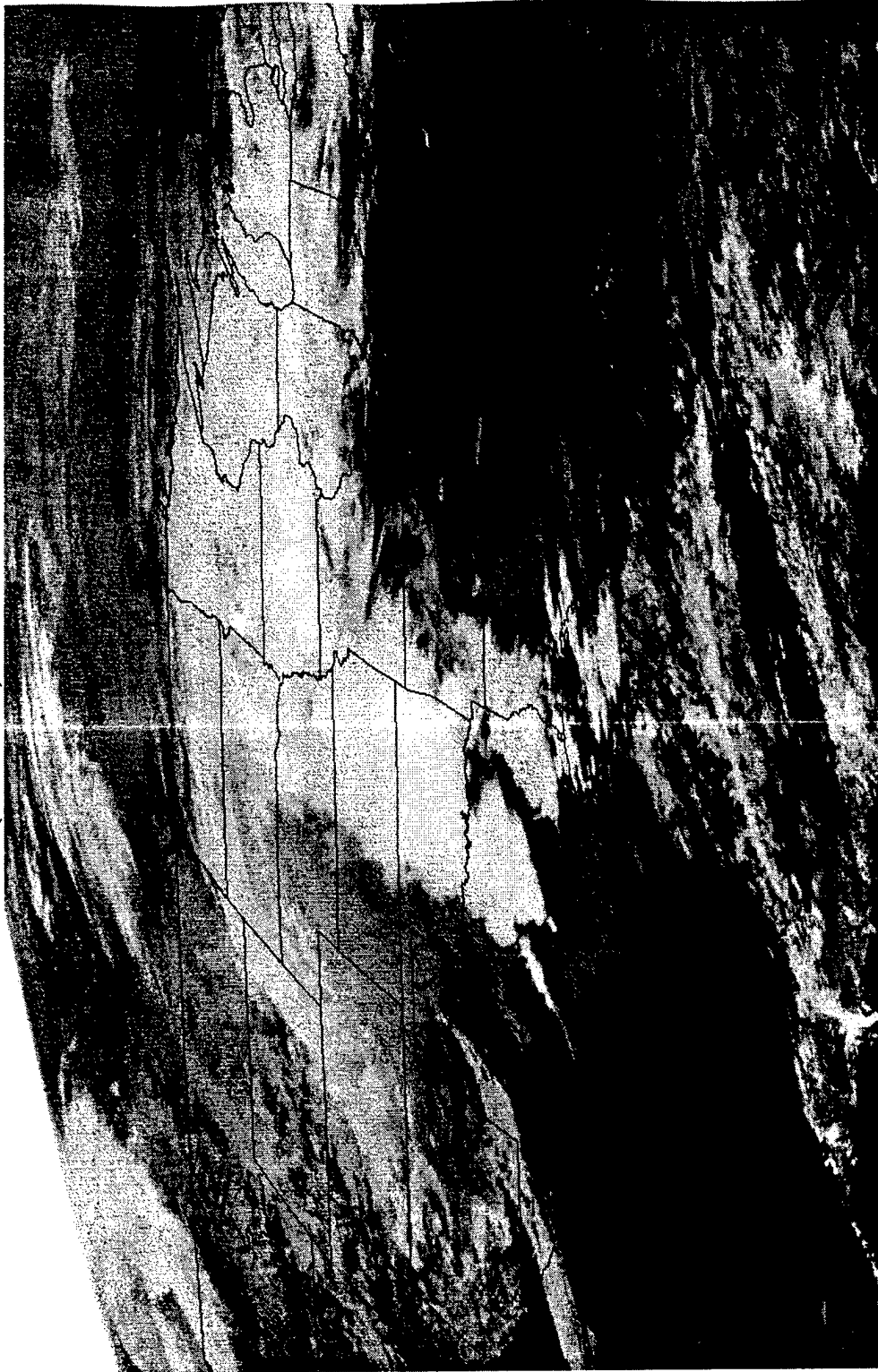


Figure 4.4 Inverted IR (CH4) image for 10 Apr 95 1745Z

These "inverted" images result in higher (warmer) radiance values being represented by darker pixels, instead of by brighter pixels as they would in the visible. Used for the sake of comparison with visible imagery, this convention means that clouds or surface features appear darker where they are warm and whiter where they are cool. Thus, the highest, coldest (mostly ice) cloud tops and snow cover (with low IR radiances) appear white in this channel, and the land, water bodies, and lower liquid water clouds appear darker varying with their warmer temperature (higher radiances). This presents a problem for detecting low clouds at night, because their radiating temperatures can be nearly the same as the background (land or sea).

Since in this channel the radiometer is effectively measuring emitted temperatures in the field of view and not reflected energy, some poor reflectors display different qualities that are not apparent in a visible image (Brimacombe, 1981). For example, thin high cirrus clouds consisting mainly of ice crystals at low temperatures, while occasionally transparent in the visible, are well distinguished in the IR. Although, they may appear warmer from higher sub-cirrus radiances penetrating through. Also, sea surfaces in the visible, except for sun glint, are consistently very dark, but show up as various dark gray shades due to temperature variations. Temperature variations that occur naturally from day to night and with seasonal and latitudinal changes will affect the overall appearance of infrared images. When breaks between clouds in the field of view are smaller than the resolution of the sensing instrument, higher radiances from underlying surfaces will be combined with the cloud top resulting in an incorrectly integrated radiance for the pixel. These errors tend to favor a warmer pixel radiance and might reduce the contrast between the surface and cloud or infer the cloud to exist at a lower altitude.

4.2.2.3 Shortwave IR (SIR) Band

More recently, the use of the shortwave infrared (SIR) window channel (3.5 - 4.0 μm) has become an important tool for researchers and forecasters, though it must be used with some caution. The appearance of the shortwave IR image is complex during the day, because it includes both radiative contributions from reflected solar radiation and emitted terrestrial radiation in varying fractions dependent upon the solar illumination and the surface's (cloud, land, or water) spectral properties (Figure 4.5).

Surfaces with high reflectivities in this band (liquid water clouds) are observed as surfaces with higher brightness temperatures (satellite images appear darker) than the actual temperature, because a portion of the sun's radiation is added (reflected) to the near-blackbody radiation emitted from the cloud surface (Liljas, 1986) (see Figure 4.6).

A very important property of the SIR spectral band is that ice is very absorptive of these wavelengths. Snow covered ground and sea ice are highly absorptive and scatter very little of the radiation in this band. Clouds composed mainly of ice crystals could absorb more radiation than those made up of liquid water droplets of like numbers and sizes. But more importantly, most water clouds are composed of a larger distribution of much smaller particles on the order of the incident wavelength in this channel (Scorer, 1986). Not only is there much less absorption from typical ice clouds (cirrus), but the additional solar reflection component from the water clouds results in much greater radiances received by satellite sensors. The shortwave IR image's interpretation is not as straightforward as each of the previous channels, since it cannot quantitatively establish cloud-top temperatures like thermal IR, nor can it reveal all cloud features as easily represented by visible imagery. This band tends to display more characteristics typical of the visible regime during the day and the thermal infrared band at night.

While the shortwave infrared channel shares much in common with the two previously described spectral bands, its imagery is somewhat hard to interpret without a review of its channel characteristics that are listed above in the summary of Hunt's (1973) study. Some other aspects of clouds in the shortwave IR band follow from research by Arking and Childs (1985), Scorer (1986), Liljas (1986), and others. Daytime fog and low stratus have a high reflectivity due their large distribution of small water droplets and appear darker (warmer) to the satellite sensor from the increased radiance. But during the night, they appear slightly cooler (brighter) in this wavelength versus the thermal IR channel (d'Entremont and Thomason, 1987; Ellrod, 1995; Nelson and Ellrod, 1996). Thin cirrus (ice) clouds though cold appear relatively warmer at night, especially when over low clouds, due to their high transmissivity and resultant upwelling radiance contamination from below (Ellrod, 1992). Low clouds over snow cover or ice on water bodies appear dark owing to their higher reflection and absorption combination (Kidder and Wu, 1984; Allen et al., 1990). Developing cumulonimbus and towering cumulus clouds appear warmer (darker) than do

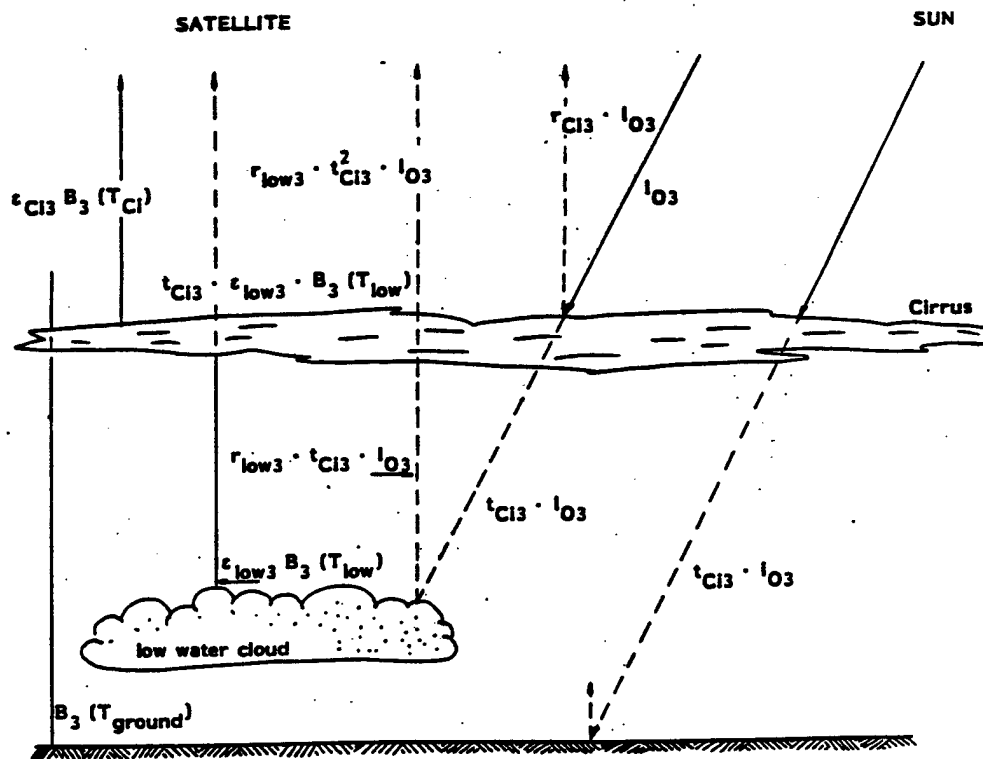


Figure 4.5 Schematic showing the radiation components reaching channel 2 of GOES-8 imager (adapted from Liljas 1986)

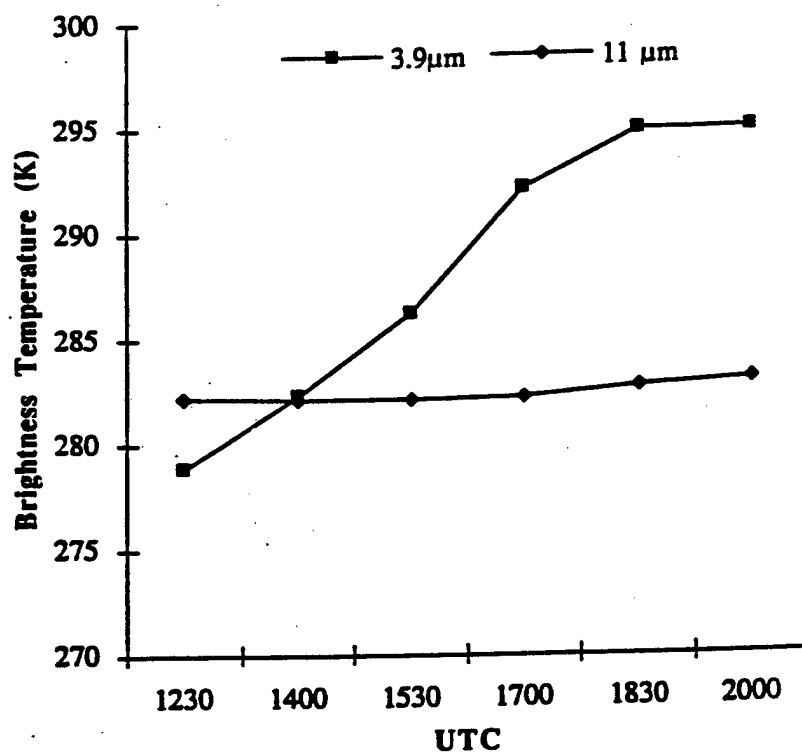


Figure 4.6 Brightness temperature difference versus time for SIR and LIR channels on GOES-VAS (from Kleespies 1995)

decaying cumulonimbus (brighter), because they are mainly liquid water topped during formation and glaciated when mature or dissipating. Sometimes warm, dark cores will appear in a developing or mature cumulonimbus cirrus shield (Setvak and Doswell, 1991). These are likely the result of greater absorption by larger, supercooled liquid water drops and reflection by larger numbers of smaller liquid droplets which have been pushed aloft to extremely high and cold levels by the strong updrafts within the storm. Detection of clouds during the night using the shortwave IR band is much like that of the thermal IR band, but with not nearly as strong of a blackbody return, since the dominant radiant energy feature is only the emission from each surface. While this channel can be used to identify clouds at night (Olesen and Grassl, 1985; d'Entremont, 1986), it is not used within the scope of this study.

In research studies, the shortwave IR channel has been used alone and in conjunction with other satellite channels to interrogate many atmospheric and Earth surface phenomenon (Ellrod, 1992; Kleespies, 1989). Kidder and Wu (1987) and Prins and Menzel (1992) have used the channel to detect very hot surface temperature regions such as industrial hot spots, volcanoes, mass burning, or forest fires. Use of the SIR and LIR channels through a channel differencing scheme led to an improved ability to detect nighttime rainfall (Ellrod, 1994). Arking and Childs (1985) used the visible, shortwave IR, and thermal IR bands on the Advanced Very High Resolution Radiometer (AVHRR) to determine cloud fraction, cloud-top temperature, optical thickness, and cloud microphysical properties. Some researchers have devised schemes to remove the emitted portion of the radiation in this channel by digitally subtracting the emitted radiance of another channel, assumed to be nearly the same in the thermal infrared, in order to isolate the solar component. This process has been used to support the study of global feedback mechanisms caused by clouds in a global change scenario. Other researchers (Allen et al., 1990; Lee et al., 1996; Kleespies, 1995) using polar-orbiting and geostationary satellite instruments have used this process to quantitatively investigate continental and marine cloud properties during the daytime. More recently, several qualitative applications of this channel have appeared. They can identify low clouds over snow cover and identify thin stratus clouds. The images have been used to identify shiptrack effects on marine stratus caused by changes in reflectivity due to cloud particle size changes from ship exhaust. It has also been suggested that

the SIR band can be applied with other channels to detect large supercooled water droplet regions that present icing hazards to aircraft (Menzel and Purdom, 1994; Ellrod, 1996a).

4.2.2.4 Water Vapor Band

Another imager channel coming into more frequent usage, known as the water vapor channel, takes advantage of upper atmospheric water vapor absorption in the spectral band between 5.4 and 7.1 μm , and most commonly centered at 6.7 μm in the IR regime. At this wavelength, most of the sensed terrestrial energy comes from the middle to top of the troposphere roughly between 300mb and 600mb (Kidder and Vonder Haar, 1995). This band is used to infer middle to upper tropospheric water vapor or humidities. Since this is not a water vapor window channel, low level features can not be resolved unless the sensed column is extremely dry where there would be a lack of attenuation of surface radiance by water vapor. In this case, the water vapor image would appear dark as is the convention for high radiances in infrared imagery. For abundant atmospheric moisture or thick high or middle clouds, the imagery appears white owing from the lack of IR radiance being sensed. While this imagery can detect clouds that are deep in moisture, it is most commonly used to monitor the water vapor movement for cloud-free regions through a satellite image looping procedure. Sinking motions within the troposphere can be implied due to adiabatic warming and drying processes resulting in dark regions on the imagery. The opposite is true for rising motions with adiabatic cooling and condensation processes resulting in whiter areas (looking much like clouds).

4.2.2.5 Microwave Region

The passive imaging of the microwave portion of the Earth's EM spectrum has been a rich source of data on precipitation, atmospheric and surface temperatures, ocean surface characteristics, cloud water, water droplet phase, and soil moisture. In addition, the microwave instruments have the capability to measure the polarization of the sensed radiation from the land, ocean, and clouds. This also assists in the detection of the above phenomena. While not the purpose of this study, much research has been devoted towards further understanding and utilizing the breadth of information from microwave imagery. Lawyer

(1995) developed a satellite derived icing index based mainly on passive microwave imaging data from polar orbiting satellites. His methods paralleled those of Jones and Vonder Haar (1990) and helped to retrieve cloud liquid water estimates over continental areas. Their research has shown that with proper knowledge of the land surface properties (specifically ground moisture and surface emissivity), the satellite-retrieved estimates of cloud liquid water can give a fairly good idea of the cloud regions' icing potential for non-precipitating clouds. When used in conjunction with other remote sensing methods, passive microwave imaging can be a powerful tool for the researcher or forecaster.

4.3 Analysis and Display Methods for Satellite Imagery

Several satellite imagery display methods that have been commonly used in the past will next be discussed. Also, some new display and analysis techniques involving multispectral combinations of satellite image channels will be described prior to their use in this study.

4.3.1 Black and White / Grayscale / Color Enhancements

The typical channels of early GOES imagery were primarily displayed individually as a black and white (B/W) linear scale image with intermediate gray shades denoting varying values of radiances or albedos. Infrared channel images were usually inverted for display in order that the coldest cloud tops would match that of the brightest cloud tops in the visible channel imagery. Image processors displayed up to 256 (8-bit) gray shades on their monitors, ranging linearly from black (zero) to white (255). Although a processor was capable of producing 256 tones of gray, only a limited range of them can be discerned by the image interpreter's eye. Thus, a wide assortment of gray shading enhancement scales to produce a better contrast for the observer were developed to take advantage of the thermal characteristics of the LIR imagery. This led to better ways to assess cloud height and type than for unenhanced linear scale LIR images. In addition, techniques of false color enhancement (creating color shadings unlike that which is seen by the human eye) have greatly improved the prospects for visual interpretation of meteorological and land surface phenomenon in satellite imagery. It has been found that such colorized imagery is easier to interpret than the more conventional single-channel B/W imagery.

4.3.2 Multispectral RGB Color Enhancement Method

With better imagery display technology and improvements of the channels on more recent polar orbiting and GOES satellites, methods incorporating combinations of satellite channels (known as multispectral combinations) have come into greater usage. Multispectral analysis involves the use of different satellite spectral channels together in order to highlight a desired parameter. This technique enables a fast application of all available channels, and avoids the visual inspection of a number of separate B/W or color enhanced images. Some atmospheric phenomena can be more easily identified by using satellite data from more than one channel in a multispectral image, such as fog or thin cirrus over low clouds. Color composite imagery is not a new concept and the use of different multispectral techniques to detect atmospheric or surface phenomenon has been commonly used in the research community in the past two decades. Studies by Colwell (1983), d'Entremont and Thomason (1987), Kleespies (1989), and more recently Bellec and Le Gleau (1992) have all explored ways of creating new multispectral color composite images for display and applying their use to meteorological features. Andreadis et al. (1995) also have gone on to investigate other means for displaying a color composited image using the three components of color as perceived by the human eye, namely the hue, saturation, and intensity.

One method which will be explored in this study involves simultaneously combining three B/W satellite images into a color enhanced product. This process involves the assignment of each of the three channels each to one of the color "guns" (red (R), green (G), and blue (B)) used in typical television image production. The resulting composite image is then referred to as being RGB enhanced. For each color image plane, there exists a range of resulting colors that the color guns will produce varying with the contribution from the channel. For example, the red gun ranges from dark red to pink to white depending on the display scale for the image pixels according to each channel's display convention (white representing hot brightness temperatures for uninverted IR or cold for inverted IR). If for any given image pixel, the measured brightness temperatures are the same, then the contributions to the color guns will be the same (d'Entremont and Thomason, 1987). When any three channels are combined, equal contributions of red, green, and blue will yield a shade of gray in the color image. But more commonly, the varying contributions of each channel create a rainbow of colors varying in hue with the resulting colors a

combination of the red, green, and blue guns. The intermediate colors for the RGB image are cyan (green-blue), yellow (red-green), and magenta or purple (red-blue). To quantify the RGB color combination of the three channels may be easier when all three channels are in the IR regime, since it would be more likely that the brightness temperatures would correlate for similar RGB contributions. However, the resulting image would not take advantage of the different spectral characteristics for visible, SIR, and LIR regimes. So, in the case of RGB combinations of different spectral channels, the interpretation is best left to a qualitative understanding of the phenomena highlighted through its use.

4.3.3 Multispectral Channel Differencing (ΔT_B) Method

Satellite channel differencing methods have been around for quite some time and have been frequently used in cloud classification schemes. Channel differencing commonly involves the manual or automated digital subtraction of brightness temperatures (T_B) for each image pixel of two different satellite imagery channels in the IR regime creating new composite imagery with a new, resultant brightness value (ΔT_B). A study by Shenk and Curran (1973) used this method to detect cirrus clouds and infer their heights. Crosiar et al. (1989) also used this technique to automate cloud detection over oceans during the night. Allen et al. (1990) showed that this method can help to distinguish clouds from underlying surface snow cover or ice cover. Dills et al. (1996a and 1996b) used the channel differencing method to infer and detect cloud phase, low clouds, fog, and surface features. Again, these combinations of the various IR satellite channels provide additional valuable information for detecting cloud and near-surface features with respect to using each IR channel separately.

For this study, the channel differencing method follows that of Ellrod (1996a) (described previously in Chapter 2) and was limited to GOES-8 channels 2 and 4. These channels were chosen in order to utilize some of their unique spectral characteristics during the daytime. These spectral properties have been previously described. To maximize the detected reflective component of the CH2 radiance, the satellite image times were selected during a daytime period with a high solar zenith angle and satellite viewing angle in the vicinity of the region. Then, to simplify the interpretation of the daytime 3.9 μ m (CH2) image, the emitted radiation (or thermal) component was subtracted from it by using the 10.7

micron (CH_4) radiance creating the desired ΔT_b for use in the study. Thus, dominant liquid water cloud features should be evident from the magnitude of the reflected solar component with the greatest ΔT_b representing smaller liquid droplets and moderate ΔT_b indicative of the more hazardous larger cloud droplets at cloud top. The idea is to use the unique daytime spectral properties and radiance values of these two IR channels and their variation with cloud microphysical properties together to combine into a channel differenced product. Then, after comparison to the sensed albedo from the visible channel 1, an indication of cloud microphysics (cloud droplet size and phase) for potential icing conditions from interrogation of cloud-top regions should be the result.

4.4 GOES-8 Imager

4.4.1 GOES Background

In the early 1970's, NASA research and development began the Geostationary Operational Environmental Satellite (GOES) program within the National Oceanic and Atmospheric Administration (NOAA). Several spin stabilized satellites were built and in October 1975 GOES-1 was launched, which introduced a new era of satellite service. Overseas the European communities have maintained a series of geostationary satellites (Meteosat), as have the Japanese with the GMS. A good summary of the European Meteosat satellite's capabilities is contained in Mason and Schmetz (1992). Unlike polar-orbiting satellites which travel around the Earth in a low altitude orbit several times a day, these geostationary satellites remain nearly fixed at a point about 35.8 km above the Equator. Imagery for these early GOES satellites were provided by the Visible and Infrared Spin Scan Radiometer (VISSR). GOES significantly advanced our ability to observe weather systems day and night by providing regular interval visible and infrared imagery of the Earth's surface and atmospheric moisture, thus becoming a critical part of National Weather Service (NWS) operations. Since GOES-4 was launched in 1980 through the recently retired GOES-7, several more spectral bands had been added and the introduction of the VISSR Atmospheric Sounder (VAS) enabled active sensing of atmospheric temperature and moisture as well as imaging capabilities. Although these new instruments represented improvements in satellite sensing skill, some compromises were made (Menzel and Purdom, 1994). First, imaging and sounding could not be done at the same time.

Secondly, past GOES satellite imaging radiometers would spin continuously (100 rpm) while performing its sensor duties. The spinning GOES-VAS viewed the Earth roughly 5% of the time, so it was not possible to attain signal-to-noise ratios needed for either high-quality soundings or greater spatial resolution data. This left the sounding data to be taken only in special experiments and research during dwell sounding mode, when no imaging was to be undertaken.

Understanding the need for a better imaging and sounding platform, NOAA began in 1985 the development of the next generation of satellites, GOES I-M, each designed for a five-year lifetime. Finally, in April 1994, GOES-8 (formerly GOES-I in development) was successfully launched and now resides at 75°W longitude (Figure 4.7). This was followed nearly one year later by GOES-9, which will be moved to its permanent location near 135°W after its checkout period. The most significant change from previous GOES satellites results from its stabilization technique. GOES-8 is three-axis stabilized, which enables the instruments to always be pointed at the Earth. This system allows better multispectral imaging accuracy with improved spatial resolution, the sounder and imager (now separate instruments) to collect data at the same time, more stable calibration, and more precise image framing registration. Figure 4.8 shows a sketch of the GOES-8 imager. The new earth-oriented geostationary spacecraft design required new scanning, navigation, calibration, and thermal control systems (Menzel and Purdom, 1994). For more efficient imaging with near-continuous viewing of the earth, the scanning system moves in boustrophedon fashion (i.e. moving (slewing) back and forth west to east then east to west). Also, more precise pointing techniques using a star sensing system as a fixed reference allows imager and sounder pixels to be located within 4 km at nadir. To improve calibration, looks to space and reference blackbodies are external to the instrument unlike the previous GOES-VAS. Finally, to accommodate the large daily thermal changes (varying by tens of degrees Kelvin) that occur with staring instruments, better monitoring of thermal gradients and focal properties has been introduced. This means that the sensor takes no longer than 30 minutes between looks at its blackbody, ensuring that the calibration equation linear coefficients remain within specified noise levels.

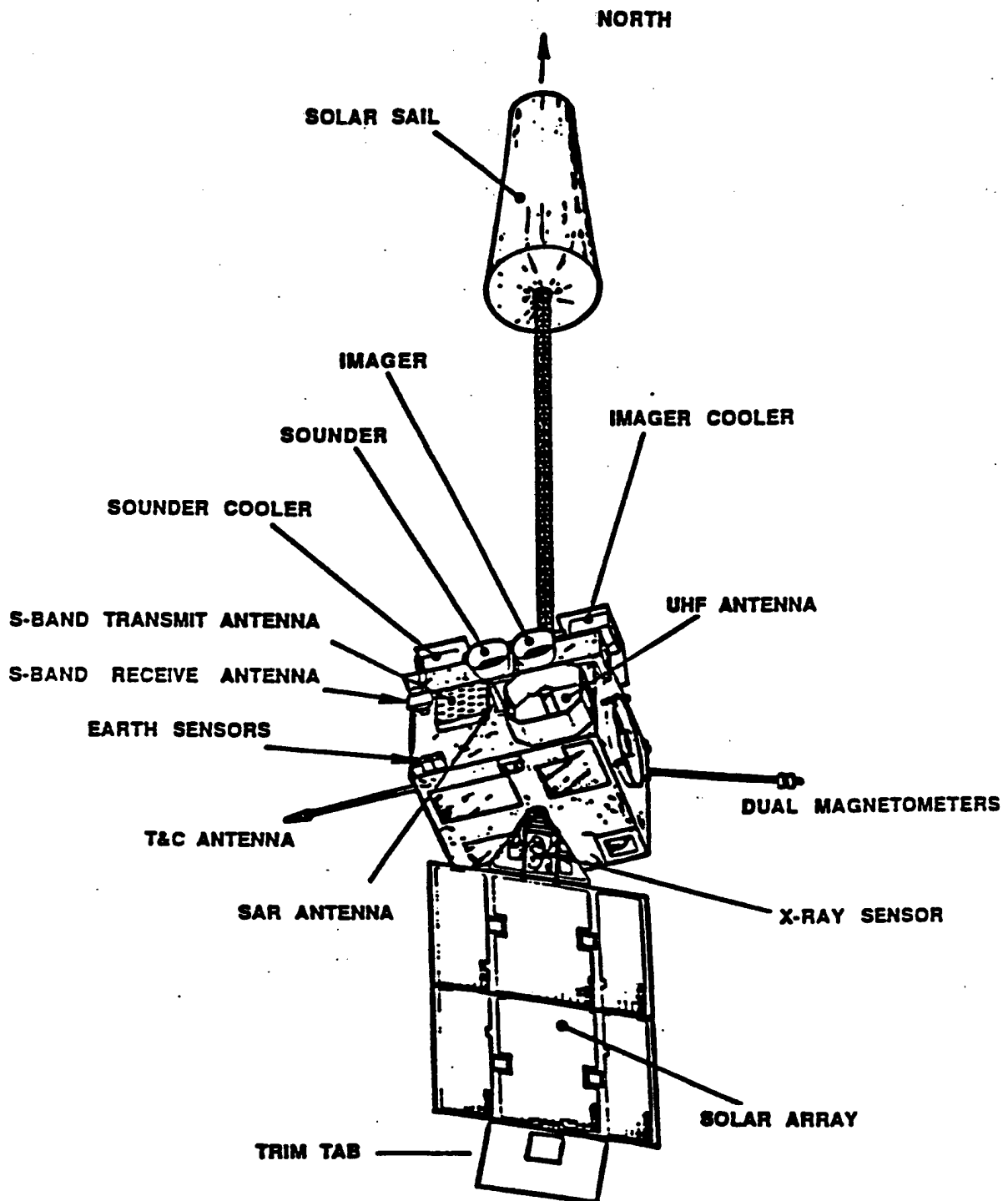


Figure 4.7 Sketch of GOES-8 spacecraft (from Kidder and Vonder Haar 1995)

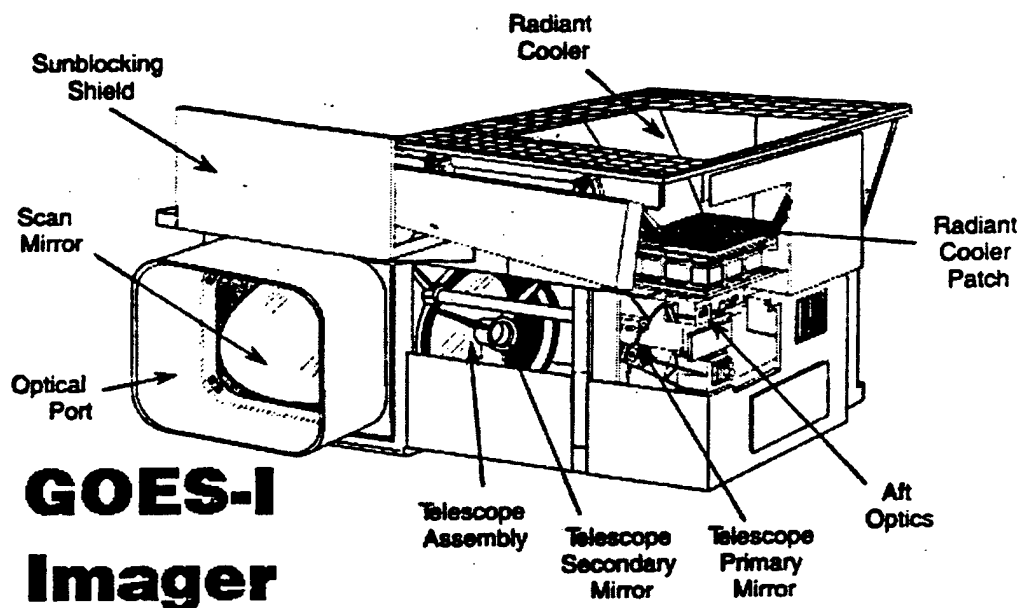


Figure 4.8 Sketch of the GOES-8 Imager (from Kidder and Vonder Haar 1995)

4.4.2 Imager Characteristics Compared to GOES-VAS

The GOES-8 imager has a five channel multispectral capability consisting of a visible band (Channel 1: $0.52 - 0.72 \mu\text{m}$), three infrared window bands (Channel 2: shortwave IR (SIR)— $3.78 - 4.03 \mu\text{m}$, Channel 4: thermal IR (LIR)— $10.2 - 11.2 \mu\text{m}$, Channel 5: another longwave IR— $11.5 - 12.5 \mu\text{m}$), and a water vapor absorption band (Channel 3: $6.47 - 7.02 \mu\text{m}$). A summary of the GOES-8 imager's instrument and channel characteristics can be found in Tables 4.1a and 4.1b at the end of this section. Table 4.2 describes the instrument features for both the GOES-8 imager and sounder. The scanning part of the radiometer is a mirror which reflects energy into a telescope. Both visible and infrared energy are handled by the same optics, however different detection elements are used for different spectral bands. Visible data is swept out 8 lines at a time with eight silicon photodiode detectors (Kidder and Vonder Haar, 1995). The IR window channels are swept out two lines at a time, while the water vapor channel is swept

out one line at a time. Channels 3-5 use a mercury cadmium tellurium (HgCdTe) detector and the SIR Channel 2 uses an indium antimonide (InSb) detector. The spectral response of each band is determined by the sensor optics, such as beam splitters or filters, and by the detector properties. The imager provides the visible data at nearly 1 km ground resolution (comparable to GOES-VAS), but with 10-bit precision and a more stable linear response to radiance. The detectors sense a voltage that is converted into a digital brightness count value (Ellrod and Nelson, 1996b). The transmitted data stream contains calibration coefficients for users wishing to convert the digital count values to radiances (IR) and albedos (VIS).

A comparison of the characteristics of the GOES-7 (VAS) and GOES-8 imagers can be found in Table 4.3a. By using star references and traditional landmarks, the imagery is navigated to within 2-4 km compared to 3-10 km with VAS. The GOES-8 imager provides simultaneous IR imagery in four channels (one more than VAS). The ground resolution of the IR channels is much improved over that possible with VAS. The SIR channel has roughly four times the resolution, and the longwave IR channels have twice the resolution, while the water vapor channel has nearly the same resolution. At nadir, the ground resolution is 4 km for the IR window bands and 8 km for the water vapor band. The radiometric accuracy and onboard calibration yield brightness temperatures within 1 K accuracy and 0.3 K relative precision at most temperature ranges (Menzel and Purdom, 1994). Additionally, the noise levels are reduced nearly three times over the GOES-VAS. The GOES-8 imager also slightly reduced the amount of oversampling of its infrared channels, because of its better signal-to-noise ratios than the VAS.

For real-time weather forecasting, the GOES-8 data must be transmitted nearly instantaneously to field users. A new ground data processing system for the next generation GOES satellites permits efficient dissemination of imagery data and products to users (Menzel and Purdom, 1994). This is done using a completely redesigned GOES I-M Variable (GVAR) format for direct-receive users (like the Cooperative Institute for Research in the Atmosphere - CIRA/CSU) and existing GOES-Tap services for others. The GVAR format lets users receive real-time calibrated information from the imager and the sounder. Because of the difference in sampling frequency and resolution of GOES I-M versus the previous GOES-VAS, direct receive imagery from GOES-8 appears stretched in the east-west direction with respect to

GOES-7. This data stream is also being archived for future use, like previous GOES data starting in 1978. User access to the GOES archive is coordinated through the NESDIS Satellite Data Services Division.

With the recent successful launchings of two next-generation satellites (GOES-8/9) and their upgraded sensor packages, researchers are rushing to apply the improved remote sensing capabilities. Because the new series of GOES satellites produces imagery images as often as every 15 minutes with much better resolution, the potential for using these products operationally has greatly increased. This is especially true for the SIR Channel 2 (3.9 μm), since capabilities in this channel on past satellites have been very limited. The signal-to-noise ratio for the SIR band approaches that of the LIR band at warm temperatures, which helps in the quantitative analysis of Earth surface and cloud-top properties. Better satellite imagery display systems with looping capabilities also promise to extend their usefulness. In addition, the scan patterns for the GOES-8 imager is much more flexible than those on the GOES-VAS. It is even possible to suspend a full-disk scan to perform a rapid scan of a small area, and then resume the larger scan. This capability lets researchers or severe weather forecasters to more finely interrogate a small geographic region with maximum resolution at very short time intervals (on the order of minutes depending on the area size).

4.4.3 Spectral Improvements Over GOES-7

In their paper, Menzel and Purdom (1994) did a thorough comparison of the spectral packages for the imager on GOES-7 and the improved imager on GOES-8. Though published before the launch of GOES-I (8), their simulations of GOES-I imagery and knowledge of the different channel characteristics provide a good source expected improvements (listed in Table 4.3b). These channel by channel advances are summarized below. In the visible, major improvements are in 10-bit versus 6-bit imagery and increased sampling frequency. The oversampling should allow for better cloud-edge detection, while the data storage improvement will provide sixteen times more available (1024 versus 64) brightness levels or gray-shades. This enables a wider range of image enhancements that could upgrade cloud-top and cloud-edge feature detection for use in determining cloud-drift winds, better quality and extended use of visible imagery in low-light situations, potential detection of haze and pollution, and improved daytime cloud

height measurements using both stereo and cloud shadow techniques. For the SIR window channel, major improvements in resolution (2x4 km vs. 4x16 km) and better radiometric sensitivity at warmer temperatures will greatly increase the ability to detect fog at night, locate water clouds over snow in the daytime, delineate between SLW and ice clouds during the daytime, and locate thermally hot surface areas. It should also help to identify the hurricane eye when it is obscured by cirrus clouds and better determine sea surface temperatures. In the water vapor channel, the spatial resolution is enhanced by twice that of the VAS and signal-to-noise is improved by three times. This should provide better identification of middle and upper level moisture patterns and synoptic weather features when viewed in a looping sequence. In the LIR channel, a near fourfold increase in spatial resolution will help to provide more refined cloud-top features, severe storm identification, and heavy rainfall estimations. The split window (11.5 - 12.5 μm) channel will experience an eight-fold increase in resolution and covers a wider spectral width than VAS. Its resulting signal-to-noise refinement, same as the LIR channel, should give more accurate low-level moisture indications and enhanced sea surface temperature retrievals.

Table 4.1a GOES-8 imager instruments' characteristics (from Kidder and Vonder Haar 1995)

Parameter	Value
Optics	Cassegrainian telescope 31.1-cm-diameter primary mirror Focal length 381.2 cm
Earth location accuracy	$\pm 30 \mu\text{rad}$ (rms)
Channel coregistration	$\pm 28 \mu\text{rad}$
Scanning rate	
Full disk	25 min
3000 \times 3000-km area	3.1 min
500 \times 500-km area	20 s
Channels	Five (0.65, 3.9, 6.75, 10.7, 12.0 μm)
Digitization	10 bits
Date rate	2.6208 Mbits s ⁻¹
In-orbit calibration	
IR (channels 2–5)	Space and internal 290-K blackbody
Visible (channel 1)	None
Size	
Sensor module	115 \times 80 \times 75 cm
Electronics module	67 \times 43 \times 19 cm
Power supply	29 \times 20 \times 16 cm
Mass (3-module total)	120 kg
Power consumption	119 W, daily average

Table 4.1b GOES-8 imager channels' characteristics (from Kidder and Vonder Haar 1995)

Channel	1	2	3	4	5
Wavelength (μm)	0.55–0.75	3.8–4.0	6.5–7.0	10.2–11.2	11.5–12.5
Detector type	Silicon photodiode	InSb	HgCdTe	HgCdTe	HgCdTe
Noise or NE ΔT	± 8 counts	0.15 K at 300 K 3.5 K at 230 K	0.3 K at 230 K	0.2 K at 300 K 0.4 K at 230 K	0.2 K at 300 K 0.4 K at 230 K
NE ΔL (mW m ⁻² sr ⁻¹ cm)		0.0058	0.044	0.31	0.35
IFOV (μrad)	28	112	224	112	112
Ground resolution (km)	1.0	4.0	8.0	4.0	4.0
Sampled resolution at subpoint (E–W \times N–S, km)	0.57 \times 1.0	2.3 \times 4.0	2.3 \times 8.0	2.3 \times 4.0	2.3 \times 4.0

Table 4.2 GOES-8 imager and sounder instrument features (from Menzel and Purdom 1994)

Feature	Imager	Sounder
Optical aperture	31.1 cm	31.1 cm
Type optics	Cassegrain	Cassegrain
Methods of scan	Two axes, continuous Linear E/W 64 μ rad (2.3 km) Line step N/S 224 μ rad (8 km)	Two axes, step and dwell E/W 280- μ rad steps N/S 1120- μ rad steps (or 2240- μ rad with 0.1- or 0.2-s dwell)
Spatial resolution	Visible 28 μ rad (1 km) IR windows 112 μ rad (4 km) H ₂ O band 224 μ rad (8 km)	242 μ rad (10 km)
Sampling	Visible 1.75/IGFOV* IR windows 1.75/IGFOV H ₂ O band 3.5/IGFOV	Four IGFOVs sampled at the same time
Sampling rate	20° s ⁻¹ 183.3 μ sec per pixel (IR) 45.8 μ sec per pixel (vis)	40 soundings s ⁻¹ 0.1, 0.2, or 0.4 s per sample
Spectral band coregistration	$\pm 28 \mu$ rad	Within 22 μ rad of IR 10.7- μ m window
Data output	10-bit quantization	13-bit quantization
Data rate	2.6208 Mb s ⁻¹	40 kb s ⁻¹
Time between space looks	2.2 s (nominally for large frame) 9.2 or 36.6 s (nominally for small frame)	2 min
Time between blackbody calibrations	10–30 min	20 min

*Instantaneous geometric field of view

Table 4.3a GOES-7 and GOES-8 imager characteristics (from Menzel and Purdom 1994)

Wavelength (μm)	IGFOV (km) E/W \times N/S	SSR (km) E/W \times N/S	Noise
GOES-7			
0.55–0.75	0.75 \times 0.86	0.75 \times 0.86	6-bit data \pm 2 counts 3σ
3.84–4.06	13.8 \times 13.8	3.0 \times 13.8	0.25 K @ 300 K, 6.00 K @ 230 K
6.40–7.08	13.8 \times 13.8	3.0 \times 13.8	1.00 K @ 230 K
10.4–12.1	6.9 \times 6.9	3.0 \times 6.9	0.10 K @ 300 K, 0.20 K @ 230 K
12.5–12.8	13.8 \times 13.8	3.0 \times 13.8	0.40 K @ 300 K, 0.80 K @ 230 K
GOES-8			
0.52–0.72	1.0 \times 1.0	0.57 \times 1.0	10-bit data \pm 8 counts 3σ
3.78–4.03	4.0 \times 4.0	2.3 \times 4.0	0.15 K @ 300 K, 3.50 K @ 230 K
6.47–7.02	8.0 \times 8.0	2.3 \times 8.0	0.30 K @ 230 K
10.2–11.2	4.0 \times 4.0	2.3 \times 4.0	0.20 K @ 300 K, 0.40 K @ 230 K
11.5–12.5	4.0 \times 4.0	2.3 \times 4.0	0.20 K @ 300 K, 0.40 K @ 230 K

Table 4.3b Expected improvements in GOES-8 imager products (from Menzel and Purdom 1994)

<ul style="list-style-type: none"> • More details in imagery (4-km IR resolution, oversampled visible, better signal to noise, higher bit depth). • Improved composite imagery (five spectral bands). • Low-light visible imagery (10-bit visible data). • Better synchronization with other observations (separate imager). • Better cloud-drift winds (4-km resolution, better edge distinction). • Improved water vapor motion (winds in clear regions). • Enhanced severe storm forecasting (timely rapid imaging, derived products at 4 km, 10-bit visible data). • Timely fog detection at night (continuous 3.9-μm imaging).

Chapter 5 — Icing Case Studies Research

5.1 Overview

Traditionally, aircraft icing forecast products have specified threat regions, heights and bases, and occasionally icing type. These forecasts have been accomplished using a variety of different methods, several of which were discussed in Chapter 2. They also exhibit a large variability in forecast accuracy. The information used to prepare these forecasts has mainly included visible and infrared satellite imagery, output from numerical weather prediction models and cloud advection models, precipitation forecasts, and pilot reports. This study exploits the individual characteristics of three GOES-8 imager channels (VIS, SIR, and LIR) along with varying cloud-top microphysical properties and their change with each spectral band to develop a scheme that will infer a potential hazard for aircraft icing. Much of the background has been laid out in the previous chapters describing likely factors that could lead to a technique to better isolate the aircraft icing environment and improve horizontal and vertical spatial forecasting of this region. In consideration of the operational forecaster, the methods have been purposely kept as simple as possible in order to facilitate its usage in their environment.

To conduct a study of this type, it proved necessary to retrieve the verification data for the study first. This was only logical, since the analysis of satellite imagery would be moot without a way to determine the accuracy of a predicted icing environment or icing forecast through the only known quantification of aircraft icing on a large scale basis, namely pilot reports (PIREPs). Also, to use the PIREPs effectively, it was essential to understand the proper statistical or qualitative use of PIREPs for a research study, because as described in Chapter 2, they are not the most reliable or easiest way to confirm a scientific study (due to their subjectivity). The bulk of the data collection process time involved trying to find a source of PIREPs in a form which could be readily sorted by type, intensity, altitude, and latitude / longitude, and conveniently displayed or plotted. After trying unsuccessfully with the Aviation Weather Center (AWC; formerly the National Aviation Weather Advisory Unit (NAWAU)) in Kansas City and through contacts in the Air Force in the Air Weather Service to get the needed PIREP data, a search of the Internet provided an excellent source of this PIREP data, and accompanying decoding and plotting software (FORTRAN, C, and NCAR Graphics computer code) from the National Center for Atmospheric

Research (NCAR) Research and Applications Program (RAP). *[Thanks mainly to Greg Thompson, CSU grad, Dr. Barbara Brown, and others at NCAR/RAP: CSU grad Ben Bernstein, Dr. Marcia Politovich]*

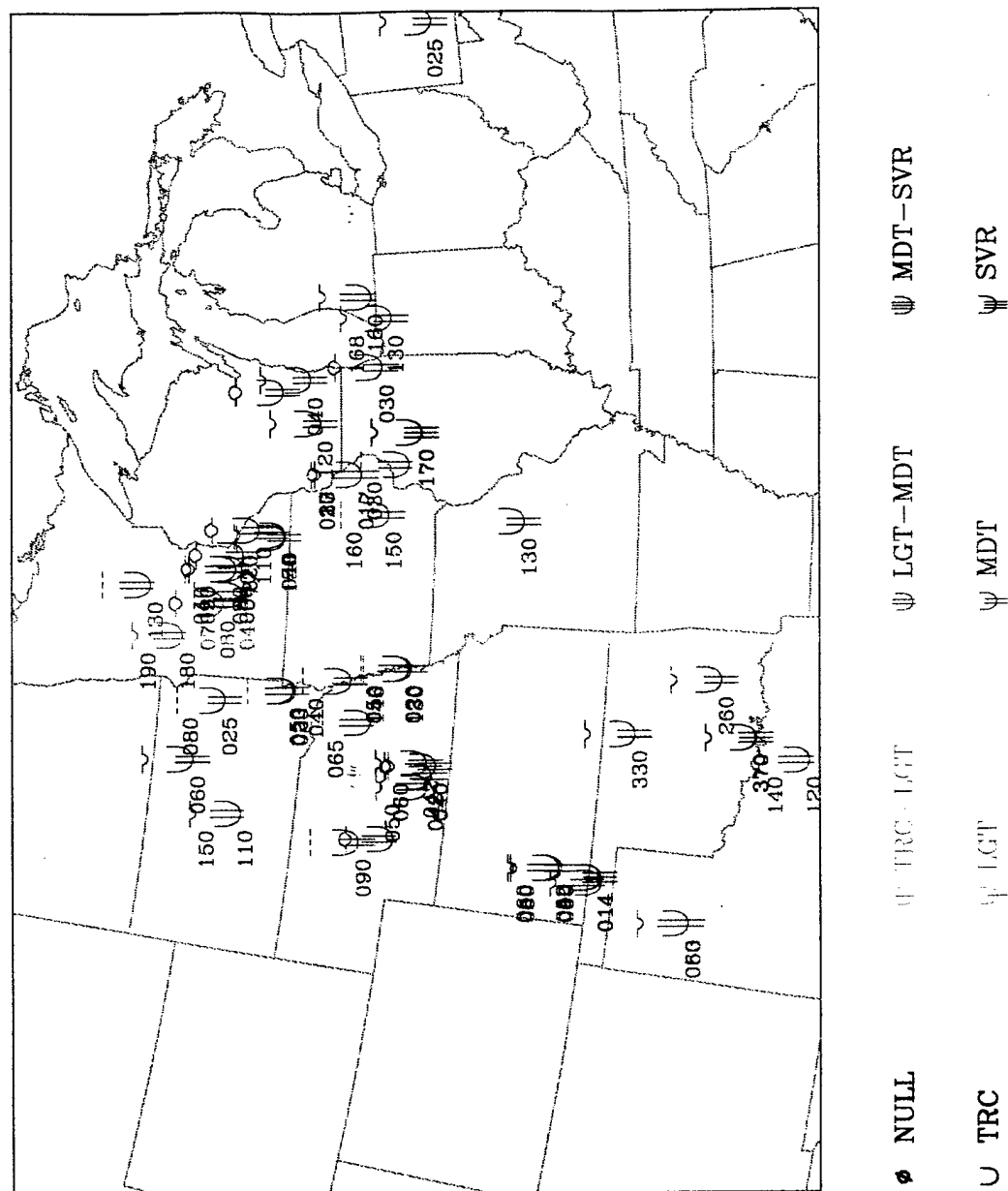
Once the desired PIREPs had been decoded and plotted, the optimal case study periods were determined through the use of prevailing synoptic conditions (significant atmospheric moisture and sufficiently cold atmospheric temperatures) and noting periods of a large number of PIREPs collections. These factors helped to narrow the likely study periods to the transitional seasons with a focus on late winter and early springtime in particular. With a narrowed scope for the case studies, my attention turned back to the satellite imagery collection and finally the analysis. Because of changes occurring with the CIRA/CSU GOES-8 imagery collection system, a few data archive losses, satellite movement from its checkout position, and image display format changes from the fall of 1994 into the spring of 1995, the cases selected for this study were limited to the period after 1 April 1995. After this date, the available archive of raw GOES-8 data was much more stable and convenient to retrieve thanks to some software developed by Duane Whitcomb of CIRA/CSU. The SubSect software package allows the user to retrieve near real-time GOES-8 imager (and sounder) data for any geographic area, as determined by the user, scanned by the satellite. The defined, sectorized images can then be viewed using another piece of software written in IDL (either Imgbar36, Imgbar41, or GVIEW standing for GVAR View). Upon finding that the satellite imagery was available for the desired case study dates, the GOES-8 imager data for channels 1, 2, and 4 was restored from the archive tapes. Then, the analysis began using techniques described below.

5.2 Data Collection

5.2.1 PIREPs

5.2.1.1 Collection and Display

All of the PIREPs came from the NCAR storage tapes and were collected via an anonymous ftp to a guest user directory into which they were transferred. They came in an encoded format that required software to decode and further software manipulation to create an icing graphic plot against a background map of the United States (as in Figure 5.1). This software was also made available to me via anonymous



ftp to NCAR. The massive number crunching of the PIREPs' software was accomplished with much help from my research group's computer system expert, Rick Taft, on my remote link from Galileo to Tornado. All raw, decoded, and plotted PIREPs are separated into hour segments throughout the case study period and stored on Tornado (no doubt taking up much space). The NCAR Graphics formatted plots are also viewed on Tornado using the "idt" command. Each plot can be tailored to plot specific intensities by changing the configuration file or by selecting collection periods varying in length of time for the plot using multiple PIREP file hours to build a larger file.

5.2.1.2 Selection for Verification

Every PIREP within a 3 hr PIREP file period, before or after, the analyzed satellite image's time were used in the verification of the methods listed below applied for icing conditions. This window of time was chosen so that an adequate number of PIREPs could be obtained to verify each time period. Additionally, the 6 hr window takes into account the reporting timing errors that are inherent in the PIREP database. Studies have shown that by setting a certain temporal window for PIREP collection around the desired analysis time, the statistical benefits of the study verification far outweigh the possible errors that may be introduced (Politovich and Olson, 1991; Brown et al., 1993).

5.2.2 Case Selection

5.2.2.1 Case 1 (10 Apr 95)

Case 1 covered an area approximately 2400 km by 1200 km over the Northern Rockies, Northern and Central Plains, and western Great Lakes of the central United States. This area (grid region shown in Figure 5.2) covered portions of Montana, Wyoming, Colorado, North and South Dakota, Nebraska, Kansas, northern Oklahoma, Minnesota, Iowa, Missouri, Wisconsin, Illinois, Michigan, Indiana, Kentucky, and western Ohio. The date and time (10/1745Z April 1995; Julian Day 100) were mainly chosen, because of a known abundance of PIREPs, on which to base the study verification, were collected during the day in the vicinity of a dynamic spring-time storm system. The necessary elements for icing to occur on a large scale were present as abundant warm, Gulf of Mexico moisture streamed northward to meet the cold,

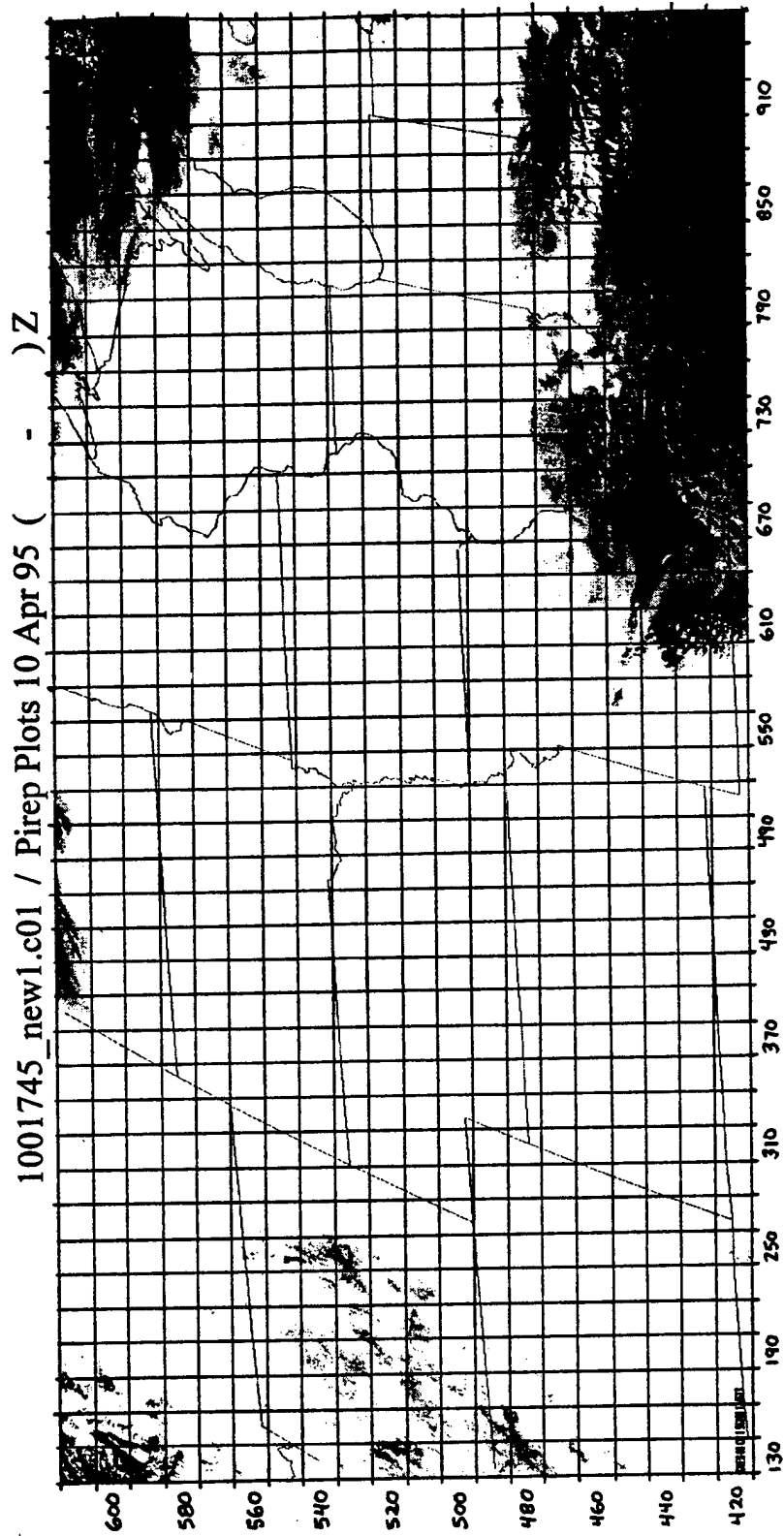


Figure 5.2 Example grid overlaying visible image at 10/1745Z Apr 95

continental polar air mass plunging southward out of Canada (see Figures 5.3 and 5.4). The air masses converged on the Central Plains creating a wide area of cloud coverage. For both cases, as would be expected, the convective (cumuliform) clouds dominated the cloud shield along and ahead of the frontal zones (both cold and warm fronts), and nearly uniform stratiform cloud decks trailed the surface low to the north and west.

At 10/12Z Apr 95, a strong, cold upper-level low pressure system (see Figure 5.5) was continuing to deepen over northern New Mexico and starting to move north-eastward into the Central Plains. The return flow of Gulf of Mexico moisture was enhanced by the strong pressure gradient between the deepening surface low pressure center in northern Texas and a region of high pressure parked over the southeast U.S. (see Figure 5.6). A high pressure system (continental polar air mass) over Ontario and the northern Great Lakes was helping to feed a broad area of cold air into the Central Plains and Great Lakes regions. Precipitation in the form of snow showers occurred most of the day over eastern Colorado and north-eastward through central Minnesota, while rain showers and thunderstorms were prevalent from eastern Texas through eastern Kansas, western Missouri, and into northern Illinois (see Figure 5.7). Two of the most important ingredients for aircraft icing conditions are the upper-level temperatures and moisture. These elements are clearly evident from the upper-level analyses of 10/12Z at 850mb (roughly 5000 ft (050) altitude above MSL), 700mb (roughly 10000 ft (100) above MSL), and 500mb (roughly 18000 ft (180) above MSL), as temperatures for the region of interest ranged from +15°C to -28°C and dewpoint depressions were low (between 0 and 5) particularly for the lower levels (see Figures 5.8 and 5.9). By 10/18Z, near the icing analysis time, much of the Northern Plains had surface temperatures of +3°C or less. Thus, the probability was high that the potential icing conditions could have extended very close to the ground, which is a potentially hazardous situation for smaller aircraft.

5.2.2.2 Case 2 (11 Apr 95)

Case 2 included much of the same area in the central United States though slightly larger with the addition of portions of northern New Mexico, northern Arkansas, and Tennessee. It occurs one day after Case 1 on 11/1745Z April 95 (Julian Day 101). The synoptic situation is much the same, yet shifted

CONUS -- CH1



Figure 5.3 Example visible GOES-8 image from 10/1815Z Apr 95

CONUS -- CH2

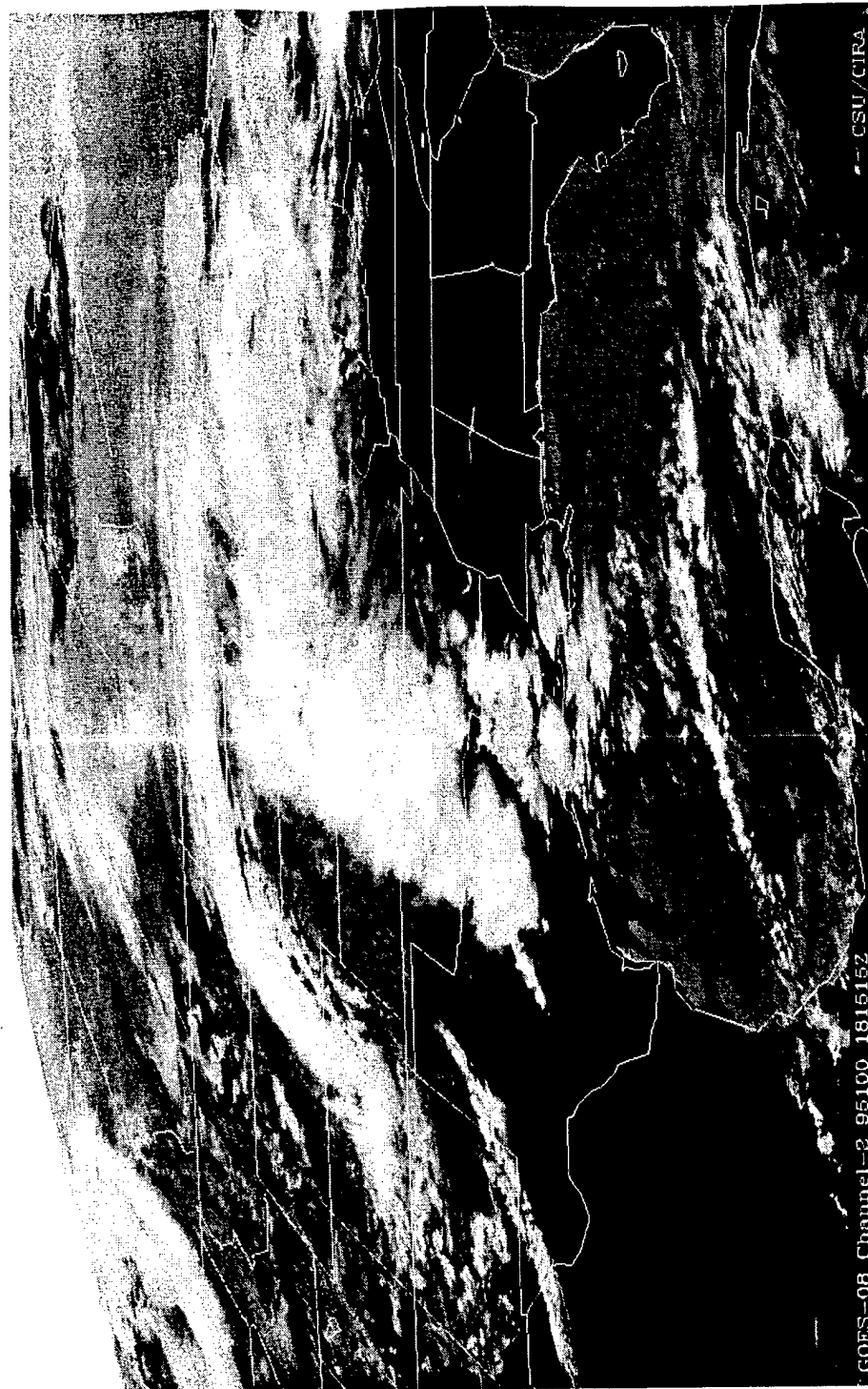


Figure 5.4 Example SIR GOES-8 image from 10/1815 Apr 95

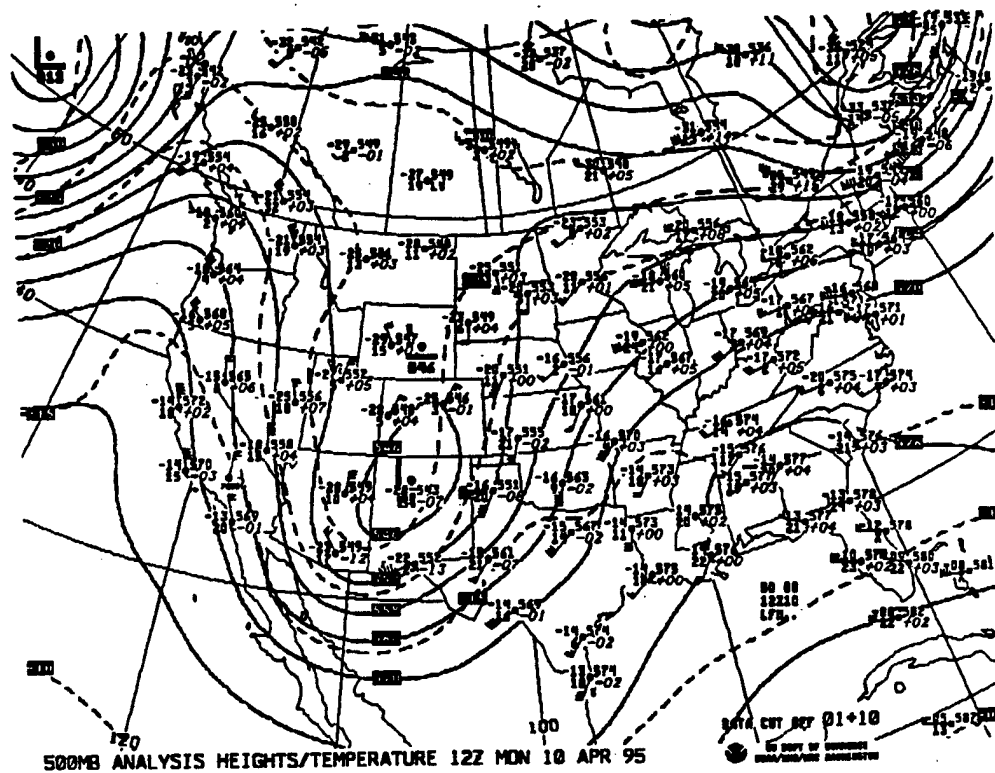


Figure 5.5 Upper air weather chart (500mb) for 10/1200Z Apr 95

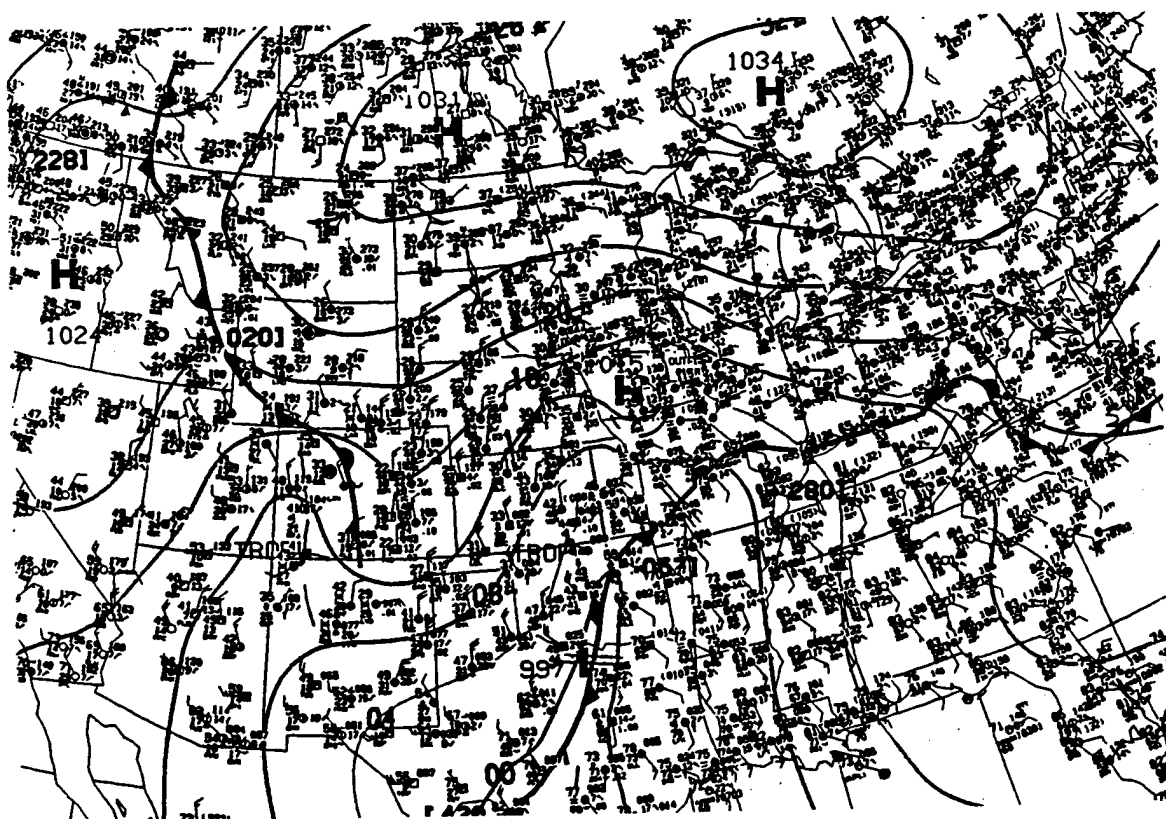


Figure 5.6 Surface weather chart for 10/1800Z Apr 95

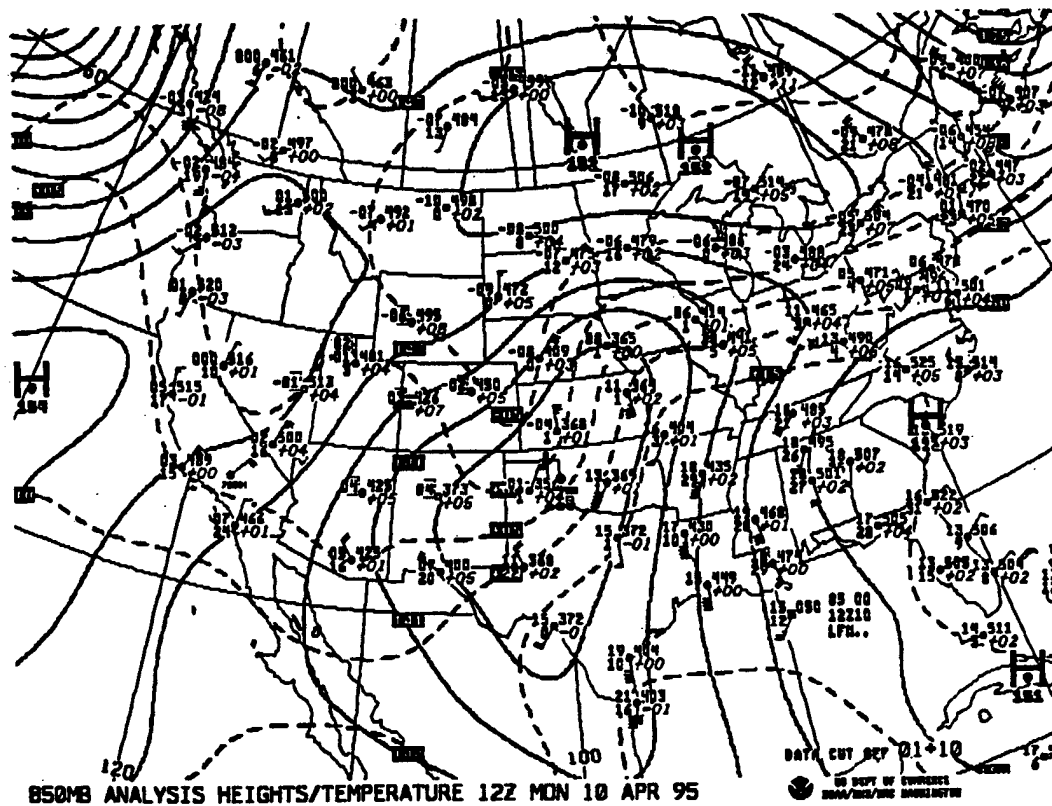


Figure 5.8 Upper air weather chart (850mb) for 10/1200Z Apr 95

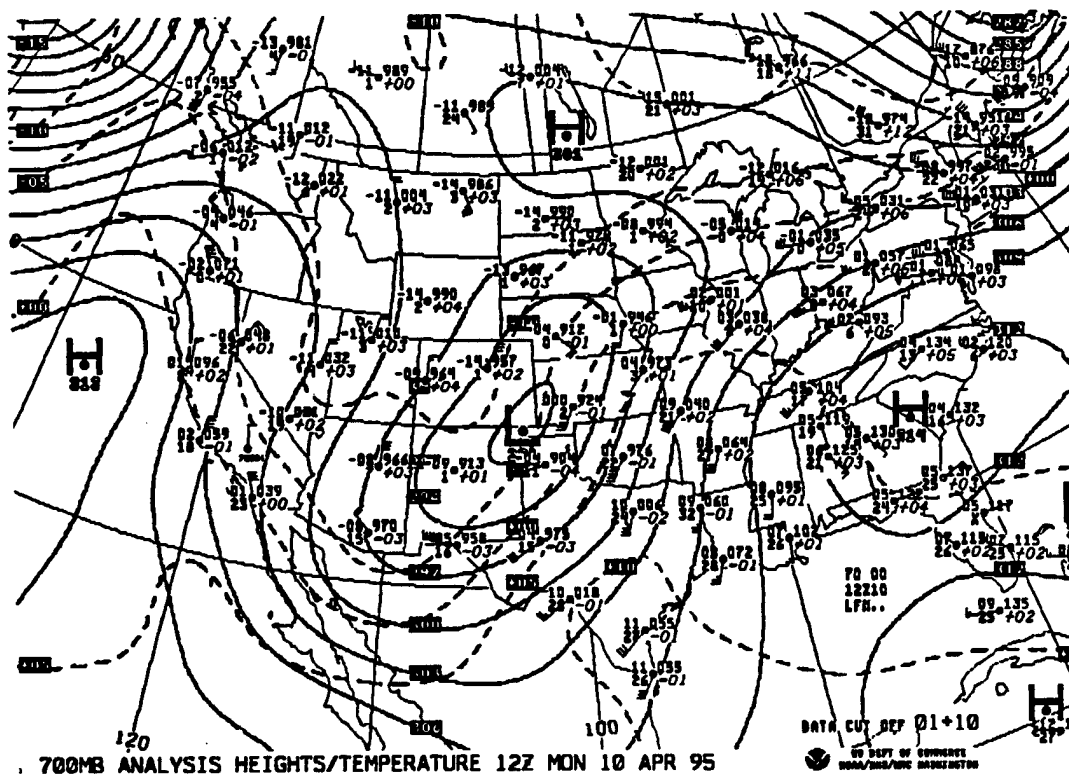


Figure 5.9 Upper air weather chart (700mb) for 10/1200Z Apr 95

slightly eastward. By 11/12Z, the upper-level low pressure center (see Figure 5.10) over northwest Kansas had nearly cut-off from the steering flow to its north, allowing it to drift much more slowly and maintain the icing conditions for an extended period of time. It turns out that this synoptic system didn't fully release its grip over the continental U.S. until 14 April. At the surface (see Figure 5.11), the maturing frontal system and occluding low pressure center over Iowa was helping to spread a mixed bag of precipitation types over the central U.S. Snowfall continued to accumulate in a band from eastern Colorado through Minnesota, while showers and thunderstorms continued from Wisconsin and Illinois southward to the Gulf coast (see Figure 5.12). The extensive coverage of precipitation and snowfall amounts can be seen with this storm system (see Figures 5.13 - 5.16). From the 11/12Z Apr 95 upper-level analyses (see Figures 5.17 and 5.18), it is evident that some of the necessary parameters for icing environments are still present over the region of study. Air temperatures range from +15°C to -27°C with most of the dewpoint depressions remaining low, representing a high relative humidity for levels below 15000 ft MSL.

5.2.3 Satellite Imagery

5.2.3.1 Collection

Raw 10-bit GOES-8 data for the study period is archived on digital (8-mm exabyte) tapes, recorded and stored by CIRA. The imagery data is condensed into 8-bits from the 10-bit raw data on the tapes to facilitate the display constraints of the monitor. Case study dates were selected and the corresponding tapes were used to restore the raw data into my directory on the CSU Atmospheric Science Building's CIGS Room Windows NT (named IRIS) operating computer system. With the help of the SubSect and SectDef image processing software, the selected raw imagery data was reduced to specified regions. Primarily using the GVIEW function of the IDL display software written by Kelly Dean of CIRA/CSU the images were displayed, enhanced, and edited on a 1024 X 1024 pixel screen.

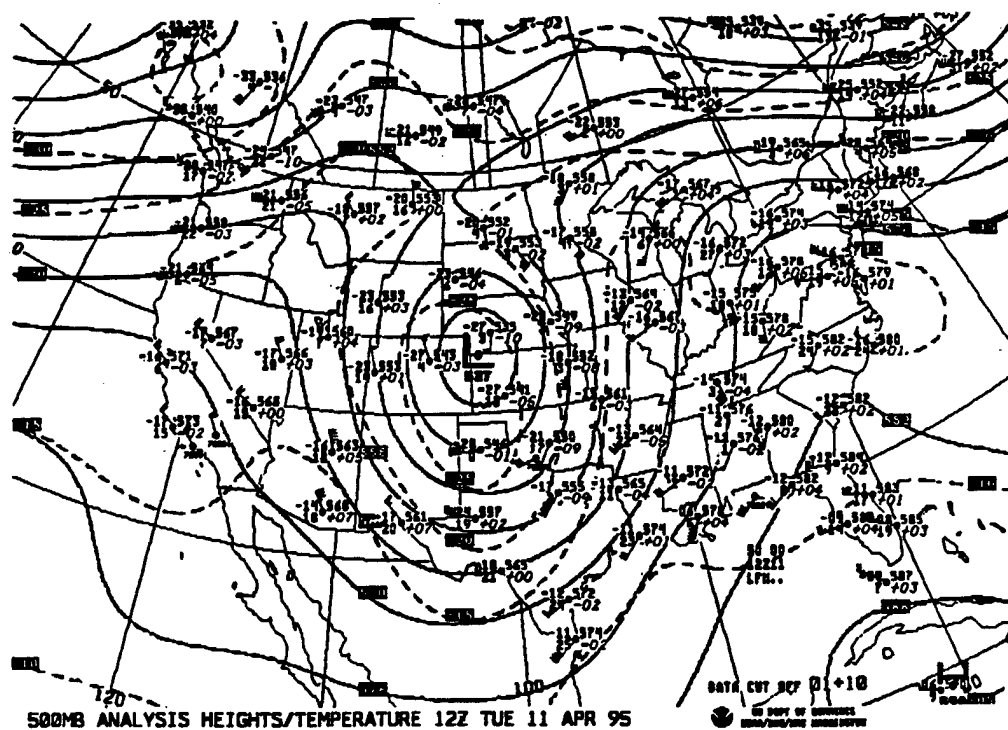


Figure 5.10 Upper air weather chart (500mb) for 11/1200Z Apr 95

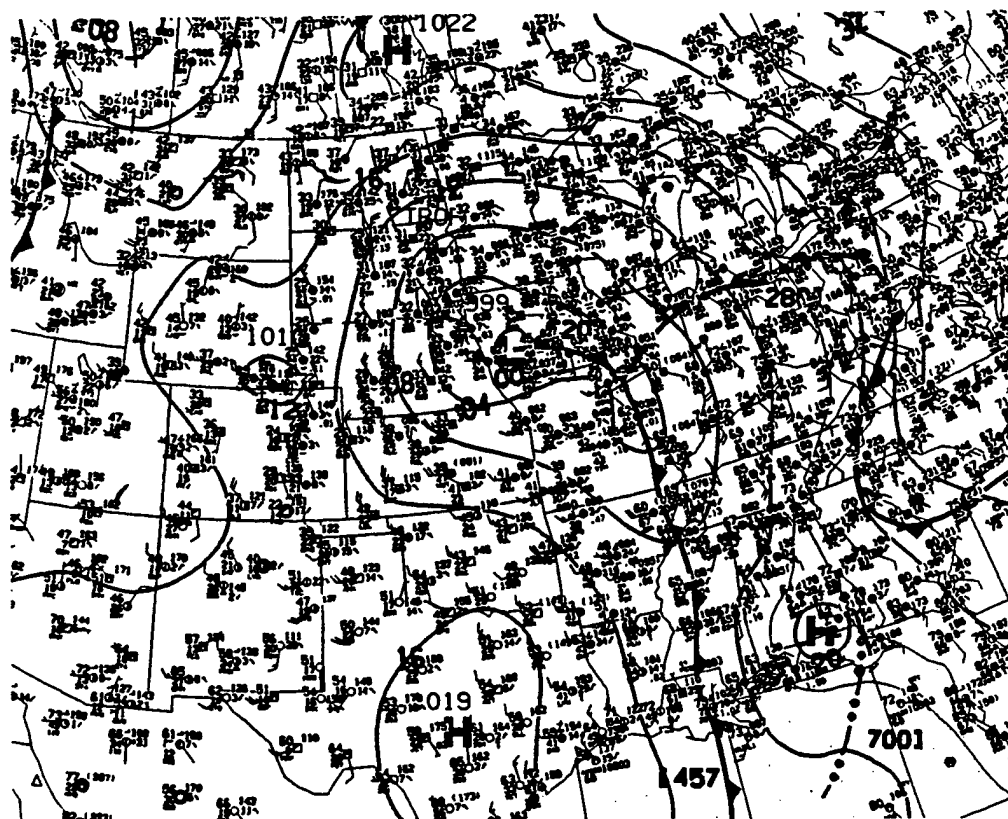


Figure 5.11 Surface weather chart for 11/1800Z Apr 95

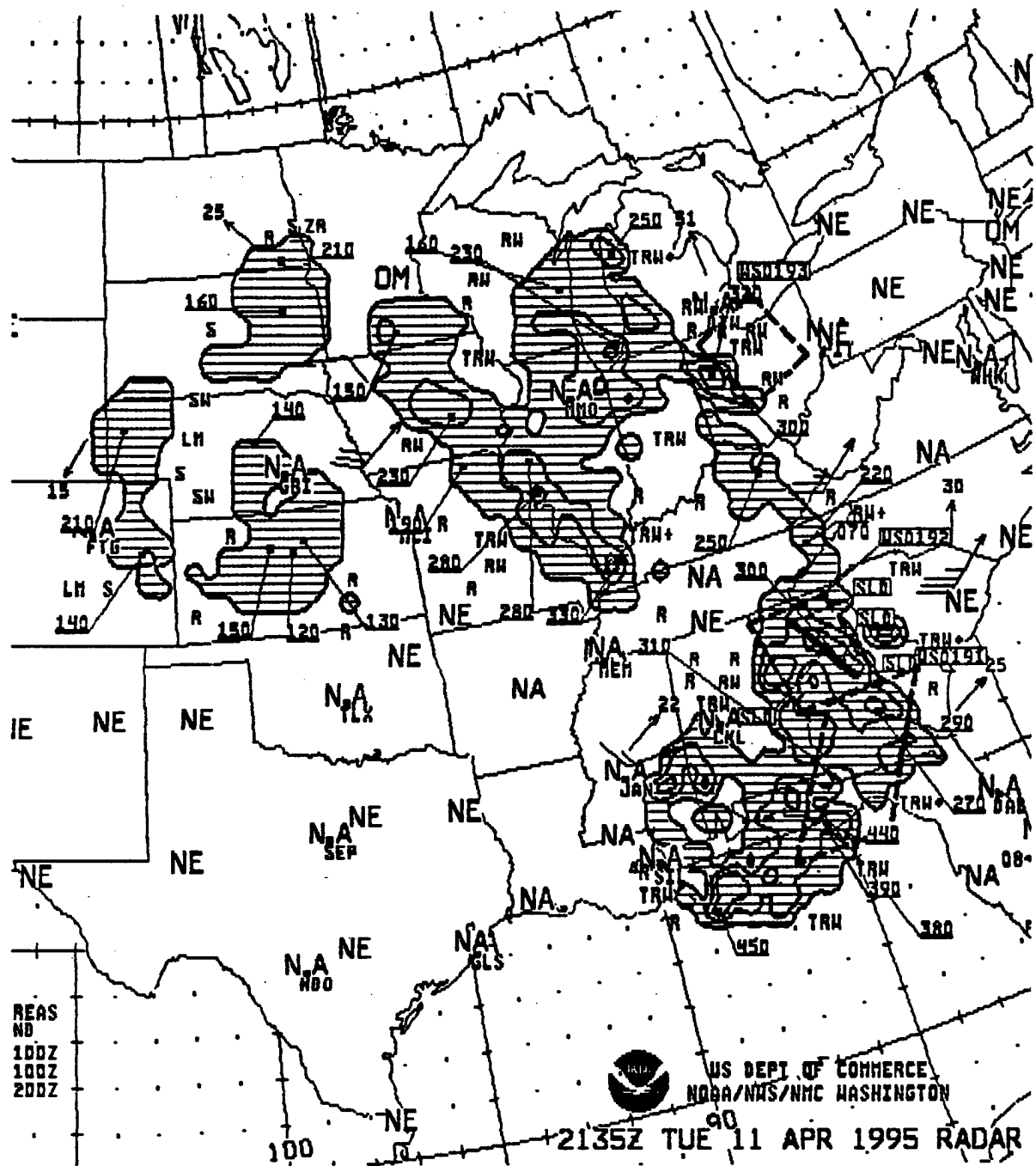


Figure 5.12 Weather radar summary for 11/2135Z Apr 95

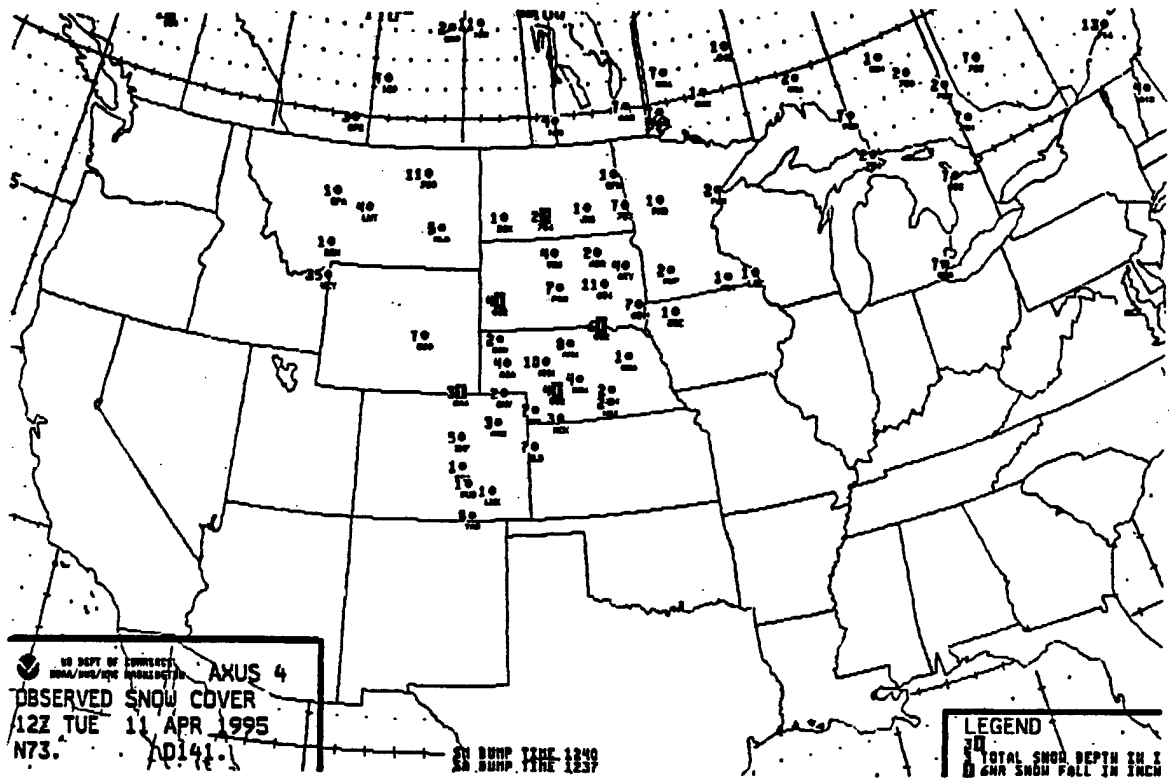


Figure 5.15 Observed snow cover summary for 11/1200Z Apr 95

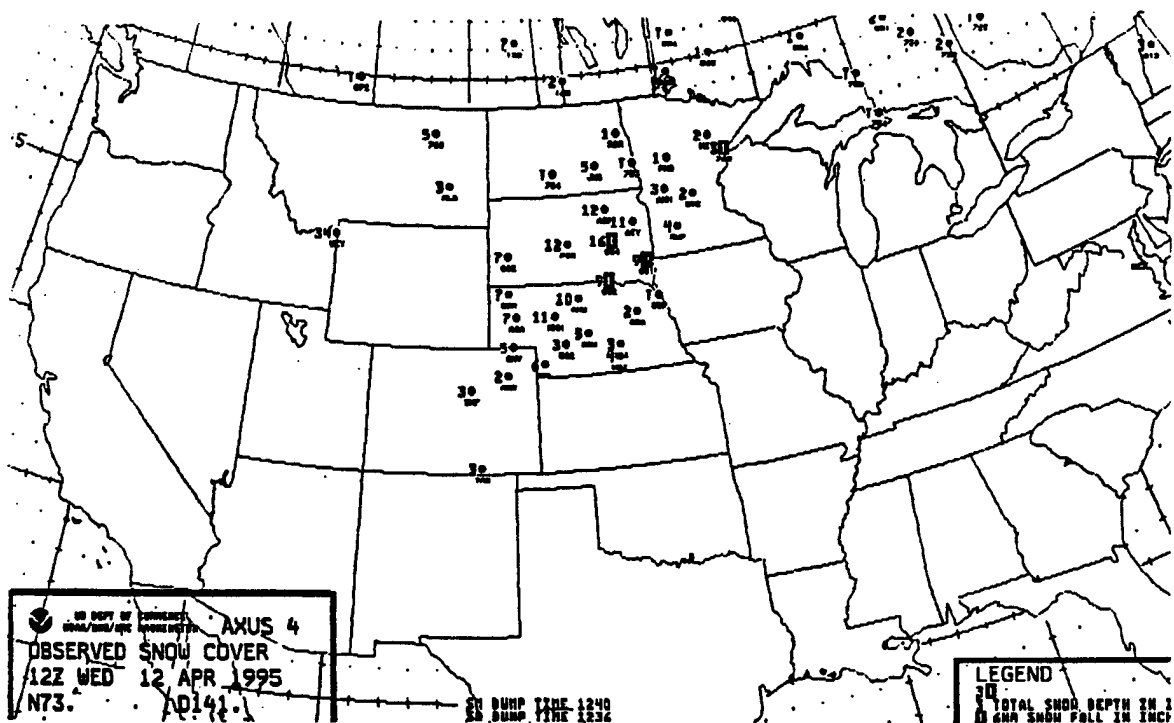


Figure 5.16 Observed snow cover summary for 12/1200Z Apr 95

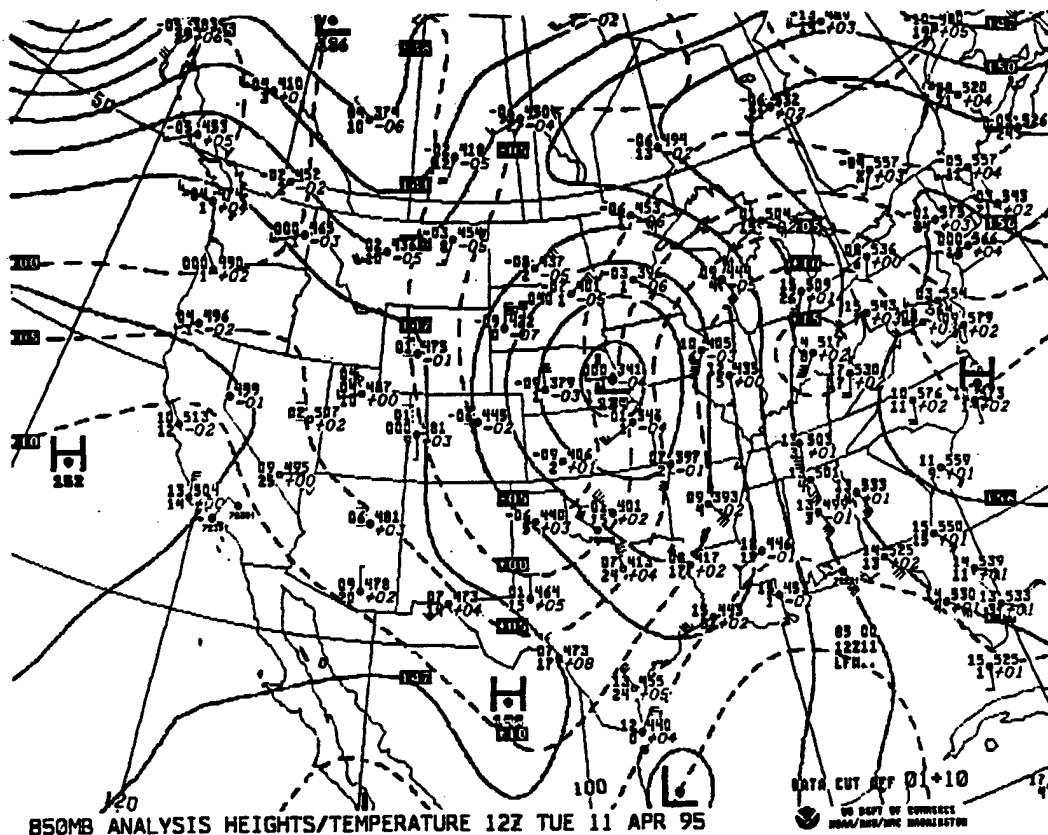


Figure 5.17 Upper air weather chart (850mb) for 11/1200Z Apr 95

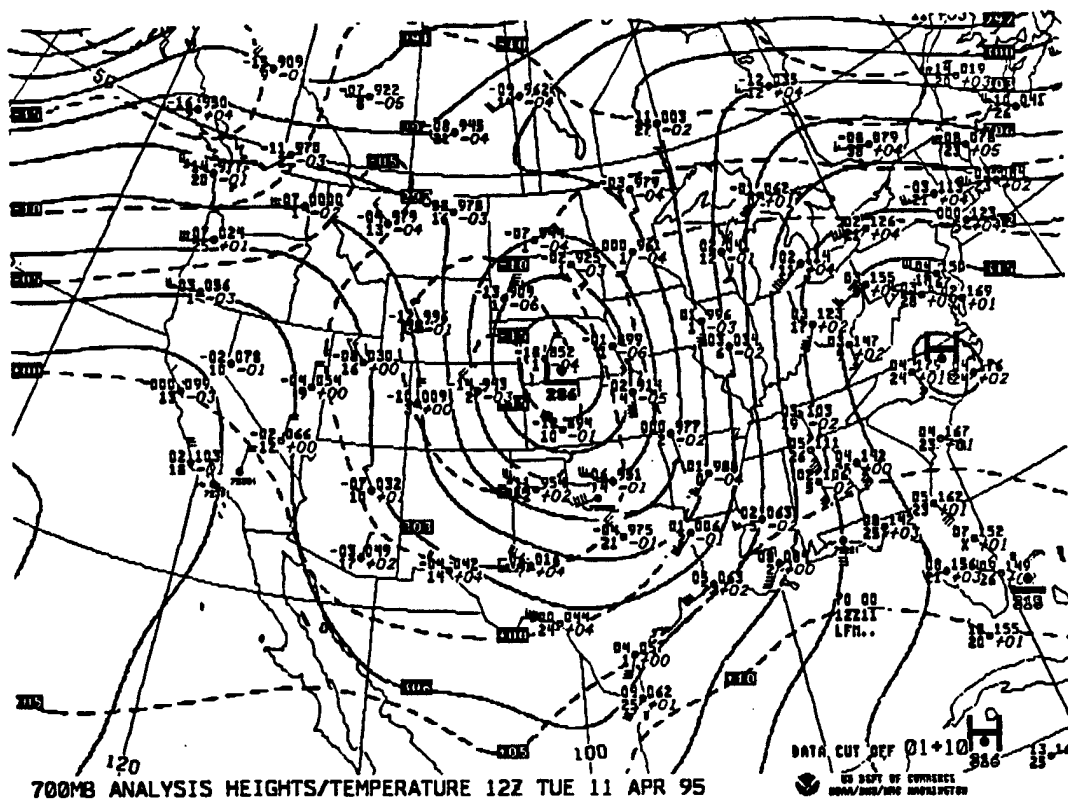


Figure 5.18 Upper air weather chart (700mb) for 10/1200Z Apr 95

5.2.3.2 Display

GVIEW enables the user to interrogate the displayed imagery by the computer mouse movement of an on-screen cursor (+) to a desired point on the image. A mouse click on the point creates a "pixel dump" to a small window on the screen which displays the valuable information needed for this study. Each pixel dump gives the X-Y monitor image pixel coordinates, pixel count value, brightness temperature (T_b) in degrees Kelvin (for CH2, 4) or albedo value (for CH1) ranging from zero to one, and the Earth latitude and longitude of the selected image pixel. Since there is not a quick and easy way at this time to dump this data directly into a data file, care was taken to write down each pixel dump value from a predetermined sector grid into an empty spreadsheet grid for later manual entering. For future reference, one should be able to write some IDL code that would do this, but it was beyond the reach of my capabilities and time limits at present. Additionally, there should be a similar way to display a grid of pixel dump values in a user determined sector size to easily view all pixel values at once for a region on the image.

5.2.3.3 Selection

For Cases 1 and 2, pixel dump values (brightness temperature for IR and albedo for visible) for each of the three channels were selected according to the grid region (shown in Figure 5.2) with each value assumed representative of the entire sector (roughly 10x20 pixels). While this method is quite tedious for large areas and fine grids, it represents the simplest way to retrieve the required data values. The Case 1 and Case 2 grids were determined by the large cloud field as seen from the CH1 image and a rough idea of atmospheric temperatures, since for icing one needs a cloud and a certain temperature regime. The fact that a grid is used instead of the exact image pixel associated with each PIREP causes some problems over regions where the cloud cover is not uniform in levels or texture, as would be the case for embedded cumulus within a stratiform region, edges of cloud shields, or for areas of widely broken / scattered cloud top elements at different levels. This would lead to somewhat erroneous satellite-sensed cloud-top values and thus, incorrectly assigned grid values.

5.2.4 Rawinsonde (Sounding) Data

The rawinsonde or upper-air sounding data used to support this study was collected with the help of Steve Finley (CSU/Atmos Science. Dept. Computer System Coordinator), who maintains archived upper air data in GEMPAK format. A C-programming language script was run to recover the required upper-air soundings on the desired dates for stations across the north-central United States with complete coverage of the desired grid region for case 1. The data was collected and stored, and viewed (using Ghostview) on separate PC's (Aurora and Horizon) in the Atmospheric Science Dept. Weather Lab. These in-situ soundings give the most accurate knowledge of the vertical profile of ambient air and dewpoint temperatures, and winds. Unfortunately, the wide horizontal spacing of these stations (~ 400 km) through this area does not lead to a great resolution for the region. Their representativeness of the atmosphere around the station extends approximately 150-200 km radially or more so downstream of the station.

The sounding data in some cases can give a good idea of the air mass and environment in which the icing events occurred and icing altitudes can be related to temperatures using U.S. Standard Atmosphere profiles. However, they should be used with some caution in the vicinity of frontal zones where air masses change rapidly due to the turbulent nature of the convection which usually takes place there. For comparison purposes to PIREPs, they would only be useful if within these areas of the nearest rawinsonde location. Since the soundings take place only routinely twice a day (12Z, 00Z), some care must be used in interpolating between the soundings for comparisons that take place in the middle of the day. The hard copies of the soundings are shown in a standard GEMPAK Skew-T, Log-P format, which also calculates some atmospheric stability indices for the sounding.

5.2.5 Upper Air, Surface, and Forecast Weather Charts

Weather charts of surface and upper-air features were collected from the archive stored across from the Weather Lab. Paper copies were made of the surface and standard upper-air level analyses (850mb, 700mb, 500mb, 300mb) that coincided as close as possible to the desired times. These charts can help to estimate horizontal temperature and moisture regimes across the grid region. The surface chart was also used to confirm the CH4 temperature retrievals of surface targets with known land and water surface

temperatures. Radar summary charts were collected to confirm the presence of thunderstorm activity, precipitation, and cloud base and tops. Some NGM forecast model charts were collected to see if they were accurately handling the storm systems development. The Eta model forecasts are a basis for some of the icing forecasting algorithms in use today at the Aviation Weather Center.

5.3 Icing Study

5.3.1 Methodology

For this study, several assumptions need to be made and an understanding of the potential crudeness of the verification items (PIREPs) must be weighed against the benefits of their use. Additionally, some limiting factors, such as computer software compatibility and display capabilities, specific PIREP and satellite data collection, satellite imagery interpretation, and computer programming and time limitations must be taken into consideration during a review of the research process.

5.3.1.1 Temperature Regime

An in-situ aircraft icing study by Pobanz et al. (1994) determined that cloud-top temperature (CTT) ranges of -5 to -16°C were found to characterize SLW at cloud-tops during known icing encounters with large drop regions by a research aircraft. While cloud-top temperatures deduced from infrared satellite imagery may contain some error, CH4 IR brightness temperatures can still be used in a relative sense to create boundaries or threshold techniques to infer icing conditions for a cloud system with the help of PIREPs comparisons and verification. For Cases 1 and 2, the CTT thresholds for the suspected icing zone (IZ) were set between +3°C and -25°C (or 276K to 248K). These limits are set to take into consideration the dynamic temperature increase of the airframe, inversion layers where cloud tops may exist warmer than the interior, and moderately deep or growing cumuliform clouds with slightly colder cloud tops. During the study, it became evident that many icing reports occurred within a colder CTT zone, and it was dubbed the convective zone (CZ). The CZ ranged from -25°C to -63°C (or 248K to 210K).

5.3.1.2 Supercooled Liquid Water (SLW) Locations

Detection of supercooled liquid water (SLW) cloud droplets is essential in the detection of icing environments. Popa Fotino et al. (1986) found from statistical analysis that using ground based remote sensing techniques, they could correlate 75 percent of the confirmed icing cases with SLW measurements alone. Ideally, these methods will be able to distinguish regions of SLW or more importantly large SLW droplets from satellite sensing of their cloud tops. Additionally, Pobanz et al. (1994) found that under proper conditions large SLW droplets tended to develop and congregate in layers near the tops of some stratiform clouds.

5.3.2 Multispectral Channel Differencing (ΔT_b) Study

5.3.2.1 Past Studies

Brightness temperature differencing methods (using $\Delta T_b = 3.9\mu\text{m}$ (SIR) minus $10.7\mu\text{m}$ (LIR)) have been previously considered by Liljas (1986), Ellrod (1996a), and others previously mentioned. Liljas, using the SIR and LIR channels from a polar-orbiting satellite, encountered some interference or noise problems that curtailed a thorough study of this differencing method for daytime usage. Ellrod has just recently put forth the first paper trying to use quantified ΔT_b results to detect aircraft icing regions. His study (more detail in Chapter 2) concentrated on large, stratiform cloud areas during the winter and spring seasons, used visible channel imagery to gain additional qualitative information, and also relied on PIREPs as a rough verification tool. Ellrod determined that there seems to be some skill in correlating icing PIREPs to potential icing regions.

5.3.2.2 Application to Cases 1 and 2

The first method used for the April cases involves the use of GOES-8 imager channels 1, 2, and 4 (VIS, SIR, LIR). It follows closely to the method suggested by Ellrod (1996a), but with some slight changes. Much of the description of the channel differencing (ΔT_b) technique is described in Chapter 4. Digital CH2 and CH4 IR brightness temperatures (T_b) and CH1 visible albedo values were collected for each sector within a region (shown in Figure 5.2) of vast cloud cover, some of which was convective

(cumuliform) and some stratiform. The PIREPs (125 for Case 1; 164 for Case 2) taken roughly within 3 hours of the satellite imagery time were matched to each respective sector on the grid and corresponding values of T_B and albedo were assigned to each PIREPs by location. These values were inserted into a spreadsheet for graphical analysis (reference FIG in Chap 6- CH2-4.xls). The LIR channels' brightness temperatures were then subtracted from those of the SIR channel (CH2 - CH4). The result gives a measure of the extra reflected radiance component sensed from the cloud tops by CH2, since during the daytime, the emitted component of the CH2 radiance is nearly (assumed) equal to that of CH4 (of which emission is the only significant component of the sensed radiance). This is important, because as shown in Chapter 2, the variance in cloud-top reflectivity is largely a function of the cloud particle size and phase (liquid or ice). For a suspected icing hazard, the cloud must have SLW droplets present at cloud top or within the cloud, and larger SLW droplets contribute to a greater icing hazard. Using these differenced IR T_B values and the visible albedo values for the PIREPs together in a scatter plot (see Figures 6.1, 6.2, 6.8, and 6.9), some interesting and some seemingly obvious findings can be noted, which are discussed in the next chapter.

Since the cloud-top CH4 T_B values can be roughly assumed to equal the cloud-top temperature (CTT), this information can be useful to estimate the height of the cloud top to compare to the icing PIREP altitude and whether the cloud top temperature falls into a known icing temperature zone (IZ) (using $+3^{\circ}\text{C}$ to -25°C or $276\text{K} - 248\text{K}$). Using the rawinsonde data for stations closest to each PIREP, the icing altitudes can also be compared to determine the approximate temperature for the levels at which the icing occurred and sounding estimated CTT's can be used to verify the precision of the CH4 CTT retrievals. Additionally, upper-air and surface weather charts, and radar summaries are used to further confirm the overall synoptic conditions.

5.3.2.3 Strengths and Weaknesses of Method

While this particular method can be used only during the daytime when there is a T_B difference between CH2 and CH4, the majority of the PIREPs occur during the daytime when commercial and business air traffic is at a maximum. This method has several strengths over other icing prediction

methods. Most importantly, when the digitally differenced image can be automated for display, it can give a real-time indication of icing threat areas to a trained operational forecaster from visual inspection over large geographical areas. The greater resolution, multispectral imagery available from the GOES-8/9 series of satellites show potential to improve the assessment of icing hazards over continental as well as over oceanic regions where little in-situ measurements are available on which to base model forecasts. Though this technique also has several weaknesses. Unlike the icing algorithm forecast methods mentioned in Chapter 2, this method would have to be automatically combined or overlaid with other data to infer cloud depths and heights which could then be used to make an icing forecast. Additionally, this method falters when trying to sense icing conditions for most convective or very cold ice cloud tops.

5.3.3 Multispectral RGB Color Enhancement Study

Separate channels with false color and RGB enhanced images were also investigated. The RGB method assigns each a satellite image channel to each of the colors (Red, Green, Blue). The resultant image is a rainbow of colors with varying hues resulting from the assignment of each channel to a range of hues within each primary color. RGB or other false color methods have not been widely used in the past and only recently have more studies concentrated on the potential scientific applications for these methods with hope of developing cloud or land feature identification techniques.

With Kelly Dean's help, a program called "bcolor" running in IDL was created to select individual channel GOES-8 raw imagery and assign them in any order to RGB and display the image on the terminal screen using the GVIEW function. This method was not designed to determine icing regions quantitatively, so the pixel dump value was not a concern in this case, due mainly to the difficulty in determining and understanding the resultant combined value's significance. The IR channel (2 and 4) imagery were also inverted so as to compare favorably with the CH1 image (i.e. clouds would appear white or light colored for all images). Using the techniques described in Chapter 4, regarding Red-Green-Blue (RGB) image enhancement, two different combinations of channels seemed to hold some promise for detecting potential icing environments. They included GOES-8 channels 1, 2, and 4. The addition of the visible channel to the IR channels helps to give the combined image more textural features. The two RGB

combinations, which will be described in further detail in Chapter 6, are indicated by the three channel numbers as assigned to the sequence of red, green, and blue. They are referred to as 241 (CH2-red, CH4-green, CH1-blue) and 411 (CH4-red, CH1-green and blue).

Chapter 6 — Results and Conclusions of the Icing Studies

NOTE: All Figures and Tables are at the end of this chapter (ordered as they appear in the text).

6.1 Discussion of Results

6.1.1 ΔT_B Method for Case 1 — 10 April 1995

From the 10 Apr 95 (Julian Day 100) case, the cloudy region over the Northern Plains through the western Great Lakes region has been analyzed using the multispectral channel differencing (ΔT_B) method mentioned in the previous chapter. For the 125 PIREP set, the icing intensities covered the full range from a Trace (1) to Severe (7), although over half of the icing PIREPs (46 of 86) were of significant intensity (Lgt-Mdt or greater; denoted as (4+) icing PIREPs) (see Tables 6.1a-c). Overall, the cloud shield within the area of interest was mostly convective in nature with only small regions of stratiform cloud tops evident over the western Plains states.

From the case 1 scatter plot of CH2-CH4 (ΔT_B) vs. CH1 (Figures 6.1a-d), we find a clustering (81%) of all icing (1-7) PIREPs within a range of cloud-top ΔT_B between 20-44°C and albedo values of 42-60 and the same is true (85%) with the greater intensity (4+) icing PIREPs. Most of the outlying PIREPs outside of the range can be explained by questionable grid values along cloud edges due to the relatively large gradient of the values across a short distance in the vicinity of the measurement or in regions of broken clouds which let some surface radiation through between the clouds. The outlying icing reports could also result from the fact that the clouds are transient and are not always properly represented properly (using this gridded scheme) over the entire six hour collection period for the PIREPs. In this case, the 4+ intensity reports generally corresponded to greater ΔT_B and albedo values. Since higher albedo values would indicate a greater visible reflective component, characteristic of water droplets versus ice crystals, and greater positive ΔT_B between CH2 and CH4 would tend to result from warmer and liquid (smaller) droplet cloud tops with a greater reflective component, this analysis would provide a good indication of and agreement for potential icing conditions within these particular cloud regions. However, when these ΔT_B and albedo range thresholds are applied to the spreadsheet grid of pixel dump values (shown in Tables 6.2a-d) by coloring the grid sectors which are within the ranges, the result is only a gridded reflection of

the combined cumuliform and stratiform cloud shield. These ranges for which the PIREPs clustered just proved that they occurred in clouds, which is a given, without respect to either type of cloud.

When the cumuliform cloud tops (convective zone (CZ) - CH4 brightness temperatures less than minus 25°C) were screened out leaving only the stratiform cloud tops (see Figures 6.2a-b) (icing zone (IZ) CH4 brightness temperatures from +3°C to -25°C) grid sectors (shown in Tables 6.2c-d / shaded in the color pink), a better indication of icing conditions resulted. While the shaded regions in Tables 6.2c-d for the CH2-CH4 (ΔT_b) grid values represented stratiform regions better, it did also highlight the cloud-top temperature (CTT) regions along the cloud shield edges of convective or cirrus clouds which are not expected to be used in the icing detection technique. The ΔT_b values for the IZ were in the higher part of the range (30-44) which is representative of a greater reflected component from CH2 for liquid droplets. But, again these range of values were not characteristic of icing regions only. There seemed to be nearly as many instances of these values in the unshaded CZ portion of the spreadsheet, leading to the result that the channel difference method is not a particularly stand-alone technique for icing detection in all type of clouds.

Highlighting the region of the IZ using only CH4 T_b on the grid (see Figure 6.3) gives a better visual representation of the stratiform areas against the visible CH1 image for that time. The cloud types are also qualitatively verified from the individual GOES-8 channel imagery (see Figures 6.4a-d). Then, transferring the stratiform cloud area to the composite PIREP plot for the 6 hr period encompassing the analysis time (15-21Z) (see Figure 6.5) gives an idea of how the icing PIREPs compared to the stratiform regions alone. It is obvious from inspection of the icing PIREP and cloud-top CH4 temperature (CTT) data that during Case 1 most of the icing PIREPs coincided with very cold CTTs, which were mainly in the vicinity of convective cloud plumes and thunderstorm activity. The greater intensity icing PIREPs of magnitude 4+ were mainly in a convective, CTT temperature zone (CZ) between 248K and 205K (-25°C to -68°C) (see Figure 6.2b). The PIREPs within the stratiform region were sparse, possibly due to a lack of flight through the area, but the majority of the PIREPs in the area were of the significant 4+ intensity (particularly over western Nebraska and Kansas). A rawinsonde analysis from North Platte, NE (LBF) (Figure 6.6) shows an atmosphere that would be conducive to icing conditions at altitudes between the

surface and 15000 ft AGL. The same holds true for the Dodge City, KS (DDC) (Figure 6.7) sounding which would indicate icing conditions for the levels between the surface and 9000 ft AGL. A nice clustering of a few moderate intensity (4+) icing PIREPs were reported in these areas and at these altitudes, which also means that this area might be a good candidate for this satellite analysis technique.

The introduction of the negative (none or null) icing reports (Figure 6.1a) to the analysis did nothing more but confirm that the majority of the null PIREPs were beneath very cold clouds or over clear areas where the satellite was sensing surface temperatures only. This is often the case when the CH2-CH4 T_B difference (ΔT_B) is smaller, because most land surfaces are not very reflective, so that the radiance sensed in CH2 is nearly the same as that in CH4. Also, many of the null PIREPs occurred within the stratiform areas, however they were for altitudes above the stratiform cloud deck.

6.1.2 ΔT_B Method for Case 2 – 11 April 1995

From the 11 Apr 95 case, a similar cloudy region to Case 1 over the Northern Plains through the western Great Lakes region has been analyzed using the multispectral channel differencing (ΔT_B) method mentioned in the previous chapter. For the 164 PIREP set, the icing intensities covered the full range from a Trace (1) to Severe (7), and only 40% of the icing PIREPs (44 of 109) were of significant intensity (Lgt-Mdt or greater; denoted as (4+) icing PIREPs) (see Tables 6.3a-d). Overall, the cloud shield within the area of interest was much more stratiform in nature (with respect to Case 1) resulting in almost equal cloud coverage between the convective and stratiform regions. Areas with regions of stratiform cloud tops were evident over the western and central Plains states, and over northern Wisconsin.

From the scatter plot of CH2-CH4 (ΔT_B) vs. CH1 (Figures 6.8a-d), we find a clustering (87%) of all icing (1-7) PIREPs within a range of ΔT_B between 10-44°C (or somewhat broader (darker) than Case 1) and albedo values of 40-60 (similar to Case 1) and the same is true with the greater intensity (4+) icing PIREPs (86%). As with Case 1, most of the outlying PIREPs outside of the range can be explained by questionable grid values along cloud edges due to the relatively large gradient of the values across a short distance in the vicinity of the measurement or in regions of broken clouds which let some surface radiation through between the clouds. In this case, the 4+ intensity reports also generally corresponded to greater

ΔT_B and albedo values. However, when these ΔT_B and albedo range thresholds are again applied to the spreadsheet grid of pixel dump values (shown in Tables 6.4a-d) by coloring the grid sectors which are within the ranges, the result is the same as in Case 1 with the entire cloud shield being outlined. These ranges for which the PIREPs clustered just proved that they occurred in clouds, which is a given, without respect to either type of cloud.

When the cumuliiform cloud tops (convective CTT zone (CZ)) were screened out leaving only the stratiform cloud tops (see Figures 6.9a-b) (icing CTT zone (IZ) shaded in the color pink) grid sectors (shown in Tables 6.4c-d), a better indication of icing conditions resulted similarly to Case 1. The shaded regions in Tables 6.4c-d for the CH2-CH4 (ΔT_B) grid values again represented stratiform regions better. Unlike Case 1, the ΔT_B values for the IZ were in the evenly distributed within the range (10-44). But, again these range of values were not characteristic of icing regions only, and there seemed to be nearly as many instances of these values in the unshaded CZ portion of the grid. This leads to a similar result for Case 1, that the channel difference method is not a particularly stand-alone technique for icing detection.

Highlighting the region of the IZ using only CH4 T_B on the grid (see Figure 6.10) again gives a better visual representation of the stratiform areas against the visible CH1 image for that time. Comparatively, this case was much less convective overall than in Case 1 as can be seen from the larger stratiform cloud regions in the individual GOES-8 channel imagery (see Figures 6.11a-c). Transferring the stratiform cloud area to the composite PIREP plot for the 6 hr period encompassing the analysis time (15-21Z) (see Figure 6.12) gives an idea of how the PIREPs compared to the stratiform regions alone. It is obvious from inspection of the icing PIREP and cloud-top CH4 temperature (CTT) data that also during this period most of the icing PIREPs coincided with very cold CTT's. The greater intensity icing PIREPs (IP) of magnitude 4+ were again mainly in a convective CTT zone between 248K and 205K (-25°C to -68°C) (see Figure 6.9b) over the mid Mississippi River Valley area. The PIREPs within the stratiform region were more abundant in Case 2, but there was no clear majority of PIREPs of the significant 4+ intensity (though most occurred over eastern Nebraska, Kansas and Arkansas). In fact, the amount of 4+ PIREPs overall decreased from Case 1 (46 to 44), while the overall number icing PIREPs increased from 86 to 109. This result may indicate that the more significant icing cases over the entire cloud region is due

mainly to convective cloud encounters (as seen in Case 1), however more but less intense icing encounters occur within stratiform cloud areas. A rawinsonde analysis from Omaha, NE (OAX) (Figure 6.14), for Topeka, KS (TOP) (Figure 6.15), and from other stations near the stratiform cloud regions (Figures 6.13 and 6.15-17) shows an atmosphere that would be conducive to icing conditions at altitudes between the surface and 12000 ft AGL. Again, some clustering of moderate intensity (4+) icing PIREPs were reported in these areas and at these altitudes, which again confirms that this area might be a good candidate for this satellite analysis technique.

6.1.3 RGB Method for 10 Apr 95

When the RGB-411 combination technique is used for imagery taken at 10/1815Z Apr 95 (see Figure 6.18), several cloud features can be readily distinguished by visual interrogation when checked against individual channel imagery for confirmation. The lowest clouds appear a dark green-blue or cyan color. Middle clouds transitioning from liquid to ice phase clouds tend to correlate with a light shade of cyan and the lightest pinkish hues. Then, the deepest (convective and likely ice-topped) clouds with the coldest tops appear white or nearly white. Some upwelling surface radiance seems to be bleeding through the northern fringes of the thin, cirrus clouds from North Dakota through the Great Lakes, making them appear darker red or pink instead of a whiter shade. Using this combination seems particularly useful in distinguishing low, middle and high clouds with the convective thunderstorm tops very evident as the brightest whites. As far as icing detection, the majority of the 4+ icing PIREPs (over western Kansas, eastern Nebraska and South Dakota, southern Minnesota and northern Illinois; see Figure 6.5) seem to correspond to the darkest pink shades and lightest blue shades with no consistent hue being dominant throughout the region. Also, there are not enough PIREPs in other regions of the image (western South Dakota and Nebraska and with these colors to make a distinct or consistent probability for icing conditions. For use as a forecasting tool, this combination may be helpful to outline areas as a first guess for icing regions.

A qualitative inspection of the RGB-241 imagery from the same date and time assists in further resolving the highest clouds (bright white, light pinks, and yellows) from the middle and lower cloud decks

(see Figure 6.19). Again the lowest clouds appear dark blue with middle clouds in a color range from dark cyan to lighter cyan for higher middle clouds, and the yellow hue clouds represent thin cirrus. Then, the pinkish or lavender hues seem to signal the change from the liquid to ice phase clouds, since their presence over Colorado, Wyoming, and South Dakota correlate well with a conspicuous lack of positive icing PIREPs. Yet, the pinkish tinged cloud tops over eastern Nebraska are in an area of 4+ intensity icing PIREPs. This may be a result of its close proximity to the deeper convection occurring just to the south (bright white clouds).

6.2 Conclusions

Whereas Ellrod (1996a) confined himself to only applying this technique to nearly uniform stratiform (mainly "warm") cloud regions, this study first attacked a bigger problem, namely the entire synoptic system with both convective (cumuliform) and stratiform regions at different levels, to see how it would do at detecting icing conditions for all types of clouds, which. Evidence from this study agrees that it may be wise to concentrate on stratiform regions as opposed to cumuliform cloud areas, since the satellite-based sensor has a hard time in the visible and IR "seeing" into the cloud and inferring inner cloud microphysics or phase through vertically extensive and non-uniform convective clouds. This may account for the general abundance of icing reports in the convective portions of the cloud shield while CTT's were much too cold to indicate a support for SLW collection. Conclusive results may have been better had the study taken place in February or March when a climatological maximum of icing PIREPs occurs (Brown, 1995b) or if more aircraft had chosen to fly through some of the probable areas with icing conditions.

In trying to apply the cloud-top sensed ΔT_b technique to detection of aircraft icing within all clouds in the areas of interest, the results from the two cases and techniques used in this study were not definitive enough yet to be a helpful technique for determining icing potential. Convective CTT's tended to produce erroneous assumptions of cloud phase and SLW content when only sensing their cloud tops. The ΔT_b technique seems to work best only when a specific area of stratiform clouds can first be specified. When it comes down to the efficiency of this technique within the forecaster's workload, this method unless highly automated, would not seem to provide any added value to the icing detection problem. It

may be that the grid method in which I used is far too coarse in relating specific image pixels to the specific location of each PIREP, and better results may come from a highly selective examination of the exact PIREP and pixel co-location and corresponding pixel values. This appears to be the way Ellrod (1996a) obtained his positive results.

This ΔT_B method seems destined for use on "warm" horizontally consistent (stratiform) cloud tops, instead of "cold" (cumuliform) cloud tops. The nature of deep convective clouds is such that their tops are often glaciated (consisting mainly of ice crystals), however the stronger updrafts within the cells also tend to accumulate supercooled liquid water (SLW) in regions within the cloud and sometimes near cloud top. Thus, a varying array of satellite-sensed IR temperature thresholds would be required to try to pinpoint icing regions within deep cumuliform clouds, but probably without much success.

Satellite-based microwave retrieval methods hold some promise for these types of clouds, however their returns are affected by precipitation-sized particles, which are also quite likely within these cloud types. Promising results from Lawyer (1995) (further discussed in Chapter 2) using satellite microwave cloud liquid water (CLW) retrieval techniques that can penetrate thin ice cloud tops have shown that potential icing conditions (verified by significant intensity icing PIREPs) can be inferred using CLW measurements ($CLW > 0.5 \text{ kg m}^{-2}$) in conjunction with a range of CTT's (warmer than -25°C) from LIR imagery. His CTT ranges seem to agree with the icing zone CTT's used in this study, however this study did not reach any quantitative conclusions on liquid water content of the clouds in the areas of interest. Lawyer found that very little CLW existed when CTT's were colder than -25°C , which would imply increasing numbers of ice crystals scavenging the available SLW. Also, the CLW amounts were more variable at CTT's warmer than -25°C , showing the unstable nature of the SLW within the cloud (possibly an indication of the clouds life cycle). Lawyer's work would also further indicate that microwave CLW retrievals in combination with other sensing techniques (multispectral satellite, ground-based remote sensing, or numerical weather prediction model output) would be necessary to create improved icing forecasting tools for the future

Most aircraft pilots have been educated that the existence of a deep cumuliform cloud (cumulonimbus and "towering" cumulus congestus) implies the hazard for icing conditions among other

things, and they tend to steer clear of these areas. This demonstrates another reason that there are not sufficient PIREPs available to verify the existence of icing regions within these clouds any way. Yet, aircraft pilots do not seem averse to flying through thick, non-precipitating regions of stratiform clouds even if some icing has been forecasted, as was seen from the Cole and Sand (1991) study of aircraft icing accidents. In both cases, the majority of the icing PIREPs occurred within areas outside of (with CTT's colder than) the typical icing CTT zone (IZ) (73% within the CZ and 27% in the IZ in Case 1), however many significant intensity icing PIREPs did occur within the IZ in Case 2 (44% within the IZ) when the cloud shield became more stratiform. The icing PIREP verification was fairly inconclusive for stratiform regions due to a relative lack of icing reports in some portions of the stratiform cloud deck. It is important to note that the icing PIREP intensities are used without regard to the type of aircraft which might have reported it, as intensities will vary on aircraft type and their individual anti-icing capabilities (noted in Chapter 3).

However, there would be an underlying problem for the operational aviation weather forecaster who would use the ΔT_b satellite techniques from this study. The fact that icing only in stratiform clouds would be the main application for this ΔT_b technique leaves a whole realm of convective clouds for which there is yet no clear-cut indicator of icing conditions in cumuliform clouds. This is especially important since these cloud types make up the majority of the clouds near surface frontal systems, which are the most common locations for icing conditions. Even satellite microwave cloud liquid water retrieval methods have problems with the majority of the convective (precipitating) clouds. So, the future emphasis of icing conditions detection and prediction research should likely focus on convective clouds with the most likely additional techniques coming from mesoscale numerical weather prediction models or precipitation radars that can someday closely simulate or detect individual cloud system life cycles. Model output of inner cloud structure, when combined with information from satellite and/or ground-based remote detection systems, should help to pinpoint the atmospheric layers for which icing conditions are most probable. This would maximize the efficiency of the icing forecast product, while enabling safe flight through more regions of the atmosphere.

The multispectral RGB color enhancement method does a good job at distinguishing clouds of different heights with the greatest color and shade contrast between the high and low clouds. Some information on cloud phase and SLW clouds seems evident from inspection of the middle cloud deck color hues, but the result is not yet reliably quantitative. This information could be used qualitatively to help in initial icing assessment for larger-scale cloud regions. For the prospects of the multispectral RGB enhancement method for detecting icing conditions, these color enhancements provide an easier identification of cloud heights and can be used in distinguishing stratiform clouds (relatively darker with a more uniform shade) from cumuliform clouds (mainly white or very light color shades). While there was no definitive proof found that these methods could identify potential icing regions, these do seem a valuable tool in separating clouds into their respective height categories or types. Though, for an operational forecaster, to use these RGB techniques might be too great of a task to do effectively and consistently without much practice or experience at it. Unfortunately, while the human eye is effective at distinguishing these subtle hue differences in these images, for proper accuracy and time efficiency, it would likely need to be automated using a computer's help. As of yet, it has not been shown that a computer can effectively assimilate color changes effectively enough to develop a forecast product to take advantage of these RGB methods. However, neural network (computer learning algorithms) methods are being researched presently at CSU/CIRA and other locations, which would help in the automated computer determination and processing of pixel color hues and could take advantage of these methods.

6.3 Suggestions for Future Work

Detection of potential icing environments using infrared and visible satellite imagery remains a challenge for cloud regions made up of convective clouds or a mix of both convective and stratiform types. Aircraft icing is such a complex phenomenon based on many highly and non-linearly, temporally and spatially variant atmospheric and mechanical factors, many of which have been described herein. As long as the aircraft icing problem exists, researchers will be trying new scientific techniques to try to unlock the many remaining mysteries of its formation, detection, and prediction. With further improvements in the next generation of GOES channel imagery and better analysis and display system capabilities, the wide

variety of satellite image channel combinations can be further explored to help in the detection of aircraft icing environments using the channel differencing, RGB enhancement, and other methods. In the future, improved icing environment detection and prediction will most likely result from a combination of a variety of remote sensing techniques both active and passive, such as ground-based radiometers, advanced precipitation radars, profilers, in-situ aircraft measurements, and satellite-based radiometers. Also, a better understanding of the microphysics of stratiform and cumuliform clouds, as well as precipitation formation processes, must be reached before the full compliment of conditions of an icing region can be successfully determined. Many more icing cases with better detailed PIREP data sets or other verification methods need to be examined before a definitive detection and prediction scheme will result.

In the future, as numerical models become more sophisticated in terms of their microphysical and other parameterizations, and additional, new data sources (including satellite techniques) are brought together to form improved icing algorithms, icing forecasts should continue to be more precise/accurate, while reducing the overforecasting of temporal and spatial coverage (false alarms). Also, future studies of regional biases in the performance of the algorithms and those directed towards developing methods to forecast icing severity/intensity will benefit from an improved suite of atmospheric information on icing.

Improvements in the temporal and spatial coverage of PIREPs would provide a much improved basis on which to judge the effectiveness of future aircraft icing forecasts. At the moment, a more systematic collection of icing verification would likely require the assistance of commercial and commuter airlines. Until FAA rules require pilots to give more PIREPs or a way is found to better mechanically sense the ice accretion formation and automatically record/transmit more frequent in-flight weather environment information (temperature, relative humidity, cloud droplet sizes, etc.), icing forecasting and verification will be limited to present PIREP verification methods and smaller scale experiments for evaluating icing forecasts. But, of course, if a commercial pilot is asked to fly into threatening cloudy regions or suspected aviation hazard areas that would imply possibly severe weather, one can expect that it wouldn't happen voluntarily!

Ultimately, significant advances in aircraft icing forecasts depend on better observations of icing. Direct, automated measurements of airframe ice are not likely, but indirect techniques using data from on-

board sensors of temperature and humidity might be feasible. Several major airlines are currently using automated equipment for collecting temperature and wind measurements. This data is relayed automatically by a system called ACARS (ARINC Communications, Addressing, and Reporting System, operated by Aeronautical Radio, Inc. (ARINC)). They cover a substantial portion of the continental U.S. and are being used experimentally for model initialization. Although they do not yet include humidity measurements, the equipment for providing these measurements is presently being tested.

Table 6.1a PIREPs for Case 1 (10 Apr 95 1500-2100Z)

													248 - 276K	
PIREPs			ICING (from PIREPs)							IZ - icing temp zone				
10 Apr 95					R-rime	C-clear	M-mix			N - Null	(deg C)	(0 - 100)	(deg K)	
Julian Day 100					(0)Null	(1-3)Lgt	(4-7) Mdt			I - Icing	Dual-Chan	Visible	Cld-Top	
	File Time	(# / 780)	(# / 1025)	0 - 7	R-C-M	(100s of ft AGL)		M - Mdt+		IR Diff	Albedo	IR Temp		
	GMT (Z)	Y axis	X axis	Intens	Type	Base	Top			CH2-CH4	CH1	CH4		
								N	I	M		IZ		
1	15	520	490	4	M		065		x	x	25	56	228	
2		510	650	0		050		x			52	64	205	
3	V	530	710	5			020		x	x	41	51	223	
4		560	670	3	R	040	070		x		32	53	217	
5		570	650	3	M	070			x		37	51	221	
6	16	570	210	0		240		x			37	43	x 259	
7		510	310	0		220	600	x			43	48	x 248	
8	V	510	310	3	R	046			x		43	48	x 248	
9		420	310	3	R	084			x		27	51	x 265	
10		510	390	5	M	090			x	x	36	58	x 262	
11		500	390	4	C	090			x	x	31	55	x 266	
12		500	390	1	R	090			x		31	55	x 266	
13		490	410	4	R		050		x	x	37	56	x 260	
14		500	470	4	R	042			x	x	24	49	x 230	
15		500	450	4	C	040			x	x	24	50	x 227	
16		500	450	3	R	042	060		x		24	50	x 227	
17		510	530	4	M	020	050		x	x	30	45	x 226	
18		550	530	3	C	045	075		x		21	52	x 229	
19		550	490	0		090		x			21	55	x 231	
20		560	510	3	R	060	070		x		20	53	x 241	
21		560	510	0		150	600	x			20	53	x 241	
22		560	670	3	R	020	050		x		32	53	x 217	
23		510	750	7	R	170			x	x	37	52	x 242	
24	17	580	230	0		130		x			38	37	x 261	
25		550	270	3	R	150			x		45	27	x 253	
26	V	560	370	0		150		x			11	51	x 249	
27		480	210	2		220			x		21	44	x 235	
28		460	130	0		160		x			5	37	x 262	
29		470	230	3	R	190	210		x		9	52	x 249	
30		500	390	3	M	140			x		31	55	x 266	
31		420	330	7	R	014			x	x	34	45	x 268	
32		550	530	4	M	023			x	x	21	52	x 229	
33		530	530	5	C	030	040		x	x	21	55	x 227	
34		420	430	5	R	330			x	x	43	65	x 208	
35		440	490	3	R	310			x		48	63	x 209	
36		560	670	4	R	040			x	x	32	53	x 217	
37		530	710	4	C	017			x	x	41	51	x 223	
38		450	650	0		060		x			21	10	x 276	
39		480	750	0		027		x			24	27	x 233	
40		520	850	5	R	130	168		x	x	50	39	x 219	
41		510	890	3		030			x		37	50	x 232	
42		420	930	0		060		x			6	10	x 303	
43	18	570	210	0		040		x			37	43	x 259	
44		570	210	0		057	600	x			37	43	x 259	
45	V	540	210	1	R	074			x		22	20	x 269	
46		550	270	0		130		x			45	27	x 253	
47		530	230	0		130		x			37	31	x 263	
48		530	230	0		150		x			37	31	x 263	
49		500	170	0		160		x			42	40	x 260	
50		510	290	0		140		x			13	48	x 248	

Table 6.1b PIREPs for Case 1 (10 Apr 95 1500-2100Z)

										248 - 276K									
PIREPs				ICING (from PIREPs)						IZ - icing temp zone									
10 Apr 95				R-time		C-clear		M-mix		N - Null		(deg C)		(0 - 100)		(deg K)			
Julian Day 100				(0)Null		(1-3)Lgt		(4-7) Mdt		I - Icing		Dual-Chan		Visible		Cld-Top			
File Time		(# / 780)(# / 1025)		0 - 7		R-C-M		(100s of ft AGL)		M - Mdt+		IR Diff		Albedo		IR Temp			
GMT (Z)		Y axis		X axis		Intens		Type		Base		Top		CH2-CH4		CH1		CH4	
										N		I		M				IZ	
51	18 cont	470	210	3	R	180				x		17	34					242	
52	I	510	310	0		110				x		43	48	x				248	
53	V	470	210	0		220				x		17	34					242	
54		480	250	0		180				x		10	49					243	
55		470	270	0		208	240			x		12	55	x				252	
56		440	190	0		140	230			x		20	50					239	
57		450	190	0			215			x		18	44					236	
58		470	230	1		170					x	9	52	x				249	
59		490	430	0		140	160			x		25	54					229	
60		440	330	5	R	060	080				x	38	59	x				265	
61		440	490	0		160				x		48	63					209	
62		580	590	4	R	180	190				x	32	49					247	
63		570	630	4	M	040	070				x	34	50					232	
64		580	650	0		120				x		43	48					223	
65		570	670	5	C	040					x	32	52					219	
66		570	650	3	R		070				x	37	51					221	
67		570	650	3	C	110					x	37	51					221	
68		530	710	3	C	025					x	41	51					223	
69		520	710	3		270					x	47	70					215	
70		520	810	3	R	025	030				x	38	56					219	
71		510	930	3		030					x	26	43	x				251	
72		430	910	0		110	600			x		6	9					303	
73	19	580	290	3	R	110					x	40	44	x				259	
74	I	480	230	3	R	160					x	7	45	x				249	
75	V	420	310	3		080					x	27	51	x				265	
76		490	430	0		190				x		25	54					229	
77		510	490	1		040	060				x	26	49					237	
78		510	530	5	M	130	146				x	30	45					226	
79		570	610	5	C	080					x	38	53					242	
80		570	650	4		050	060				x	37	51					221	
81		560	670	0		075				x		32	53					217	
82		560	710	0		030	085			x		37	53					219	
83		520	710	4	M		030				x	47	70					215	
84		550	750	3	C		040				x	41	55					221	
85		550	810	3	M	100					x	44	46					218	
86		520	810	5	M	021	026				x	38	56					219	
87		550	850	0		160				x		33	44					229	
88		470	770	3		210					x	18	39	x				262	
89	20	460	150	1		100	170				x	17	36	x				254	
90	I	470	210	1	R	068	110				x	17	34					242	
91	V	440	330	3	R	060					x	36	48	x				265	
92		500	450	5	C		060				x	24	50					227	
93		500	490	1	M	018					x	22	47					232	
94		550	530	5		050					x	21	52					229	
95		570	530	5	M	025	080				x	26	48					244	
96		580	490	5	R	060					x	40	44	x				249	
97		560	670	5	M	150	220				x	32	53					217	
98		560	670	3	R	020	040				x	32	53					217	
99		570	670	5	C	110					x	32	52					219	
100		520	650	5	M	150	160				x	56	55					211	

Table 6.1c PIREPs for Case 1 (10 Apr 95 1500-2100Z)

										248 - 276K	
PIREPs				ICING (from PIREPs)						IZ - icing temp zone	
10 Apr 95				R-rime	C-clear	M-mix		N - Null	(deg C)	(0 - 100)	(deg K)
Julian Day 100				(0)Null	(1-3)Lgt	(4-7) Mdt		I - Icing	Dual-Chan	Visible	Cld-Top
File Time	(# / 780)	(# / 1025)		0 - 7	R-C-M	(100s of ft AGL)		M - Mdt+	IR Diff	Albedo	IR Temp
GMT (Z)	Y axis	X axis		Intens	Type	Base	Top		CH2-CH4	CH1	CH4
								N I M			IZ
101	20 cont	530	710	5	R		037	x x	41	51	223
102	I	550	810	5	R	040		x x	44	46	218
103	V	530	810	5	C	030		x x	37	60	225
104		430	910	0		070		x	6	9	303
105	21	600	430	1	R	120		x	24	30	232
106	I	560	430	4	R	110	150	x x	44	56	243
107	V	500	470	3	M	023	035	x	24	49	230
108		500	470	3	R		070	x	24	49	230
109		510	530	0		020		x	30	45	226
110		510	530	0		057	600	x	30	45	226
111		470	430	3		080		x	27	55	220
112		440	330	4	M	042		x x	36	48	x 265
113		440	330	4	R	050	060	x x	36	48	x 265
114		600	630	4	M	130		x x	25	31	231
115		580	630	0		030		x	37	46	228
116		570	650	5	R	050		x x	37	51	221
117		570	650	5	C	030	040	x x	37	51	221
118		560	680	0		110		x	28	54	226
119		530	710	5	R		013	x x	41	51	223
120		470	630	5		130		x x	50	25	229
121		550	750	5	R	120		x x	41	55	221
122		540	810	0		030		x	40	56	224
123		560	790	5	C		130	x x	35	51	219
124		530	870	4	R	160		x x	43	35	215
125		500	830	0		011		x	37	44	233
MEAN											
				2.55	All	098		39 86 46	TOTAL	Total IZ	23 / 86
				3.71	I	089			125	All Icing)	26.74
				4.7	M	081					
										Total CZ	63 / 86
										(All Icing)	73.26

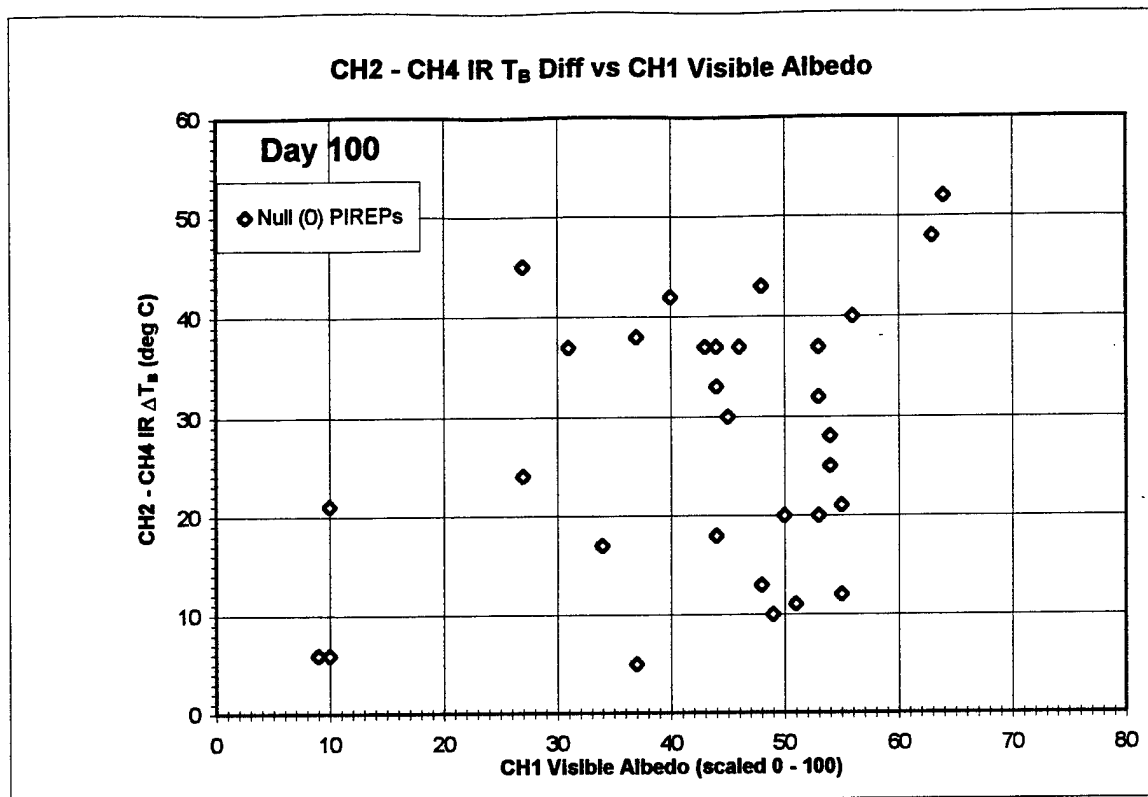


Figure 6.1a Scatter plot of null (0 intensity - no icing) PIREPs (Case 1)

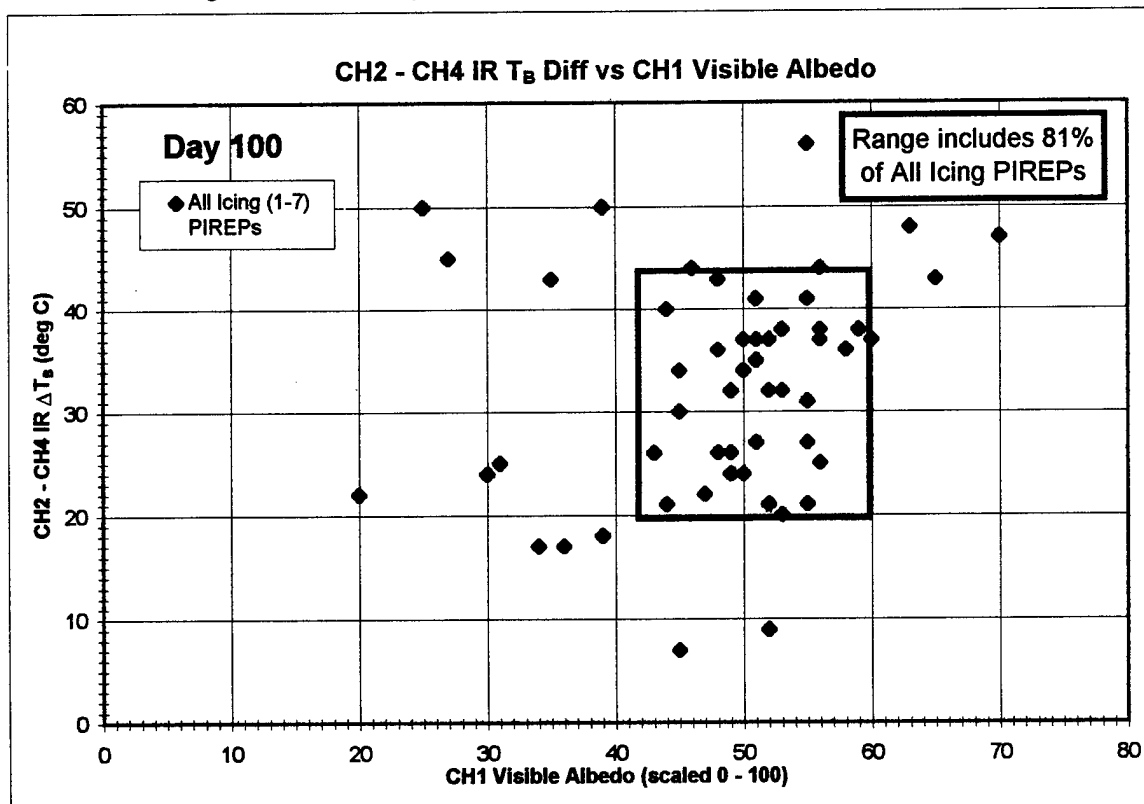


Figure 6.1b Scatter plot of all icing (1-7 intensity) PIREPs (Case 1)

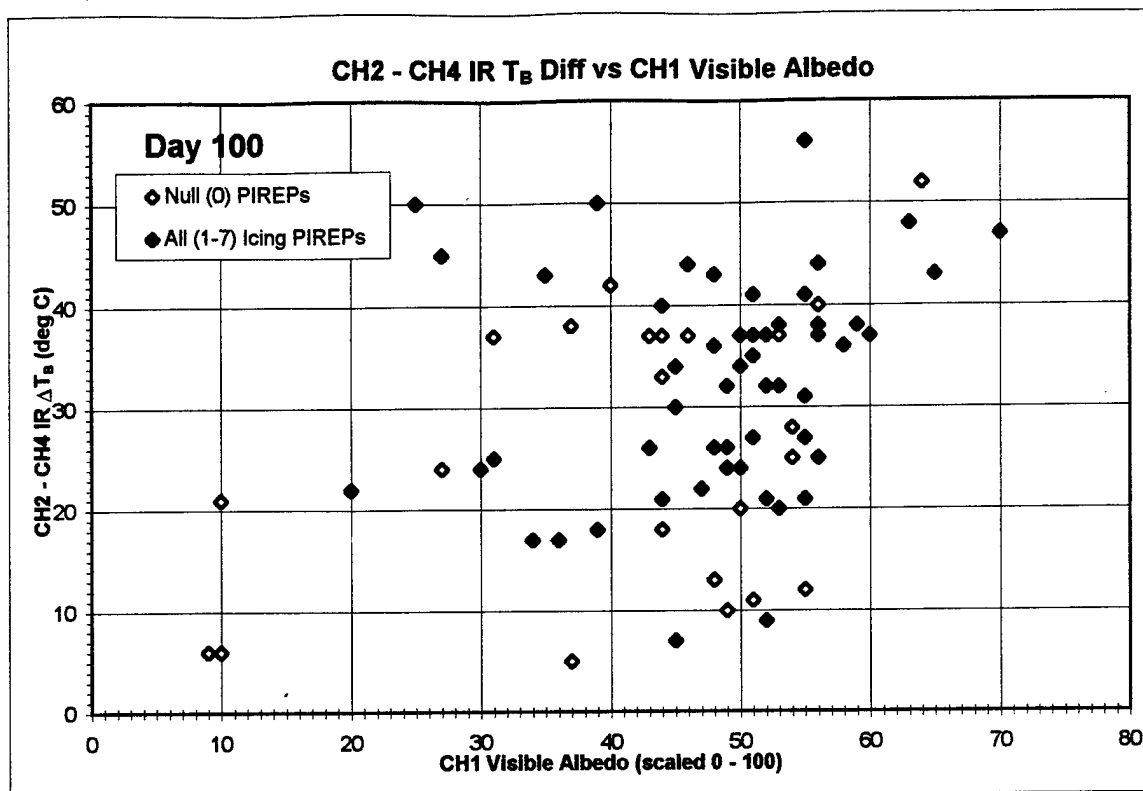


Figure 6.1c Scatter plot of null and all icing PIREPs (Case 1)

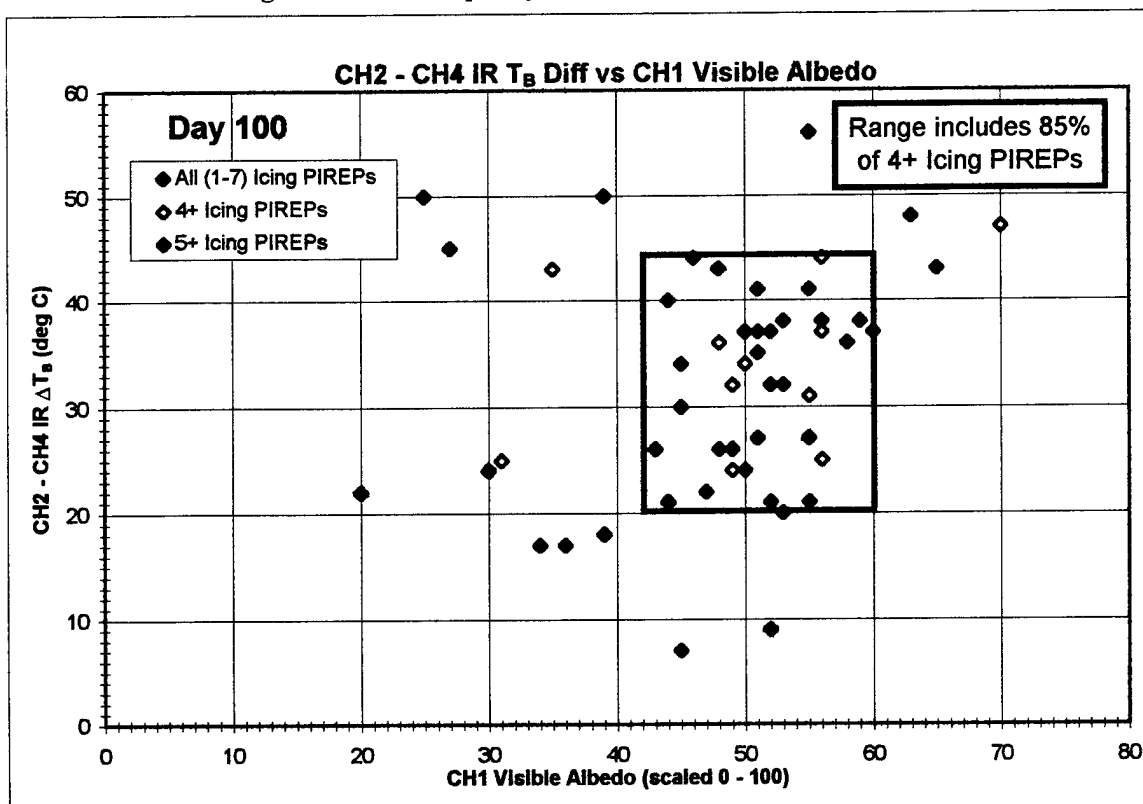


Figure 6.1d Scatter plot of all, moderate or greater (4+), and extreme (5+) icing PIREPs (Case 1)

Table 6.2a Grid of pixel dump values for Case 1 from 1745Z imagery

		10 / 1745Z Apr 95										Pixel Dump T _s Value (E-W for pixel number out of 1025)															
GOES-8		IDL > qview					(deg C)																				
CHANNEL 2		130	150	170	190	210	230	250	270	290	310	330	350	370	390	410	430	450	470	490	510	530	550				
	610				20	18	12	23	0	25	28	12	24	26	17	8	11	7	1	-19	-13	-2	-23	-23			
	600				23	3	20	-1	12	30	5	22	27	5	-9	-11	-14	-17	-18	-21	-21	-19	-23	-17			
	590				15	24	23	7	13	28	17	19	21	22	-15	-18	-21	-16	-18	-17	-18	-12	-10	2			
	580				26	19	16	26	25	26	26	23	23	-16	-18	-19	-21	-13	21	10	16	6	-3	-1			
	570				22	27	23	2	9	23	22	16	-20	-19	-19	-16	19	13	11	7	-15	-3	-7				
	560				24	12	21	20	26	26	5	-24	-22	-20	-13	22	6	14	3	-15	-12	-13	-13				
(deg C)	550				26	17	14	23	27	25	-5	-24	-20	-18	-14	20	15	3	-7	-25	-21	-13	-23	-20			
Pixel Dump	540				12	8	18	17	28	24	-23	-23	-19	-16	-7	20	20	5	-16	-22	-13	-25	-24	-26			
T _s Value	530				26	28	-8	27	20	11	-23	-17	-20	-14	20	22	22	6	-15	-11	-18	-23	-25	-14			
(N-S)	520				23	24	27	30	20	-21	-20	-18	-12	3	22	25	25	3	-10	-17	-20	-22	-22	-15			
(pixel number)	510				27	27	28	14	-15	-21	-12	18	8	17	12	25	22	3	-15	-16	-10	-16	-17	-15			
(out of 780)	500				29	29	10	-15	-23	-20	-19	-7	25	25	24	24	25	-15	-22	-19	-19	-13	-19	-2			
	490				21	26	19	-12	-19	-20	-18	-13	10	18	26	17	24	-19	-25	-19	-25	-23	-13	-10			
	480				26	26	27	20	-17	-17	-20	16	24	25	25	25	20	14	12	-25	-24	-26	-23	-19	-14		
	470				26	25	22	-17	-14	-15	-16	9	12	26	25	26	20	-4	-26	-23	-27	-24	-26	-19	-13		
	460				-6	-2	-8	-22	-17	-8	-15	12	1	24	27	21	19	6	-16	-25	-24	-20	-25	-19	-18	-17	
	450				6	-15	-18	-19	-17	-9	23	26	23	21	26	22	7	-19	-23	-26	-17	-16	-16	-12	-15		
	440				-9	-18	-19	-14	-15	-8	16	23	22	24	28	24	7	-16	-21	-20	-22	-19	-16	-13	-8	-9	
	430				-13	12	0	4	-14	5	13	28	22	22	26	29	5	-24	-21	-19	-22	-22	-24	-16	-11	-6	
	420				-11	2	-7	-9	1	11	20	26	26	19	29	23	4	-18	-19	-22	-19	-21	-13	-7	4		
GOES-8																											
CHANNEL 4		130	150	170	190	210	230	250	270	290	310	330	350	370	390	410	430	450	470	490	510	530	550				
	610				-8	1	-5	-16	-8	-12	-9	-12	-15	-8	-15	-5	-28	-22	-42	-41	-31	-31	-44	-46			
	600				-9	3	-14	-12	-8	-13	-3	-16	-13	-13	-31	-32	-42	-36	-32	-31	-29	-37	-35	-36			
Ising Zone (3 to -25 C)	590				-10	-12	-17	-9	-7	-13	-10	-19	-16	-17	-31	-36	-41	-28	-26	-32	-29	-30	-34	-36			
Conv Zone (-26 to -50 C)	580				-11	-19	-6	-12	-9	-11	-14	-20	-22	-36	-44	-36	-30	-19	-19	-26	-24	-35	-35	-33			
Deep Conv (<-50 C)	570				-19	-17	-14	-12	-4	-12	-17	-26	-39	-34	-43	-37	-23	-29	-27	-35	-45	-32	-38	-38			
	560				-19	-20	-10	-14	-15	-10	-31	-33	-44	-36	-24	-24	-26	-30	-33	-38	-45	-32	-38	-36			
(deg C)	550				-23	-19	-15	-15	-17	-20	-31	-45	-35	-31	-27	-26	-22	-31	-50	-46	-42	-34	-44	-42			
Pixel Dump	540				-15	-15	-4	-22	-5	-18	-36	-40	-27	-29	-24	-22	-15	-31	-50	-46	-37	-49	-44	-49			
T _s Value	530				-13	4	-16	-10	7	-27	-42	-35	-33	-23	-20	-17	-13	-30	-54	-43	-45	-47	-48	-58			
(N-S)	520				-13	-15	-11	-19	22	-38	-25	-33	-22	-23	-18	-15	-8	-32	-54	-43	-45	-47	-57	-57			
(pixel number)	510				-10	-2	-15	-20	-38	-33	-25	-24	-17	-16	-11	-9	-30	-47	-39	-38	-33	-47	-63	-58			
(out of 780)	500				-13	-13	-18	-40	-34	-34	-31	-17	-19	-17	-12	-7	-4	-36	-46	-43	-41	-50	-43	-51			
	490				-9	0	-1	-24	-32	-31	-22	-17	-15	-15	-11	-18	-13	-44	-48	-44	-52	-52	-50	-51			
	480				-14	-9	-23	-38	-24	-24	-24	-18	-13	-4	-11	-35	-50	-56	-57	-56	-55	-51	-45	-45			
	470				-15	-17	-23	-41	-31	-24	-28	-19	-14	-12	-4	-11	-35	-56	-57	-56	-55	-51	-45	-45			
	460				-11	-19	-32	-34	-30	-17	-21	-15	-13	-12	-3	-22	-44	-53	-57	-57	-56	-55	-50	-50			
	450				-24	-37	-35	-37	-35	-27	-17	-18	-15	-13	-8	-5	-7	-35	-51	-51	-61	-58	-49	-49			
	440				-24	-36	-35	-34	-24	-15	-15	-16	-11	-6	-4	-22	-44	-55	-64	-64	-61	-58	-49	-49			
	430				-32	-27	-23	-19	-27	-16	-13	-9	-6	-3	-13	-53	-59	-64	-67	-66	-63	-60	-47	-47			
	420				-28	-22	-18	-31	-30	-6	-1	-14	-5	-2	-23	-54	-62	-65	-68	-67	-61	-55	-42	-32			

Table 6.2b Grid of pixel dump values for Case 1 from 1745Z imagery

GOES-3		10 / 1745Z Apr 95																Pixel Dump T _b Value (E-W for pixel number out of 1025)																	
CHANNEL 2		IDL > qview																(deg C)																	
		570	580	590	600	610	630	650	670	690	710	730	750	770	790	810	830	850	870	890	910	930	950												
(deg C) Pixel Dump T _b Value (N-S) (out of 780)	610	-22	-21	-18	-17	-16	-27	-16	-17	-10	-3	-7	-6	-10	-7	-1	-8	-4	-3	-2	-1	8	10												
	600	-15	-16	-19	-17	-21	-17	-21	-12	-3	-15	-10	-16	-18	-15	-2	2	15	9	9	12	13	1												
	590	0	1	9	0	-19	-7	-1	-17	-7	-1	-23	-22	-21	-16	-15	-1	14	12	13	15	13	-1												
	580	3	6	14	8	-7	-11	9	-19	-9	-19	-18	-16	-20	-19	-19	-18	-14	-9	-10	9	14	8												
	570	8	12	7	-7	-15	-22	-19	-20	-21	-20	-21	-27	-18	-19	-18	-18	-21	-11	-7	-16	-19	-11												
	560	-15	-19	-8	-15	-17	-24	-19	-17	-24	-19	-17	-16	-16	-13	-19	-19	-17	-23	-13	-12	-13	-10	-7											
	550	-24	-14	-16	-15	-15	-15	-15	-16	-19	-16	-14	-11	-11	-20	-7	-11	-13	-11	-15	-4	-6	-10												
	540	-19	-13	-17	-16	-16	-16	-16	-15	-7	-9	-12	-11	-12	-9	-9	-11	-11	-16	-16	-9	-3	-7												
	530	-19	-13	-15	-17	-10	-6	-11	-9	-10	-9	-10	-9	-12	-11	-11	-12	-18	-15	-13	-12	-6	-7												
	520	-18	-13	-19	-8	-6	-14	-3	-11	-11	-11	-11	-12	-12	-14	-16	-19	-4	-4	-8	-9	0	11												
	510	-16	-13	-17	-16	-16	-5	-7	-10	-16	6	4	0	-12	-10	6	-3	4	-3	-4	-13	4	22												
	500	-9	-12	-12	-8	3	-12	-10	2	-4	-4	6	-13	-10	-3	-4	-8	8	7	-7	-8														
	490	-8	12	13	-8	-13	-16	-15	-15	2	-15	-13	-12	-2	-17	-11	2	6	19	13	-12														
	480	3	14	10	-10	-5	-11	15	17	10	-16	0	-9	5	18	15	19	5	7	-3	2														
	470	3	13	7	6	5	4	15	17	16	15	7	1	1	6	7	23	23	23	23	21	3													
	460	19	8	3	10	21	20	20	23	16	-13	23	10	-4	-6	10	10	21	22	25	20														
450	10	28	29	14	24	31	34	37	27	35	33	35	29	35	34	32	23	30	36	22															
440	6	23	31	29	32	36	34	36	36	36	36	37	36	36	37	33	35	36	38	39	36														
430	3	31	32	27	28	42	43	36	37	37	37	37	38	37	37	37	36	37	36	38	36														
420	11	21	32	26	27	47	36	38	36	36	36	37	37	36	36	36	36	36	36	36	36														
GOES-3																																			
CHANNEL 4		570	590	610	630	650	670	690	710	730	750	770	790	810	830	850	870	890	910	930	950														
(deg C) Pixel Dump T _b Value (N-S) (pixel number)	610	-46	-47	-46	-45	-50	-47	-48	-38	-40	-34	-29	-31	-22	-20	-15	-11	-6	-2	-2	6														
	600	-46	-47	-46	-42	-51	-46	-51	-34	-37	-36	-40	-38	-19	-13	-10	-2	5	8	5	1														
	590	-39	-38	-21	-38	-48	-48	-38	-42	-44	-44	-44	-48	-20	-22	-18	-20	-14	-5	7	-1														
	580	-31	-26	-25	-45	-50	-49	-41	-43	-46	-43	-44	-48	-40	-38	-34	-23	-23	-8	2	0														
	570	-24	-44	-31	-41	-52	-54	-49	-48	-46	-49	-46	-45	-54	-44	-38	-44	-40	-35	-48	52	38													
	560	-41	-50	-50	-48	-57	-56	-47	-54	-54	-53	-49	-46	-54	-51	-49	-47	-45	-54	-47	53	42													
	550	-49	-56	-56	-56	-58	-54	-48	-54	-56	-52	-47	-54	-51	-49	-55	-44	-53	-54	-40	44	58													
	540	-54	-58	-58	-59	-55	-62	-56	-60	-61	-59	-49	-52	-51	-48	-55	-50	-58	-58	-54	-46	55													
	530	-60	-60	-64	-63	-67	-63	-63	-63	-68	-68	-67	-57	-62	-51	-55	-55	-56	-57	-59	-46	48													
	520	-62	-63	-67	-67	-67	-62	-62	-65	-68	-62	-57	-58	-62	-50	-52	-52	-54	-51	-40	-27	17													
	510	-65	-66	-71	-71	-68	-66	-66	-66	-64	-61	-51	-51	-58	-50	-51	-47	-44	-41	-51	-22	-6													
	500	-65	-64	-66	-66	-67	-67	-67	-67	-68	-63	-48	-56	-56	-36	-40	-40	-54	-24	-24	-45	27													
	490	-50	-38	-18	-61	-63	-65	-62	-61	-51	-52	-51	-52	-51	-52	-35	-35	-38	-6	-11	-47	58													
	480	-43	-25	-35	-52	-55	-55	-55	-55	-49	-44	-40	-40	-21	-37	-35	-2	-5	-3	-19	-18	-23													
	470	-34	-18	-35	-44	-44	-18	-32	-10	2	-3	-21	-11	-25	-40	-17	-20	7	14	16	18	11													
	460	-21	-40	-39	-20	-1	5	14	3	-5	-9	5	1	4	15	12	11	11	10	3	4														
450	-19	1	0	-25	3	25	26	28	18	27	17	25	13	24	26	19	8	19	7	9															
440	-40	4	22	-7	20	30	28	29	31	30	32	32	31	30	28	30	29	32	32	30															
430	-36	0	19	9	16	28	28	35	30	31	28	32	32	32	32	33	33	31	30	31	30														
420	-25	-3	17	5	8	33	30	32	31	33	33	33	33	32	32	32	32	31	29	30	28														

Table 6.2c Grid of pixel dump values for Case 1 from 1745Z imagery

		Channel Differenced Pixel Dump T _B Value (E-W for pixel number out of 1025)																10/1745Z Apr 95					
		(deg C)																IDL > gview					
GOES-8		130	150	170	180	210	230	250	270	290	310	330	350	370	390	410	430	450	470	490	510	530	550
CH2 - CH4																							
	610			28	17	17	39	8	31	40	21	36	41	25	26	16	21	23	23	28	29	21	23
	600			32	0	34	11	20	43	8	36	40	18	22	21	28	24	21	24	10	18	12	19
	590			25	36	40	16	20	42	27	38	37	39	16	20	20	21	8	15	11	18	24	38
	580			37	38	22	38	34	37	40	43	45	22	26	17	9	15	40	36	40	42	36	32
	570			41	44	37	14	13	35	39	42	19	15	24	18	7	38	41	38	28	21	26	31
	560			43	32	31	34	41	38	36	9	22	18	11	48	32	44	38	41	30	20	25	23
	550			49	38	29	38	44	45	26	21	15	13	13	46	37	34	28	23	21	21	21	22
	540			27	23	22	39	33	42	13	17	8	13	17	42	35	36	34	24	24	24	20	23
	530			39	24	8	37	13	38	19	18	13	9	40	39	35	36	39	32	19	24	21	44
	520			36	39	38	49	42	17	9	15	10	26	40	40	33	35	44	26	25	18	25	42
	510			17	29	43	34	23	12	13	43	32	34	28	36	31	33	32	23	26	17	30	48
	500			42	47	39	25	11	14	12	10	44	42	36	31	29	21	24	24	22	37	24	56
	490		30	26	29	43	31	12	13	9	27	35	41	38	35	37	25	23	25	27	29	37	41
	480		40	35	50	43	21	7	10	40	41	43	41	36	24	28	25	26	26	31	32	38	31
	470		41	42	46	24	17	9	13	12	31	40	41	38	24	31	27	33	30	32	29	32	32
	460		5	17	24	12	13	8	6	29	16	37	39	33	22	28	28	28	33	37	30	36	37
	450		30	22	17	18	17	10	8	41	41	36	29	31	29	32	28	30	44	45	42	46	34
	440		15	18	16	20	9	16	31	39	37	35	38	28	28	34	38	34	45	48	48	55	45
	430		19	39	23	23	13	21	26	40	34	31	32	32	18	29	38	42	45	42	47	49	41
	420		17	24	11	22	31	17	21	40	37	27	34	25	36	43	43	46	47	54	48	48	36
Pixel Dump Albedo Value (E-W for pixel number out of 1025)																							
GOES-8																							
CHANNEL 1		130	150	170	180	210	230	250	270	290	310	330	350	370	390	410	430	450	470	490	510	530	550
	610			15	18	37	42	43	44	42	44	28	41	40	25	18	19	17	27	25	25	36	40
	600			29	17	42	46	46	42	30	43	41	44	27	32	38	30	36	40	38	30	38	42
	590			26	42	34	29	44	45	36	46	42	36	37	43	44	45	38	38	44	40	39	35
	580			34	42	37	37	37	45	44	47	43	44	46	49	52	46	51	44	44	41	43	45
	570			43	42	43	39	34	48	44	42	45	50	46	50	51	50	48	52	50	50	48	52
	560			38	37	26	32	29	44	37	39	41	48	51	54	51	56	53	51	52	53	52	53
	550			36	31	21	37	38	27	36	41	44	48	60	56	57	53	51	52	55	53	52	53
	540			18	24	20	45	27	30	40	44	49	48	49	53	58	57	50	53	51	50	54	54
	530			33	22	16	31	18	35	45	51	47	53	61	54	56	53	53	50	50	54	55	57
	520			35	22	24	35	34	40	49	52	48	54	61	58	53	53	51	49	56	51	53	58
	510			18	19	29	21	48	47	48	48	64	65	50	58	56	50	53	52	49	48	45	60
	500			40	47	32	40	43	44	54	49	55	55	60	55	55	49	50	49	47	44	56	54
	490	41	28	46	44	37	37	46	49	55	49	52	59	58	49	56	54	52	51	47	56	54	58
	480	29	21	43	34	44	45	49	49	53	56	56	49	50	55	55	54	51	51	56	56	57	51
	470	35	37	35	41	34	52	55	55	51	55	55	52	51	55	52	55	55	59	61	57	53	39
	460	37	36	43	50	35	46	48	50	53	53	54	63	55	53	54	57	59	64	62	64	55	45
	450	42	45	40	44	47	54	53	52	46	53	49	55	56	53	55	57	60	64	63	64	60	53
	440	49	37	47	50	56	59	55	58	52	53	48	48	52	53	56	59	64	65	63	63	67	50
	430	38	38	48	36	54	57	52	43	49	53	44	50	55	54	59	62	61	60	67	61	42	34
	420	27	44	30	33	53	48	25	44	46	51	46	48	52	47	63	65	65	68	66	53	43	37

Table 6.2d Grid of pixel dump values for Case 1 from 1745Z imagery

GOES-8 CH2 - CH4	Channel Differenced Pixel Dump T _b Value (E-W for pixel number out of 1025)																10 / 1746Z Apr 95																							
	570	580	590	600	610	620	630	640	650	660	670	680	690	700	710	720	730	740	750	760	770	780	790	800	810	820	830	840	850	860	870	880	890	900	910	920	930	940	950	
	24	26	28	30	32	34	36	38	40	42	44	46	48	50	52	54	56	58	60	62	64	66	68	70	72	74	76	78	80	82	84	86	88	90	92	94	96			
	33	35	37	39	41	43	45	47	49	51	53	55	57	59	61	63	65	67	69	71	73	75	77	79	81	83	85	87	89	91	93	95	97	99	101	103	105	107		
	39	41	43	45	47	49	51	53	55	57	59	61	63	65	67	69	71	73	75	77	79	81	83	85	87	89	91	93	95	97	99	101	103	105	107	109	111	113		
	34	36	38	40	42	44	46	48	50	52	54	56	58	60	62	64	66	68	70	72	74	76	78	80	82	84	86	88	90	92	94	96	98	100	102	104	106	108		
	32	34	36	38	40	42	44	46	48	50	52	54	56	58	60	62	64	66	68	70	72	74	76	78	80	82	84	86	88	90	92	94	96	98	100	102	104	106	108	
	32	34	36	38	40	42	44	46	48	50	52	54	56	58	60	62	64	66	68	70	72	74	76	78	80	82	84	86	88	90	92	94	96	98	100	102	104	106	108	
	26	28	30	32	34	36	38	40	42	44	46	48	50	52	54	56	58	60	62	64	66	68	70	72	74	76	78	80	82	84	86	88	90	92	94	96	98	100	102	104
	25	27	29	31	33	35	37	39	41	43	45	47	49	51	53	55	57	59	61	63	65	67	69	71	73	75	77	79	81	83	85	87	89	91	93	95	97	99	101	
	36	38	40	42	44	46	48	50	52	54	56	58	60	62	64	66	68	70	72	74	76	78	80	82	84	86	88	90	92	94	96	98	100	102	104	106	108	110	112	
	41	43	45	47	49	51	53	55	57	59	61	63	65	67	69	71	73	75	77	79	81	83	85	87	89	91	93	95	97	99	101	103	105	107	109	111	113	115		
	44	46	48	50	52	54	56	58	60	62	64	66	68	70	72	74	76	78	80	82	84	86	88	90	92	94	96	98	100	102	104	106	108	110	112	114	116	118		
	49	51	53	55	57	59	61	63	65	67	69	71	73	75	77	79	81	83	85	87	89	91	93	95	97	99	101	103	105	107	109	111	113	115	117	119	121	123		
	42	44	46	48	50	52	54	56	58	60	62	64	66	68	70	72	74	76	78	80	82	84	86	88	90	92	94	96	98	100	102	104	106	108	110	112	114	116	118	
	37	39	41	43	45	47	49	51	53	55	57	59	61	63	65	67	69	71	73	75	77	79	81	83	85	87	89	91	93	95	97	99	101	103	105	107	109	111		
	40	42	44	46	48	50	52	54	56	58	60	62	64	66	68	70	72	74	76	78	80	82	84	86	88	90	92	94	96	98	100	102	104	106	108	110	112	114	116	
	46	48	50	52	54	56	58	60	62	64	66	68	70	72	74	76	78	80	82	84	86	88	90	92	94	96	98	100	102	104	106	108	110	112	114	116	118	120	122	
	31	33	35	37	39	41	43	45	47	49	51	53	55	57	59	61	63	65	67	69	71	73	75	77	79	81	83	85	87	89	91	93	95	97	99	101	103	105		
	27	29	31	33	35	37	39	41	43	45	47	49	51	53	55	57	59	61	63	65	67	69	71	73	75	77	79	81	83	85	87	89	91	93	95	97	99	101		
	46	48	50	52	54	56	58	60	62	64	66	68	70	72	74	76	78	80	82	84	86	88	90	92	94	96	98	100	102	104	106	108	110	112	114	116	118	120	122	
	39	41	43	45	47	49	51	53	55	57	59	61	63	65	67	69	71	73	75	77	79	81	83	85	87	89	91	93	95	97	99	101	103	105	107	109	111	113		
	38	40	42	44	46	48	50	52	54	56	58	60	62	64	66	68	70	72	74	76	78	80	82	84	86	88	90	92	94	96	98	100	102	104	106	108	110	112		
	40	42	44	46	48	50	52	54	56	58	60	62	64	66	68	70	72	74	76	78	80	82	84	86	88	90	92	94	96	98	100	102	104	106	108	110	112	114	116	
	48	50	52	54	56	58	60	62	64	66	68	70	72	74	76	78	80	82	84	86	88	90	92	94	96	98	100	102	104	106	108	110	112	114	116	118	120	122	124	
	37	39	41	43	45	47	49	51	53	55	57	59	61	63	65	67	69	71	73	75	77	79	81	83	85	87	89	91	93	95	97	99	101	103	105	107	109	111		
	40	42	44	46	48	50	52	54	56	58	60	62	64	66	68	70	72	74	76	78	80	82	84	86	88	90	92	94	96	98	100	102	104	106	108	110	112	114	116	
	28	30	32	34	36	38	40	42	44	46	48	50	52	54	56	58	60	62	64	66	68	70	72	74	76	78	80	82	84	86	88	90	92	94	96	98	100	102	104	
	48	50	52	54	56	58	60	62	64	66	68	70	72	74	76	78	80	82	84	86	88	90	92	94	96	98	100	102	104	106	108	110	112	114	116	118	120	122	124	
	31	33	35	37	39	41	43	45	47	49	51	53	55	57	59	61	63	65	67	69	71	73	75	77	79	81	83	85	87	89	91	93	95	97	99	101	103	105		
	46	48	50	52	54	56	58	60	62	64	66	68	70	72	74	76	78	80	82	84	86	88	90	92	94	96	98	100	102	104	106	108	110	112	114	116	118	120	122	
	39	41	43	45	47	49	51	53	55	57	59	61	63	65	67	69	71	73	75	77	79	81	83	85	87	89	91	93	95	97	99	101	103	105	107	109	111	113		
	40	42	44	46	48	50	52	54	56	58	60	62	64	66	68	70	72	74	76	78	80	82	84	86	88	90	92	94	96	98	100	102	104	106	108	110	112	114	116	
	38	40	42	44	46	48	50	52	54	56	58	60	62	64	66	68	70	72	74	76	78	80	82	84	86	88	90	92	94	96	98	100	102	104	106	108	110	112	114	
	40	42	44	46	48	50	52	54	56	58	60	62	64	66	68	70	72	74	76	78	80	82	84	86	88	90	92	94	96	98	100	102	104	106	108	110	112	114	116	
	40	42	44	46	48	50	52	54	56	58	60	62	64	66	68	70	72	74	76	78	80	82	84	86	88	90	92	94	96	98	100	102	104	106	108	110	112	114	116	
	40	42	44	46	48	50	52	54	56	58	60	62	64	66	68	70	72	74	76	78	80	82	84	86	88	90	92	94	96	98	100	102	104	106	108	110	112	114	116	
	40	42	44	46	48	50	52	54	56	58	60	62	64	66	68	70	72	74	76	78	80	82	84	86	88	90	92	94	96	98	100	102	104	106	108	110	112	114	116	
	40	42	44	46	48	50	52	54	56	58	60	62	64	66	68	70	72	74	76	78	80	82	84	86	88	90	92	94	96	98	100	102	104	106	108	110	112	114	116	
	40	42	44	46	48	50	52	54	56	58	60	62	64	66	68	70	72	74	76	78	80	82	84	86	88	90	92	94	96	98	100	102	104	106	108	110	112	114	116	
	40	42	44	46	48	50	52	54	56	58	60	62	64	66	68	70	72	74	76	78	80	82	84	86	88	90	92	94	96	98	100	102	104	106	108	110	112	114	116	
	40	42	44	46	48	50	52	54	56	58	60	62	64	66	68	70	72	74	76	78	80	82	84	86	88	90	92	94	96	98	100	102	104	106	108	110	112	114	116	
	40	42	44	46	48	50	52	54	56	58	60	62	64	66	68	70	72	74	76	78	80	82	84	86	88	90	92	94	96											

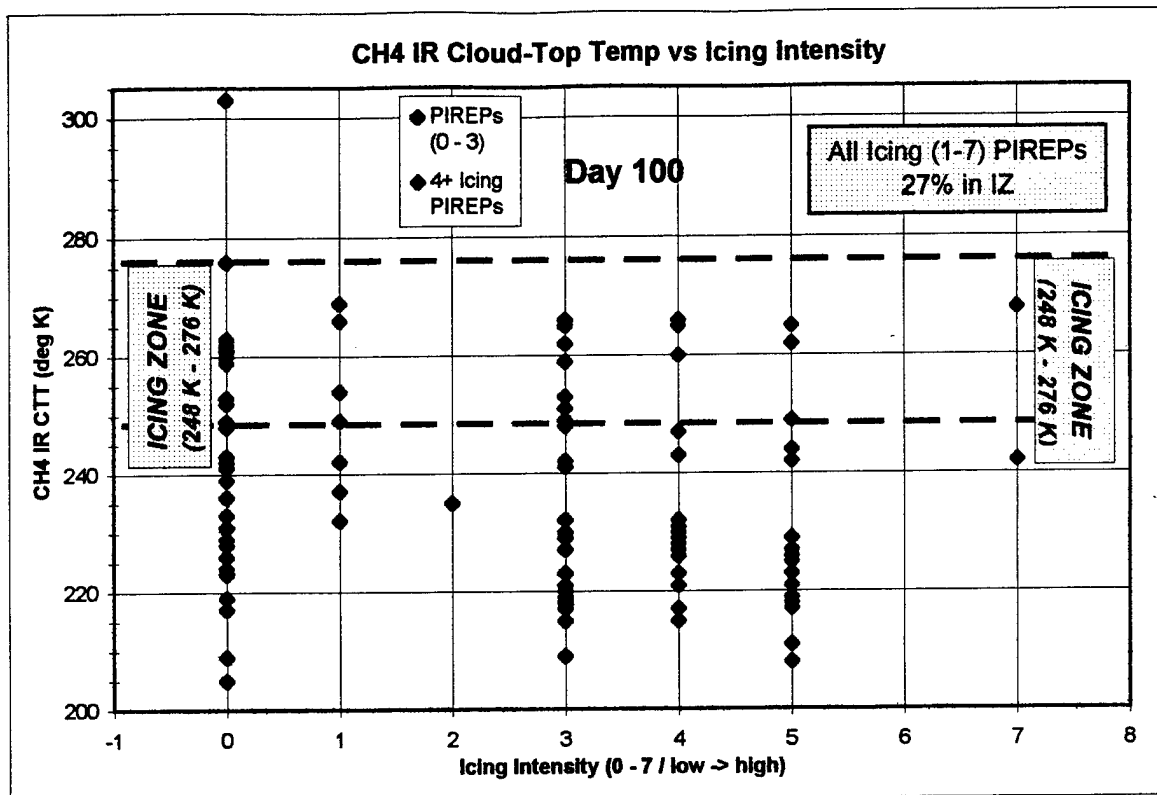


Figure 6.2a Scatter plot of all PIREPs (0-7 intensity) within the Icing Zone (IZ) (Case 1)

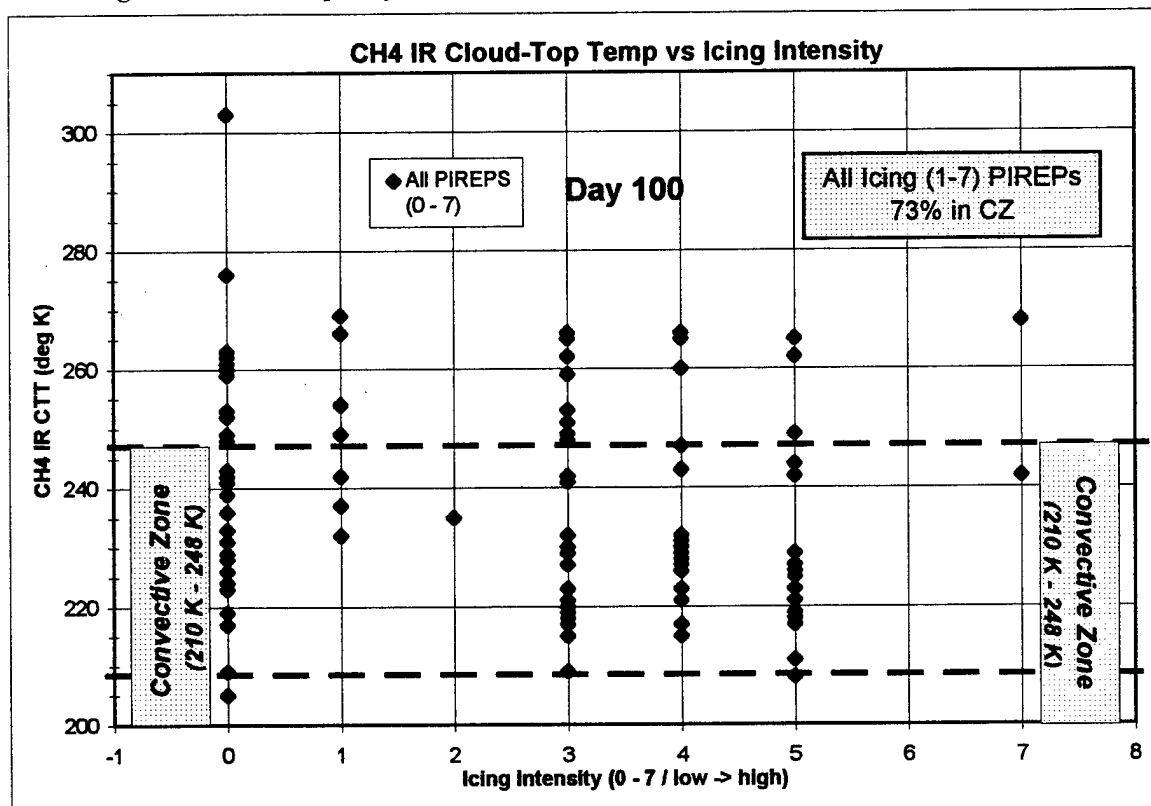


Figure 6.2b Scatter plot of all PIREPs within the Convective Zone (CZ) (Case 1)

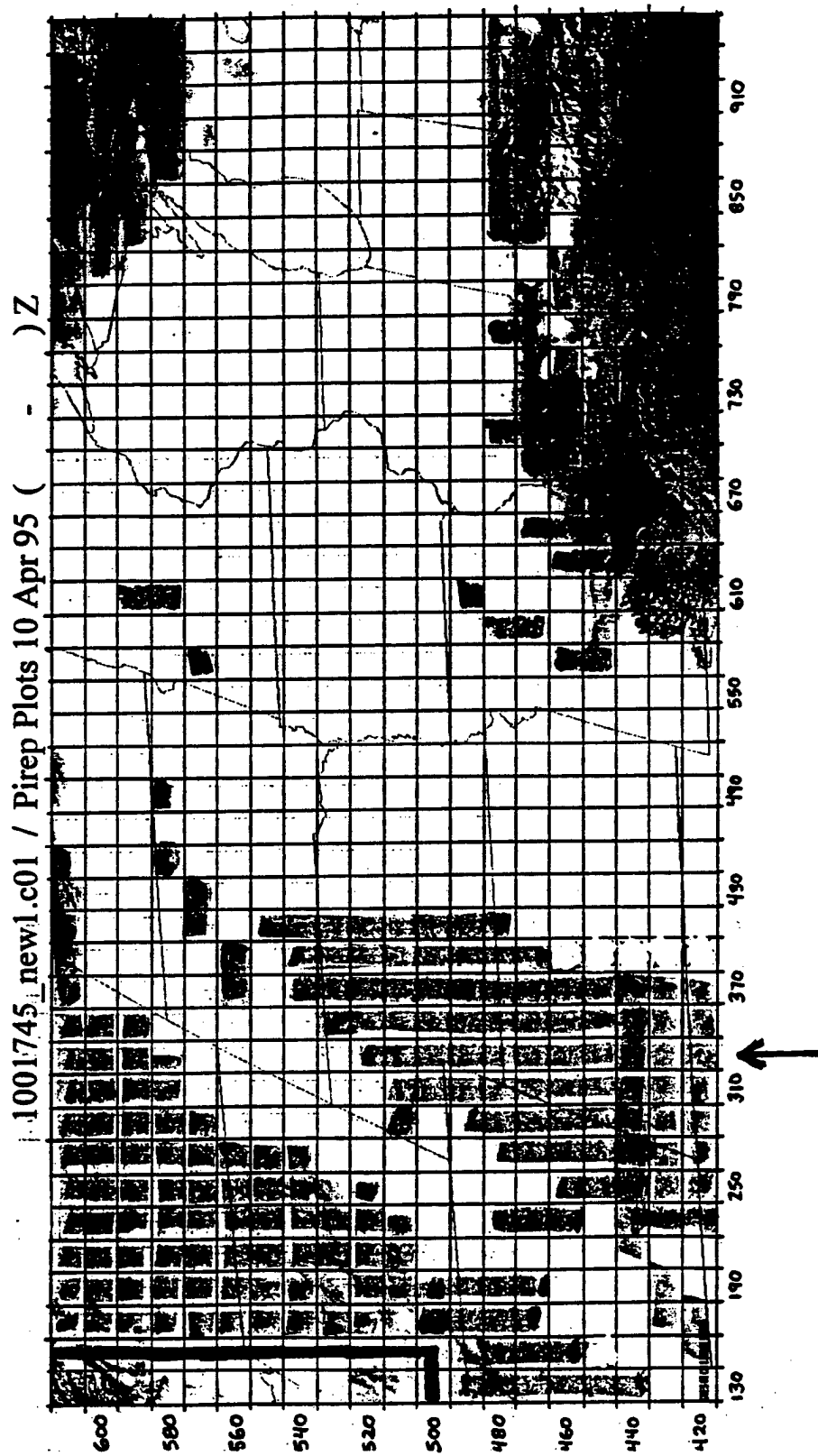


Figure 6.3 Grid showing shaded sectors representing stratiform cloud tops within IZ (Case 1)

GOES-8 CH1 10/1745Z Apr 95

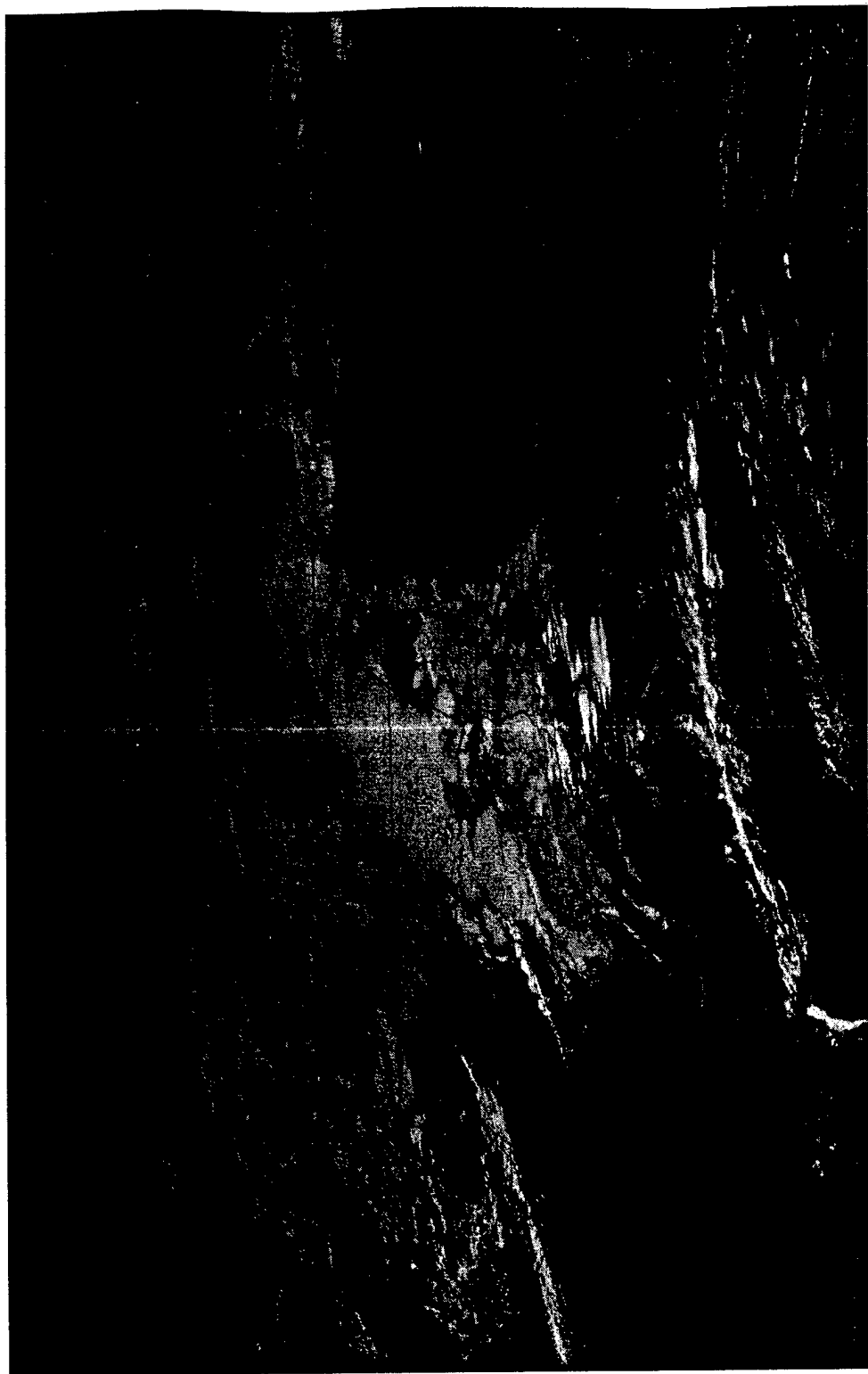


Figure 6.4a GOES-8 channel 1 (visible) image of U.S. for 10/1745Z Apr 95 (Case 1)

GOES-8 CH1(inverted) 10/1745Z Apr 95

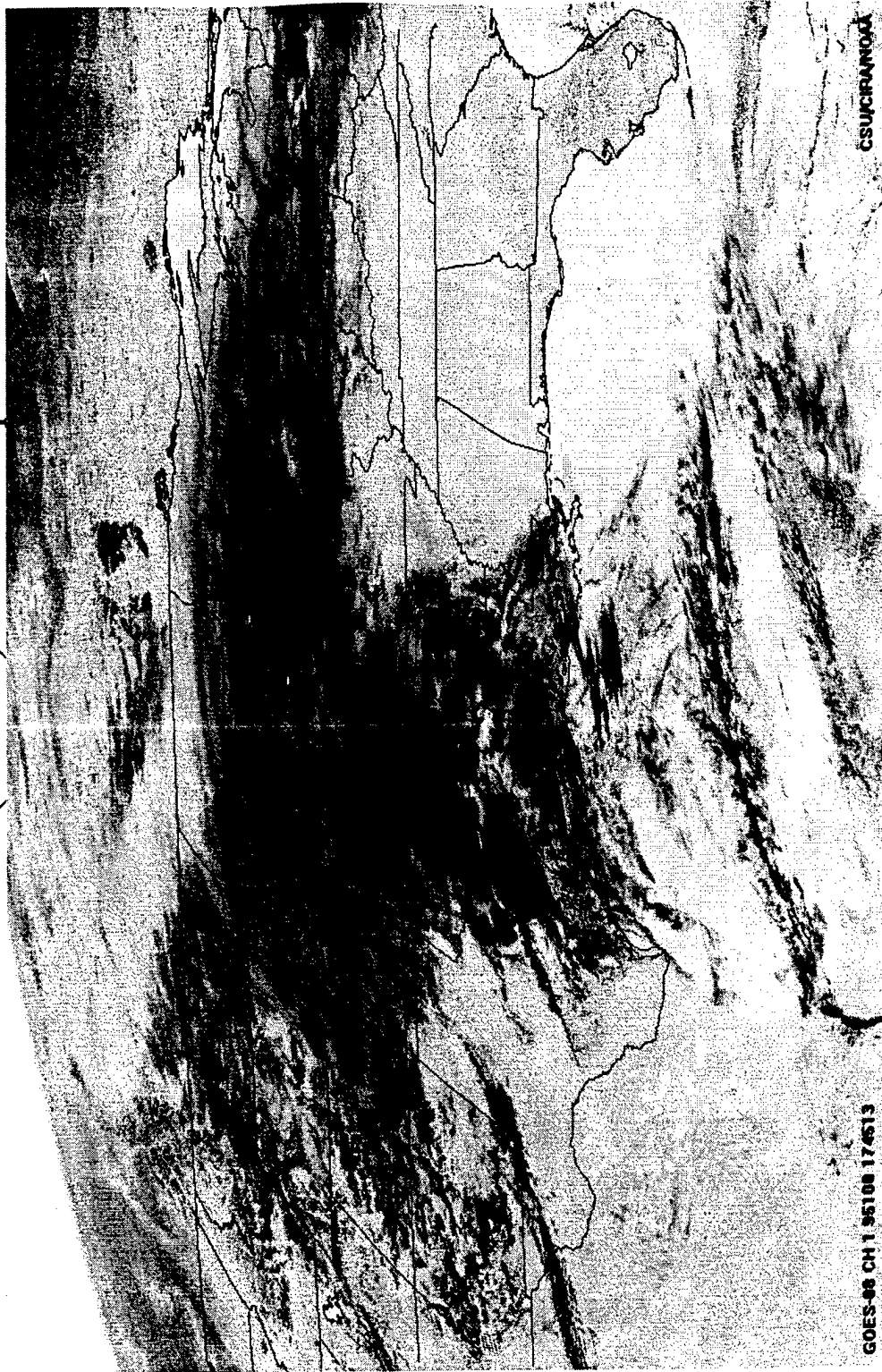


Figure 6.4b GOES-8 channel 1 (inverted visible) image of U.S. for 10/1745Z Apr 95 (Case 1)

GOES-8 CH2 10/1745Z Apr 95

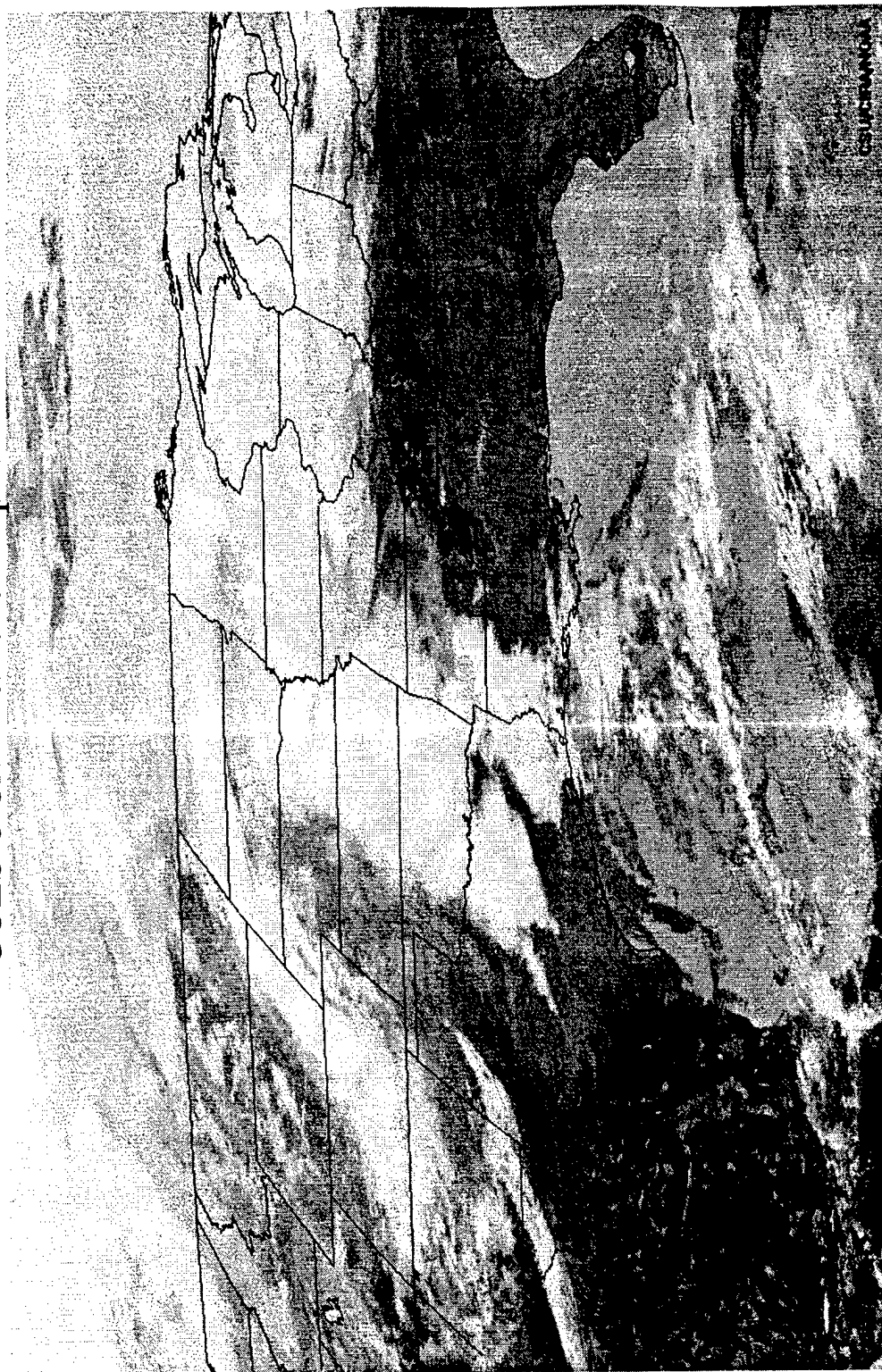


Figure 6.4c GOES-8 channel 2 (inverted SIR) image of U.S. for 10/1745Z Apr 95 (Case 1)

GOES-8 CH4 10/1745Z Apr 95

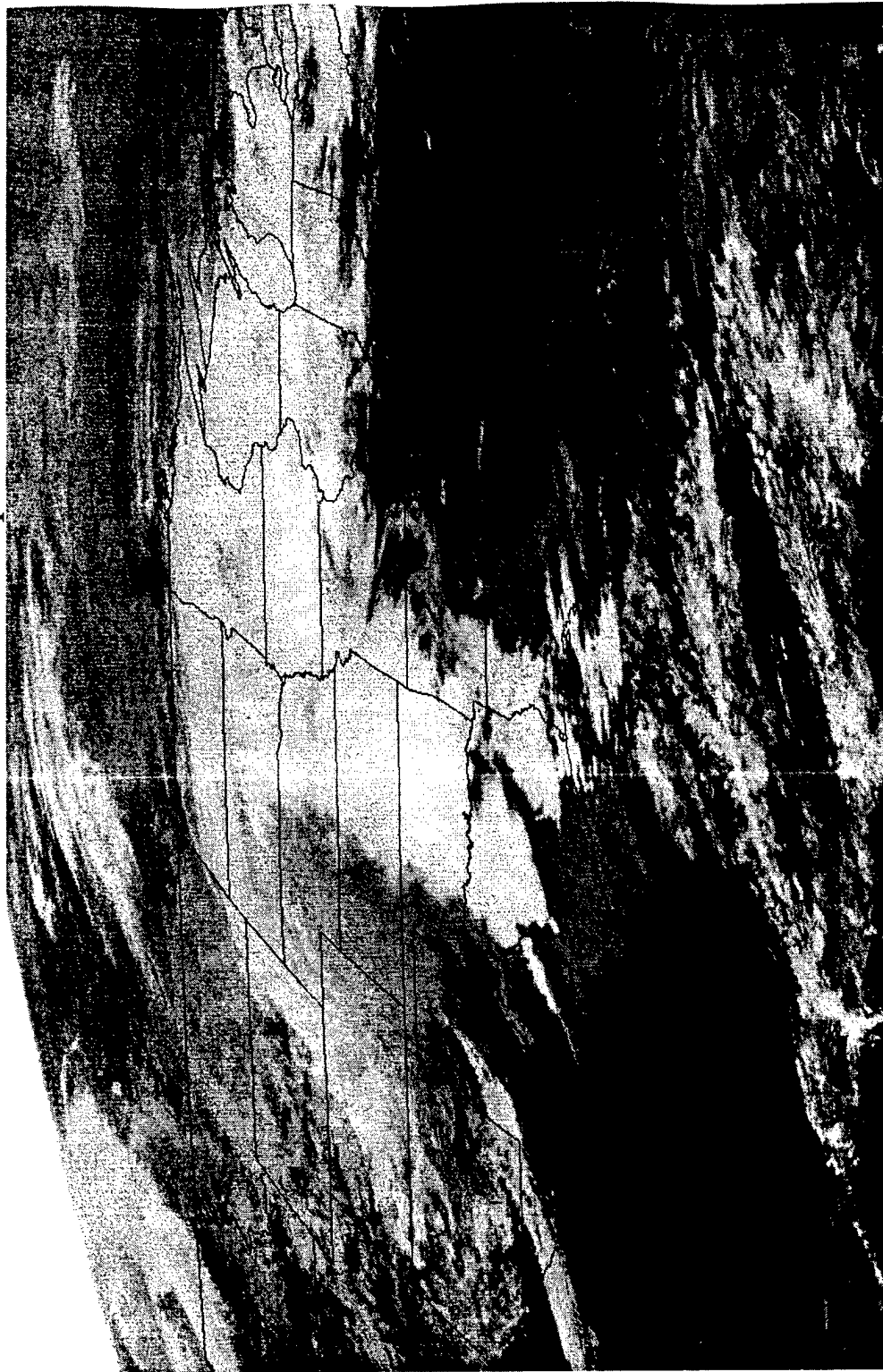
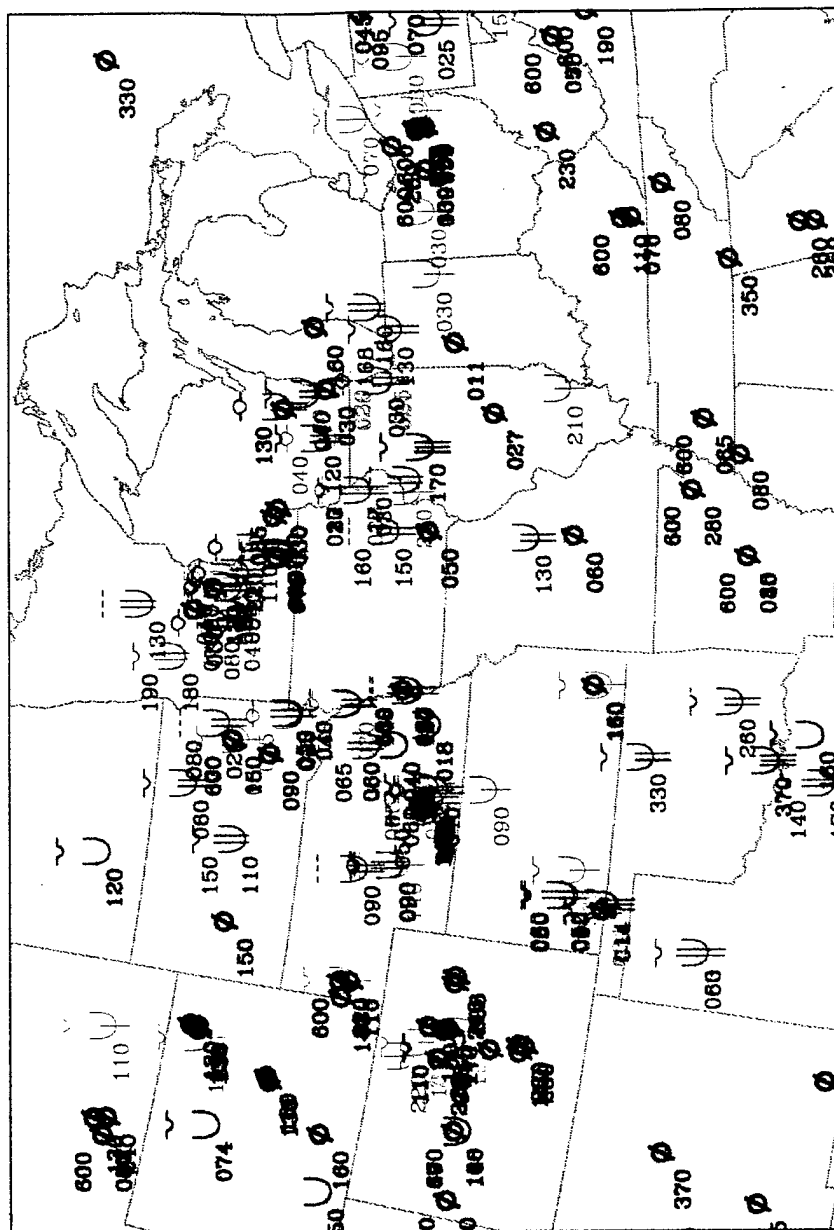


Figure 6.4d GOES-8 channel 4 (inverted LIR) image of U.S. for 10/1745Z Apr 95 (Case 1)



○ NULL □ TRC □ LGT □ MDT-SVR
 △ TRC △ LGT △ MDT △ SVR

Figure 6.5 Composite plot of all PIREPs from 1500-2100Z on 10 Apr 95 (Case 1)

950410/1200 72562 LBF LIFT: 21 KINX: 3 SWET: 99 TOTL: 23
 CAPE: 0 CINS: 0 LFCV: 913 BRCH: 0

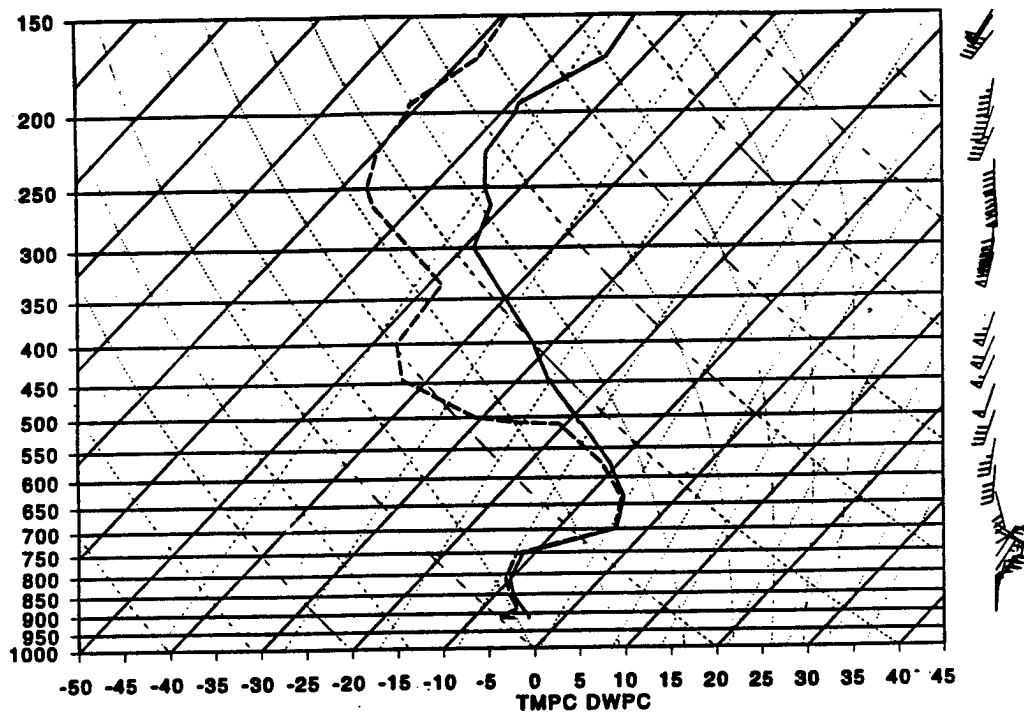


Figure 6.6 Skew-T, log-P diagram for North Platte, NE (LBF) at 10/1200Z Apr 95 (Case 1)

950410/1200 72451 DDC LIFT: 19 KINX: 7 SWET: 122 TOTL: 25
 CAPE: 0 CINS: 0 LFCV: 914 BRCH: 0

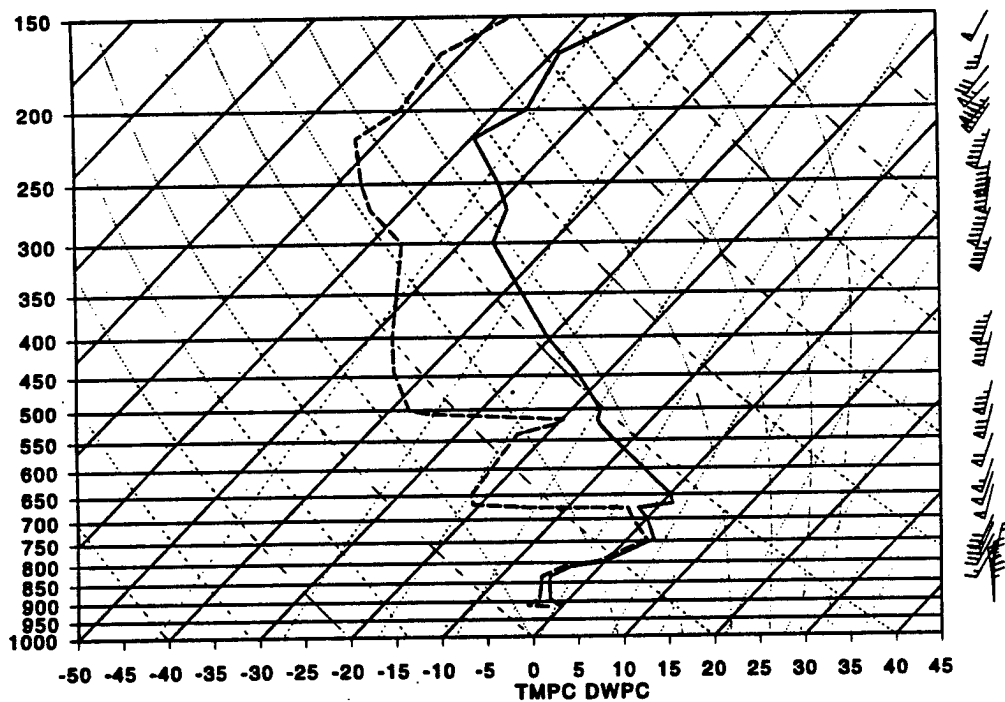


Figure 6.7 Skew-T, log-P diagram for Dodge City, KS (DDC) at 10/1200Z Apr 95 (Case 1)

Table 6.3a PIREPs for Case 2 (11 Apr 95 1500-2100Z)

													248 - 276K	
PIREPs			ICING (from PIREPs)							IZ - icing temp zone				
11 Apr 95					R-rime	C-clear	M-mix	N - Null			(deg C)	(0 - 100)	(deg K)	
Julian Day 101					(D)Null	(1-3)Lgt	(4-7)Mdt	I - Icing			Dual-Chan	Visible	Cld-Top	
	File Time	(# / 780)	(# / 1025)	O - 7	R-C-M	(100s of ft AGL)	M - Mdt+			IR Diff	Albedo	IR Temp		
	GMT (Z)	Y axis	X axis	Intens	Type	Base	Top			CH2-CH4	CH1	CH4		
								N	I	M		IZ		
1	15	500	230	3	R	130			x		27	45	x 255	
2		550	350	4	R	100	130		x	x	35	55	224	
3	V	610	570	5	M	170			x	x	15	49	242	
4		620	570	0		016		x			23	39	245	
5		510	530	5	M	040	050		x	x	14	52	236	
6		500	510	5	M	060	065		x	x	30	51	x 259	
7		500	490	3	R	050			x		36	53	x 261	
8		500	490	0		060	600	x			36	53	x 261	
9		450	490	3	M	030	050		x		41	40	x 263	
10		430	490	3	M	037			x		14	15	280	
11		410	530	4		040			x	x	31	51	x 267	
12		510	630	0		150		x			26	46	240	
13		610	710	0		068	600	x			25	50	x 248	
14		610	710	1	R	018	063		x		25	50	x 248	
15		600	850	6	R	130	150		x	x	24	49	x 262	
16		510	770	3	R	205	215		x		16	51	238	
17	16	500	450	3	R	054	070		x		35	52	x 257	
18		500	450	4	M	029			x	x	35	52	x 257	
19	V	500	490	0		024	600	x			36	53	x 261	
20		510	530	3	R	040	060		x		14	52	236	
21		520	530	3	R	110	120		x		20	56	233	
22		470	510	3	R	030			x		34	46	x 261	
23		430	530	3	M	035	040		x		31	44	x 271	
24		610	710	1	R	020	070		x		25	50	x 248	
25		500	750	3	R				x		13	50	244	
26		490	770	3	R	150			x		26	52	x 249	
27		460	770	5	R	140	160		x	x	14	46	241	
28		450	770	3	C	100			x		17	41	235	
29		450	770	4	M	090			x	x	17	41	235	
30		460	810	3	M	110	130		x		13	41	239	
31	17	530	250	3	R	140			x		12	14	289	
32		530	250	0		120		x			12	14	289	
33	V	500	250	0		100		x			22	40	x 263	
34		500	230	0		160		x			27	45	x 255	
35		500	210	0		140		x			21	38	x 258	
36		510	230	0		200		x			33	19	x 265	
37		620	570	0		014		x			23	39	245	
38		500	410	3	R	095			x		40	46	x 254	
39		430	410	0		290	600	x			11	11	280	
40		470	510	4	R	030			x	x	34	46	x 261	
41		470	530	3	M	024	046		x		19	42	239	
42		470	550	3	M	070			x		17	43	x 257	
43		430	530	3	R	035	045		x		31	44	x 271	
44		440	570	3	R	140			x		18	57	240	
45		400	590	5	R	130	160		x	x	9	54	x 257	
46		470	630	0		060		x			21	56	240	
47		560	670	3		150	160		x		26	47	224	
48		580	630	3	R	140			x		28	48	235	
49		600	650	1	R	040	055		x		35	50	x 251	
50		600	710	5			040		x	x	37	51	x 252	

Table 6.3b PIREPs for Case 2 (11 Apr 95 1500-2100Z)

										248 - 276K		
PIREPs		ICING (from PIREPs)						IZ - icing temp zone				
11 Apr 95								N - Null		(deg C)	(0 - 100)	(deg K)
Julian Day 101								I - Icing		Dual-Chan	Visible	Cld-Top
File Time	(# / 780)	(# / 1025)	O - 7	R-C-M	(100s of ft AGL)	M - Mdt+	IR Diff	Albedo	IR Temp			
GMT (Z)	Y axis	X axis	Intens	Type	Base	Top				CH2-CH4	CH1	CH4
							N	I	M			IZ
51	17 cont	610	850	0		042	x			33	54	x 250
52		610	850	0		080	x			33	54	x 250
53	V	510	710	3	M	130		x		31	55	x 249
54		490	710	3	C	130		x		27	56	225
55		530	810	6	R	195		x	x	42	51	244
56	18	520	230	3	R	150		x		14	16	284
57		500	210	0		140	x			21	38	x 258
58	V	500	250	1		160		x		22	40	x 263
59		470	230	3	R	080	170	x		8	51	x 250
60		470	230	3	R	160	210	x		8	51	x 250
61		470	230	3	R	180	245	x		8	51	x 250
62		470	190	0		200	600	x		29	40	x 249
63		440	130	0		150		x		7	47	x 267
64		440	130	0		160		x		7	47	x 267
65		600	450	0		040		x		15	41	236
66		580	490	3	R	120			x	17	51	229
67		570	550	0		050		x		27	51	222
68		500	370	1	R	090	130		x	35	52	x 252
69		500	450	3	M	070	110		x	35	52	x 257
70		500	470	4	C	120			x	40	48	x 261
71		500	470	0		220	600	x		40	48	x 261
72		500	490	1	R	060			x	36	53	x 261
73		500	490	0		075	600	x		36	53	x 261
74		460	330	0		110		x		32	25	x 264
75		470	530	0		130		x		19	42	239
76		620	690	5	R	070			x	37	48	227
77		610	710	5	R	150			x	25	50	x 248
78		580	650	3	R		030		x	29	48	225
79		560	670	0		100		x		26	47	224
80		560	710	3	R	022	130		x	27	30	x 254
81		570	770	0		033	600	x		28	32	x 266
82		530	770	0		080		x		15	52	241
83		490	670	3	C	070			x	26	54	231
84		470	690	5	M	120	145		x	28	57	223
85		500	770	0		050		x		16	52	236
86		490	770	0		075		x		26	52	x 249
87		400	950	0		074	600	x		27	61	x 261
88	19	470	130	3	R	130	160		x	38	24	x 260
89		500	230	0		090		x		27	45	x 255
90	V	480	270	3	R	150	180		x	8	54	246
91		480	270	3	R	090			x	8	54	246
92		490	290	3	R	140			x	18	50	235
93		470	330	0		090		x		6	36	x 253
94		500	370	0		020	142	x		35	52	x 252
95		510	470	3	R	025			x	30	52	x 262
96		510	470	0		080	600	x		30	52	x 262
97		510	530	3			067		x	14	52	236
98		540	650	4	M	120	130		x	27	53	223
99		490	550	5	M	060			x	5	52	244
100		440	530	3	C	045			x	33	42	x 266

Table 6.3c PIREPs for Case 2 (11 Apr 95 1500-2100Z)

													248 - 276K	
PIREPs				ICING (from PIREPs)						IZ - icing temp zone				
11 Apr 95				R-time	C-clear	M-mix	N - Null			(deg C)	(0 - 100)	(deg K)		
Julian Day 101				(O)Null	(1-3)Lgt	(4-7)Mdt	I - Icing			Dual-Chan	Visible	Cld-Top		
File Time	(# / 780)	(# / 1025)	O - 7	R-C-M	(100s of ft AGL)		M - Mdt+			IR Diff	Albedo	IR Temp		
GMT (Z)	Y axis	X axis	Intens	Type	Base	Top				CH2-CH4	CH1	CH4		
							N	I	M			IZ		
101	19 cont	440	530	0		060	600	x			33	42	x 266	
102	I	440	570	0		060	600	x			18	57	240	
103	V	410	650	4	R	130	140		x	x	23	58	x 253	
104		600	850	1		080			x		24	49	x 262	
105		560	770	1	M	120			x		13	18	x 263	
106		530	790	4	M	100	140		x	x	15	46	243	
107		490	770	0		050		x			26	52	x 249	
108		510	830	5		230	250		x	x	28	47	226	
109		510	910	5	R	150	170		x	x	34	14	x 260	
110		400	850	6		070			x	x	12	54	241	
111	20	490	270	0		110		x			20	48	232	
112	I	590	530	0		110		x			18	51	228	
113	V	620	570	1	M	020			x		23	39	245	
114		560	490	4	C	090			x	x	28	50	228	
115		530	530	0		070		x			22	55	231	
116		510	490	3	R	070			x		31	39	x 265	
117		490	450	4	R	050			x	x	42	44	x 259	
118		500	490	5	R	045	065		x	x	36	53	x 261	
119		510	530	5	R	028			x	x	14	52	236	
120		430	490	0		080	600	x			14	15	280	
121		620	790	3	C	030			x		25	52	x 254	
122		580	650	1	C	027	038		x		29	48	225	
123		580	650	0		085		x			29	48	225	
124		560	650	3	R	120	130		x		39	51	221	
125		530	710	5	R	145	155		x	x	15	49	243	
126		520	670	3	R	100			x		33	55	220	
127		480	650	0		190		x			27	54	236	
128		430	670	5	M	145	160		x	x	22	46	x 251	
129		560	790	0		160		x			18	14	x 271	
130		520	730	5	M	140			x	x	19	46	241	
131		520	730	3	M	160			x		19	46	241	
132		520	790	5	R	270			x	x	10	56	240	
133		520	810	0		110		x			28	55	234	
134		610	930	0		032		x			30	49	237	
135		490	890	5	M	140			x	x	22	21	x 249	
136	21	450	170	0		170	600	x			5	28	x 271	
137	I	600	450	3	R	070			x		15	41	236	
138	V	610	570	3		040	084		x		15	49	242	
139		570	530	3	C		050		x		32	54	222	
140		490	410	0		170	600	x			42	38	x 253	
141		470	430	4	M	060	100		x	x	39	27	x 255	
142		610	690	5	R	004	040		x	x	33	50	240	
143		570	590	3	M	144			x		24	53	225	
144		570	690	3	R	125	130		x		26	47	232	
145		530	530	0		060	600	x			22	55	231	
146		540	630	0		080		x			22	49	232	
147		540	670	3	M	140	150		x		37	52	220	
148		480	550	3	M	070			x		14	49	246	
149		470	550	5	M	075			x	x	17	43	x 257	
150		420	530	0		050		x			29	44	x 267	

Table 6.3d PIREPs for Case 2 (11 Apr 95 1500-2100Z)

--	--	--	--	--	--	--	--	--	--	--	--	--	--	--	--	--	--	--	--	--	--	--	--	--	--	--	--	--	--	--	--	--	--	--	--	--	--	--	--	--	--	--	--	--	--	--	--	--	--	--	--	--	--	--	--	--	--	--	--	--	--	--	--	--	--	--	--	--	--	--	--	--	--	--	--	--	--	--	--	--	--	--	--	--	--	--	--	--	--	--	--	--	--	--	--	--	--	--	--	--	--	--	--	--	--	--	--	--	--	--	--	--	--	--	--	--	--	--	--	--	--	--	--	--	--	--	--	--	--	--	--	--	--	--	--	--	--	--	--	--	--	--	--	--	--	--	--	--	--	--	--	--	--	--	--	--	--	--	--	--	--	--	--	--	--	--	--	--	--	--	--	--	--	--	--	--	--	--	--	--	--	--	--	--	--	--	--	--	--	--	--	--	--	--	--	--	--	--	--	--	--	--	--	--	--	--	--	--	--	--	--	--	--	--	--	--	--	--	--	--	--	--	--	--	--	--	--	--	--	--	--	--	--	--	--	--	--	--	--	--	--	--	--	--	--	--	--	--	--	--	--	--	--	--	--	--	--	--	--	--	--	--	--	--	--	--	--	--	--	--	--	--	--	--	--	--	--	--	--	--	--	--	--	--	--	--	--	--	--	--	--	--	--	--	--	--	--	--	--	--	--	--	--	--	--	--	--	--	--	--	--	--	--	--	--	--	--	--	--	--	--	--	--	--	--	--	--	--	--	--	--	--	--	--	--	--	--	--	--	--	--	--	--	--	--	--	--	--	--	--	--	--	--	--	--	--	--	--	--	--	--	--	--	--	--	--	--	--	--	--	--	--	--	--	--	--	--	--	--	--	--	--	--	--	--	--	--	--	--	--	--	--	--	--	--	--	--	--	--	--	--	--	--	--	--	--	--	--	--	--	--	--	--	--	--	--	--	--	--	--	--	--	--	--	--	--	--	--	--	--	--	--	--	--	--	--	--	--	--	--	--	--	--	--	--	--	--	--	--	--	--	--	--	--	--	--	--	--	--	--	--	--	--	--	--	--	--	--	--	--	--	--	--	--	--	--	--	--	--	--	--	--	--	--	--	--	--	--	--	--	--	--	--	--	--	--	--	--	--	--	--	--	--	--	--	--	--	--	--	--	--	--	--	--	--	--	--	--	--	--	--	--	--	--	--	--	--	--	--	--	--	--	--	--	--	--	--	--	--	--	--	--	--	--	--	--	--	--	--	--	--	--	--	--	--	--	--	--	--	--	--	--	--	--	--	--	--	--	--	--	--	--	--	--	--	--	--	--	--	--	--	--	--	--	--	--	--	--	--	--	--	--	--	--	--	--	--	--	--	--	--	--	--	--	--	--	--	--	--	--	--	--	--	--	--	--	--	--	--	--	--	--	--	--	--	--	--	--	--	--	--	--	--	--	--	--	--	--	--	--	--	--	--	--	--	--	--	--	--	--	--	--	--	--	--	--	--	--	--	--	--	--	--	--	--	--	--	--	--	--	--	--	--	--	--	--	--	--	--	--	--	--	--	--	--	--	--	--	--	--	--	--	--	--	--	--	--	--	--	--	--	--	--	--	--	--	--	--	--	--	--	--	--	--	--	--	--	--	--	--	--	--	--	--	--	--	--	--	--	--	--	--	--	--	--	--	--	--	--	--	--	--	--	--	--	--	--	--	--	--	--	--	--	--	--	--	--	--	--	--	--	--	--	--	--	--	--	--	--	--	--	--	--	--	--	--	--	--	--	--	--	--	--	--	--	--	--	--	--	--	--	--	--	--	--	--	--	--	--	--	--	--	--	--	--	--	--	--	--	--	--	--	--	--	--	--	--	--	--	--	--	--	--	--	--	--	--	--	--	--	--	--	--	--	--	--	--	--	--	--	--	--	--	--	--	--	--	--	--	--	--	--	--	--	--	--	--	--	--	--	--	--	--	--	--	--	--	--	--	--	--	--	--	--	--	--	--	--	--	--	--	--	--	--	--	--	--	--	--	--	--	--	--	--	--	--	--	--	--	--	--	--	--	--	--	--	--	--	--	--	--	--	--	--	--	--	--	--	--	--	--	--	--	--	--	--	--	--	--	--	--	--	--	--	--	--	--	--	--	--	--	--	--	--	--	--	--	--	--	--	--	--	--	--	--	--	--	--	--	--	--	--	--	--	--	--	--	--	--	--	--	--	--	--	--	--	--	--	--	--	--	--	--	--	--	--	--	--	--	--	--	--	--	--	--	--	--	--	--	--	--	--	--	--	--	--	--	--	--	--	--	--	--	--	--	--	--	--	--	--	--	--	--	--	--	--	--	--	--	--	--	--	--	--	--	--	--	--	--	--	--	--	--	--	--	--	--	--	--	--	--	--	--	--	--	--	--	--	--	--	--	--	--	--	--	--	--	--	--	--	--	--	--	--	--	--	--	--	--	--	--	--	--	--	--	--	--	--	--	--	--	--	--	--	--	--	--	--	--	--	--	--	--	--	--	--	--	--	--	--	--	--	--	--	--	--	--	--	--	--	--	--	--	--	--	--	--	--	--	--	--	--	--	--	--	--	--	--	--	--	--	--	--	--	--	--	--	--	--	--	--	--	--	--	--	--	--	--	--	--	--	--	--	--	--	--	--	--	--	--	--	--	--	--	--	--	--	--	--	--	--	--	--	--	--	--	--	--	--	--	--	--	--	--	--	--	--	--	--	--	--	--	--	--	--	--	--	--	--	--	--	--	--	--	--	--	--	--	--	--	--	--	--	--	--	--	--	--	--	--	--	--	--	--	--	--	--	--	--	--	--	--	--	--	--	--	--	--	--	--	--	--	--	--	--	--	--	--	--	--	--	--	--	--	--	--	--	--	--	--	--	--	--	--	--	--	--	--	--	--	--	--	--	--	--	--	--	--	--	--	--	--	--	--	--	--	--	--	--	--	--	--	--	--	--	--	--	--	--	--	--	--	--	--	--	--	--	--	--	--	--	--	--	--	--	--	--	--	--	--	--	--	--	--	--	--	--	--	--	--	--	--	--	--	--	--	--	--	--	--	--	--	--	--	--	--	--	--	--	--	--	--	--	--	--	--	--	--	--	--	--	--	--

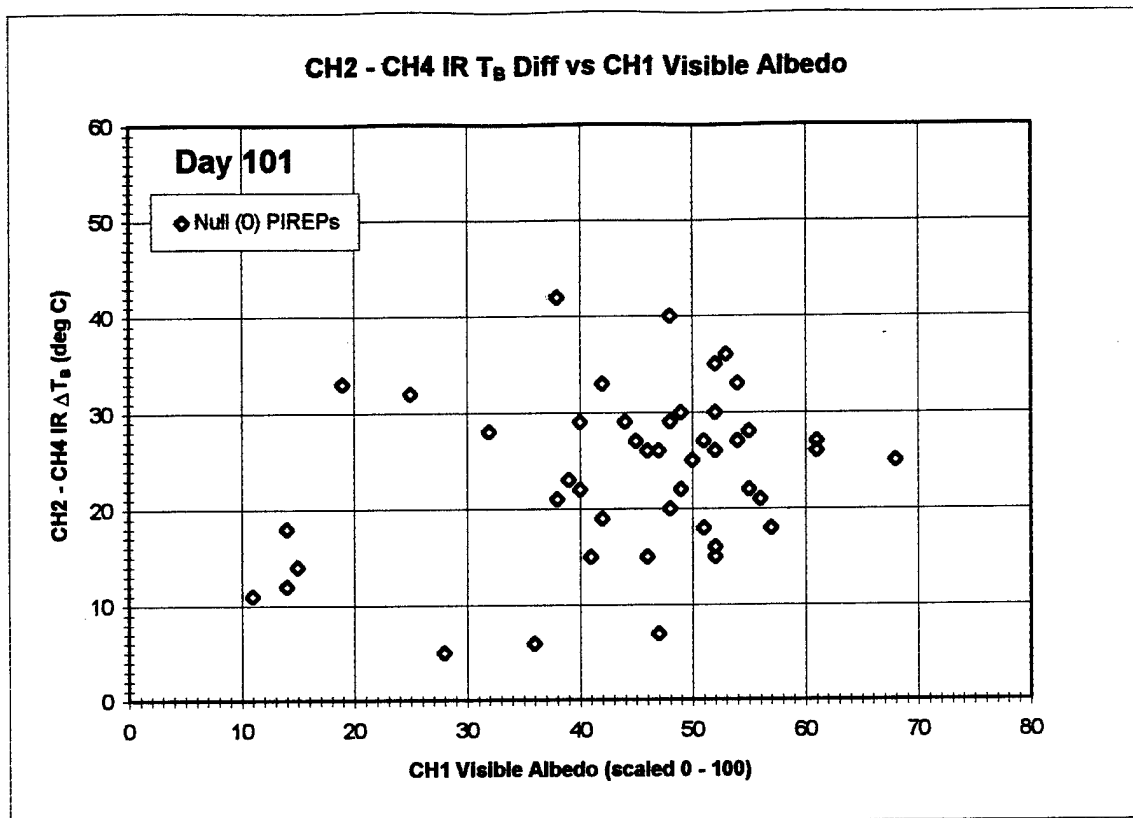


Figure 6.8a Scatter plot of null (0 intensity - no icing) PIREPs (Case 2)

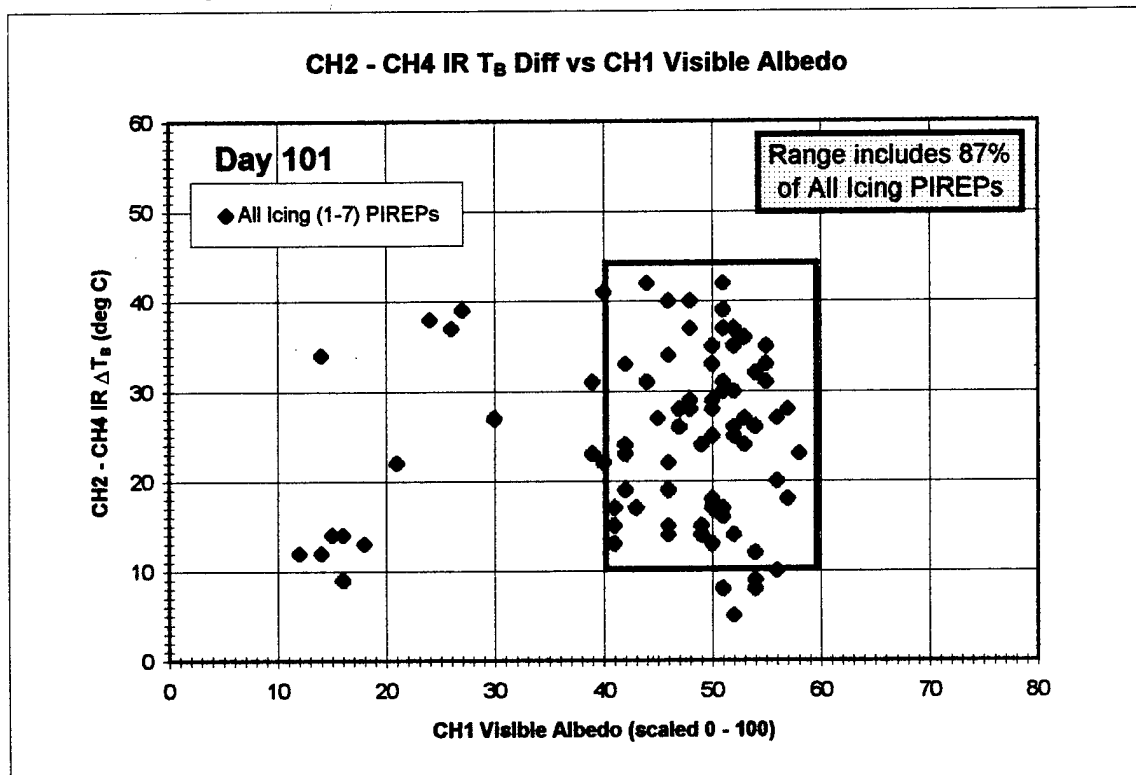


Figure 6.8b Scatter plot of all icing (1-7 intensity) PIREPs (Case 2)

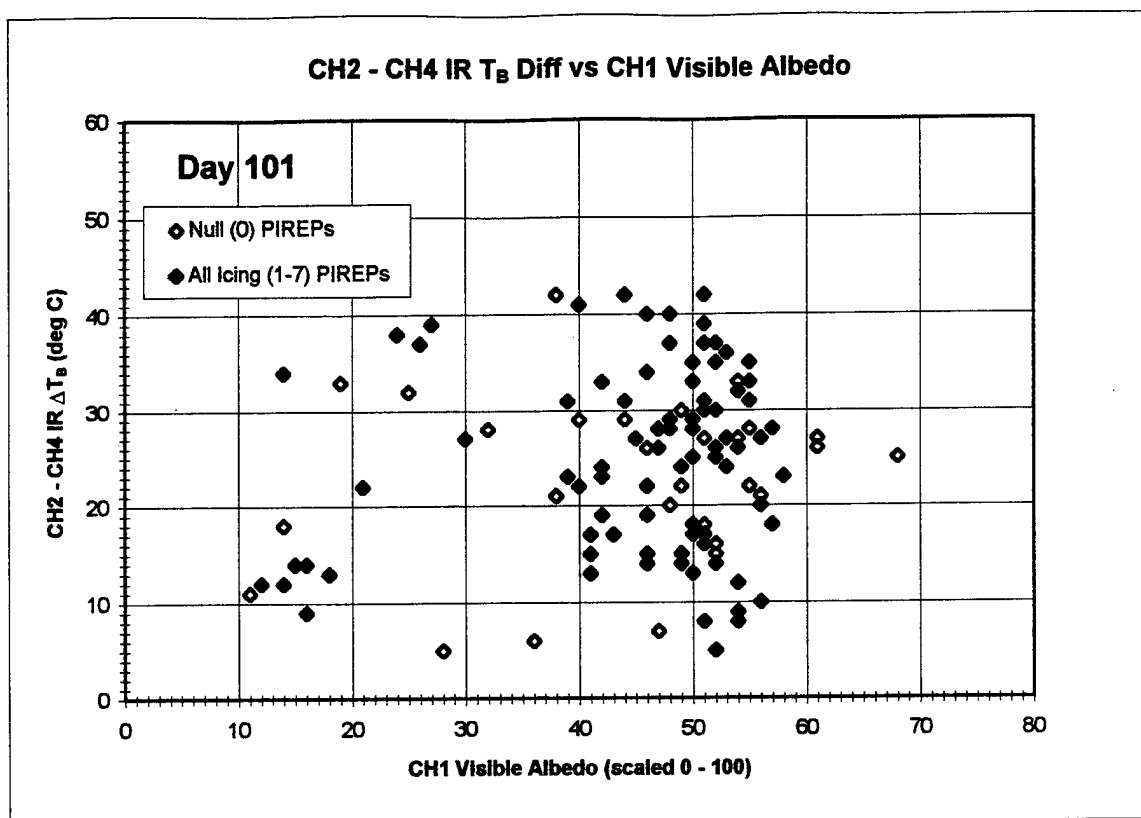


Figure 6.8c Scatter plot of null and all icing PIREPs (Case 2)

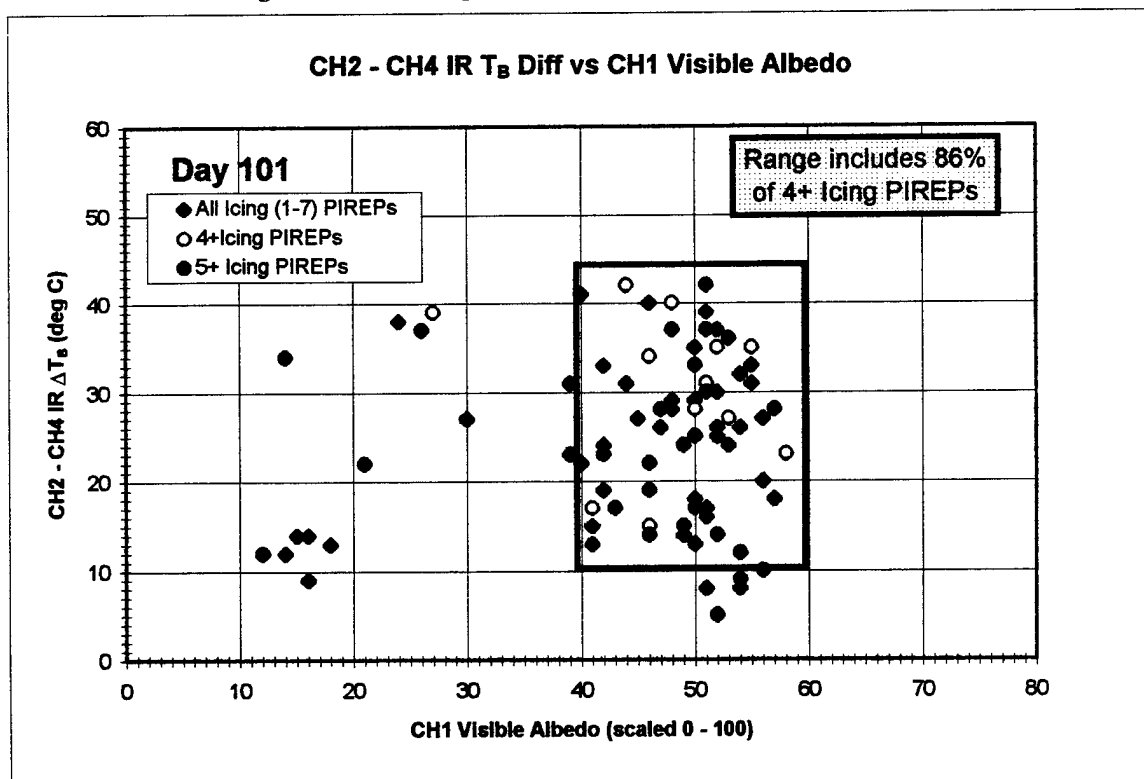


Figure 6.8d Scatter plot of all, moderate or greater (4+), and extreme (5+) icing PIREPs (Case 2)

Table 6.4a Grid of pixel dump values for Case 2 from 1745Z imagery

		11 / 1745Z Apr 95																Pixel Dump T _b Value (E-W for pixel number out of 1025)																	
GOES-8		IDL > qview																(deg C)																	
CHANNEL 2		130	150	170	180	210	230	250	270	280	310	330	350	370	390	410	430	450	470	490	510	530	550												
	620														19	22	20	18	0	9	-13	-15	-4												
	610														22	22	10	-15	-14	-20	-16	-17	-14												
	600														20	-9	-24	-22	-16	-18	-23	-21	-27												
	590														-8	-26	-18	-12	-16	-21	-28	-27	-21												
	580														-15	-8	-16	-20	-24	-27	-25	-22	-23												
	570														-20	-10	-10	-13	-18	-22	-24	-19	-24												
	560														-14	-14	-16	-11	-7	-17	-20	-13	-25												
	550														13	26	19	22	-2	-15	-20	-19	-22												
	540														14	17	25	16	-7	1	-18	-15	-20												
	530														22	20	23	12	0	-15	-23	-20	-19												
	520														22	20	24	25	18	-8	-2	-20	-16												
	510														27	21	24	25	19	23	-12	-23	-26												
	500														24	26	18	25	19	28	24	16	-17	-19											
	490														23	21	22	28	26	26	2	-8	-24												
	480														16	21	22	28	27	29	16	12	-13												
	470														21	22	28	27	29	25	23	22	-15	1											
	460														25	24	24	28	31	27	25	17	-14												
	450														24	24	28	30	29	31	30	24	-14												
	440														27	26	29	22	23	24	28	26	-15												
	430														13	16	16	22	20	21	26	29	23												
	420														14	17	18	17	18	24	27	23	27												
	410														17	17	21	17	18	24	27	23	27												
	400														22	22	20	20	20	21	29	25	24												
															18	21	22	21	20	21	29	27	29												

Table 6.4b Grid of pixel dump values for Case 2 from 1745Z imagery

[illegible]

Table 6.4c Grid of pixel dump values for Case 2 from 1745Z imagery

[illegible]

Table 6.4d Grid of pixel dump values for Case 2 from 1745Z imagery

GOES-8 CH2 - CH4		11 / 1745Z Apr 95										Channel Differenced Pixel Dump T _a Value (deg C)										Channel Differenced Pixel Dump T _a Value (E-W for pixel number out of 1025)									
		IDL > qview										(deg C)																			
		570	590	610	630	650	670	690	710	730	750	770	790	810	830	850	870	890	910	930	950										
(deg C) Pixel Dump T _a Value (N-S) (pixel number) (out of 780)	620	23	28	33	38	42	37	32	39	28	24	25	41	35	33	38	38	43	39	27											
	610	15	15	32	35	47	40	33	35	34	39	39	34	36	33	32	36	38	30	33											
	600	27	41	31	22	36	29	30	35	28	28	28	28	37	24	27	35	36	34	28											
	590	23	17	21	27	22	24	23	25	25	24	33	32	31	37	42	3	27	22	22											
	580	24	19	23	28	28	24	21	21	30	28	27	32	32	34	13	15	8	22	21											
	570	26	24	28	27	39	31	26	26	24	25	28	23	24	31	9	21	10	3	8											
	560	32	28	29	35	39	28	38	27	27	13	31	46	35	7	7	12	5	12	21											
	550	25	35	21	27	31	35	21	16	17	30	23	37	27	30	28	10	28	9	19											
	540	32	27	22	22	27	37	21	19	13	36	18	31	46	35	1	9	15	24	7											
	530	28	25	26	22	32	25	15	15	32	25	15	42	47	11	12	14	14	13	6											
	520	26	27	24	21	21	33	24	28	19	13	12	10	28	41	18	19	14	11	7											
	510	17	26	26	24	24	26	28	31	18	15	16	19	19	28	32	38	37	34	4											
	500	18	18	17	32	29	26	26	31	14	13	16	22	25	29	23	25	9	12	19											
	490	24	25	27	23	26	26	27	27	16	18	28	28	23	26	23	19	22	22	15											
	480	15	23	12	20	27	26	30	29	27	19	17	27	16	22	18	20	31	16	24											
470	22	18	27	21	28	25	28	25	21	19	17	27	18	17	23	22	23	16	29												
460	27	17	25	28	33	28	23	25	18	19	14	15	13	17	20	23	24	32	17												
450	15	49	15	29	28	18	30	32	27	19	17	19	17	16	20	28	26	38	20												
440	18	25	28	34	20	23	18	22	20	22	18	22	22	19	27	34	29	21	39												
430	15	19	16	34	25	22	21	25	24	23	17	16	21	24	28	27	31	23	11												
420	35	14	15	30	22	24	18	19	28	20	16	15	15	22	28	39	35	40	16												
410	37	10	36	28	23	20	20	21	22	25	20	19	19	20	32	29	35	23	32												
400	27	9	21	21	33	25	18	23	16	22	22	21	21	21	12	28	32	28	24												
GOES-8 CHANNEL 1	570	590	610	630	650	670	690	710	730	750	770	790	810	830	850	870	890	910	930	950											
	620	39	41	45	46	47	48	48	50	49	48	52	44	48	54	54	53	55	53	50											
	610	43	47	47	46	48	50	51	51	49	49	43	49	53	54	53	49	53	48	45											
	600	48	53	51	51	49	50	48	48	48	51	38	40	48	48	48	38	37	38	43											
	590	49	51	47	48	48	48	48	48	48	48	40	42	52	52	40	10	7	38	35											
	580	50	53	53	53	51	47	48	48	47	46	33	34	40	46	11	7	11	35	38											
	570	50	54	53	53	51	47	48	48	47	46	33	34	40	46	15	22	10	7	12											
	560	51	51	51	49	51	47	48	48	47	46	33	34	40	46	11	8	10	9	11											
	550	51	51	51	49	51	47	48	48	47	46	33	34	40	46	11	11	12	14	15											
	540	54	54	53	53	52	52	50	51	51	51	44	45	51	51	23	11	12	17	12											
	530	57	57	55	51	52	52	50	50	50	50	42	43	51	51	12	12	12	12	13											
	520	57	54	54	51	52	52	50	50	50	50	42	43	51	51	17	24	14	11	11											
	510	51	50	57	51	51	51	50	50	50	50	42	43	51	51	25	15	14	10	11											
	500	51	53	53	53	53	53	53	53	53	53	42	43	51	51	33	21	12	13	11											
	490	57	57	57	53	54	54	54	54	54	54	42	43	51	51	40	24	12	12	11											
480	57	57	57	53	54	54	54	54	54	54	42	43	51	51	47	24	12	12	11												
470	57	57	57	53	54	54	54	54	54	54	42	43	51	51	52	23	12	10	10												
460	61	59	58	55	56	56	56	56	56	56	42	43	51	51	56	40	14	20	10												
450	47	57	58	52	54	54	54	54	54	54	42	43	51	51	50	44	23	14	26												
440	57	58	58	52	54	54	54	54	54	54	42	43	51	51	50	44	23	14	26												
430	58	58	58	52	54	54	54	54	54	54	42	43	51	51	50	44	23	14	26												
420	58	58	58	52	54	54	54	54	54	54	42	43	51	51	50	44	23	14	26												
410	50	53	53	53	53	53	53	53	53	53	42	43	51	51	50	44	23	14	26												
400	50	53	53	53	53	53	53	53	53	53	42	43	51	51	50	44	23	14	26												

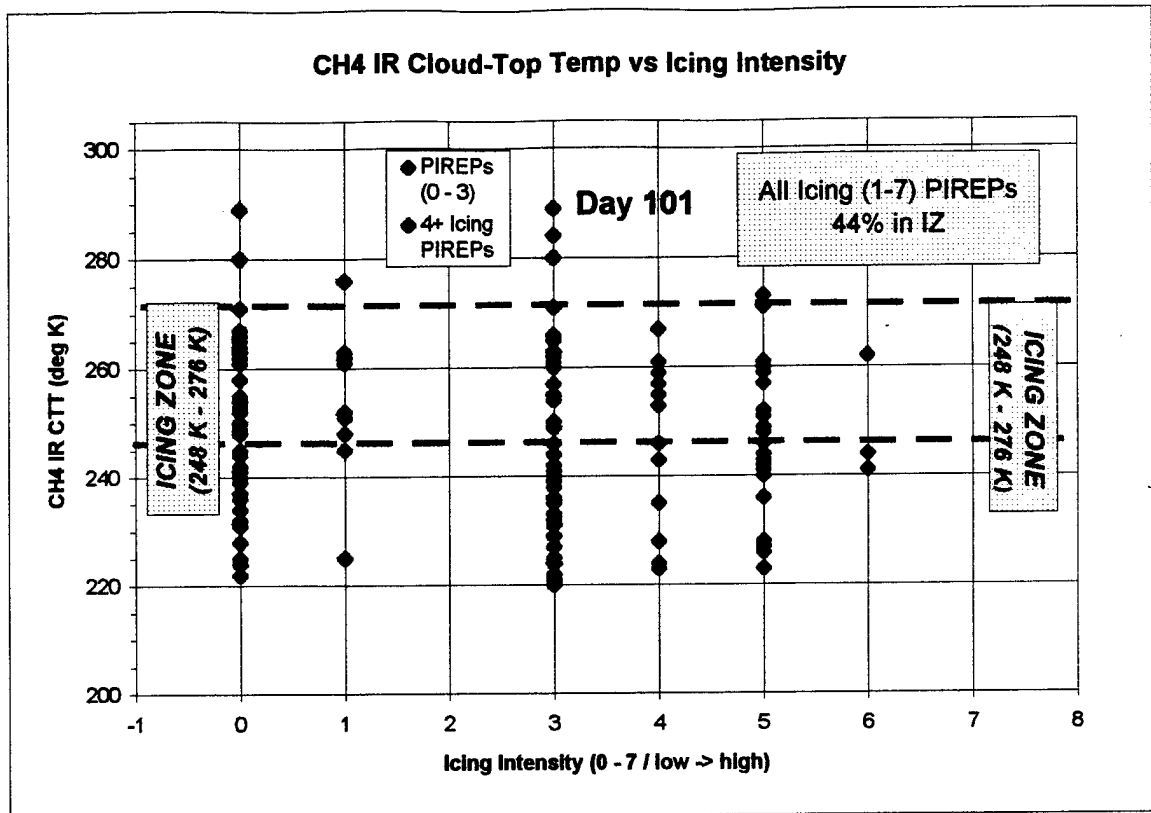


Figure 6.9a Scatter plot of all PIREPs (0-7 intensity) within the Icing Zone (IZ) (Case 2)

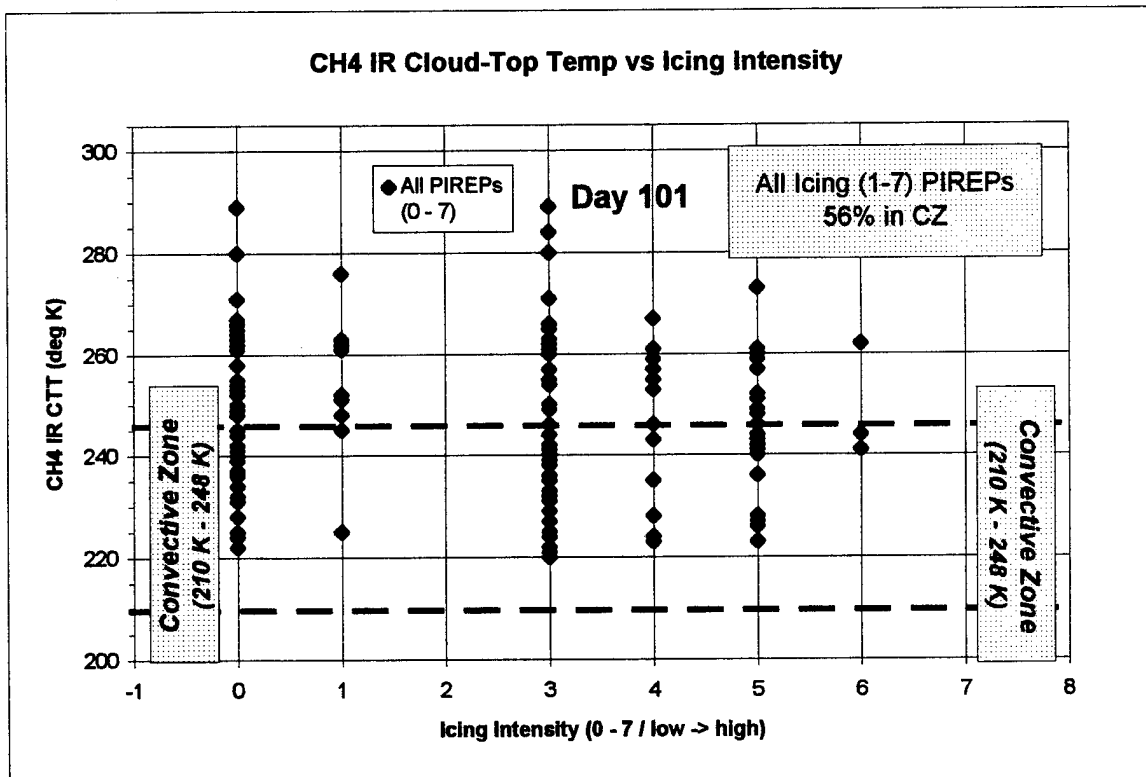


Figure 6.9b Scatter plot of all PIREPs within the Convective Zone (CZ) (Case 2)

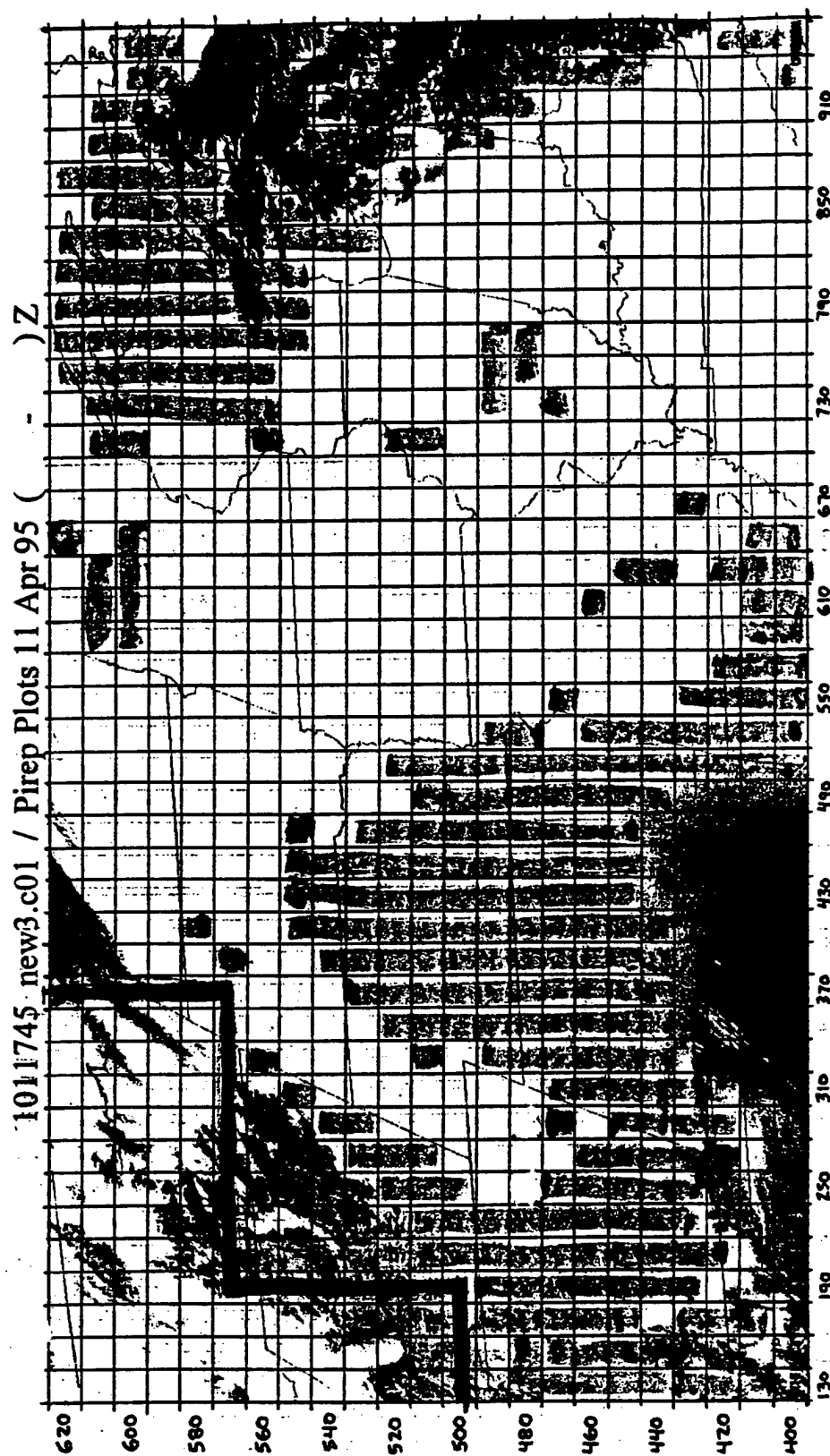


Figure 6.10 Grid showing shaded sectors representing stratiform cloud tops within IZ (Case 2)

GOES-8 CH1 11/1745Z Apr 95

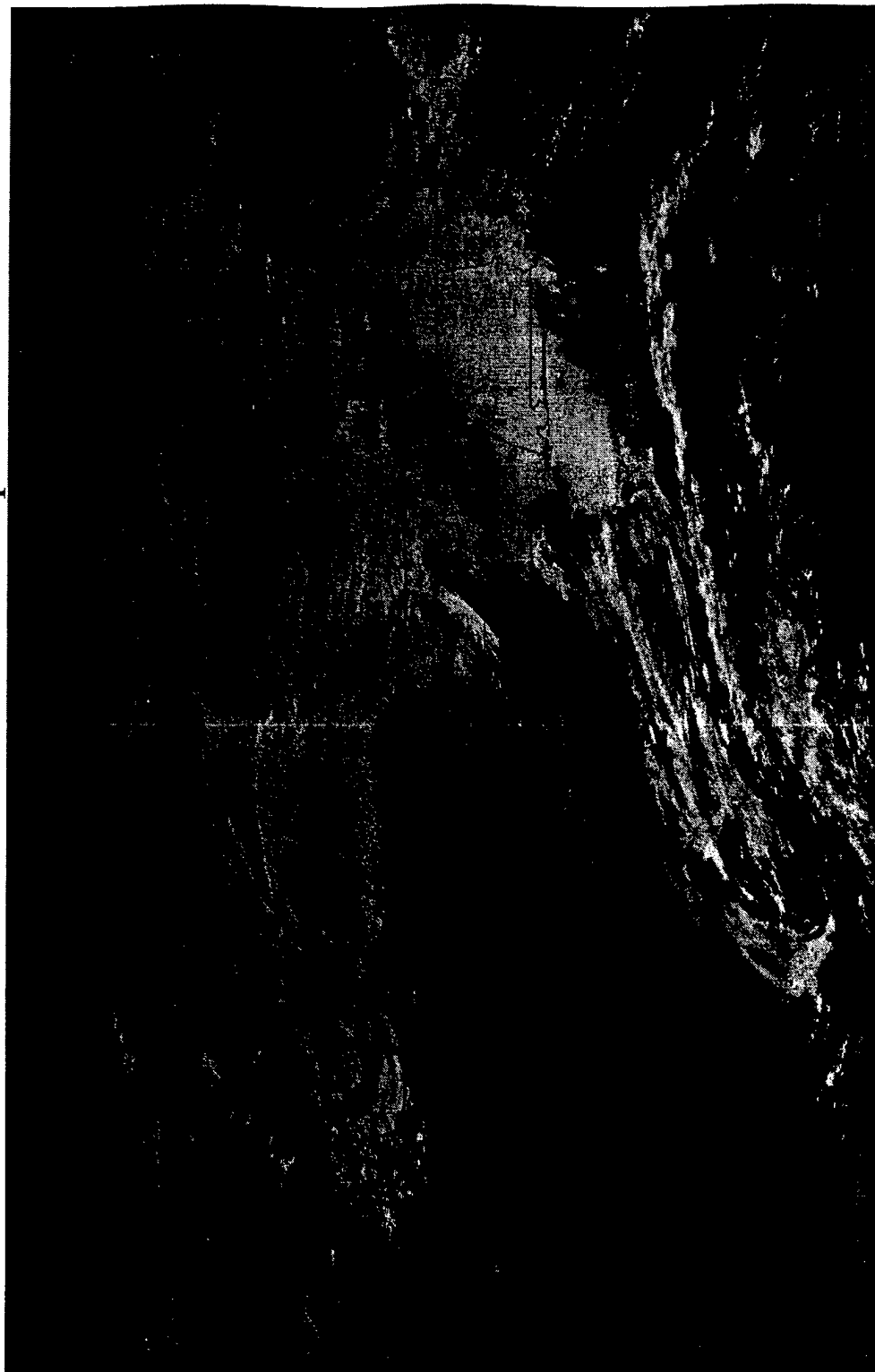


Figure 6.11a GOES-8 channel 1 (visible) image of U.S. for 11/1745Z Apr 95 (Case 2)

GOES-8 CH2 11/1745Z Apr 95

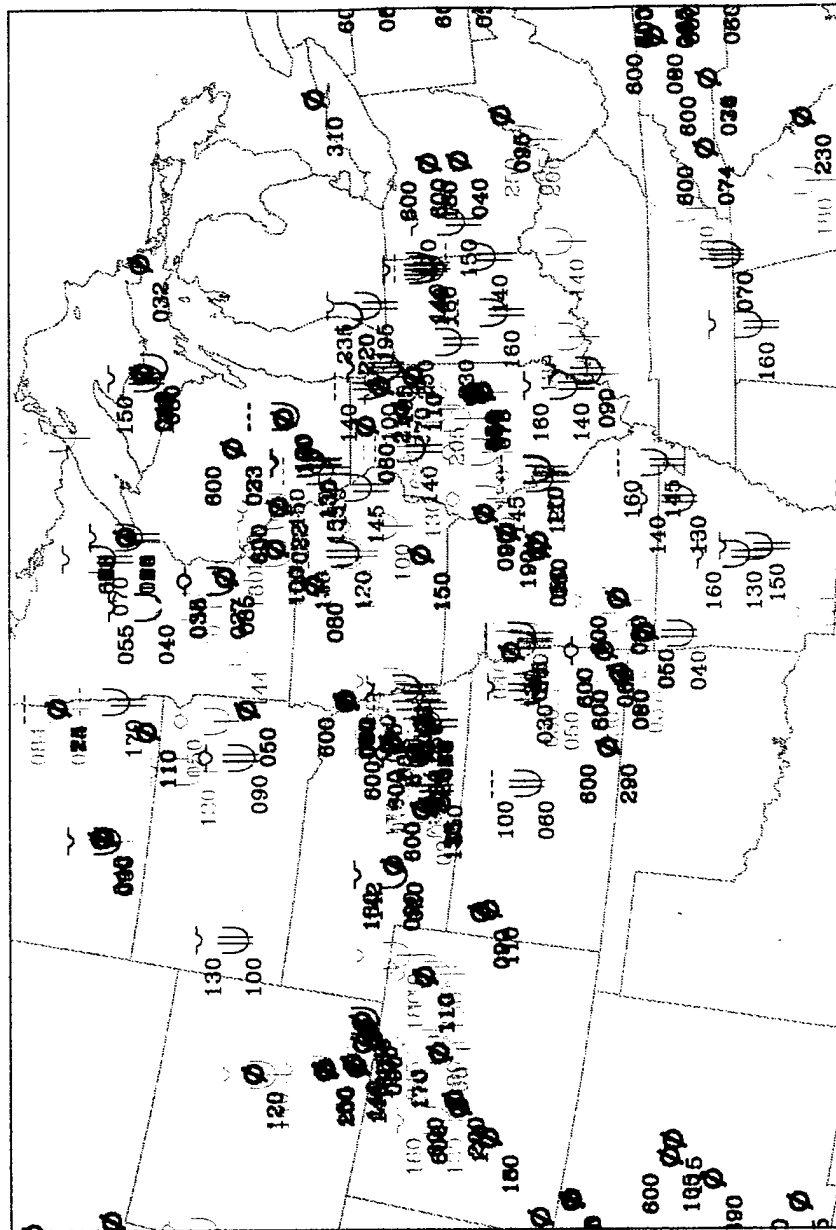


Figure 6.11b GOES-8 channel 2 (inverted SIR) image of U.S. for 11/1745Z Apr 95 (Case 2)

GOES-8 CH4 11/1745Z Apr 95



Figure 6.11c GOES-8 channel 4 (inverted LIR) image of U.S. for 11/1745Z Apr 95 (Case 2)



● NULL ⊕ TRC ⊕ LGT-MDT ⊕ MDT-SVR

⊕ TRC ⊕ LGT-MDT ⊕ MDT-SVR

Figure 6.12 Composite plot of all PIREPs from 1500-2100Z on 11 Aug 95 (Case 2)

950411/1200 72562 LBF LIFT: 15 KINX: 7 SWET: 80 TOTL: 35
 CAPE: 0 CINS: 0 LFCV: 910 BRCH: 0

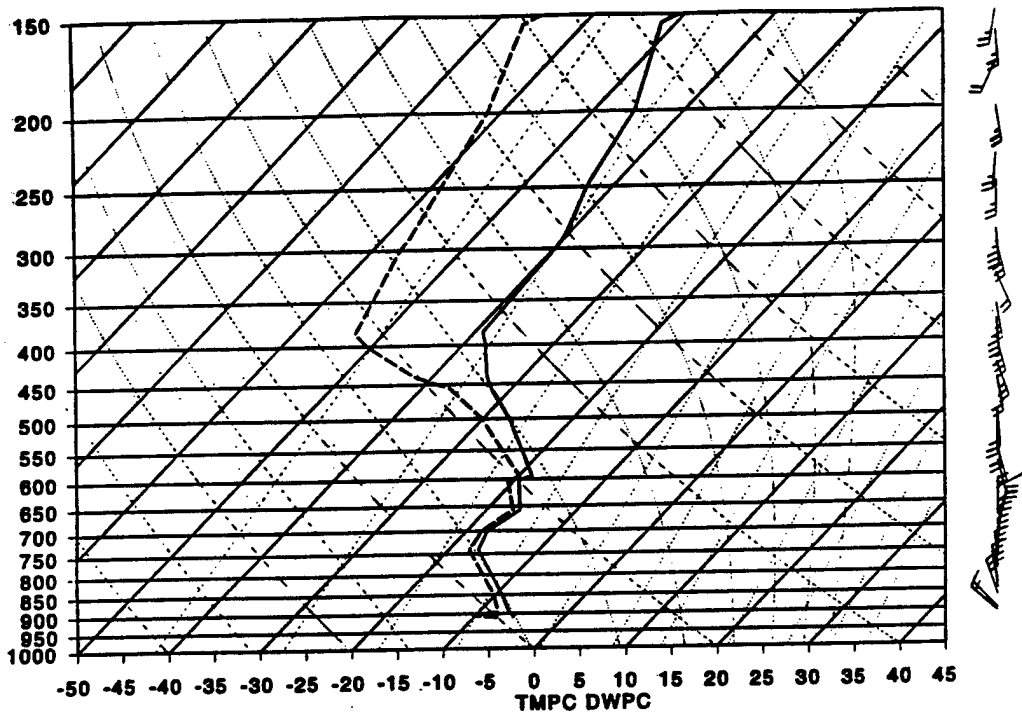


Figure 6.13 Skew-T, log-P diagram for North Platte, NE (LBF) at 11/1200Z Apr 95 (Case 2)

950411/1200 72558 OAX LIFT: 17 KINX: 19 SWET: 86 TOTL: 39
 CAPE: 0 CINS: 0 LFCV: 963 BRCH: 0

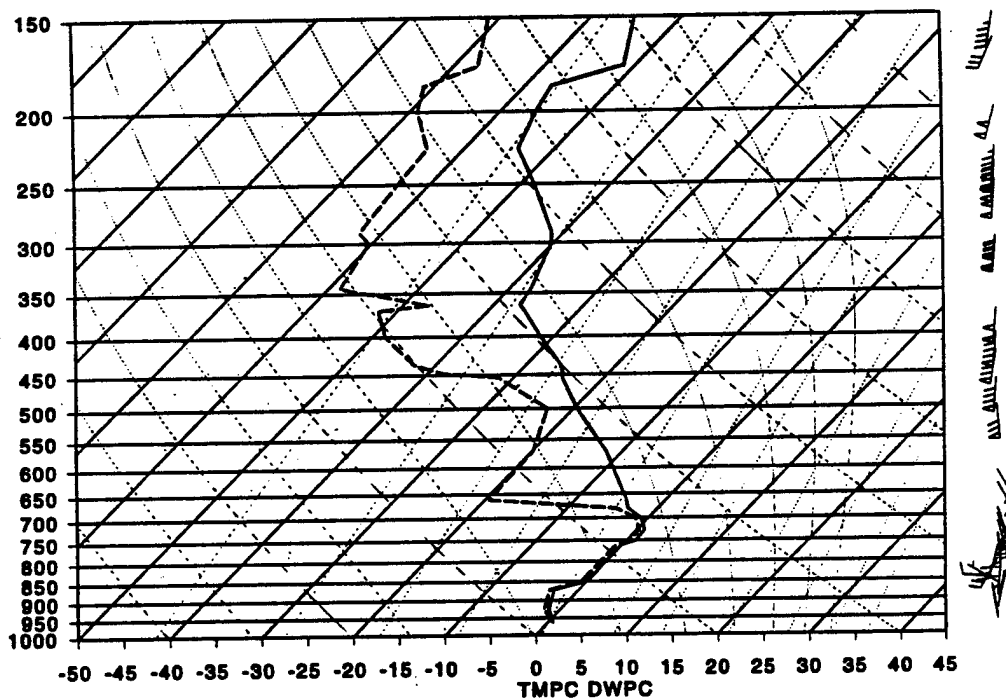


Figure 6.14 Skew-T, log-P diagram for Omaha, NE (OAX) at 11/1200Z Apr 95 (Case 2)

950411/1200 72458 TOP LIFT: 18 KINX: 12 SWET: 128 TOTL: 33
CAPE: 0 CINS: 0 LFCV: 972 BRCH: 0

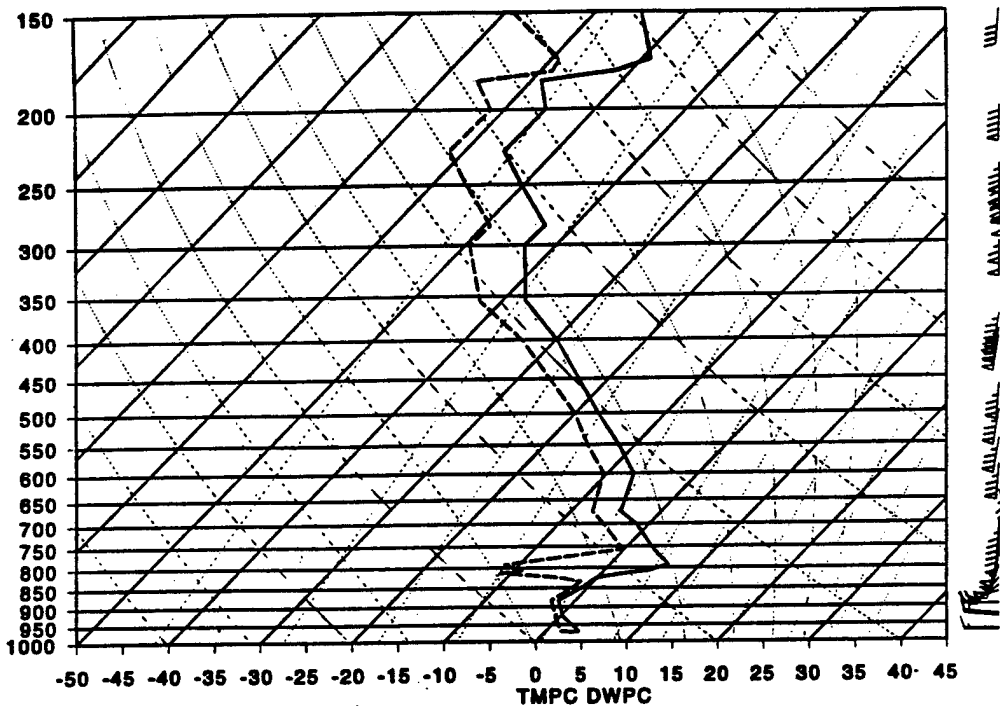


Figure 6.15a Skew-T, log-P diagram for Topeka, KS (TOP) at 11/1200Z Apr 95 (Case 2)

950411/1200 72489 DNR LIFT: 11 KINX: -9999 SWET: -9999 TOTL: -9999
CAPE: 0 CINS: 0 LFCV: 832 BRCH: 0

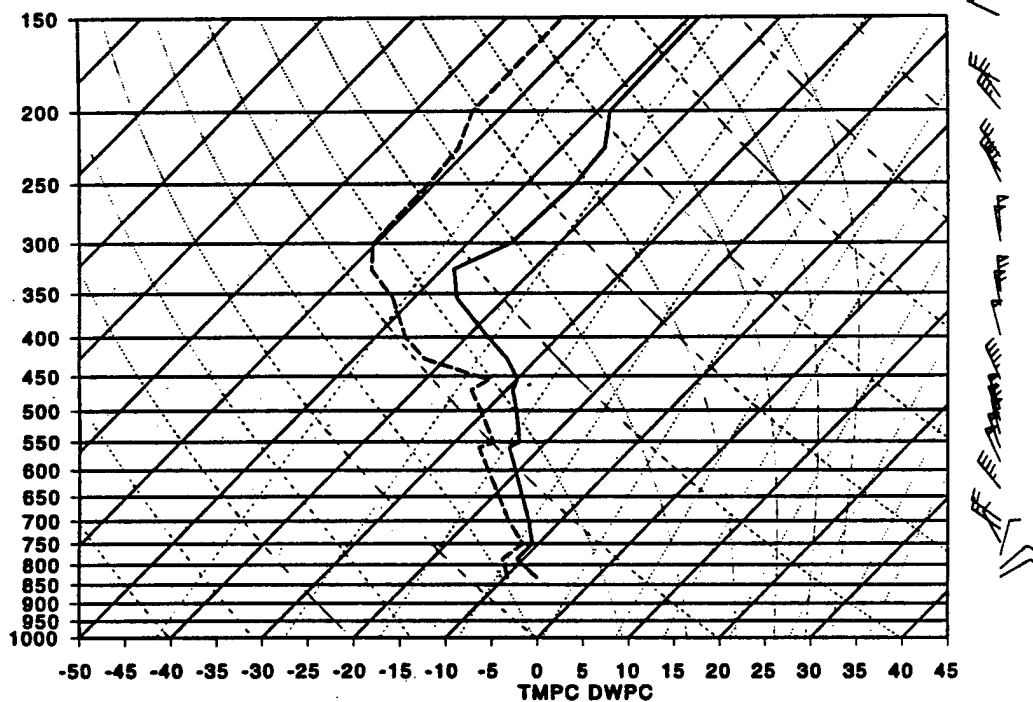


Figure 6.15b Skew-T, log-P diagram for Denver, CO (DNR) at 11/1200Z Apr 95 (Case 2)

950411/1200 72349 UMN LIFT: 16 KINX: 25 SWET: 178 TOTL: 42
 CAPE: 0 CINS: 0 LFCV: 957 BRCH: 0

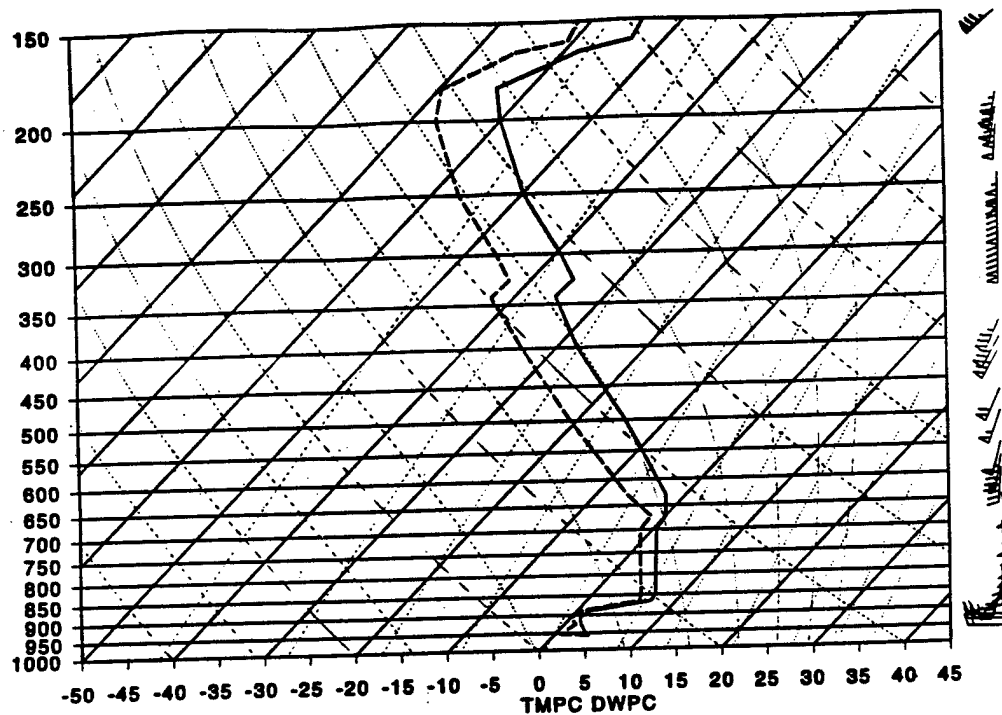


Figure 6.16 Skew-T, log-P diagram for Springfield, MO (UMN) at 11/1200Z Apr 95 (Case 2)

950411/1200 72645 GRB LIFT: 24 KINX: 16 SWET: 178 TOTL: 42
 CAPE: 0 CINS: 0 LFCV: 989 BRCH: 0

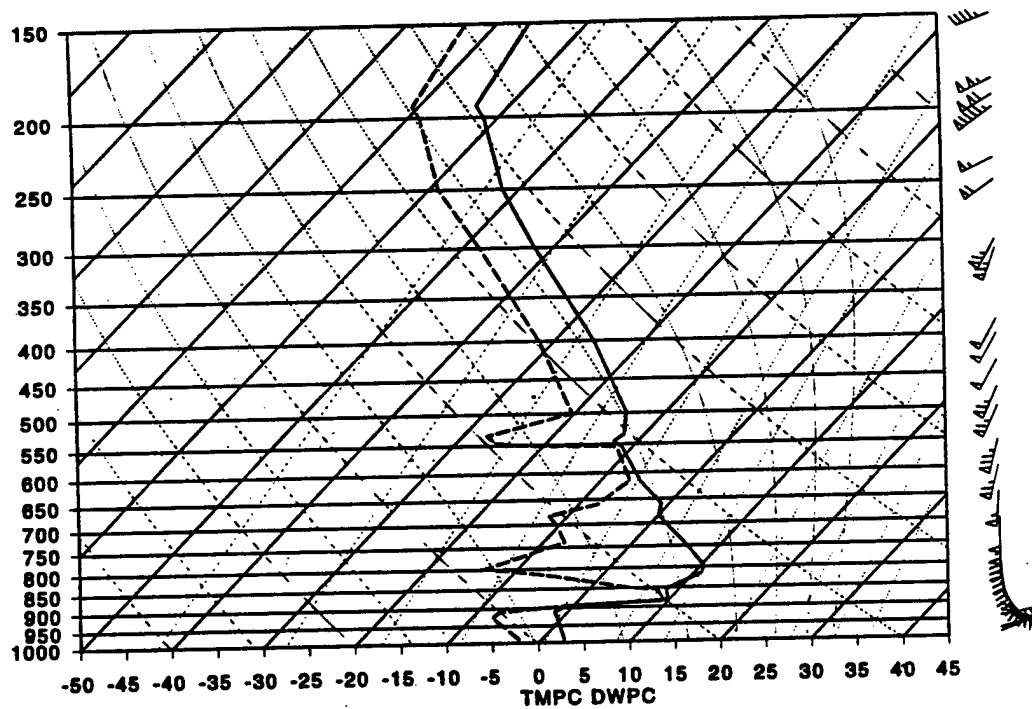


Figure 6.17 Skew-T, log-P diagram for Green Bay, WI (GRB) at 11/1200Z Apr 95 (Case 2)

MULTI -- 411



Figure 6.18 Multispectral RGB-411 imagery for 10/1815Z Apr 95

MULTI -- 241



Figure 6.19 Multispectral RGB-241 imagery for 10/1815Z Apr 95

REFERENCES

- Air Weather Service (AWS), 1980: *Forecaster's Guide on Aircraft Icing*. Air Weather Service AWS/TR-80/001, U.S. Air Force, Scott AFB, Illinois.
- Allen, Jr., R.C., P.A. Durkee, and C.H. Wash, 1990: Snow/cloud discrimination with multispectral satellite measurements. *J. Appl. Meteor.*, **29**, 994-1004.
- Andreadis, I. E. Glavas, and P. Tsalides, 1995: Image enhancement using colour information. *Int. J. Remote Sens.*, **16**, 2285-2289.
- Arking, A., and J.D. Childs, 1985: Retrieval of cloud cover parameters from multispectral satellite images. *J. Climate Appl. Meteor.*, **24**, 322-333.
- Bader, M.J., J.R. Grant, A.J. Waters, and G.J. Forbes, 1994: *Images in Weather Forecasting: A Practical Guide for Interpreting Satellite and Radar Imagery*. Cambridge University Press, New York, NY, 499 pp.
- Bain, M. and J.F. Gayet, 1982: Aircraft measurements of icing in supercooled and water droplet / ice crystal clouds. *J. Appl. Meteor.*, **21**, 631-641.
- Bellec, B., and H. Le Gleau, 1992: The multispectral colour-composite technique: An improved method to display meteorological satellite imagery. *Int. J. Remote Sens.*, **13**, 1981-1998.
- Brandes, E.A., J. Vivekanandan, J.D. Tuttle, and C.J. Kessinger, 1995: A study of thunderstorm microphysics with multiparameter radar and aircraft observations. *Mon. Wea. Rev.*, **123**, 3129-3143.
- Brimacombe, C.A., 1981: *Atlas of Meteosat Imagery*. European Space Agency (ESA) Scientific and Technical Publications, Noordwijk, Netherlands, 495 pp.
- Brown, B.G., and A.H. Murphy, 1996a: Verification of aircraft icing forecasts: The use of standard measures and meteorological covariates. *Thirteenth Conf. on Probability and Statistics in the Atmos. Sci.*, San Francisco, CA, 21-23 February, Amer. Meteor. Soc.
- , G. Thompson, R.T. Buintjes, R. Bullock, and T. Kane, 1996b: Intercomparison of in-flight icing algorithms. Part II: WISP94 Statistical verification results. Submitted to *Wea. Forecasting*.
- , R. Bullock, G. Thompson, and R.T. Buintjes, 1995a: WISP94 real-time icing prediction and evaluation program (WRIPEP): Statistical issues and forecast verification results. Preprints, *Sixth Conf. on Aviation Weather Systems*, Dallas, TX, Amer. Meteor. Soc., 207-212.
- , 1995b: Statistical climatology of icing events and forecasts over the continental United States. *Sixth Int'l Meeting on Statistical Climatology*, Galway, Ireland, 19-23 June.
- , T.L. Fowler, B.C. Bernstein, and G.S. Forbes, 1993: Use of pilot reports for verification of aircraft icing diagnoses and forecasts. Preprints, *Fifth Int'l Conf. of Aviation Weather Systems*, Vienna, VA, Amer. Meteor. Soc., 277-281.

- Bunting, J.T., and K.R. Hardy, 1984: Cloud identification and characterization from satellites. *Satellite Sensing of a Cloudy Atmosphere*, A. Henderson-Sellers, Ed., Taylor & Francis, Philadelphia, PA, 203-240.
- Cober, S.G., G.A. Isaac, and J.W. Strapp, 1995: Aircraft icing measurements in east coast winter storms. *J. Appl. Meteor.*, **34**, 88-100.
- Cole, J. and W.R. Sand, 1991: Statistical study of aircraft icing accidents. Preprints, *29th Aerospace Sciences Meeting*, Reno, NV, 7-10 January. Amer. Inst. Aero. and Astron., Washington, D.C., AIAA-91-0558.
- Colwell, R.N. (editor), 1983: *Manual of Remote Sensing*, Second Edition, 2 Vols, Falls Church, VA, American Society of Photogrammetry, 2400 pp.
- Cooper, W.A., W.R. Sand, M.K. Politovich, and D.L. Veal, 1984: Effects of icing on performance of a research airplane. *J. Aircraft*, **21**, 708-715.
- Crosiar, C., T.F. Lee, and A. Caughey, 1989: Nighttime cloud classification using two infrared channels of the AVHRR. Preprints, *Twelfth Conf. On Wea. Anal. and Forecasting*, Amer. Meteor. Soc., 521-523.
- Curry, J.A., and G. Liu, 1992: Assessment of aircraft icing potential using satellite data. *J. Appl. Meteor.*, **31**, 605-621.
- d'Entremont, R.P., and L.W. Thomason, 1987: Interpreting meteorological satellite images using a color-composite technique. *Bull. Amer. Meteor. Soc.*, **68**, 762-768.
- , 1986: Low and midlevel cloud analysis using nighttime multispectral imagery. *J. Climate Appl. Meteor.*, **25**, 1853-1869.
- Dept. of the United States Air Force (USAF), 1992: *Weather for Aircrews*, AF Manual 51-12, Vol I and II.
- Dills, P.N., D.W. Hillger, and J.F.W. Purdom, 1996a: Distinguishing between different meteorological phenomena and land surface properties using the multispectral imaging capabilities of GOES-8. Preprints, *Eighth Conf. on Satellite Met. & Ocean.*, Atlanta, GA, Amer. Meteor. Soc., 339-342.
- , J.F. Weaver, and K.J. Schrab, 1996b: Fog and stratus observations as seen with GOES-8 multispectral imager data. Preprints, *Eighth Conf. on Satellite Met. & Ocean.*, Atlanta, GA, Amer. Meteor. Soc., 343-346.
- Ellrod, G.P., 1996a: The use of GOES-8 multispectral imagery for the detection of aircraft icing regions. Preprints, *Eighth Conf. on Satellite Met. & Ocean.*, Atlanta, GA, Amer. Meteor. Soc., 168-171.
- , and J.P. Nelson III, 1996b: Assessment of GOES-8 imager data quality. Preprints, *Eighth Conf. on Satellite Met. & Ocean.*, Atlanta, GA, Amer. Meteor. Soc., 105-109.
- , 1995: Advances in the detection and analysis of fog at night using GOES multispectral infrared imagery. *Wea. Forecasting*, **10**, 606-619.
- , 1994: Potential use of GOES-I multispectral infrared imagery for nighttime detection of precipitation. Preprints, *Seventh Conf. on Satellite Met. & Ocean.*, Monterey, CA, Amer. Meteor. Soc., 164-167.
- , 1992: Potential applications of GOES-I 3.9 μ m infrared imagery. Preprints, *Sixth Conf. on Satellite Met. & Ocean.*, Atlanta, GA, Amer. Meteor. Soc., 184-187.

- Federal Aviation Administration (FAA), 1977: *Aviation Weather Services*. Supplement to Aviation Weather, AC 00-6A.
- Forbes, G.S., Y. Hu, B.G. Brown, B.C. Bernstein, and M.K. Politovich, 1993: Examination of conditions in the proximity of pilot reports of aircraft icing during STORM-FEST. Preprints, *Fifth Int'l Conf. of Aviation Weather Systems*, Vienna, VA, Amer. Meteor. Soc., 282-286.
- Fuchs, W., and K.P. Schickel, 1995: Aircraft icing in visual meteorological conditions below low stratus clouds. *Atmospheric Research*, **36**, 339-345.
- Gayet, J.F., M. Bain, and R.G. Soulage, 1984: Role of ice crystals on ice accretion processes. *Proceedings of Second Int'l Workshop on Atmospheric Icing of Structures*, Trondheim, Norway, 65-69.
- Guttman, N.B. and R.K. Jeck, 1987: Aircraft icing environment in low ceiling conditions near Washington, D.C. *Wea. Forecasting*, **2**, 114-126.
- Hansman, Jr., R.J., 1989: The influence of ice accretion physics on the forecasting of aircraft icing conditions. Preprints, *Third Int'l Conf. on the Aviation Weather System*, Anaheim, CA, Amer. Meteor. Soc., 154-158.
- , and M.S. Kirby, 1987: Comparison of wet and dry growth in artificial and flight icing conditions. *J. Thermophysics and Heat Transfer*, **1**, 215-221.
- , and M.S. Kirby, 1986: Measurement of ice growth during simulated and natural icing conditions using ultrasonic pulse-echo techniques. *J. Aircraft*, **23**, 492-498.
- , 1985: Droplet size distribution effects on aircraft ice accretion. *J. Aircraft*, **22**, 503-508.
- Hoffmann, H.E., 1990: The icing of the wing and of the elevator of an aircraft. *Fifth Int'l Workshop on Atmos. Icing of Structures (IWAIS '90)*, Tokyo, Japan, B1-1-(1)-(4).
- , 1988: Icing degree moderate to severe: If and where in clouds. *16th Congress Int'l Council of Aeronautical Sci. (ICAS)*, Jerusalem, Israel, 1801-1812.
- Hunt, G.E., 1973: Radiative properties of terrestrial clouds at visible and infra-red thermal window wavelengths. *Quart. J. Roy. Meteor. Soc.*, **99**, 346-369.
- Jones, A.S., and T.H. Vonder Haar, 1990: Passive microwave remote sensing of cloud liquid water over land regions. *J. Geophysical Research*, **95**, 16,673-16,683.
- Kidder, S.Q., and T.H. Vonder Haar, 1995: *Satellite Meteorology: An Introduction*, San Diego, CA, Academic Press, 466 pp.
- , and H.T. Wu, 1987: A multispectral study of the St. Louis area under snow-covered conditions using NOAA-7 AVHRR data. *Remote Sens. of Environ.*, **22**, 159-172.
- , and H.T. Wu, 1984: Dramatic contrast between low clouds and snow cover in daytime 3.7 micron imagery. *Mon. Wea. Rev.*, **112**, 2345-2346.
- Kieth, C.W., and D. Cornell, 1995: A comparison of aircraft icing forecast models. Preprints, *Sixth Conf. on Aviation Weather Systems*, Dallas, TX, Amer. Meteor. Soc., 431-435.
- Kleespies, T.J., 1995: The retrieval of marine stratiform cloud properties from multiple observations in the 3.9 μ m window under conditions of varying solar illumination. *J. Appl. Meteor.*, **34**, 1512-1524.

——, 1989: Multispectral image analysis of hurricane Gilbert. Preprints, *Fourth Conf. On Satl. Meteor. and Oceanography*, San Diego, CA, Amer. Meteor. Soc., 54-58.

Knapp, D.I., 1992: Verification report: Comparison of various icing analysis and forecast techniques. Air Force Global Weather Center, 5 pp.

Lawyer, D.T., 1995: Exploratory study of an icing index from satellite remote sensing of cloud liquid water. M.S. thesis, Dept. of Atmospheric Science, Colorado State University, 111 pp.

Lee, T.F., J. Turk, K. Richardson, J. Hawkins, C. Skupniewicz, and P.A. Durkee, 1996: Use of products based on the GOES-8 3.9 micron imager as forecast tools. Preprints, *Eighth Conf. on Satellite Met. & Ocean.*, Atlanta, GA, Amer. Meteor. Soc., 179-182.

——, J.R. Clark, and S.D. Swadley, 1994: Potential applications of the SSM/I cloud liquid water parameter to the estimation of marine aircraft icing. *Wea. Forecasting*, 9, 173-182.

Liljas, E., 1986: Use of the AVHRR 3.7 micrometer channel in multispectral cloud classification. *SMHI Promis-Rapporter*, Nr 2, January.

Marwitz, J.D. et. al., 1996: Meteorological conditions associated with the ATR72 aircraft accident near Roselawn, Indiana on 31 October 1994. Submitted to *Bull. Amer. Meteor. Soc.*

Mason, B., and J. Schmetz, 1992: Meteorological satellites. *Int. J. Remote Sens.*, 13, 1153-1172.

Menzel, W.P., and J.F.W. Purdom, 1994: Introducing GOES-I: The first of a new generation of geostationary operational environmental satellites. *Bull. Amer. Meteor. Soc.*, 75, 757-781.

Murphy, A.H., and R.L. Winkler, 1987: A general framework for forecast verification. *Mon. Wea. Rev.*, 115, 1330-1338.

Nelson III, J.P., and G.P. Ellrod, 1996: Improved GOES-8 multispectral (10.7 μ m-3.9 μ m) satellite imagery to detect stratus and fog at night. Preprints, *Eighth Conf. on Satellite Met. & Ocean.*, Atlanta, GA, Amer. Meteor. Soc., 172-176.

Newton, D.W., 1978: An integrated approach to the problem of aircraft icing. *J. Aircraft*, 15, 374-380.

Olesen, F-S., and H. Grassl, 1985: Cloud detection and classification over oceans at night with NOAA-7. *Int. J. Remote Sens.*, 6, 1435-1444.

Olsen, W., R. Shaw, and J. Newton, 1984: Ice shapes and the resulting drag increase for a NACA 0012 airfoil. NASA TM-83556.

Osborne, Jr., L.F., 1989: Remote detection of aircraft icing hazards by doppler radar. Preprints, *Third Int'l Conf. on the Aviation Weather System*, Anaheim, CA, Amer. Meteor. Soc., 164-167.

Pobanz, B.M., J.D. Marwitz, and M.K. Politovich, 1994: Conditions associated with large-drop regions. *J. Appl. Meteor.*, 33, 1366-1372.

Politovich, M.K., B.B. Stankov, and B.E. Martner, 1995: Determination of liquid water altitudes using combined remote sensors. *J. Appl. Meteor.*, 34, 2060-2075.

——, 1993: Aircraft icing: Meteorological effects on aircraft performance. Preprints, *Fifth Int'l Conf. on Aviation Weather Systems*, Vienna, VA, Amer. Meteor. Soc., 435-439.

- , and R. Olson, 1991: An evaluation of aircraft icing forecasts for the continental United States. Preprints, *Fourth Int'l Conf. On Aviation Weather Systems*, Paris, France, Amer. Meteor. Soc., 234-238.
- , 1989a: Aircraft icing caused by large supercooled droplets. *J. Appl. Meteor.*, **28**, 856-868.
- , 1989b: Measurements of hazardous icing conditions. Preprints, *Third Int'l Conf. on the Aviation Weather System*, Anaheim, CA, Amer. Meteor. Soc., 159-163.
- Popa Fotino, I.A., J.A. Schroeder, and M.T. Decker, 1986: Ground-based detection of aircraft icing conditions using microwave radiometers. *IEEE Trans. Geosci. Remote Sensing*, **6**, 975-982.
- Prins, E.M., and W.P. Menzel, 1992: Geostationary satellite estimation of biomass burning in South America. *Int. J. Remote Sens.*, **13**, 2783-2799.
- Rao, K.P., S.J. Holmes, R.K. Anderson, J.S. Winston, and P.E. Lehor, 1990: *Weather Satellites: Systems, Data, and Environmental Applications*. Amer. Meteor. Soc., 503 pp.
- Rasmussen, R., M. Politovich, J. Marwitz, W. Sand, J. McGinley, J. Smart, R. Pielke, S. Rutledge, D. Wesley, G. Stossmeister, B. Bernstein, K. Elmore, N. Powell, E. Westwater, B. Stankov, and D. Burrows, 1992: Winter Icing and Storms Project (WISP). *Bull. Amer. Meteor. Soc.*, **73**, 951-974.
- Sand, W.R. and M.K. Politovich, 1991: A program to improve aircraft icing forecasts. Preprints, *29th AIAA Aerospace Sciences Meeting*, Reno, NV, 7-10 January. Amer. Inst. of Aero. and Astron., Washington, D.C., AIAA-91-0557.
- , 1985: Aircraft icing conditions--"Normal and Unusual". *J. Air Law and Commerce*, **19**, I-3-I-17.
- , W.A. Cooper, M.K. Politovich, and D.L. Veal, 1984: Icing conditions encountered by a research aircraft. *J. Climate Appl. Meteor.*, **23**, 1427-1440.
- Schickel, K.P., H.E. Hoffmann, K.T. Kriebel, 1994: Identification of icing water clouds by NOAA AVHRR satellite data. *Atmospheric Research*, **34**, 177-183.
- Schott, J.R., and A. Henderson-Sellers, 1984: Radiation, the atmosphere, and satellite sensors. *Satellite Sensing of a Cloudy Atmosphere*, A. Henderson-Sellers, Ed., Taylor & Francis, Philadelphia, PA, 45-89.
- Schultz, P. and M.K. Politovich, 1992: Toward the improvement of aircraft-icing forecasts for the continental United States. *Wea. Forecasting*, **7**, 491-500.
- Scorer, R.S., 1986: *Cloud Investigation By Satellite*. Halsted Press, West Sussex, England, 356 pp.
- Setvak, M., and C.A. Doswell III, 1991: The AVHRR channel 3 cloud top reflectivity of convective storms. *Mon. Wea. Rev.*, **119**, 841-847.
- Shenk, W.E., and R.J. Curran, 1973: A multi-spectral method for estimateing cirrus cloud top heights. *J. Appl. Meteor.*, **12**, 1213-1216.
- Shin, J., B. Berkowitz, H. Chen, and T. Cebeci, 1991: Prediction of ice shapes and their effect on airfoil performance. Preprints, *29th AIAA Aerospace Sciences Meeting*, Reno, NV, 7-10 January. Amer. Inst. of Aero. and Astron., Washington, D.C., AIAA-91-0264.

Smart, J.R., P.T. McCaslin, and J.A. McGinley, 1992: Forecasting meteorological conditions associated with aircraft icing during the winter icing and storms project (WISP). Preprints, *Symposium on Weather Forecasting*, Atlanta, GA, Amer. Meteor. Soc., 88-94.

Stankov, B.B., and A.J. Bedard, Jr., 1994: Remote sensing observations of winter aircraft icing conditions: A case study. *J. Aircraft*, 31, 79-89.

Thompson, G., T.F. Lee, R.T. Brintjes, and R. Bullock, 1996a: Using satellite data to reduce areal extent of predicted icing. Submitted to *Wea. Forecasting*.

-----, R.T. Brintjes, B.G. Brown, and F. Hage, 1996b: Intercomparison of in-flight icing algorithms. Part I: WISP94 real-time icing prediction and evaluation program. Submitted to *Wea. Forecasting*.

-----, R.T. Brintjes, and B.G. Brown, 1995: A comprehensive icing prediction and evaluation program. Preprints, *Sixth Conf. on Aviation Weather Systems*, Dallas, TX, Amer. Meteor. Soc., 243-248.

Tucker, W.B., 1983: *Current Procedures for Forecasting Aviation Icing*. US Army Corps of Engineers, Special Report 83-24.

Weber, E.M., and S. Wilderotter, 1981: *Satellite Interpretation*. Air Weather Service, 3rd Wea. Wing, 3WW Technical Note-81/001, Offutt AFB, NE, 95 pp.